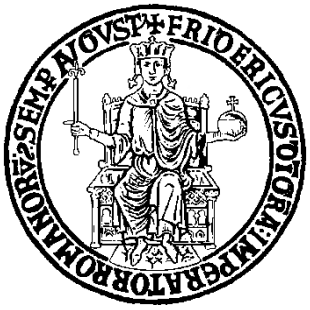

UNIVERSITY OF NAPLES FEDERICO II

DEPARTMENT OF INDUSTRIAL ENGINEERING

- MECHANIC AND ENERGETIC SECTION -

PH.D. SCHOOL IN INDUSTRIAL ENGINEERING – XXXII CYCLE

NUMERICAL INVESTIGATIONS OF INNOVATIVE SI ENGINES SUITABLE FOR HYBRID POWERTRAINS WITH REDUCED CO_2

Doctoral Thesis

Ph.D. School Coordinator
Prof. Michele Grassi

Tutor
Prof. Fabio Bozza
Dr. Ing. Vincenzo De Bellis

Ph.D. Candidate
Daniela Tufano

Contents

List of figures

List of tables

Abbreviation and nomenclature

Acronyms

0D-1D-3D	Zero-One-Three-dimensional
ACC	Adaptive Cruise Control
ADAS	Advanced Driver Assistance Systems
AI	Auto Ignition
ARPA-E	Advanced Research Project Agency -Energy
ATDC	After firing top dead center
Ba	Battery
BEV	Battery Electric Vehicle
BMEP	Brake Mean Effective Pressure
BSFC	Brake Specific Fuel Consumption
BSG	Belted Starter Generator
BTDC	Before top dead center
B-TDC	Bottom-Top Dead Center
BTE	Brake Thermal Efficiency
CAD	Crank angle degree
CAV	Connected and Automated Vehicles
CI	Compression Ignition
Cl	Clutch
CNG	Compressed Natural Gas
CO_2	Carbon dioxide
CoV	Coefficient of Variation
CSP	Conventional Spark Plug
DI	Direct Injection
DoE	Design of Experiment
DP	Dynamic Programming
DSF	Dynamic Skip Fire
ECM	Electronic Control Module
ECU	Engine Control Unit

EDM	Enhanced Driver Model
EG	Electric Generator
EGR	Exhaust Gas Recirculation
E-LIVC	Early-Late Intake Valve Closing
EM	Electric Motor
EMS	Energy Management Strategy
ETESS	Efficient Thermal Electric Skipping Strategy
EU	European Union
FTP	Federal Test Procedure
GB	Gear-Box
GHG	Greenhouse Gas
H_2	Hydrogen
HEV	Hybrid Electric Vehicle
ICE	Internal Combustion Engine
IMEP	Indicated Mean Effective Pressure
IMPO	Integral of Modulus of Pressure Oscillations
ITE	Indicated Thermal Efficiency
IVC/O	Intake Valve Closing/Opening
KDE	Kernel Density Estimator
LHV	Lower heating value
MAPO	Maximum Amplitude of Pressure Oscillations
MC	Main-Chamber
MBT	Maximum Brake Torque
MCE	Multi Cylinder Engine
MFB	Mass fraction burned
MGU	Motor Generator Units
NEDC	New European Driving Cycle
NO_X	Nitrogen oxides
OBD	On-Board Diagnostic
PC	Pre-Chamber

PCSP	Pre-chamber Spark Plug
PFI	Port Fuel Injection
PHEV	Plug-in Hybrid Electric Vehicle
PM	Particle Matter
PMP	Pontryagin minimum principle
RB	Rule-Based
RDE	Real Driving Emission
RMSE	Root Mean Squared Error
SA	Spark Advance
SCE	Single Cylinder Engine
SI	Spark Ignition
SoC	State of Charge
SPaT	Signal Phase and Timing
VCR	Variable Compression Ratio
VD&PT	Vehicle Dynamics and Powertrain
VVA/L/T	Variable Valve Actuation/ Lift/ Timing
WI	Water Injection
WLTC	Worldwide harmonized Light-Duty vehicles Test Cycle
WOT	Wide Open Throttle

Latin Symbols

a	Acceleration for the EDM model
A_L, A_T A_w A_{tot}	Laminar / turbulent / wet/ total flame area
b	Deceleration for the EDM model
B	Bore
c_0	Tuning constant for the ETESS model
c_1	Braking Aggressiveness for the EDM model
c_d	Discharge coefficient
c_{fd0}, c_{fdm}	Tuning constants of tumble decay function
c_{jet}	Fresh charge entrainment multiplier for the combustion model

c_{Kin0}	Tuning constant of inlet flow coefficient
c_{PKk}	Tuning constant of turbulence Production
c_{rT0}, c_{rTm}	Parameters for tumble radius adjustment
c_{Tin0}	Tuning constant of tumble flow coefficient
c_{trans}	Laminar turbulent transition multiplier for the combustion model
c_{wc}	Wall combustion tuning multiplier for the combustion model
c_{wrk}	Wrinkling multiplier for the combustion model
D_3	Fractal dimension
$\mathbf{D_L}$	Diffusivity
E	Energy
e	Internal energy
f	Function
f_d	Decay function of tumble
H	Hamiltonian
H	Piston position referred to cylinder head
H	Piston position referred to cylinder head
I	Current
J	Performance index
k	Turbulent kinetic energy
K	Mean flow kinetic energy
k	Ratio of the specific heats
k	Turbulent kinetic energy
K	Mean flow kinetic energy
K_{pist}	Kinetic energy related to piston motion
K_T	Kinetic energy related to tumble motion
L	Cost function
L_{min}, L_{max}	Minimum / maximum flame front wrinkling scale
$\mathbf{L_t}$, $\mathbf{L_k}$	Integral and Kolmogorov length scale
m	Mass
p	Pressure
P	Power

$\mathbf{Q}$	Heat transfer
$\boldsymbol{R}$	Gas constant/ Coefficient of determination
$\boldsymbol{r_{crit}}$	PC critical radius for MC combustion start
$\mathbf{r_f}$	Flame radius
$\boldsymbol{r_T}$	Tumble radius
$\boldsymbol{s}$	Distance
$\mathbf{S_L}$	Laminar Flame Speed
$\mathbf{T}$	Temperature /Torque/ Tumble angular momentum
$\boldsymbol{t}$	Time
$\mathbf{t_{trans}}$	Characteristic time scale
$\boldsymbol{u}$	Control variable, power-split
$\boldsymbol{U}$	Variation range of the control variable
$\boldsymbol{u'}$	Turbulence intensity
$\boldsymbol{v}$	Velocity
$\mathbf{V}$	Volume
$\boldsymbol{x}$	State variable
$\boldsymbol{X}$	Variation range of the state variable
$\mathbf{x_b}$	Mass Fraction Burned
$\mathbf{x_b}$	Burned gas fraction
$\mathbf{X_{EGR}}$	Mass Fraction of Residual Gas

Greek symbols

$\mathbf{\Phi}$	Equivalence ratio
$\boldsymbol{\Lambda_T}$	Taylor length scale
α	Constant for the laminar speed correlation
β	Constant for the laminar speed correlation / Penalization factor
δ	Acceleration Exponent for the EDM model
δ_L	Flame Thickness
ε	Dissipation rate
γ	Penalizing factor in DP cost function

η	Efficiency
λ	Relative air/fuel ratio / Costate
ν_t	Turbulent viscosity
θ_{offset}	Speed limit offset for the EDM model
ρ	Density
τ	Entrainment characteristic time

Subscripts

0	Initial
10 / 50 / 90	Referring to 10 / 50 / 90% of mass fraction burned
aero	Aerodynamic
b	Burned
batt	Battery
cyl	Related to the cylinder
el	Electric
entr	Entrainment
eq	Equivalent
f	Final, fuel
fractal	Related to fractal approach
in	Incoming
inj	Injected
jet	Related to turbulent jet
min	Minimum
out	Outcoming
pwt	Powertrain
ref	Reference
roll	Rolling
th	Thermal
trac	Tractive
u	Unburned

Superscripts

$\dot{}$	Temporal derivative
*	Optimal

Abstract

The problem of atmospheric air pollution, caused by the Internal Combustion Engines (ICEs), has never been greater than today. Car manufacturers, driven by more and more stringent legislations, are continuously forced to find proper technical solutions to deal with this challenge, without giving up on the high standards regarding engine performance. In particular, the new emission limit for the CO_2 recently set for the 2026, with a target of 80 g/km of CO_2 along the WLTC, has never pushed so much the automotive manufacturers in developing innovative and clean solutions to improve the fuel economy of the vehicle fleets. However, how to solve this problem is still an open debate. On the one hand, the complete disappearance in few years of the ICE-based propulsion systems in the automotive sector, replaced by fuel cell and/or Battery Electric Vehicles (BEVs) seems to be expected. On the other hand, several analyses declare that potential benefits of a BEV cannot be easily defined. Indeed, if the CO_2 formed during the entire vehicle life cycle is considered, the emissions from the two antagonist vehicles become comparable, to such an extent that ICE-based vehicles could be even better than the "*zero-emission*" alternatives. As often happen, the truth is somewhere in-between, hence, it should be expected in the years to come rather than a pure electric or ICE-based mobility a scenario characterized by variegated technologies that are best suited to the contest in which they are employed. This means that ICE-based vehicles, HEVs, PHEVs, BEVs or even Fuel Cell based vehicles, will coexist in the market for a long time, pushing car manufactures to overcome the limits related to each technology.

On the light of the above concerns, the topic of this research activity is to numerically investigate, through a hierarchical simulation-level approach, innovative SI engines, eventually suitable for hybrid powertrains, with a strongly reduced CO_2 impact. To this aim, two different ICEs are analyzed, assessing their CO_2 emission along the WLTC. The former is a downsized turbocharged VVA 2-cylinder engine, for a conventional vehicle application, defining the reference for the state of art of ICE-based propulsion system. The latter is an innovative 4-cylinder SI engine, equipped with an active pre-chamber ignition system, which guarantees an ultra-lean operation all over the engine operating range. Here, HEV/PHEV architectures are considered for the vehicle simulation. Additionally, the potential fuel economy as well as CO_2 benefits, coming from Connected and Automated Vehicles (CAV), are investigated through a numerical methodology able to benchmark these last on a real world-scenario.

The simulation efforts carried out to assess the previous objectives is mainly effected in a 0D/1D modelling environment, where the whole engine system is schematized through a network of 1D pipes and 0D cylinders, the latter described in term of in-house developed quasi-dimensional models of the in-cylinder phenomena. In particular, the flame propagation in the conventional engine is modeled according to a well-assessed version of the fractal combustion model developed at the University of Naples Federico II. Whereas, for the pre-chamber engine, a dedicated and innovative procedure, still based on the fractal theory, is developed, since, differently from conventional SI ICEs, only a few predictive combustion models were available in the current literature at the beginning of this activity. The reliability of the overall simulation models is checked for both the engines through the comparisons with 3D or experimental data, using a unique engine-dependent set of tuning constants. Once verified that the physics included in the model is accurate enough to guarantee a good agreement, the model is utilized as a predictive tool for deriving the complete performance maps of both a conventional and a pre-chamber engine.

To this aim, a Rule-Based (RB) calibration strategy is also implemented in both the models to identify the optimal values of each control variable in whole operating plane. Of course, the reliability of the RB calibration is demonstrated, too, through the comparison with the outcomes of a general-purpose optimizer, for both the engine architectures. The RB methodology demonstrates to furnish control parameter close to the optimizer, in a very limited computational time.

Finally, the engine maps are embedded in vehicle simulations to quantify the CO_2 emission over a WLTC, for many different engine and vehicles architectures. In parallel to the above activities, a dedicated off-line Energy Management Strategy, named ETESS, for the HEV is also developed aiming to minimize the CO_2 emission along a prescribed mission. The ETESS is compared with the well-known Pontryagin Minimum Principle (PMP) in terms of management of the control units and vehicle performance outcomes. Although the ETESS can only furnish a sub-optimal solution, the reduced computational time to the respect of the PMP suggests the possibility to implement it for an on-line application, with limited penalization.

The results carried out in this research activity show that the ICE-based system can reach 94.81g/km CO_2 along the WTLC. However, this value is still far away from the EU target of 80 g/km CO_2 of 2026. On the contrary, PHEV architecture combined with a pre-chamber engine, able to achieve a maximum Indicted Thermal Efficiency (ITE) around 50%, attains a CO_2 emission equal to 43.0 g/km along the same regulatory driving cycle.

Although this impressive result, it has to remark that in the current regulation the CO_2 emissions necessary for charging the battery is not included, leading to a not representative enough results of the real condition. On the contrary, the HEV configuration reaches 88.8 g/km CO_2, very close to the EU ambitious target, suggesting that the combination of these two technologies could be a suitable solution for the years to come. Additionally, connected and autonomous vehicle, thanks to the possibility to use the look-ahead information from the route can further improve the CO_2 reduction of about 15-17%, respect to a vehicle not equipped with this technology.

1. Introduction

Nowadays, climate change and global warming are considered as the major environmental problems to be faced by our societies. The solution of these ambitious challenges requires a series of harmonized actions, such as a growing share of renewable sources, the reduction of carbon fuels use, improvements in energy conversion efficiency, and structural changes in the economy, all driven and supported by the introduction of a stringent legislation.

The trend of the Greenhouse Gas (GHG) emissions by sector is reported in the time frame from 1990 to 2015 in *Figure 1-1a*. The actions taken by the European Union (EU) during those years were already able to determine a consistent CO_2-equivalent drop, leading in the 2017 to overcome the 20% reduction target, as set by EU for 2020, reaching a 21.7% of lower GHG [1]. However, the transport sector was not characterized by the same gradual decline in emissions as other ones, Figure 1-1 gray line. Indeed, only from the 2007 the transport-related CO_2 emissions started to marginally reduce with a value in 2015 still higher than the one in 1990. Since the transportation sector represents a huge portion of global emission (24%), second only to energy supply and industry (40%), the only way to reach the EU 2030 target of 40 % reduction of GHG is to further improve all the technologies connected to this area, above all the ones related to the road transport, which accounts for nearly 70% of all GHG emissions of the whole sector, *Figure 1-1 right*.

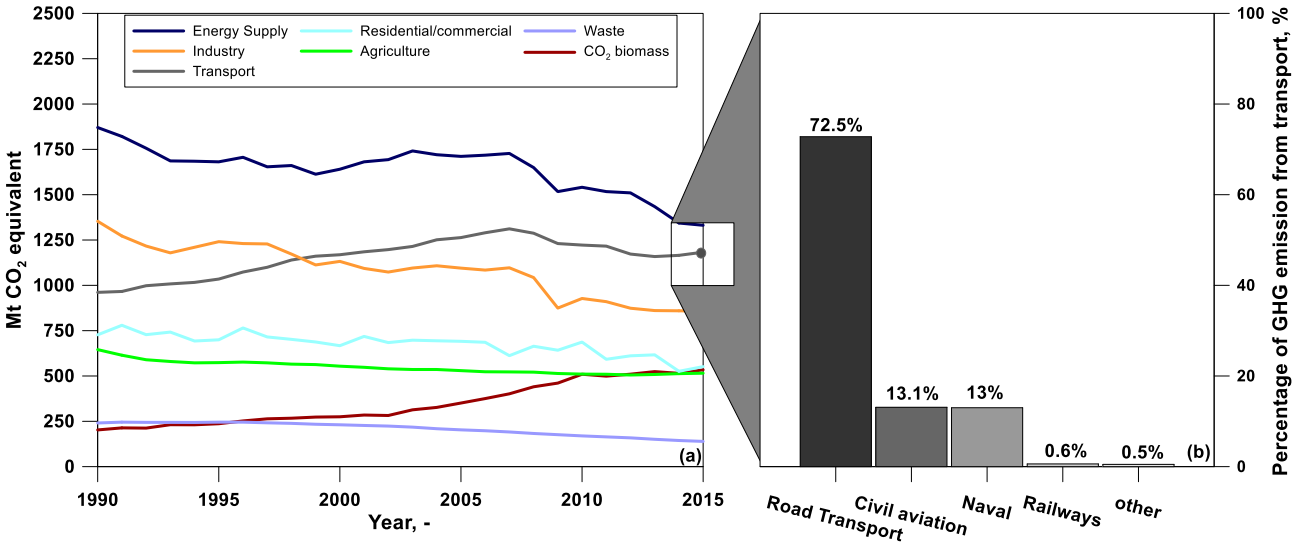

Figure 1-1 GHG emissions by aggregated sector, Mt of equivalent CO_2 and percentage of GHG from the only transport sector [1].

To control GHG emissions in the road sector, a new emission limit for CO_2 was recently set, with a target of 80 g/km of CO_2 as an average for all new passenger cars in 2026. The introduction of this limitation combined with the ones related to the pollutant emissions, listed in *Figure 1-2*, has never pushed so much the automotive manufacturers in developing innovative and clean solutions to improve the fuel economy of the vehicle fleets. However, the debate about how to reach these ambitious targets is still open [2][3].

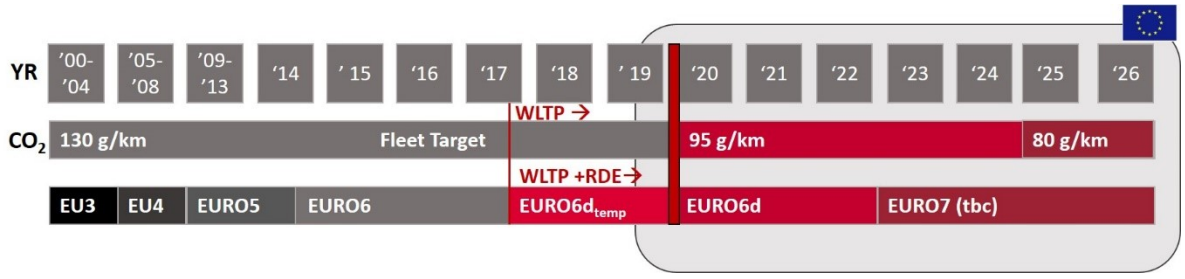

Figure 1-2 CO_2 and pollutant emissions limits roadmap

In 2013, the U.S. Environmental Protection Agency discovered that some Volkswagen vehicles equipped with diesel engine were emitting more than 40 times the NO_X declared on the lab test. The automaker admitted that almost 500k vehicles were equipped with illegal ECU software, designated to detect the regulatory approval test. This emission scandal erupted also in Europe and worldwide, involving 11 million of vehicles, and other car manufactures, such as BMW, Porsche, Audi, which were put under investigation [4]. As a consequence, the majority of the European cities such as Paris, Athens or Stuttgart announced to ban Diesel engine by 2050. This scandal hit the entire automotive sector, from Diesel to gasoline based fuel propulsion system, leading to the idea that the Internal Combustion Engines (ICE) would disappear within a few years, due to their inability to respect the stringent EU regulation [5]. In a few years, a full-electric mobility, based on Battery Electric Vehicles (BEVs), was considered the most promising solution, persuasively supported by politicians and public opinion, since it guarantees "*zero-emissions*" at the tail-pipe. Alternative propulsion architectures, such as Hybrid Electric Vehicles (HEVs) and Plug-in HEV (PHEVs), were only considered useful as a temporary transition from standard ICE-powered vehicles to a full electric mobility. However, apart from any preconceived belief, it was soon realized that a consistent comparison requires to consider the CO_2 emitted by the vehicle along its entire life cycle, as shown in *Figure 1-3*. Under this point of view, the declared potential benefits of a BEV cannot be easily defined, as it had been initially thought. Indeed, if the CO_2 formed during the vehicle production and the one generated during the battery charging are included in the analysis, the emissions from the two antagonist vehicles become comparable, to such an extent that ICE-based vehicles could be even better then apparently "greener" alternatives.

Moreover, the type of the energy source considered for producing the electricity aimed at feeding the battery, strongly affects the CO_2 production, indeed only when renewable energy sources are used, those technologies can lead to consistent benefits. Since the availability of the renewable energy is limited and country-dependent, BEV or PHEV cannot be considered as the only practical alternative.

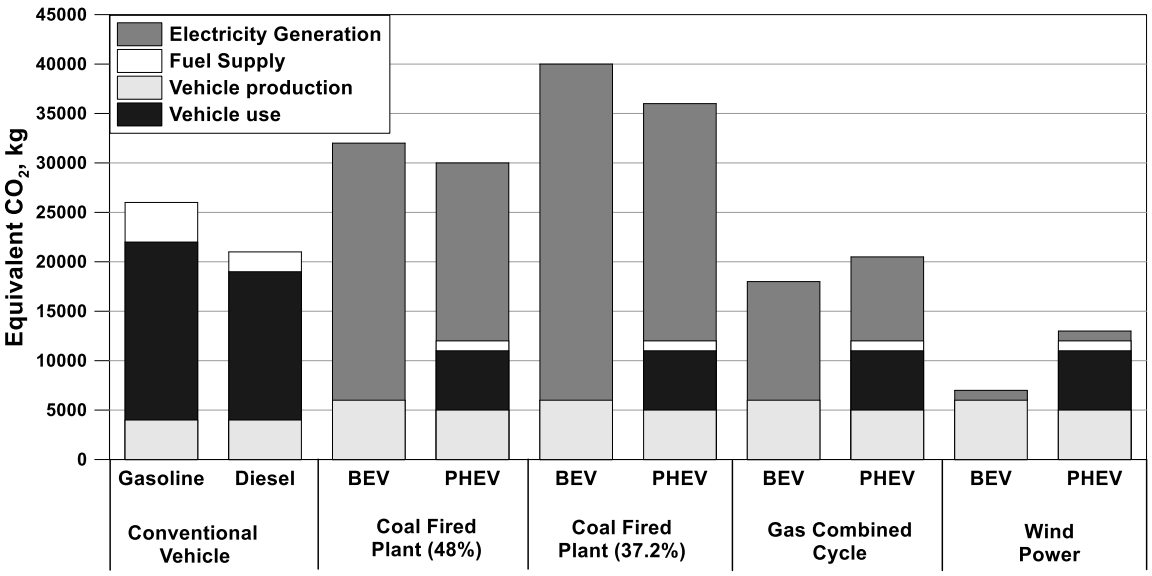

Figure 1-3 Life cycle of the equivalent CO_2 of a compact car for different drive trains (120000km)[6].

As an example, in *Table 1.1* the average CO_2 for BEV vehicles along the related regulatory approval driving cycle for different countries is reported. It was evaluated starting from the energy required to accomplish the whole regulatory driving cycle, and then converted through an average emission factor. This last was defined for each geographical area, taking into account the average CO_2 produced per kWh of the power plants. It is evident that only the country characterized by a low emission factor can actually reach the target through the employment of BEV. The last but not the least aspect to be analyzed is the customer expectation: the higher ownership cost of the BEV, combined to the high battery charging-time and to the low autonomy, strongly limits the market acceptance and diffusion [7].

In the light of those concerns, rather than a *pure-electric* future, it should be expected in the years to come, an *eclectic* scenario, characterized by variegated technologies that are best suited to the contest in which they are employed. This means that ICE-based vehicles, HEVs, PHEVs, BEVs or even Fuel Cell based vehicles, will coexist in the market for a long time, pushing car manufactures to overcome the limits related to each technology.

Table 1.1 Estimated CO_2 emissions for different geographical area.

	Country	Emission factor, gCO_2/kWh	CO_2 BEV g/km	Limit, g/km	Country	Emission factor, gCO_2/kWh	CO_2 BEV g/km	Limit, g/km
Europe	Italy	431	**80.2**	95(2020)	USA	586	109.0	105
	France	105	**19.5**	"	Canada	196	**36.5**	"
	Spain	341	**63.4**	"	China	1075	200.0	117
	Greece	767	142.7	"	India	1800	334.8	113
	UK	623	115.9	"				
	Germany	615	144.4	"				

In particular, for the ICEs, a further effort to improve their efficiency is mandatory if employed in conventional vehicles or hybrid ones. Concerning Spark-Ignition (SI) engines, high efficiency downsized engines with VVA architectures [8] are now state-of-the-art. Additional benefits are expected from advanced anti-knock measures, such as Variable Compression Ratio (VCR) [9], cooled Exhaust Gas Recirculation (EGR) [10], and Water Injection (WI) [11]. Combustion systems that work with very lean air/fuel mixture are achieving resounding interest due to the possibility to further increase the engine efficiency [12],[13],[14]. Regarding the electric application, automakers are moving toward the improvement of the battery/motor system, maintaining acceptable costs. The future challenge is to have propulsion systems with light weight, long autonomy/life and with the possibility to quickly recharge the batteries [15]. Recently, with HEV and PHEV penetration in the market, the powertrain controls that consider the propulsion system as whole, started to be analyzed, too. Here the focus turns from optimizing the single components (the engine, the electric unit, the transmission, etc.) to a new paradigm, where the operation of each sub-component of the whole propulsion system is co-optimized by an energy management controller. Therefore, the Energy Management Strategy (EMS) becomes essential to minimize the fuel consumption and the CO_2 emissions, as well [16],[17].

In the light of the above considerations, the aim of this research activity is to numerically investigate, through a hierarchical simulation-level approach, innovative SI engines, eventually suitable for hybrid powertrains, with a strongly reduced CO_2 impact. To this aim, two different ICEs have been analysed, assessing their CO_2 emission along the WLTC.

The first one is a downsized turbocharged VVA 2-cylinder engine, for conventional vehicle application. The impact of combining well-known technologies for the reduction of fuel consumption are preliminary considered to define a state of art ICE-based propulsion system.

The second one is an innovative 4-cylinder SI engine, equipped with an active pre-chamber ignition system, which guarantees an ultra-lean operation (relative air/fuel ratio equal to 2), all over the engine operating plane.

Numerical engine and vehicle analyses, extensively described in this PhD Thesis, show that this innovative engine can achieve a maximum Indicted Thermal Efficiency (ITE) of around 50% and, embedded in a PHEV architecture, it is able to attain a CO_2 emissions as low as 50 g/km along the WLTC.

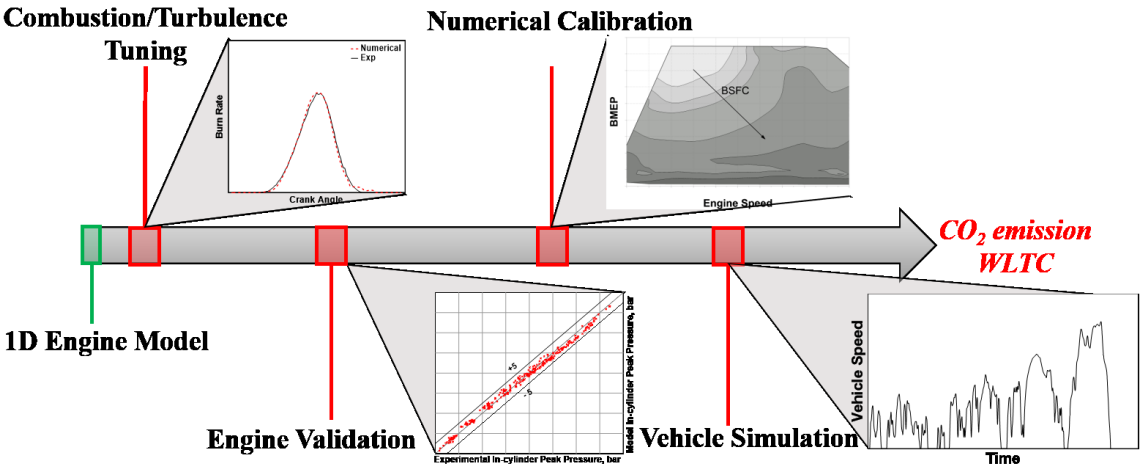

Figure 1-4 Main modelling steps of the research activity.

For both the engines under study, the methodology and main modelling steps reported in *Figure 1-4* were followed. Firstly, the geometry of the tested engine is schematized in a commercial modelling framework, following a 1D description of the flow inside the intake and the exhaust pipes. Phenomenological 0D sub-models are employed to reproduce in-cylinder phenomena such as turbulence, combustion and heat transfer. In particular, for the conventional engine, a quite-standard version of the fractal combustion model [18], developed at the University of Naples Federico II [19], was coupled as a user procedure to the commercial 1D code. For the combustion simulation inside the pre-chamber engine architecture, instead, a dedicated and original procedure, still based on the fractal theory, was developed. In particular, the original model was largely enhanced with the aim to describe all the basic phenomena occurring in an engine fitted with a PC, such as mixture preparation, turbulence evolution, flame area enhancement, burn rate development, etc. This represents an important achievement of this PhD Thesis, since, differently from conventional SI ICEs [19],[20], only a few predictive combustion models, capable to describe the basic physics behind a pre-chamber combustion system, were available in the current literature [21], [22], [23] at the beginning of this activity. Once developed, both engine models were tuned and validated according to 3D calculations and experimental data, by identifying a single set of tuning constants. For the conventional engine, a large validation data set was available, covering the whole engine operating map. For the pre-chamber engine, numerical results were firstly compared to experimental data taken on a prototype single-cylinder engine, and then, the same model, with few enhancements, was applied to foresee the multi-cylinder engine maps.

To this aim, for both engines, a Rule-Based (RB) calibration strategy was also set up, aiming to properly define the optimal control parameter setting for each operating condition, trying to mimic the experimental calibration procedure at the test bench. Finally, once the engine maps were developed, these last were embedded in a vehicle simulation with the aim to quantify the CO_2 emission over a WLTC. The downsized turbocharged 2-cylinder engine was tested in a conventional powertrain/vehicle, while a parallel/series HEV/PHEV architecture was considered for the pre-chamber one. In this last case, a dedicated EMS was also developed during this research activity. The latter is an off-line local optimization procedure, for a parallel/series hybrid vehicle, able to minimize the CO_2 emissions along a prescribed driving cycle.

The thesis is divided as follows. Firstly, a brief overview of internal combustion engine will be reported, describing the relevant physical phenomena occurring inside it, such as turbulence, combustion and knock. State of the art technologies aiming to improve the engine efficiency of the modern ICEs will be then presented. Among these, the advantages and main features of a pre-chamber engine will be particularly put into evidence. The physical sub-models developed to simulate engine phenomena will be illustrated, with particular emphasis on in-cylinder processes. Then, simulation results will be shown, analysing the tuning, the validation, and the numerical engine calibration procedures, providing the whole engine maps of the analysed engines. Finally, the vehicle simulation development and results will be reported and discussed.

An additionally study, reported in last chapter of this PhD Thesis, has been carried out at the Ohio State University, Center for Automotive Research (CAR) as part of the ongoing ARPA-E NEXTCAR project [24]. In particular, the goal of the 4 months research activity was the development of a numerical methodology to benchmark and evaluate the fuel economy benefits of a Connected and Autonomous vehicle over real-world driving scenarios. To this extent a Monte Carlo simulation [25] has been designed to determine the statistical distribution of the fuel consumption induced by driver behavior and Signal Phase and Timing (SPaT) conditions. The outcomes of this methodology would support the aim of this project, mainly to demonstrate that it is possible to achieve at least a 20% reduction in the fuel consumption of future CAVs compared to a baseline vehicle, without these Vehicle Dynamic and Powertrain (VD&PT) control technologies.

It is important to mention that the research work related to the development of the pre-chamber ultra-lean engine was supported by a European H2020 project EAGLE (*Efficient Additivated Gasoline Lean Engine*: https://h2020-eagle.eu/), having the objective to develop a prototype SI engine achieving 50% Brake Thermal Efficiency (BTE), and 50 g/km of CO_2 emissions along the WLTC.

The project involves 8 important EU partners and strongly integrates experimental and numerical activities, some of which reported in this thesis. This, on one side, underlines the vitality of the research in these fields, and, on the other side, denotes the increasing relevance of the simulations in the engine/vehicle development process.

Acknowledgements

 “This project has received funding from the European Union's Horizon 2020 research and innovation programme under grant agreement No 724084”

References

[1] https://www.eea.europa.eu/publications/european-union-greenhouse-gas-inventory-2017

[2] Ntziachristos, L., Mellios, G., Samaras, Z., "What is the real-world CO_2 reduction benefit of the 95 g/km passenger car average emission target to be reached by 2020," *Procedia-Social and Behavioral Sciences* 48: 2048-2057, 2012, doi: 10.1016/j.sbspro.2012.06.1178.

[3] Fontaras, G., Zacharof, N., Ciuffo, B., "Fuel consumption and CO_2 emissions from passenger cars in Europe–Laboratory versus real-world emissions," *Progress in Energy and Combustion Science* 60:97-131, 2017, doi: 10.1016/j.pecs.2016.12.004.

[4] Nemeth, K. and Carvalho, J.M., "Dieselgate and Consumer Law: Repercussions of the Volkswagen scandal in the European Union" *Journal of European Consumer and Market Law*, 6 (1), pp.35-35,2017, ISSN: 2364-4710.

[5] Sperling, D., "Future drive: Electric vehicles and sustainable transportation," Island Press, 2013, ISBN: 9781559633277.

[6] Helms, H., M. Pehnt, U. Lambrecht, A. Liebich., "Electric vehicle and plug-in hybrid energy efficiency and life cycle emissions," In 18th International Symposium Transport and Air Pollution, vol. 3, p. 113, 2010.

[7] Thiel, C., Perujo, A., Mercier, A, "Cost and CO_2 aspects of future vehicle options in Europe under new energy policy scenarios," *Energy policy*, 38, 7142-7151, (2010), doi:org/10.1016/j.enpol.2010.07.034.

[8] Hara, S., Suga, S., Watanabe, S., Nakamura, M., "Variable valve actuation systems for environmentally friendly engines," Hitachi Review, 58(7), 319-324, 2009,

[9] Roberts, M., "Benefits and Challenges of Variable Compression Ratio (VCR)," SAE Technical Paper 2003-01-0398, 2003, doi:10.4271/2003-01-0398.

[10] Francqueville, L., Michel, J., "On the Effects of EGR on Spark-Ignited Gasoline Combustion at High Load," *SAE Int J Engines* 7(4):1808-1823, 2014, doi:10.4271/2014-01-2628.

[11] Hoppe, F., Thewes, M., Baumgarten, H., Dohmen, J., "Water injection for gasoline engines: Potentials, challenges, and solutions," *International J of Engine Research* 17(1):86-96, 2016, doi:10.1177/1468087415599867.

[12] Germane, G., Wood, C., Hess, C., "Lean Combustion in Spark-Ignited Internal Combustion Engines - A Review," SAE Technical Paper 831694, 1983, doi:10.4271/831694.

[13] Moriyoshi, Y., Kuboyama, T., Kaneko, M., Yamada, T., Sato, H., "Fuel Stratification Using Twin-Tumble Intake Flows to Extend Lean Limit in Super-Lean Gasoline Combustion," SAE Technical Paper 2018-01-1664, 2018, doi:10.4271/2018-01-1664.

[14] Ji, C. Wang, S., "Effect of hydrogen addition on combustion and emissions performance of a spark ignition gasoline engine at lean conditions," *International journal of hydrogen energy*, 34(18), pp.7823-7834, doi:10.1016/j.ijhydene.2009.06.082.

[15] Amjad, S., Neelakrishnan, S., Rudramoorthy, R., "Review of design considerations and technological challenges for successful development and deployment of plug-in hybrid electric vehicles," *Renewable and Sustainable Energy Reviews*, 14(3), 1104-1110, 2010, doi:org/10.1016/j.rser.2009.11.001.

[16] Serrao, L., Onori, S., Rizzoni, G., "A ComparativeAnalysis of Energy Management Strategies for Hybrid Electric Vehicles," ASME. J. Dyn. Sys., Meas., Control. 133(3):031012-031012-9, 2011, doi: 10.1115/1.40032607.

[17] Pisu, P. and Rizzoni, G., "A Comparative Study Of Supervisory Control Strategies for Hybrid Electric Vehicles," *IEEE Transactions*, 506-518, doi: 10.1109/TCST.2007.894649.

[18] Gouldin, F., "An application of Fractals to Modeling Premixed Turbulent Flames," *Combustion and Flame* 68(3):249-266, 1987, doi:10.1016/0010-2180(87)90003-4.

[19] De Bellis, V., Severi, E., Fontanesi, S., Bozza, F., "Hierarchical 1D/3D approach for the development of a turbulent combustion model applied to a VVA turbocharged engine. Part II: Combustion model", Energy Procedia 45: 1027-1036, 2014,doi:10.1016/j.egypro.2014.01.108.

[20] Grill, M., Billinger, T. and Bargende, M., "Quasi-dimensional modeling of spark ignition engine combustion with variable valve train," SAE Technical Paper, 2006-01-1107, 2006, doi:10.4271/2006-01-1107.

[21] Demesoukas, S., Caillol, C., Higelin, P., Boiarciuc., "Zero-Dimensional Spark Ignition Combustion Modeling-A Comparison of Different Approaches," SAE Technical Paper, 2013-24-0022, 2013, doi:10.4271/2013-24-0022.

[22] Hiraoka, K., Nomura, K., Yuuki, A., Oda, Y. et al., "Phenomenological 0-Dimensional Combustion Model for Spark-Ignition Natural Gas Engine Equipped with Pre-Chamber," SAE Technical Paper 2016-01-0556, 2016, doi:10.4271/2016-01-0556.

[23] Shojaeefard, M. H., Keshavarz, M. "Flame propagation model for a rotary Atkinson cycle SI engine," International Journal of Automotive Technology, 19(1), 9-25, 2018, doi:10.1007/s12239-018-0002-7.

[24] https://arpa-e.energy.gov/?q=arpa-e-programs/nextcar.

[25] Metropolis, N. Ulam, S., "The Monte Carlo method," Journal of the American statistical association, 44(247), 335-341, 1949.

2. Overview of Internal Combustion Engine

An internal combustion engine has the aim to produce mechanical power from the chemical energy contained in the fuel, which is burned or oxidized inside the engine itself. Nowadays, SI and Compression Ignition (CI) engines are widely used in the transport and power generation sectors due to their simplicity, ruggedness and high power/weight ratio. Since this thesis is focused on SI engine for automotive application, only this kind of system will be briefly recalled in this chapter.

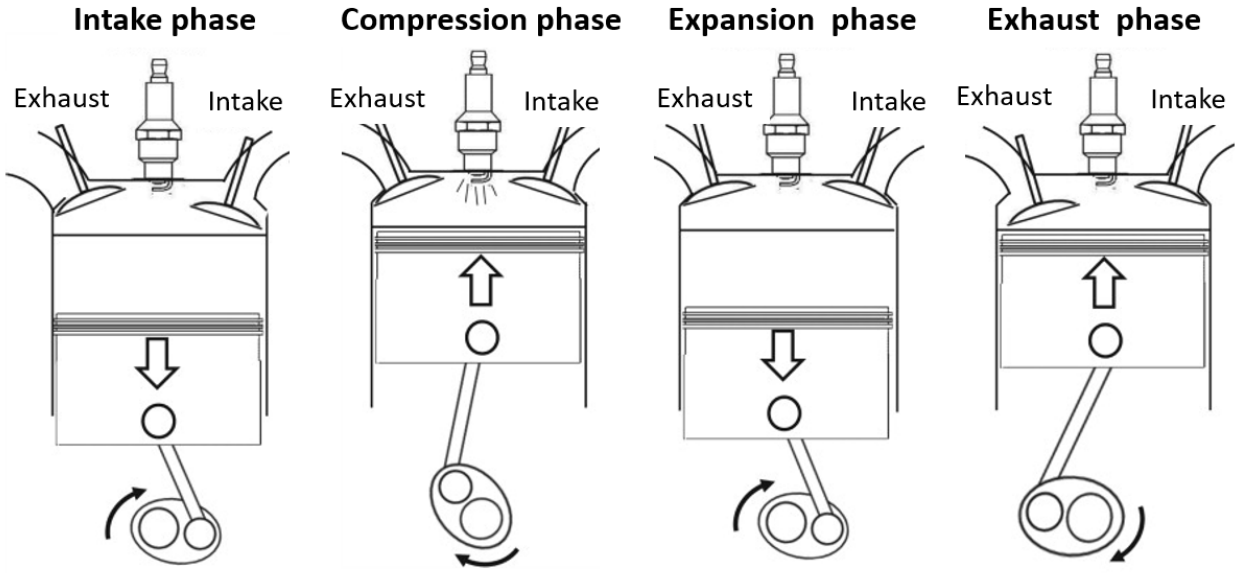

Figure 2-1 The four phases of a four-stroke SI engine.

In particular, the majority of SI ICEs for car application are characterized by a four-stroke working cycle in which each cylinder requires four strokes of its piston, two revolutions of the crankshaft, to realize the thermodynamic cycle [1]. A schematization of the operating cycle for an SI engine and its phases are illustrated in *Figure 2-1*. The four phases of this cycle, not exactly corresponding to the piston strokes, are the following:

1. *Intake phase*: begins at the Intake Valve Opening (IVO) and ends at the Intake Valve Closing(IVC). Generally, to optimize the cylinder filling, the IVO is usually realized before the TDC (0-40 CAD) and the IVC is delayed 40/50 CAD after the BDC.
2. *Compression phase*: when the intake valves are closed, the mixture inside the cylinder, fresh air or premixed air/fuel, is compressed through a volume reduction. The combustion is then started close to the TDC, leading to a rapid increment of the pressure and temperature inside the cylinder.
3. *Expansion phase*: starts conventionally at the TDC and finishes when the exhaust valves open (EVO). During this phase the piston collects useful work from the energy released during the combustion process.

4. *Exhaust phase*: It is divided in two sub-phases: spontaneous exhaust (from EVO to BDC) and forced exhaust (from BDC to EVC). In the former, the pressure inside the cylinder is higher than the exhaust manifold, leading the natural escape of the burned gasses from the cylinder to the exhaust pipes. In the latter, the piston movement from the BDC to the TDC pushes the exhaust gasses outside the cylinder. As soon as the intake valves are opened, the cycle starts again.

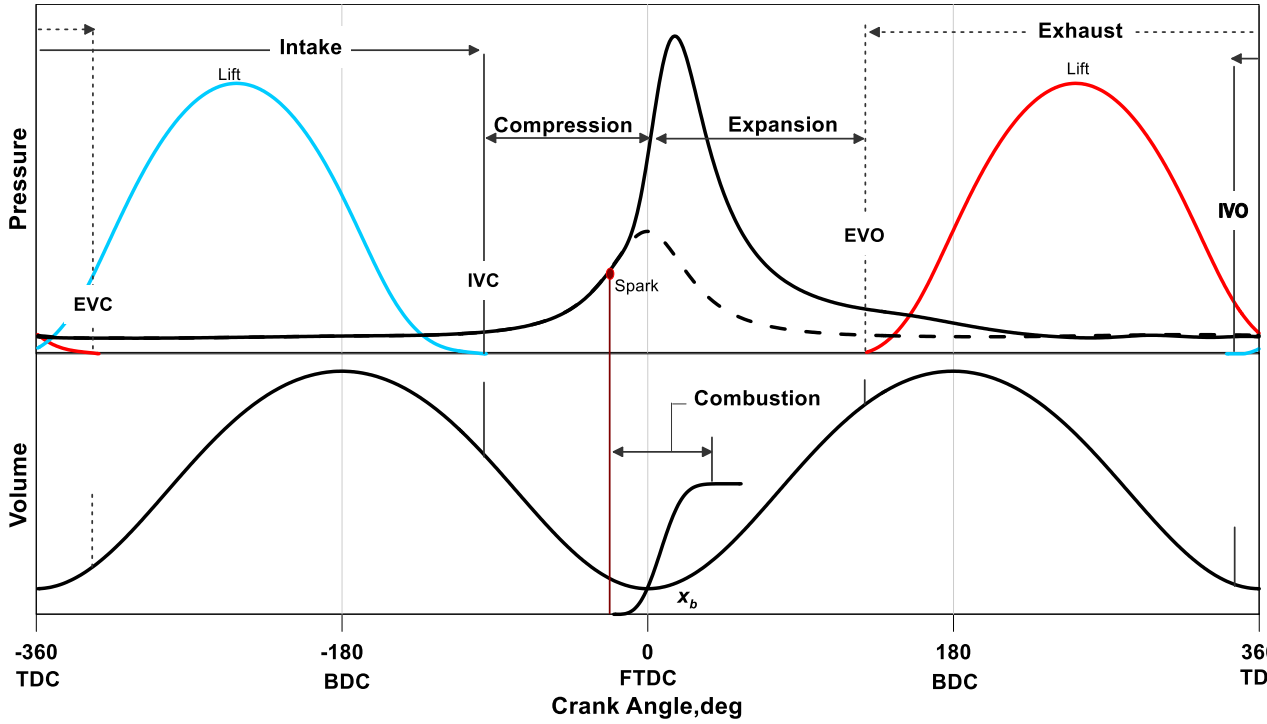

Figure 2-2 (top) pressure traces and valve lift profiles in fired/motored conditions, (bottom) cylinder volume and mass fraction burned x_b as a function of the crank angle [1].

The sequence of the events described above can be seen in *Figure* 2-2 in which valves timing, volume and pressure traces in motored (dashed line) and fired condition (continues line) are reported as a function of the crank angle for a conventional SI engine. Each phase has an important role on the power and efficiency of the overall cycle. Indeed during the intake phase, the proper amount of air/fuel mixture has to be introduced in the cylinder in order to get the prescribed load level with the correct mixture quality for the combustion. The intake pipes geometry, the throttle valve and the turbocharging system, if available, control the air flow, whereas the fuel can be injected in two different ways, namely a Port Fuel Injection (PFI) or a Direct Injection (DI). In the former, through a low-pressure system, the fuel is injected into the intake port, in the latter, the fuel is supplied directly into the cylinder at a higher pressure. High pressure injection, indeed, is required to ensure the fuel penetration, diffusion and vaporization. DI systems allow to improve the fuel consumption, with the possibility, in case of fuel wall impingement, of increased Particle Matter (PM), if compared with a PFI [2].

The intake ports have also to guarantee a proper gas motion inside the cylinder, since it influences the combustion process, the heat transfer and the air/fuel mixing. Through different orientation of the intake ports, geometry of the valves and shape of the combustion chamber, it is possible to generate three main gas motions: the tumble, the swirl, and the squish. The purpose of introducing this motion into combustion chambers is to increase the combustion rate and/or to ensure the mixing of the charge. As soon as the electric discharge across the spark plug is realized, generally with a certain advance before the TDC, the combustion starts. The turbulent flame develops from the spark plug, propagates into the combustion chamber and extinguishes with the contact of the walls. The combustion process rapidly increases the pressure inside the cylinder *Figure 2-2* and its duration is typically in the range of 40-60 CAD. Once the expansion phase ends, the exhaust phase occurs, enabling the cylinder scavenging process and the admission of the fresh charge for the next cycle.

2.1. Turbulent combustion

In a conventional SI engine, the combustion, generally initiated toward the end of the compression stroke at the spark plug, is mainly characterized by the interaction between the flame development and a turbulent flow. The flame is generated by the electric discharge in the spark plug, while the flow field is produced during the intake process and modified along the compression stroke. In *Figure 2-3*, the 2D flame evolution obtained in [3], by digital imaging of an optically accessible single cylinder PFI engine is shown.

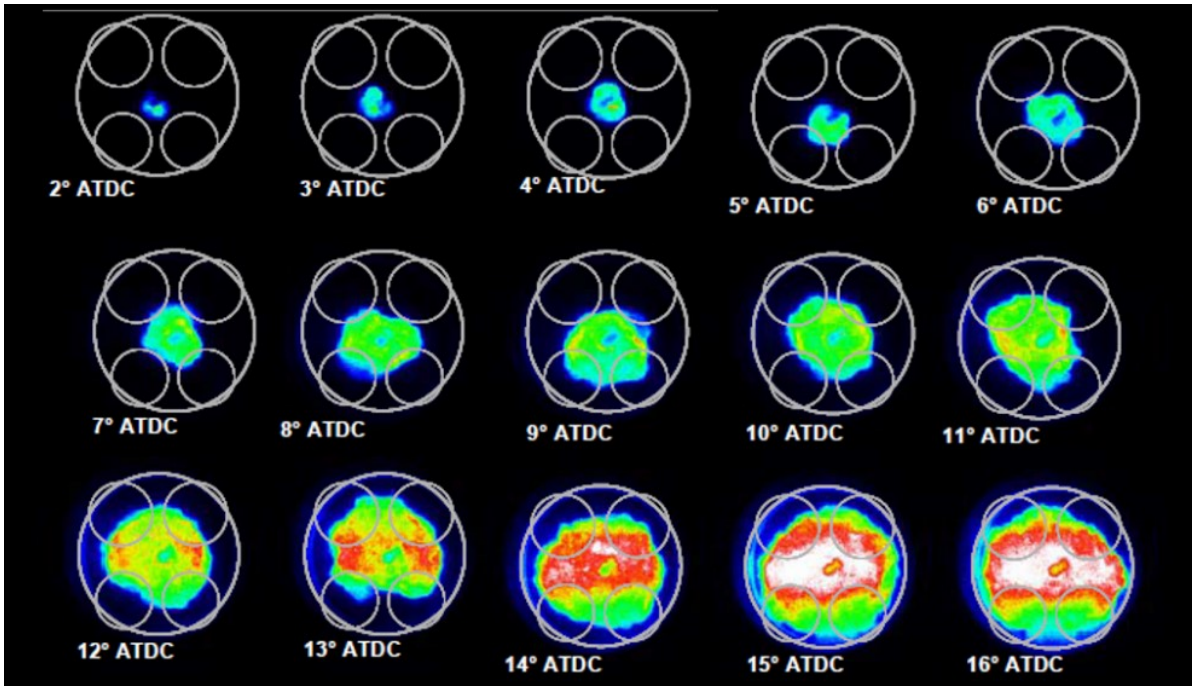

Figure 2-3 UV-visible digital images of the flame propagation [3], SA= 3 CAD.

Different selected crank angles are reported with the aim to describe the main phases of the combustion process. After the *spark ignition*, occurring at 3 CAD BTDC, the first flame is visible at 2 CAD ATDC with an approximately circular outline. This initial phase is called *early flame development*, where the flame mainly propagates in laminar condition.

Then, around 6 CAD ATDC, an irregular shape of the flame is noticeable due to the turbulent flow interaction, creating wrinkles and corrugating the flame front. This produces an increment of the burning rate, starting the phase called *turbulent flame propagation*. Then, when the flame reaches the cylinder walls, around 15-16 ATDC, the combustion ends, getting in the *flame termination phase*.

The laminar flame speed, the turbulent field inside the cylinder, and the SA setting play very important roles in the combustion process. Indeed, the SA has to be properly selected with the aim to obtain the Maximum Brake Torque (MBT) and power. On the one hand, a very early start of combustion, black line, increases the pressure peak during the compression stroke, leading to a lower expansion work. On the other hand, an extremely delayed spark timing, blue line, moves the pressure peak late along the expansion stroke, reducing the available work from the cycle. Hence, the optimal SA is the one that ensure the biggest area of the available work (red line), as reported in *Figure 2-4*. This value depends on engine design, operating conditions, air/fuel ratio, etc. Generally, for a conventional SI engine, SA is set with the aim to burn the 50% of the mixture (50 % Mass Fraction Burned, MFB_{50}) at 7-8 CAD ATDC [1]. However, as better explained in the following, MBT operation is not allowed if an abnormal combustion process is detected (knock phenomenon). In such conditions, the SA is delayed preventing the occurrence of this event.

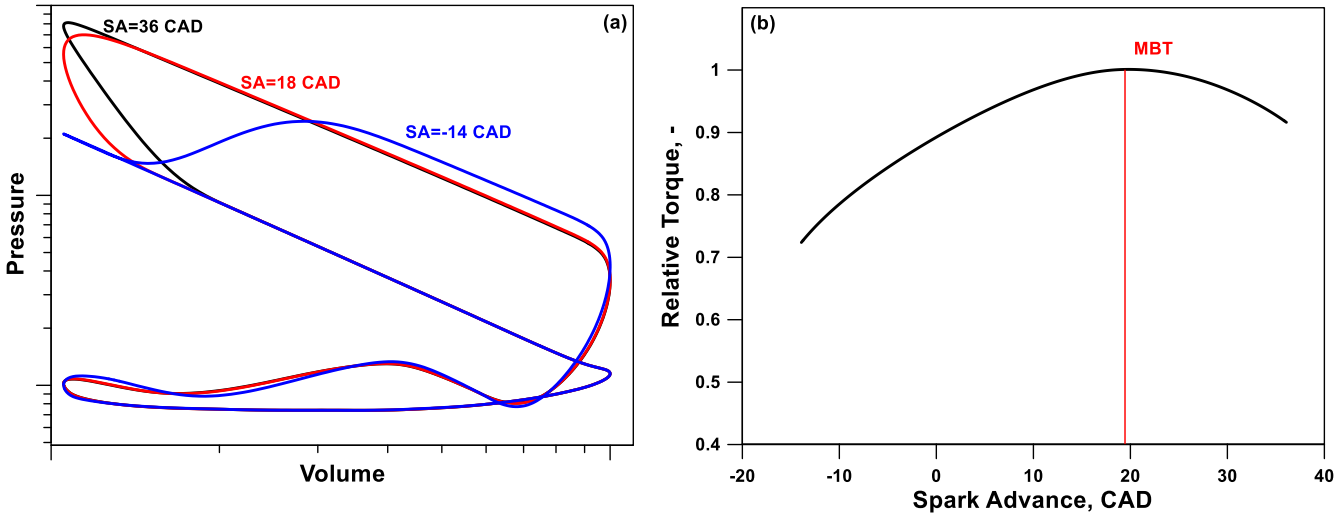

Figure 2-4 (a) Logarithmic P-V diagram for three different spark timing, (b) effect of spark advance on brake torque at constant speed and air-fuel ratio.

After the spark event, a flame kernel is created between the spark plug electrodes. As previously mentioned, a smooth quasi-laminar flame of reduced thickness δ_L initially develops, characterized by a laminar flame speed (S_L). It is defined as the velocity of the unburned gases moving into a planar flame front under laminar flow conditions. Generally, S_L is experimentally evaluated in a spherical closed vessel by propagating a laminar flame radially outward from the vessel centre at controlled pressure and temperature [4]. Starting from the collected data, different correlations can be found in literature [5][6], most of them based on the following power law formula:

$$S_L = S_{L,0}\left(\frac{T_u}{T_0}\right)^{\alpha}\left(\frac{p}{p_0}\right)^{\beta} \tag{2.1}$$

where $S_{L,0}$ is the flame speed at reference temperature and pressure T_0, p_0 and α, β are two constants which take into account the pressure and temperature dependency. In *Figure 2-5a*, the experimental $S_{L,0}$ is plotted for different fuels and equivalence ratios. The laminar flame speed presents a peak near stoichiometric or slightly rich air/fuel mixture for all the fuels considered, justifying the need to always operate SI ICEs close this value. In *Figure 2-5b-c,* the typical temperature, pressure and EGR dependence of a well-assessed S_L correlation [4] is depicted. In particular, temperature and pressure have an opposite impact, the higher the temperature (pressure), the higher (lower) S_L. Whereas, the EGR rate, dark green lines, always causes, as expected, a substantial reduction in the laminar burning velocity.

Considering typical condition of an SI ICE, the maximum laminar flame speed for gasoline is around 100 cm/s. If this was the velocity in which the flame propagates inside the combustion chamber, it would not be possible to complete the combustion in time before the exhaust valves open. For this reason, a turbulent flow necessary for the enhancement of the combustion velocity is always developed inside the combustion chamber.

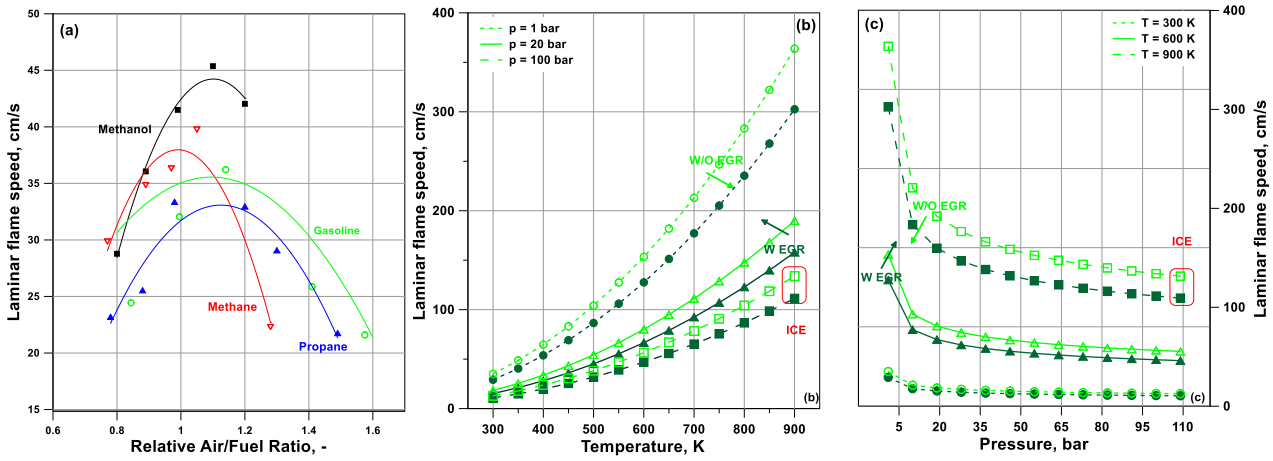

Figure 2-5 (a) Experimental $S_{L,0}$ and its polynomial fits for different fuels as a function of the relative air/fuel ratio at 1 atm and 300K, (b-c) gasoline laminar flame speed correlation [4] for different pressures, temperatures and EGR mass-fractions at stoichiometric condition.

The turbulence phenomenon is a 3D unsteady, rotational and highly diffusive flow, characterized by the presence of disordered eddies, ranging over a wide length scale interval. The largest eddies are limited in size by the system boundaries, whereas the smallest ones are restricted by the molecular diffusion. The interaction among the eddies of various scales is responsible of a transfer of energy sequentially from the larger eddies gradually to the smaller ones, through a process known as the turbulent energy cascade. Due to the irregularity of a turbulent flow, this phenomenon is often characterized through statistical methods [1].

In particular, for an ICE, an ensemble-averaging approach is used, in which the main quantities are evaluated at a fixed crank-angle θ over many consecutive engine cycles. In this approach, however, the turbulent quantities also include the cyclic variations. The ones more often considered are the mean velocities components $(\bar{u}, \bar{v}, \bar{w})$ and the turbulent velocities components (u', v', w') related by the following expressions:

$$u(\theta) = \bar{u}(\theta) + u'(\theta);\ v(\theta) = \bar{v}(\theta) + v'(\theta);\ w(\theta) = \bar{w}(\theta) + w'(\theta); \tag{2.2}$$

To easily characterize the turbulent field inside the cylinder, the rough hypothesis of a homogenous and isotropic turbulent flow is usually introduced. In this case, two main length scales can be identified, associated to characteristic time scales, as well:

1. *Integral length scale* (L_t): represents the largest scale structure of the flow field, characterized by low frequency and large fluctuation. It is defined as the integral of the autocorrelation coefficient of the fluctuating velocity at two adjacent points in the flow with respect to the distance between the points.

2. *Kolmogorov length scale* (L_k)*:* is the smallest scale of the turbulent motion, in which the dissipation into heat of the turbulent kinetic energy takes place.

The interaction between the flame and the turbulent flow field determines different combustion regimes. Each regime is associated to a peculiar flame evolution and shape. One of the most common classification of the flame/turbulence interaction is based on the comparison of the previously defined characteristic lengths/speeds and times, summarized in *Table 2.1*.

Table 2.1 Characteristic speed, length and time scales of the turbulent combustion.

Scale	Speed	Length	Time
Chemical	S_L	δ_L	$\tau_L = \delta_L / S_L$
Kolmogorov	u_k	L_k	$\tau_k = L_k / u_k$
Integral	u'	L_t	$\tau_t = L_t / u'$

The Borghi diagram, shown in *Figure 2-6a*, can be used to easily represent this comparison and define all the possible combustion regimes that may occur in a premixed turbulent flame [7].

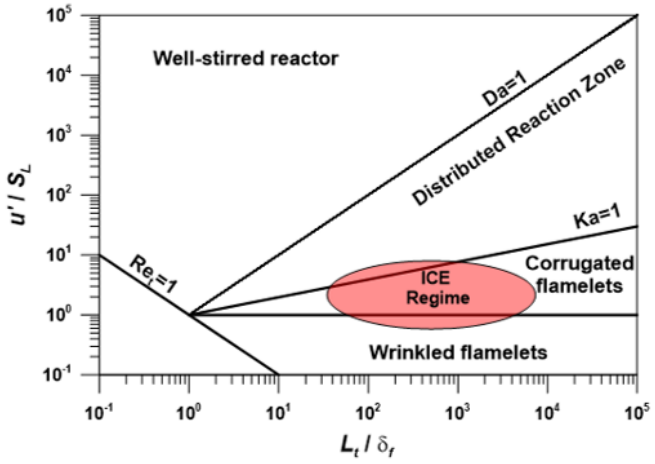

Regime	Re	Da	Ka	U'/SL	Flame
Wrinkled flamelets	>1	>1	<1	<1	
Corrugated flamelets	>1	>1	<1	>1	
Distribuited reaction zone	>1	>1	>1	>1	
Well-stirred reactor	>1	>1	>1	>1	
Broken reaction zone	>1	<1	>1	>1	

Figure 2-6 Borghi diagram and list of the turbulent premixed combustion regimes.

To this aim, three dimensionless number has to be firstly introduced:

1. *Turbulent Reynolds number*(Re) describes the ratio between inertial and viscous forces. It mainly defines the motion flow inside the system. A turbulent flow is characterized by a Re number higher than the unit.

$$Re = \frac{u' L_t}{\nu}; \qquad \rightarrow \quad \frac{u'}{S_L} = Re \left(\frac{L_t}{\delta_L}\right)^{-1} \tag{2.3}$$

2. *Damköhler number*(Da) represents the ratio between turbulent and chemical time scales. With Da lower than 1, the turbulence is much faster than the chemistry and the combustion is mainly controlled by chemical kinetics reactions. Conversely, with a Da higher than the unit, the combustion is characterized by very quick combustion reaction with respect to the turbulent phenomenon.

$$Da = \frac{\tau_t}{\tau_L} = \left(\frac{L_t}{u'}\right) / \left(\frac{\delta_L}{S_L}\right); \qquad \rightarrow \frac{u'}{S_L} = Da^{-1} \frac{L_t}{\delta_L} \tag{2.4}$$

3. *Karlovitz number*(Ka) is the ratio between chemical and Kolmogorov time scales. If Ka is lower than 1, the flame thickness is smaller than the Kolmogorov scale, thus the chemical reaction inside the flame front are not affected by turbulent filed. When Ka becomes higher than the unit, the turbulent eddies penetrate into the reactive zone of the flame.

$$Ka = \frac{\tau_L}{\tau_k} = \left(\frac{L_t}{\delta_L}\right)^{-\frac{1}{2}} / \left(\frac{u'}{S_L}\right)^{\frac{3}{2}} = \left(\frac{\delta_L}{L_k}\right)^2 ; \qquad \rightarrow \frac{u'}{S_L} = Ka^{2/3}\left(\frac{L_t}{\delta_L}\right)^{2/3} \tag{2.5}$$

The above numbers are logarithmically reported in the Borghi diagram, in which $Re = 1$, $Da = 1$ and $Ka = 1$ represent the boundaries of 5 different combustion regimes. These can be graphically seen in *Figure 2-6left* and are listed *in Figure 2-6right*, with the related flame morphology. In the *wrinkled flamelets*, the turbulence intensity is smaller than the laminar flame speed, hence the turbulence doesn't have enough energy to corrugate the flame front. Additionally, due to a Ka lower than the unit, the chemical kinetics are not sensitive to the presence of the turbulence. Indeed, the smallest eddies cannot enter the flame front since they are bigger than the flame thickness. As soon as the turbulent intensity becomes higher than the laminar speed, the combustion regime enters the *corrugated flamelets region*.

Here, the turbulence corrugates the flame front, and may also create pockets of burnt gases inside the fresh gases zone. The Ka is still lower than one, therefore also here the turbulence doesn't alter the flame structure. In the *Distributed reactions zone* Ka becomes higher than 1 and the smallest eddies enter in the pre-heat zone of the flame, but not in the reaction one since the bigger eddies are still greater than the thickness of the reaction zone. The turbulent convection inside the flame front accelerates both heat and mass transfer mechanisms. Only when Da reaches a value lower than the unit, *well stirred reaction zone*, the combustion is controlled by chemical kinetics. Indeed, the turbulence is so intense to create a perfect stirring between the reactants and the products of the combustion, avoiding the establishment of a flame front. The last regime is the broken reaction zone (Ka >>100), not visible in the Borghi diagram, in which the turbulent eddies enter the reaction zone, and for this reason no flame exists. Experimental study showed that ICE works mainly in the wrinkled and corrugated zone, red circle in the *Figure 2-6*, in which the chemical reaction can be simply described by the laminar flame proprieties. This is one of the most common hypotheses on which the majority of the combustion model are based.

2.2. Knock phenomena

The knock phenomenon is one of the most critical abnormal combustion which may can occur in an SI ICE. It is detected as a noise which is transmitted through the engine structure when autoignition of the end-gas occurs. It results in a sudden heat release, which induces a set of pressure waves propagation across the combustion chamber. This undesirable event should be avoided for different reasons. Firstly, the thermal losses increase since the pressure oscillations promotes the heat transfer, reducing the available work. Secondly, the lubricant film around the cylinder could be removed by the pressure wave reflections, leading to the seizure of the engine.

Finally, when the knock intensity is quite huge, this can damage the cylinder irreparably, as shown in the representative cases in *Figure 2-7*.

Indeed, when heavy knock occurs the heat is transferred to the combustion walls, overheating the cylinder head and piston. The higher temperature of the cylinder makes the knock even more frequent, this phenomenon resulting heavier and heavier. Without a proper control, this can lead to the engine failure in a short time.

Figure 2-7 Example of engine piston damaged by heavy knock.

The pressure waves induced by the presence of the knock generate a not uniform pressure distribution, consequently different pressure values can be recorded if the transducer is moved within the cylinder. For this reason, different methods for the measurement and the characterization of the knock intensity are proposed in the literature [8]. The one more widely adopted is the analysis of the in-cylinder pressure signals, through a pressure traducer flush-mounted in the combustion chamber. The pressure trace collected is then processed considering a band-pass filter in the range of 4-20 kHz. The low cut-off is used to filter out the regular combustion noise (low frequencies), whereas high-cut off is required to delete the signal disturbance given by the sensor resonances.

In order to quantify the magnitude of the phenomenon, a knock index has to be defined: The Integral of Modulus of Pressure Oscillations (IMPO) and Maximum Amplitude of Pressure Oscillations (MAPO) are the ones more frequently used [9]. Generally, both are evaluated for each cycle, for a prescribed crank angle window, generally 40-60 CAD starting from the spark event. Then the indexes are averaged over various consecutive cycles (at least 100). MAPO and IMPO are monitored to avoid the knock event, acting on the spark timing. Indeed, the retarding of the spark timing decreases the knock intensity, whereas an advanced spark increases the probability of knock occurrence. Consequently, the SA is selected as the one at which the MAPO/IMPO index reaches a target threshold, defined as a function of the engine speed. It is worth to underline that this abnormal combustion is the issue that limits more the compression ratio of SI ICE.

In *Figure 2-8a,* a typical measured pressure signals is reported in knock conditions, with the related amplitudes detected by an accelerometer. The multiple pressure oscillations, black line, after the TDC denotes the presence of the knock event, whereas the time delay between the two signals (black and red line) is related to the pressure oscillations propagation through the engine block. Additionally, the knock event can be characterized by different intensity as shown in *Figure 2-8b,* in which three knocking pressure cycle are depicted. The green line represents a condition of *incipient knock* (#137), for which as soon as the spark timing is slightly advanced a *heavy knock* condition occurs (#63). The blue line is a typical waveform of an acceptable very *soft knocking* condition (#95) at a lower engine speed (3000 rpm).

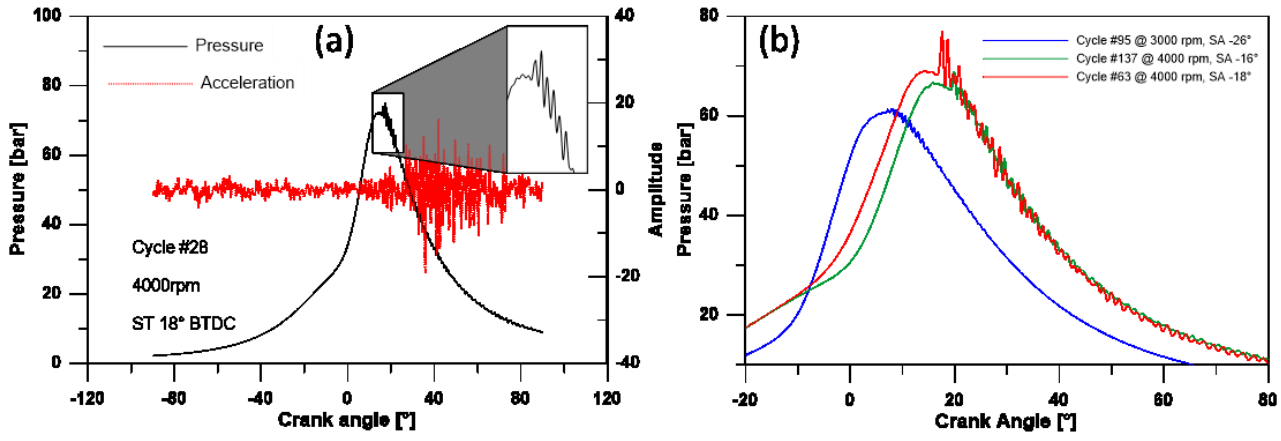

Figure 2-8 (a) Pressure trace and amplitudes detected by the accelerometer referring to the at 4000 rpm, WOT and SA=18° ATDC, (b) pressure traces for different spark advances at 4000 and 3000 rpm, WOT [10].

2.3. Cycle to Cycle variation

For a certain engine architecture, through the variation of its control variables, such as Spark Advance (SA), valve timing, throttle position or air/fuel ratio, it is possible to control the combustion process, ensuring the required load.

As known, even when the control variables remain the same, two consecutive cycles are never completely similar. Indeed, variations in local flow motion in the turbulence levels inside the cylinder, in the mixture homogeneity and composition, especially near the spark plug, result in a phenomenon called Cycle to Cycle Variation (CCV).

This phenomenon also should be limited in ICE. Indeed, the CCV mainly causes fluctuations in the rate of heat release, hence in the amount of useful work done by a single combustion event, affecting the stability of the brake torque, which directly influences the vehicle drivability. Differently from the knock, CCV cannot be completely deleted, but only limited due to its intrinsic nature. Experimentally, it has been observed that the early stage of the flame development is the most critical combustion phase for the CCV. A combustion that begins slowly, such as in presence of excess of air or high fraction of residual gas, will have more probability of being characterized by cycle variations.

Generally, the intensity of the CCV is based on the acquisition and the post-processing of consecutive pressure traces (300-500), analysing the Coefficient of Variation (CoV) of some parameter connected to in-cylinder pressure, burning process or engine performance. The CoV of the Indicated Mean Effective Pressure (IMEP) and the one associated to the in-cylinder peak pressure are the ones more commonly adopted. Generally, the former is used for defining the engine drivability and its value should be lower than 2-3%. While the latter more directly affects the knock onset and generally it can assume values higher than the CoV of the IMEP.

Due to the CoV phenomenon, for a fixed operating condition, a train of pressure cycle will be visible for which the average, the fastest and the slowest cycles are generally considered for the engine control. In particular, the optimal spark timing is usually selected with reference to the average cycle. If close-to-knock conditions are concerned, the extreme cycles have to be monitored with particular care, since these lasts limit the engine operation. Indeed, the fastest cycles limit the compression ratio and define the fuel octane requirement due to its highest probability of knocking. On the contrary, the slowest cycles impose the lean operating limit, since they are the ones with the highest probability to have an incomplete combustion.

2.4. State of art of technologies

Although ICEs were developed for the first time more than a century ago, the research related to the improvement of their efficiency as well as to the reduction of their pollutant emission is still on going. Concerning Spark Ignition (SI) ICEs, widespread methods for efficiency improvement have been investigated during this last decade. As already pointed out, the state of art are high efficiency downsized engines with Variable Valve Actuation (VVA) architectures [11].

Various numerical and experimental activities have demonstrated that is possible to improve the efficiency by using different VCR concepts, including Two-Stage systems (TSCR) and continuously variable devices [12]. Another technique aiming at reducing the BSFC levels is the adoption of external cooled EGR. The latter, depending on the load level, allows the decreasing of the pumping losses, the knock tendency and the mixture overfueling [13]. A further solution for knock suppression is the liquid water injection either within the cylinder or at the intake port, revealing notable efficiency improvements, around 16 %, at low speed and high load [14]. In this thesis, the combination and mutual effects of all of those considered techniques will be numerically assessed.

2.4.1. Variable Valve Actuation

The VVA technologies are used to add flexibility to the engine valve train by simultaneously or individually varying lift, duration and phase of the intake or exhaust valves. Two main types of these systems can be identified: Variable Valve Timing (VVT) and Variable Valve Lift (VVL). Both allow to control the air flow and the turbulent field inside the combustion chamber, contributing to improve fuel consumption or, and engine performance. The modification of the valves profile can be achieved through different mechanism: a simple mechanical device, an electro-hydraulic/mechanical system or a cam-less system [15]. Some car manufactures prefer electro-hydraulic/mechanical devices, since these last represent a good compromise between control flexibility and cost. Indeed, the cam-less device is not yet in production due to its high cost and difficulties in the control. An extensive review of those technologies can be found in [15].

In particular, a VVA, commercially known as “Multi-Air”[16], and a VVT systems were employed for the conventional and the pre-chamber engine, respectively. Both the technologies adopt an *Early Intake Valve Closing (EIVC)*, as illustrated in *Figure 2-9* with the aim to reduce the fuel consumption. In the VVT system the early closure is obtained through a rigid shift of the intake valve profile, on the contrary in VVA one, the valve lift is modified, too, maintain the same IVO. Generally, an EIVC strategy is used at partial load to decrease the pumping loses and at high-load for knock mitigation, acting on the reduction of the effective compression ratio. The main drawback of this methodology is the poor in-cylinder turbulence, and the undesirable gas-dynamic noise with a fully opened throttle angle at very low load.

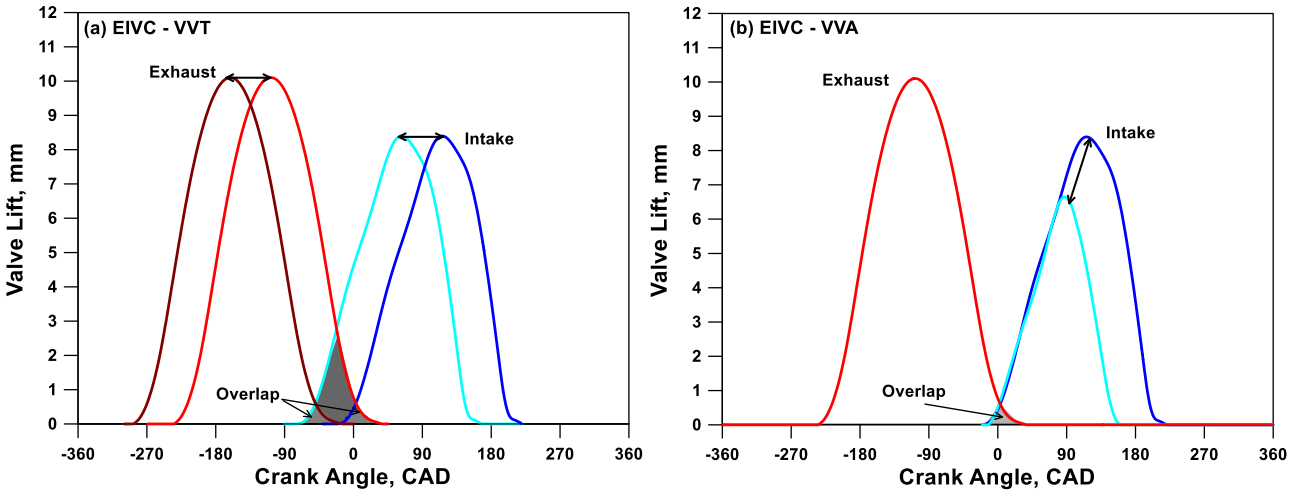

Figure 2-9 EIVC strategy in a VVT (a) and VVA(b) system.

However, it has to remark that for a VVA system, the above advantages can be achieved maintaining the conventional exhaust valve event, since the IVO remains unchanged. On the contrary, for a VVT system, it could be necessary modifying the exhaust event to avoid scavenging issues, since the advancement of the IVO increases the valves overlap. Consequently, in a VVT system of only the intake side, like in the engine under study, the EGR amount has to be monitored.

2.4.2. Variable Compression Ratio (VCR)

Generally, the compression ratio of SI ICE is limited at high load condition, where the knock tendency is high. However, at mid/low load the preferable Compression Ratio (CR) should be greater to improve the thermodynamic efficiency. Therefore, the aim of a VCR is to automatically modify the compression ratio as a function of the engine load and speed allowing the reduction of the fuel consumption at mid/low load, due to the increment of the efficiency. This can be achieved with TSCR or with a continuously variable device. In the former, only two compression ratios can be selected as a function of the operating point, mainly the lower(higher) at high(medium) load. In the latter, more expensive, the CR is continuously modified with the aim to ensure the best thermodynamic efficiency at each engine condition. Although, this technology can lead to high benefits, it is highly limited by the cost and by the mechanical complexity [17].

2.4.1. Recirculating exhaust gas and Water Injection

The EGR technique was firstly used in diesel engine in order to limit NO_X emission through the reduction of the combustion temperature by the dilution of the fresh gases with a proper amount of recirculated exhaust gas.

However, with the establishment on the market of turbocharged downsized SI engine, characterized by high-power density and higher combustion temperatures, the problem of NO_X production becomes relevant also for these engines. Differently from Diesel engine, exhaust gas recirculation allows to obtain different advantages depending on the operating condition. On the one hand, this technique is used to decrease throttling losses at part load. Indeed, in order to keep a certain load, at increasing EGR, the throttle can be progressively opened, reducing the pumping loss. On the other hand, EGR reduces NO_X emissions, due to the reduction of the in-cylinder temperature [18] as well as the Diesel engine case. If the EGR is cooled, it can be also used to reduce the risk of knocking combustion, at high load.

The gas recirculation can be classified into internal EGR and external EGR. The former is achieved by increasing the valve overlap during exhaust stroke, through an advanced system able to rapidly change the valve timing. In the latter, exhaust gases are taken from the exhaust port and reintroduced in the cylinder through the inlet port by an external circuit, also including an EGR-cooler. It is relatively low-cost, since it only need a dedicated EGR control valve and an EGR-cooler, able to control the EGR rate and temperature in different working conditions [13].

Water injection is not a novel concept. It was born in aircraft field around the 40'and, as the EGR technique, is returned of interest, when downsized turbocharged SI ICE have been introduced on the market. It is a method, known as anti-knocking injection, that allows to cool the combustion chamber by injecting liquid water inside the cylinder. The heat subtracted by the subsequent water evaporation, drastically reduces the temperature of the gases, mitigating the knock tendency. In a turbocharged engine, the water injection also reduces the overfuelling usually required at high speed to control the turbine inlet temperature below a safe temperature level (around 950 °C). The better combustion phasing, the reduced overfuelling and the possibility to also increase the compression ratio of the engine, can lead to strong improvements of the fuel consumption [19] in a high speed, high load operating zone.

2.4.2. Dynamic skip firing

The Dynamic Skip Firing (DSF) is an advanced system that can independently control the firing decision of each cylinder on the engine. This allows to significantly reduce the engine pumping losses and improve the combustion efficiency compared with standard, throttled engine operation [20]. With this technology, the part load conditions are, indeed, achieved controlling the number of firing cylinder rather than the throttle position. I.e. with the reduction of the load, the numbers of the firing cylinders decrease, unless the torque demand is zero in which all the cylinders are turned off, without acting on the throttle device.

Additionally, by reducing or eliminating the engine braking, more of the vehicle's kinetic energy can be potentially recovered. As a consequence, DSF offers additional benefits if combined with hybrid vehicles. However, the DSF has to comply with noise, vibration and harshness issues, limiting the declared advantages.

2.5. Ultra-lean combustion

The advantages obtained by all the described technologies highly depend on the engine operating condition. As an example, VVA/VVT entails a reduction in the pumping losses, improving the fuel consumption at low load and providing some enhanced knock resistance at high load. However, when knocking phenomena become more relevant, different solutions must be adopted, such as water injection or cooled external EGR. In the recent years, moreover, the car manufactures are moving towards innovative SI engine architectures with unconventional combustion concepts aiming to obtain substantial advantages in the whole engine plane.

Indeed, with the introduction of the Real Driving Cycle for vehicle homologation, it is mandatory to develop a high-efficiency engine in the majority of its operating conditions.

In particular, combustion systems that work with very lean air/fuel mixtures are of particular interest due to the possibility of simultaneously reducing the NO_X raw emissions and the fuel consumption in the whole engine plane. The fuel benefits mainly derive from a higher specific heats ratio, minor heat losses and higher knock resistance, *Figure 2-10a*. Whereas, the lower combustion temperatures allow to reduce NO_X production [21] and the excess of air also guarantees low CO and HC raw emissions, *Figure 2-10b* [22]. However, flame-propagation based SI-ICEs are able to only work with a small amount of excess air, limiting the real advantage of this combustion concept. Indeed, lean conditions reduce the laminar flame speed, leading to unacceptable cyclic variability, misfire and huge HC-CO formation [21], [1].

With the purpose to extend these restrictions, different solutions have been developed in the current literature. Stratified lean combustion has been attempted for many years aiming to realize a close-to-stoichiometric air/fuel ratio at the spark plug with various strategies, such as wall guided, flow guided or spray guided solutions,[23], [24]. More recently, Moriyoshi et al [25] have shown that it is possible to generate a slight vertical fuel stratification through a twin-tumble intake flows, aiming to reduce the cycle-to-cycle fluctuations. To completely avoid the problems related to the extremely low flame speed at lean condition, alternative, flame-less combustion concepts have been proposed, such as the Homogeneous Charge Compression Ignition (HCCI) [26]. HCCI however showed serious problems in controlling of ignition timing, limited power output, and weak cold-start capability.

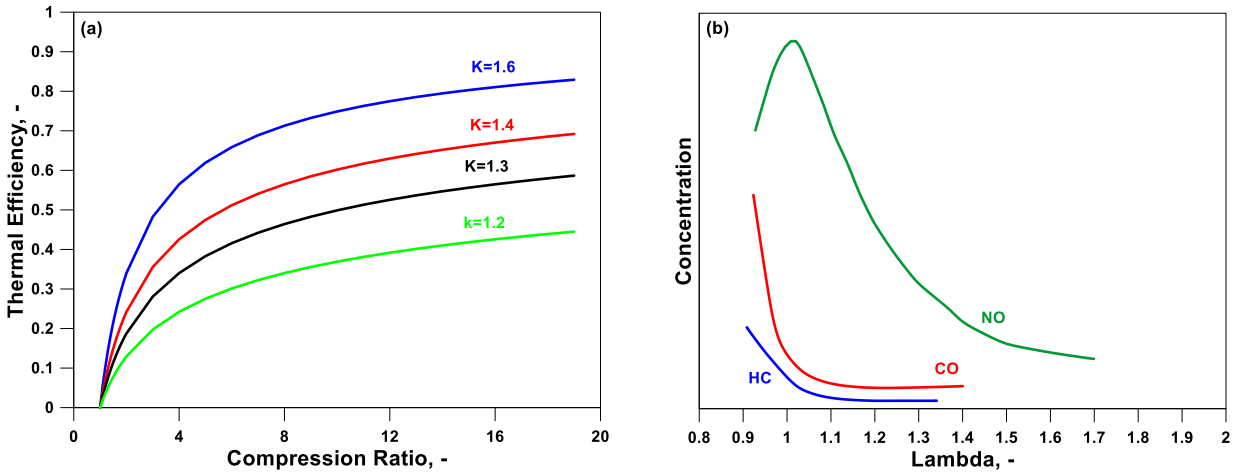

Figure 2-10 (a)Thermal efficiency as a function of the compression ratio for 4 different heat ratio, k,(b) NO,CO,HC concentration as a function of lambda for SI ICE.

Some HCCI variants are still under study, such as the Spark-Assisted Compression Ignition (SACI), proposed in [27].This combustion mode promotes a controlled auto-ignition of a lean or diluted unburned mixtures by a spark-initiated flame propagation.

A practical solution to easily implement an ultra-lean combustion is the utilization of a Pre-Chamber (PC) ignition system, where a small volume, housing the spark-plug, is connected to the Main-Chamber (MC) through small orifices. In this system, the combustion process starts at the spark plug and propagates in the MC one, in the form of multiple turbulent jets of hot gas ejected from the pre-chamber. These jets penetrate the main-chamber, increase the turbulence of the cylinder charge and allow the ignition and a stable flame propagation even under extremely lean mixtures [28],[29].

The main issues that have to be complained by all those engine architectures, are mainly related to the precise control of the combustion development, and the related emission formation.

More complex after-treatment systems are in fact required, alternative to the classical three-way catalyst. Since in this PhD thesis, the latter technology will be mainly investigated, in the following section more details on this novel architecture will be addressed.

2.5.1. Pre-chamber engine

Pre-chamber system is a long-known technology firstly mentioned by Riccardo in 1918 [30]. It was largely used in the Diesel engine with the aim to improve the air/fuel mixing rate. In this engine, the PC, a volume connected with the main-combustion chamber via a one or more orifices, was employed for properly mixing the air/fuel charge by the turbulent flow generated during the compression phase. With the development of high-pressure electronic injection system, the fuel vaporization and the mixture formation and homogenization were provided by the high injection pressure more than the turbulent mixing, and this technology has been shelved.

The pre-chamber system proposed by Ricardo [30], was also applied for SI engines. A rich charge was supplied to the pre-chamber with one carburetor, and only air was introduced in the main chamber. The load was controlled by modification of the air fuel ratio and the amount of the charge supplied in the pre-chamber. However, some drawback of this system at part load operations were observed in terms of both performance and efficiency, moving the interest towards the conventional spark plug engine.

Nevertheless, over the years, steps forward were taken to improve this technology. In 1968, Gussak [31] developed the jet ignition application, named as LAG-process (Lavinia Aktivatisia Gorenia or Avalanche Activated Combustion). It was based on the "chain branching" theory developed by Semyonov. The idea was to use active species and "chain carriers" produced in the pre-chamber and then ejected in the main chamber to advance the chemical process within it. Other studies simplified the Ricardo concept, and deleted the need for auxiliary pre-chamber fueling. In [32], the pre-chamber was filled directly with the main chamber charge during the compression stroke.

The combustion starts in the pre-chamber, through a spark plug, and thank to the turbulence field it was possible to ignite mixture with a relative air ratio equal to 1.3. Although all these studies showed the possibility to strongly improve the engine efficiency, this technology was not spread in the market mainly due to the huge difficulties in the control of the combustion in the whole engine plane, further increased by the inefficiency at lean condition of the three-way catalyst.

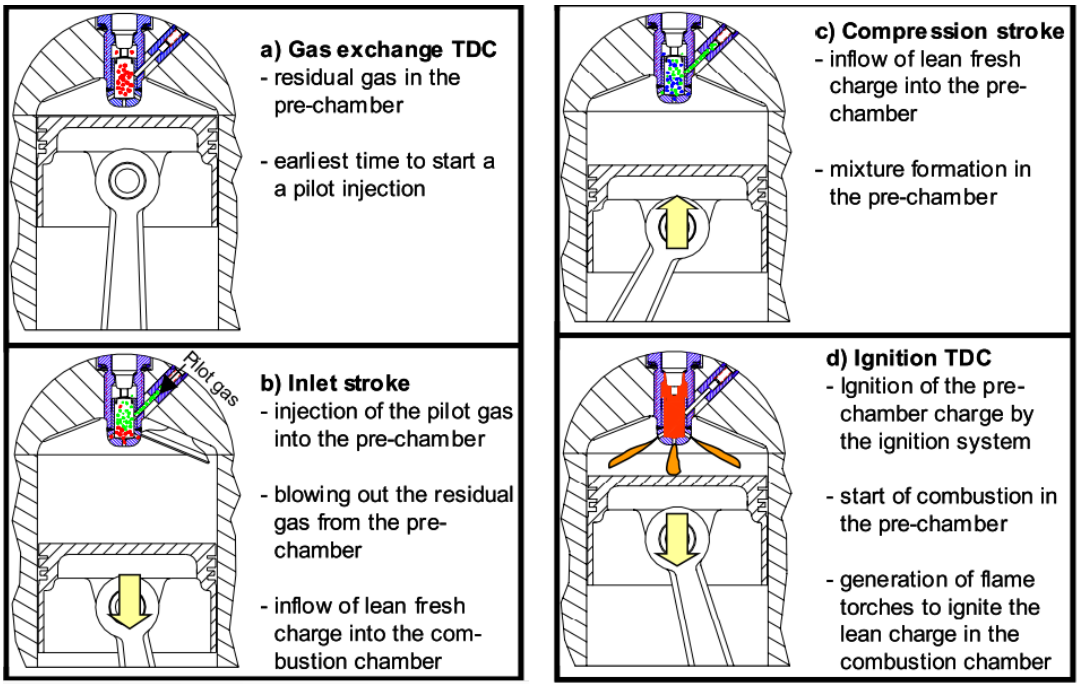

Figure 2-11 Principle phase of a pre-chamber spark plug with pilot injection [33].

Concerning our days, this technology is currently limited to Formula-1 competition and to large stationary gas engine (heavy duty for naval application). From the one side, the stationary conditions allow to easily optimize the engine system due to smaller range of operating points to be considered. From the other side, motorsport cars do not have to comply with cost and pollutant limitations. The pre-chamber application in Formula-1, as often happens, turned again the interest in this technology. Latsch et al. [33] studied a pre-chamber spark plugs with a pilot injection, summarized in *Figure 2-11*. The aim of this technology was to use a pilot injection during the inlet stroke to overcome the main issue related to the insufficient residual gas scavenging in the pre-chamber. In this study, the injected fuel in the PC more suitable for extending the lean limit was the hydrogen.

In 2015 *MALHE* [34] presented the Turbulent Jet Igniter (TJI) system, declaring that it is possible to extend the lean burn limit also with commercial fuels such as propane, gasoline and natural gas. In *Figure 2-12* the schematization of the proposed technology is reported. The TJI system consists of a pre-chamber injector and sparkplug connected with the main chamber, in which the 2% of the fuel energy is supplied in the PC and the remaining through a port fuelling in the MC.

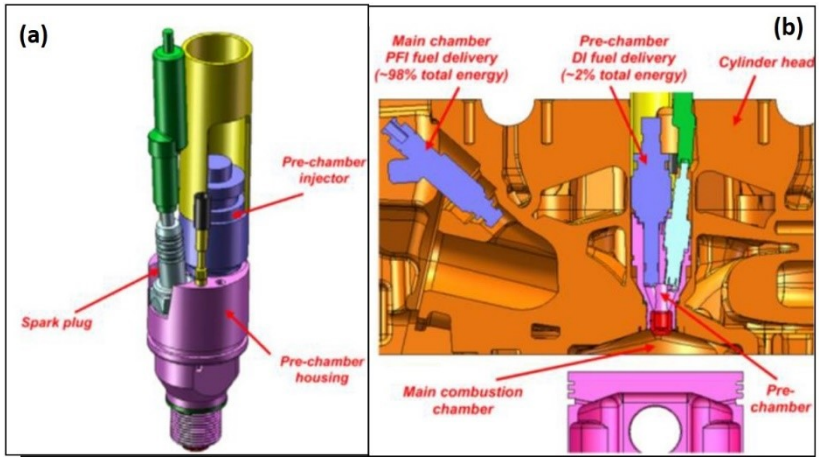

Figure 2-12 Pre-chamber (a) and overall engine scheme (b) for the TJI System.

Nowadays, as shown in *Figure 2-13*, the pre-chamber system can be divided in two main categories, passive and active. In the former, the unburned air/fuel mixture around the spark has almost the same composition as the one inside the main-chamber. It has the advantage of a low cost and engineering simplicity, but due to scavenging issues in the PC, it is not possible to work under extremely lean conditions. Whereas in the latter, a fuel metering device, such as a fuel injector, is integrated into the pre-chamber. This options allows to have stoichiometric or slight rich mixture in the pre-chamber, without compromising the possibility of lean mixture preparation in the main combustion chamber, and maintaining limited cyclic variations [35], [36].

Despite several experimental activities carried out in the recent years on active pre-chambers [37], the choice of the most suitable fuel to be injected into the PC, is still a subject of various studies. On one hand, gaseous fuels, such as methane [38] and hydrogen [39], or vaporized gasoline [40] guarantee a proper mixture homogenization before the spark event. On the other hand, because of the fuel supply infrastructure for passenger cars, nowadays liquid gasoline injection remains the most suitable option, although this can cause challenges regarding perfect mixture formation.

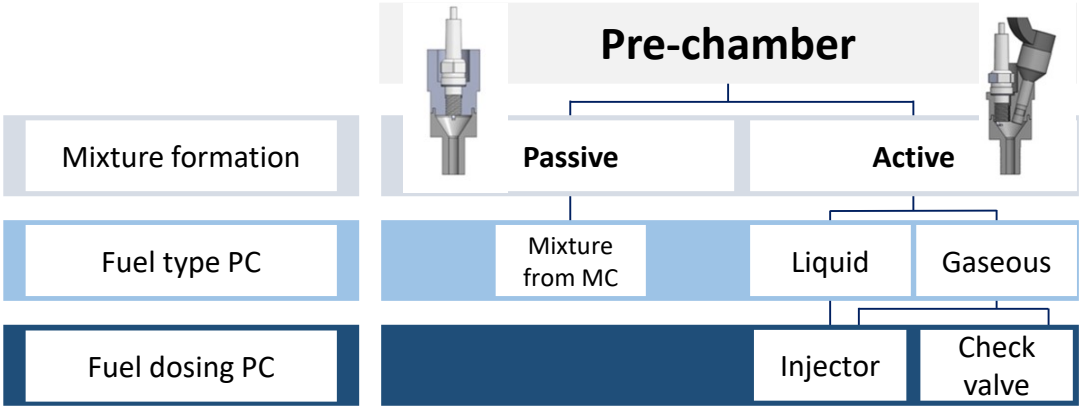

Figure 2-13 Classification of pre-chamber devices according to [29].

Independently from which pre-chamber SI engine is considered, the combustion phenomena can be described as follows. The spark plug located in the PC starts the combustions, releasing heat with a consequent increment of the pressure. As soon as the pre-chamber pressure exceeds the MC one, multiple turbulent jets of hot gas are expelled from the pre-chamber. These multiple jets start the ignition event in the MC, strongly enhancing the first stage of the combustion development. The high turbulent level of the jets combined with the establishment of multiple ignition sites allows to sustain the combustion even for extremely lean mixture, maintaining high stability [28].

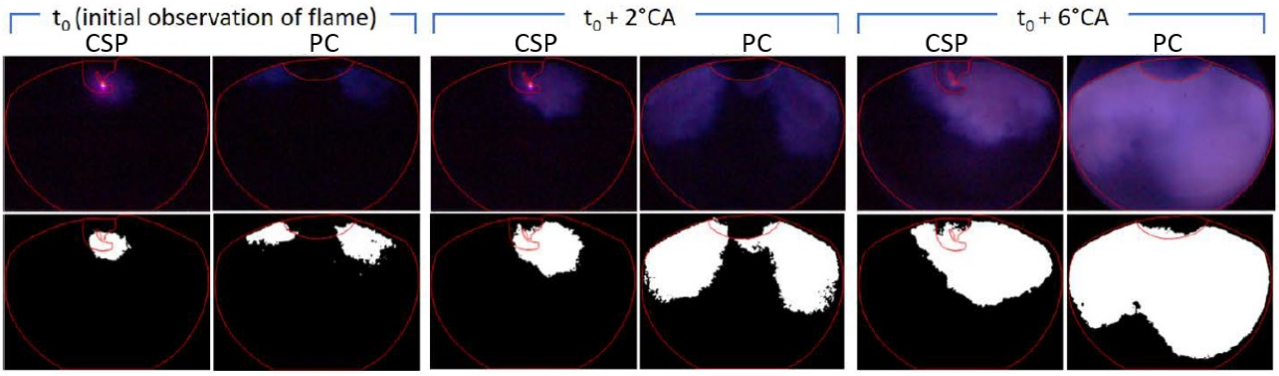

Figure 2-14 High-speed images of flame propagation comparing CSP and PC engine at 2000 rpm@16 bar BMEP [28].

Additional aspect of the combustion enhancement due to the turbulent jets can be better explained detected looking at *Figure 2-14*. In particular, some pictures of the comparison of the ignition and flame propagation process for a Conventional Spark Plug (CSP) and a pre-chamber one (PCSP) at the same engine speed and load are reported from [28]. Three crank angle positions are selected after the spark, in which t_0 corresponds to the crank angle of initial flame detection. In the top, the full light spectrum is shown, whereas in the bottom a better visualization/comparison using the Otsu [41] method is depicted.

Differently from a conventional combustion, the flame propagation in a PCSP moves from the outer area of the cylinder toward the centre of the combustion chamber. Secondly, the multiple jets of hot gasses locally increase the turbulence, strongly enhancing the combustion speed. These two effects reduce the knock tendency. First, the flame more quickly fills combustion chamber, especially its most knock-prone zones, second, the reduction of the combustion duration does not allow to reach the auto-ignition time of the end-gas. Consequently, it is possible to increase the compression ratio, and obtain further efficiency improvements.

To confirm the mentioned advantage, in *Figure 2-15* a representative comparison between spark ignition and jet ignition combustion systems at 1500rpm@3.3 IMEP is depicted [34]. *Figure 2-15a* show that it is possible to extend the lean limit up to 50% mass fraction diluent while still maintaining adequate combustion stability. The maximum improvement in terms of thermal efficiency is equal to 18% when compared to conventional stoichiometric SI engine in this operating condition. Additionally, as already mentioned, the low temperature combustion, combined with the lean condition, strongly reduce the NO_X emission.

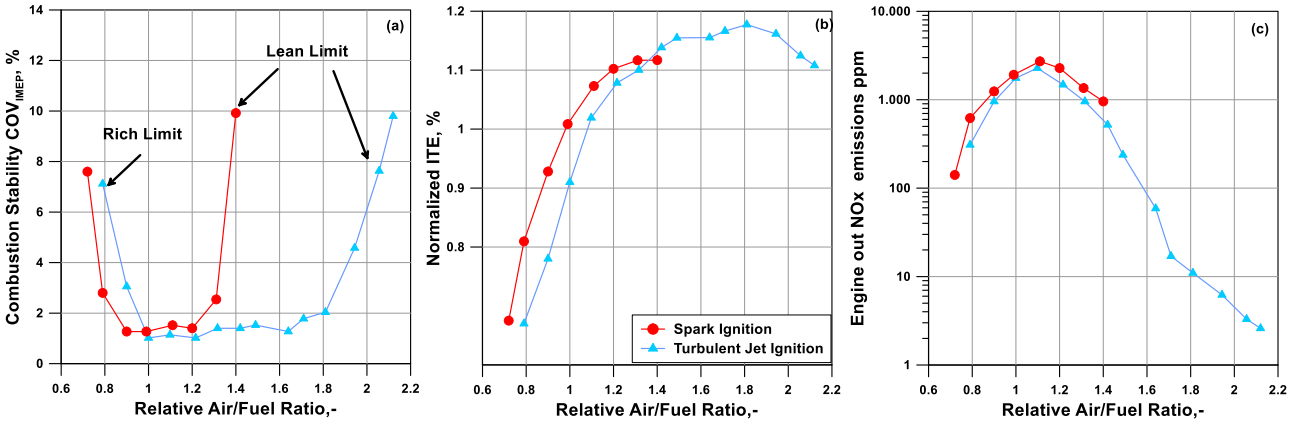

Figure 2-15 Comparison of spark ignition and jet ignition combustion systems with increased relative air/fuel ratio at 1500rpm@3.3 bar IMEP in terms of (a) combustion stability, (b) Normalized thermal efficiency, (c) NO_X emissions [34].

2.5.2. Hydrogen Injection

With the new interest in lean combustion, methodology for enhancing the combustion reactivity in order to ensure a greater combustion stability have been investigated in the recent years. In this context, the addition of a small quantities of hydrogen (H_2) in the fresh gases could significantly extend the lean limit of the combustion. Indeed, the higher laminar flame speed of the H_2 supports both the ignition and the flame propagation phases, resulting in a significant decrement of the CCV fluctuation. The addition of H_2 increases also the mixture auto-ignition resistance, leading to a further increase in the efficiency due to a better combustion phasing and to a higher compression ratio. Besides, hydrogen addition could help in decreasing the CO and HC emissions [42] and, in some conditions, mitigate the NO_X formation by optimizing the trade-off between the air/fuel ratio and the maximal temperature inside the cylinder.

References

[1] Heywood, J., B., Internal combustion engine fundamentals," Vol. 930, New York, Mcgraw-Hill, 1988, ISBN: 007028637X.

[2] Chen, L., Liang, Z., Zhang, X. and Shuai, S., "Characterizing particulate matter emissions from GDI and PFI vehicles under transient and cold start conditions," *Fuel*, 189, pp.131-140, 2017, doi:1016/j.fuel.2016.10.055.

[3] Bozza, F., Gimelli, A., Merola, S.S., Vaglieco, B.M., "Validation of a fractal combustion model through flame imaging," *SAE transactions*, pp.973-987, 2005., doi:https://www.jstor.org/stable/44722057.

[4] Metghalchi, M., Keck, J., "Laminar burning velocity of propane-air mixtures at high temperature and pressure," *Combustion and flame*, 38, pp.143-154, 1980, doi:10.1016/0010-2180(80)90046-2.

[5] Amirante, R., Distaso, E., Tamburrano, P., Reitz, R. D., "Laminar flame speed correlations for methane, ethane, propane and their mixtures, and natural gas and gasoline for spark-ignition engine simulations," *International Journal of Engine Research*, 18(9), 951-970, 2017, doi:10.1177/1468087417720018.

[6] Gülder, Ö., "Correlations of laminar combustion data for alternative SI engine fuels," SAE Technical Paper, No. 841000, 1984, doi:10.4271/841000.

[7] Peters, N., "Laminar flamelet concepts in turbulent combustion", Symposium (International) on Combustion 21(1): 1231-1250, 1988, doi:10.1016/S0082-0784(88)80355-2.

[8] Millo, F., Ferraro, C., "Knock in S.I. Engines: A Comparison between Different Techniques for Detection and Control," SAE Technical Paper 982477, 1998, doi:10.4271/982477.

[9] Brecq G., Bellettre J., Tazerout M., "A New Indicator for Knock Detection in Gas SI Engines," *International Journal of Thermal Sciences*, 42, pp.523-532, doi:10.1016/S1290-0729(02)00052-2.

[10] Siano, D., Bozza, F., D'Agostino, D. Panza, M.A., "The use of vibrational signals for on-board knock diagnostics supported by in-cylinder pressure analyses" SAE Technical Paper, 2014-32-0063, 2014, doi: 10.4271/2014-32-0063.

[11] Hara, S., Suga, S., Watanabe, S., Nakamura, M., "Variable valve actuation systems for environmentally friendly engines," *Hitachi Review*, 58(7), 319-324, 2009.

[12] Shaik, A., Moorthi, N., Rudramoorthy, R., "Variable Compression ratio engine: a future power plant for automobiles-an overview", *Proc. of the Istitution of Mechanical Engineers* Part D: Journal of Aut. Eng. 221(9):1159-1168, 2007, doi: 10.1243:09544070JAUTO573.

[13] Wei, H., Zhu, T., Shu, G., Tan, L., Wang, Y., "Gasoline engine exhaust gas recirculation–a review," *Applied energy*, 99, 534-544, 2012, doi:apenergy.2012.05.011.

[14] Hoppe, F., Thewes, M., Baumgarten, H., Dohmen, J., "Water injection for gasoline engines: Potentials, challenges, and solutions," *International Journal of Engine Research* 17(1):86-96, 2016, doi:10.1177/1468087415599867.

[15] Ahmad, T., Theobald, M. A., "A survey of variable-valve-actuation technology," *SAE Transactions*, 1651-1677, 1989, doi:https://www.jstor.org/stable/44581049.

[16] Bernard, L., Ferrari, A., Micelli, D., Perotto, A., Rinolfi, R., Vattaneo, F., "Electro-hydraulic valve control with multiair technology," MTZ worldwide, 70(12), 4-10, 2009, doi:10.1007/bf03226988.

[17] Kleeberg, H., Tomazic, D., Dohmen, J., Wittek, K., Balazs, A., "Increasing efficiency in gasoline powertrains with a two-stage variable compression ratio (VCR) system," SAE Technical Paper, 2013-01-0288, 2013, doi: 10.4271/2013-01-0288.

[18] Tabata, M., Yamamoto, T. Fukube, T., "Improving NO_x and fuel economy for mixture injected SI engine with EGR," *SAE transactions*, pp.1221-1230,1995, doi: https://www.jstor.org/stable/44633290.

[19] Bozza, F., De Bellis, V., Teodosio, L., "Potentials of cooled EGR and water injection for knock resistance and fuel consumption improvements of gasoline engines," *Applied Energy*, 169, 112-125, 2017, doi:j.apenergy.2016.01.129.

[20] Eisazadeh-Far, K., Younkins, M., "Fuel economy gains through dynamic-skip-fire in spark ignition engines," SAE Technical Paper 2016-01-0672, 2016, doi:10.4271/2016-01-0672.

[21] Rapp, V., Killingsworth, N., Therkelsen, P., et al., "Lean Combustion, 2nd Edition," *Lean-Burn Internal Combustion Engines*, Elsevier, 2016, 111-146, doi:10.1016/C2013-0-13446-0.

[22] Germane, G., Wood, C., Hess, C., "Lean Combustion in Spark-Ignited Internal Combustion Engines - A Review," SAE Technical Paper 831694, 1983, doi:10.4271/831694.

[23] Drake, M., Fansler, T Lippert, A, "Stratified-charge combustion: modeling and imaging of a spray-guided direct-injection spark-ignition engine," *Proceedings of the Combustion Institute*, 30(2), pp.2683-2691, 2005, doi:org/10.1016/j.proci.2004.07.028.

[24] Fajardo, C. Sick, V., "Flow field assessment in a fired spray-guided spark-ignition direct-injection engine based on UV particle image velocimetry with sub crank angle resolution," *Proceedings of the combustion institute*, 31(2), pp.3023-3031, 2007, doi:10.1016/j.proci.2006.08.016.

[25] Moriyoshi, Y., Kuboyama, T., Kaneko, M., Yamada, T., Sato, H., "Fuel Stratification Using Twin-Tumble Intake Flows to Extend Lean Limit in Super-Lean Gasoline Combustion," SAE Technical Paper 2018-01-1664, 2018, doi:10.4271/2018-01-1664.

[26] Stanglmaier, R., Roberts, C., "Homogeneous charge compression ignition (HCCI): benefits, compromises, and future engine applications," SAE *transactions*, pp.2138-2145,1999, doi: www.jstor.org/stable/44741335.

[27] Okita, R., "Mazda SKYACTIV-G Engine with New Boosting Technology," In Advanced Clean Cars Symposium: The Road Ahead, Air Resources Board, Sacramento, USA, 27th–28th September,2016

[28] Sens, M., Binder, E., Benz, A., Kramer, L., at al. "Pre-chamber ignition as a Key Technology for Highly Efficient SI Engines-New Approaches and Operating Strategies," 39th International Vienna Motor Symposium, Apr. 2018.

[29] Mueller, C., Morcinkowski, B., Habermann, K., Uhlmann, T., Schernus, C. "Development of a pre-chamber for spark ignition engines in vehicle applications," 4th International Conference on Ignition Systems for Gasoline Engines, Dec. 2018.

[30] Ricardo, H.R., Internal-combustion engine. 1918, Google Patents.

[31] Gussak, L., Karpov, V. Tikhonov, Y., "The application of lag-process in prechamber engines," SAE Technical Paper, 790692, 1979, doi:10.4271/790692.

[32] Noguchi, M., Sanda, S. and Nakamura, "Development of Toyota lean burn engine," SAE Technical Paper, 760757, 1976, doi:10.4271/760757.

[33] Pape, J., Getzlaff, J., Gruenig, C., Kuhnert, D. and Latsch, R., "Investigations on Pre-Chamber Spark Plug with Pilot Injection," SAE Technical Paper 2007-01-0479, 2007, doi:10.4271/2007-01-0479.

[34] Attard, W.P., Fraser, N., Parsons, P. and Toulson, E., "A Turbulent Jet Ignition Pre-Chamber Combustion System for High Fuel Economy Improvements in a Modern Vehicle Powertrain," SAE Technical Paper 2010-01-1457, 2010, doi:10.4271/2010-01-1457.

[35] Roethlisberger, R., Favrat, D., "Comparison between direct and indirect (prechamber) spark ignition in the case of a cogeneration natural gas engine, part I: engine geometrical parameters," *Applied Thermal Engineering*, 22(11), 1217-1229, 2002, doi:10.1016/S1359-4311(02)00040-6.

[36] Xu, G., Wright, Y., Schiliro, M., Boulouchos, K., "Characterization of combustion in a gas engine ignited using a small un-scavenged pre-chamber," *International Journal of Engine Research*, 2018, doi: 10.1177/1468087418798918.

[37] Jamrozik, A., “Lean combustion by a pre-chamber charge stratification in a stationary spark ignited engine,” *Journal of Mechanical Science and Technology*, 29(5):2269-2278, 2015, doi:10.1007/s12206-015-0145-7.

[38] Toulson, E., Schock, H., Attard, W., “A Review of Pre-Chamber Initiated Jet Ignition Combustion Systems,” SAE Technical Paper 2010-01-2263, 2010, doi:10.4271/2010-01-2263.

[39] Lumsden, G., Watson, H., “Optimum Control of an S.I. Engine with a λ=5 Capability,” SAE Technical Paper 950689, 1995, doi:10.4271/950689.

[40] Schumacher, M., Wensing, M., “A Gasoline Fuelled Pre-Chamber Ignition System for Homogeneous Lean Combustion Processes,” SAE Technical Paper 2016-01-2176, 2016, doi:10.4271/2016-01-2176.

[41] Otsu, N., “A Threshold Selection Method from Gray-Level Histograms,” *IEEE Transactions on Systems*, Vol. SMC-9, No. 1, 1979.

[42] Iafrate, N., Matrat, M., & Zaccardi, J. M., “Numerical investigations on hydrogen-enhanced combustion in ultra-lean gasoline spark-ignition engines,” *International Journal of Engine Research*, 1468087419870688, doi:10.1177/1468087419870688.

3. Methodologies for Internal Combustion Engine Simulation

The development of a new engine is a very complex process and the experimental activity has to comply with the all the phenomena discussed in the previous chapters, resulting in increasing cost and duration of engine development. Therefore, numerical analysis becomes essential, due to its lower costs, contributing to reduce the duration of engine development [1]. The modelling of ICE is a multidisciplinary subject that involves different fields, and it can be classified into four major categories, differing for the level of approximation used, as listed in *Table 3.1*.

Table 3.1 Classification of the numerical approaches.

Model type	Typical Application
0D	Combustion
1D	Gas Exchange
Quasi-Dimensional	Combustion
3D	Flow Field, Combustion

Zero-dimensional (0D) approaches solve the mass and the energy conservation equations under the assumption that the thermodynamic properties are only function of the time. Any space dependency is hence neglected, and the working fluid is assumed at rest. The major advantage of this approach is its ability of reproduce the in-cylinder processes in a reduced computational time. The mean drawback is the absence of pressure waves propagation in the pipes, with strong limitation in the prediction of the volumetric efficiency.

1D models allow to overcome the above limitation, since they solve the unsteady flow equations in the external pipes along the mean flow direction. In this approach every thermo-fluid-dynamic propriety is considered uniform along each section of the pipe. Usually, 1D models are coupled with a refined 0D description of in-cylinder processes (quasi-dimensional phenomenological sub-models), to accurately predict the overall engine behaviour. These last are widely used for the analysis of the global engine performance and recently, due to the good compromise between accuracy and computational time, also for supporting the engine optimization and calibration [2].

3D methodologies are based on the integration of the Navier Stokes equations, giving detailed fluid-dynamic information for the complex 3D domains. These models, due to their relevant computational effort, are employed for the simulation of the unsteady mean and turbulent flow motion within a limited portion of the engine, usually intake air-box, after-treatment devices and cylinder, for a reduced set of operating conditions.

In the present research activity, the adopted methodology is based on a 1D description of the flow inside the intake and the exhaust pipes, whereas phenomenological 0D sub-models are used to reproduce in-cylinder phenomena. Nevertheless, 3D approaches will be also utilized, mainly focusing on their role in supporting the development and validation of a 0D turbulence submodel.

3.1. 0D Approaches

As previously mentioned, in a 0D approach all the variables are univocally time-dependent and uniform in the entire control volume. As a consequence, only the mass and energy conservation equations, eq.(3.1), (3.2) need to be solved, expressed as follows:

$$\frac{dm}{dt} = \dot{m}_{in} - \dot{m}_{out} + \dot{m}_{inj} \tag{3.1}$$

$$\frac{d(me)}{dt} = -p\frac{dV}{dt} - \frac{dQ_w}{dt} + \dot{m}_{in}h_{in} - \dot{m}_{out}h_{out} + \dot{m}_{inj}{h_f}^0 \tag{3.2}$$

The first two terms of eq. (3.1) are the incoming and outcoming mass flow rate through the valves, respectively, while the last one is related to the injected fuel flow rate. In the eq. (3.2), the first term is the mechanical power exchanged by the fluid with the piston, the second one represents the heat transfer rate through the walls of the combustion chamber, and the last three terms are related to the enthalpy fluxes associated to the mass exchanges through the control surface. Generally, eq. (3.2) is reformulated as a function of the temperature variation eq. (3.3), considering the internal energy dependency on temperature and composition. With this formulation the energy released by the combustion process is expressed as a function of the burned gas fraction variation, from reactants to products, $\frac{dx_b}{dt}$.

$$\frac{dT}{dt} = \frac{1}{mc_v}\left(-p\frac{dV}{dt} - \frac{dQ_w}{dt} + \dot{m}_{in}h_{in} - \dot{m}_{ex}h_{ex} + \dot{m}_{inj}{h_f}^0 - e\frac{dm}{dt} - \frac{\partial e}{\partial x_b}\frac{dx_b}{dt}\right) \tag{3.3}$$

To solve these equations, several sub-models are used with the aim to overcome the absence of information on the velocity field. For the gas-cylinder wall heat transfer, numerous correlations are present in the current literature, mainly dependent on the in-cylinder thermodynamic state and engine speed.

The Woschni [3], the Hohenberg [4] and the Annand [5] correlations are widely adopted for ICE simulation. In this thesis, an Hohenberg-like correlation has been used and it will be described in the next section. The instantaneous flow through the valves is evaluated using the equation of the isentropic flux, in subsonic, eq. (3.4), or sonic (3.5) conditions.

$$\frac{dm}{dt} = c_d A_{ref} P_1 \sqrt{\frac{2k}{k-1}\frac{1}{RT_1}\left[\left(\frac{p_2}{p_1}\right)^{\frac{2}{k}} - \left(\frac{p_2}{p_1}\right)^{\frac{k+1}{k}}\right]} \tag{3.4}$$

$$\frac{dm}{dt} = c_d A_{ref} P_1 \sqrt{\frac{k}{RT_1}\left[\left(\frac{2}{k+1}\right)^{k+1/k-1}\right]} \tag{3.5}$$

p_1 and T_1 are the pressure/temperature of the upstream flow conditions, and p_2 refers to the downstream pressure. k is the heat capacity ratio, and A_{ref} is a reference area. The discharge coefficient c_d is the ratio between the actual and the isentropic flow, and it is evaluated experimentally under steady state conditions. Generally, this value is function of the valve geometry, lift and the flow direction (direct / reverse).

The burning rate (dx_b/dt) can be directly imposed, or, alternatively, it can be estimated through predictive combustion models. The former approach is generally implemented during the first stage of the model development. If available, the "*experimental*" burning rate can be imposed, extracted from the experimental pressure traces, solving the eq. (3.1) and (3.3) in a so-called reverse analysis. Otherwise, a Wiebe function is employed assuming a predefined burned fraction profile as a function of the crank angle.

Zero-dimensional model can be further sub-classified in three different categories, as a function of the number of the thermodynamic zones in which the control volume is divided. In particular, it is possible to use a single, a two or a multi-zone approach. Each zone is characterized by a distinct thermodynamic state with energy and mass interactions, for which the eq. (3.1) and (3.3) are solved at each time step. During the intake and the exhaust phase, it is reasonable to assume that the composition is uniform in the entire cylinder volume. As a consequence, a single zone is employed. On the contrary, as soon as the spark occurs, the combustion chamber is mainly divided in two zones, the unburned and the burned zones (two-zone approach).

Multi-zone models are also widely used when it is required to predict the pollutant emissions such as NO_X, since the presence of a temperature gradient in the unburned zone strongly affects their correct estimation.

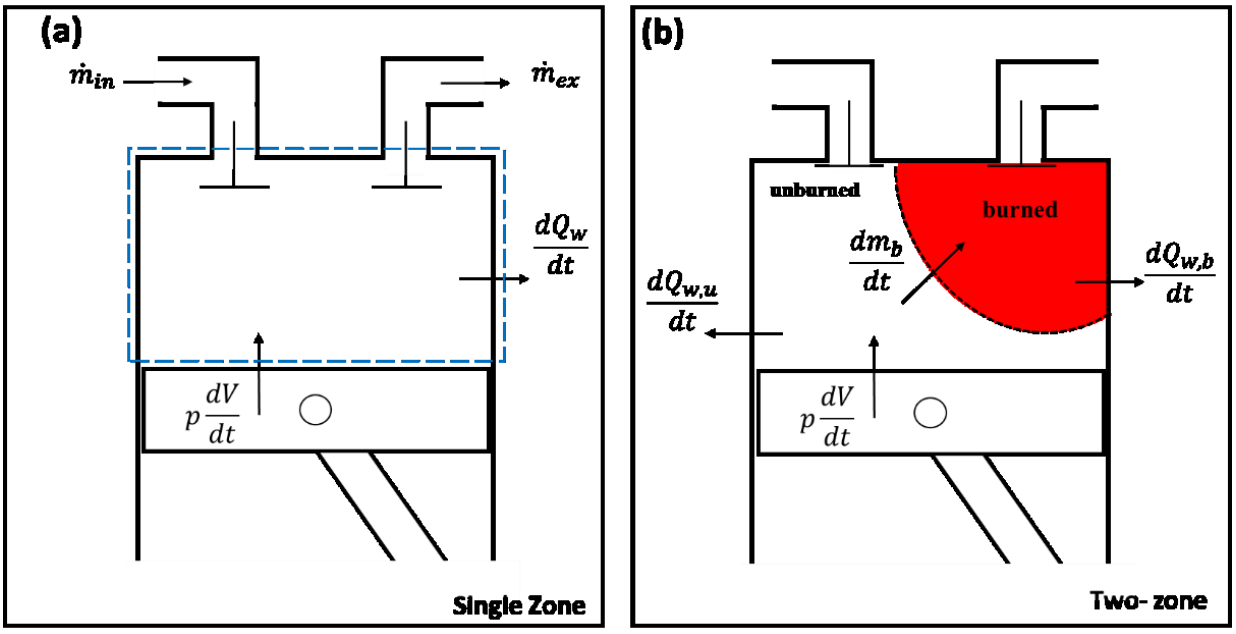

Figure 3-1 (a) Single zone combustion scheme, (b) two-zones combustion scheme.

Various combustion models for SI engines have been proposed since many years, trying to physically evaluate the burning rate, under the common hypothesis that the combustion is enhanced by the turbulence [6],[7],[8]. Basic differences between them consist in the way the laminar-turbulent flame transition occurs and, on the mechanism inducing the turbulence-related burn-rate enhancement. Other approaches are also used, such as the one introduced in [9], where the combustion chamber is described as a stochastic reactor and the combustion is modelled by probability density functions. The most widely diffused combustion model are certainly the eddy burn-up approach and the fractal one. The former describes the flame entrainment and subsequent combustion of unburned mixture, and proved to agree with the experimental burned mass fraction trends [10],[11]. The latter tries to directly describes the enhancement of flame front surface, resorting to the concepts of fractal geometry [12],[13]. Several comparisons of these approaches are present in the literature, leading to the conclusion that, except for the tuning efforts, both the models are able to reproduce with high accuracy the combustion inside conventional SI engines [6][14]. In this PhD Thesis, the fractal approach has been selected, due to a more consistent physical background, demonstrating that it can be applied, if properly extended, for both conventional SI and pre-chamber engines.

3.2. 1D Approaches

The partial differential equation system in (3.6) reports the conservative form of the flow equations (continuity, energy and momentum) under the hypothesis of an inviscid, adiabatic 1D flow schematization in a variable area pipe. In it, each thermodynamic property and the flow velocity, u, are only a function of space, x, and time, t:

$$\begin{cases} \frac{\partial \rho}{\partial t} + \frac{\partial \rho u}{\partial x} + \rho u \left(\frac{1}{\Omega}\frac{d\Omega}{dx}\right) = \frac{\partial \rho}{\partial t} + \frac{\partial \rho u}{\partial x} + \rho u \alpha_A = 0 \\ \frac{\partial (\rho E)}{\partial t} + \frac{\partial (\rho u H)}{\partial x} + \rho u H \left(\frac{1}{\Omega}\frac{d\Omega}{dx}\right) = \frac{\partial (\rho E)}{\partial t} + \frac{\partial \rho u H}{\partial x} + \rho u H \alpha_A = 0 \\ \frac{\partial (\rho u)}{\partial t} + \frac{\partial (\rho u^2 + p)}{\partial x} + \rho u^2 \left(\frac{1}{\Omega}\frac{d\Omega}{dx}\right) = \frac{\partial (\rho u)}{\partial t} + \frac{\partial (\rho u^2 + p)}{\partial x} + \rho u^2 \alpha_A = 0 \end{cases} \tag{3.6}$$

The above equations can be expressed in a more compact vector way (3.7), in which U represents the vector of the conservative variables, F is the flux vector and S characterizes the source term vector.

$$\frac{\partial U}{\partial t} + \frac{\partial F(U)}{\partial x} = S \quad U = \begin{Bmatrix} \rho \\ \rho u \\ \rho E \end{Bmatrix} ; \quad F = \begin{Bmatrix} \rho u \\ \rho u^2 + p \\ \rho u H \end{Bmatrix} \quad s = -\begin{Bmatrix} \rho u \alpha_A \\ \rho u^2 \alpha_A \\ \rho u H \alpha_A \end{Bmatrix} \tag{3.7}$$

To properly model the flow within the intake and the exhaust pipes of an ICE, additional terms must be however considered, considering the gas-wall friction, the heat exchange and the scalar transport of injected fuel and residuals species. The system then assumes the form reported in (3.8) in which the last two rows refer to the residual gases and vapour fuel fraction propagation, respectively.

$$U = \begin{Bmatrix} \rho \\ \rho u \\ \rho E \\ \rho x_r \\ \rho x_f \end{Bmatrix} ; \quad F = \begin{Bmatrix} \rho u \\ \rho u^2 + p \\ \rho u H \\ \rho u x_r \\ \rho u x_f \end{Bmatrix} \quad S = -\begin{Bmatrix} \rho u \alpha_A \\ \rho u^2 \left(\alpha_A + \frac{2 f_a}{D}\frac{u}{|u|}\right) \\ \left(\rho u H \alpha_A - \frac{4q}{D}\right) \\ \rho u x_r \alpha_A \\ \rho u x_f \alpha_A \end{Bmatrix} \tag{3.8}$$

Where, f_a is the friction coefficient estimated with the Poiseuille or Blasius formula as a function of the velocity inside the pipes.

x_r and x_f represent as said the fraction of the residual gas and vapor fuel, respectively, and are formulated according to eq. (3.9).

$$x_r = \frac{m_r}{m}; \quad x_f = \frac{m_f}{m}; \tag{3.9}$$

q represents the heat flux through the pipe walls, expressed by the eq (3.10):

$$q = \frac{1}{2}\rho|u|f_a c_p(T_{wall} - T) \tag{3.10}$$

3.3. 3D Approaches

3D models solve the Navier Stokes equations, based on the resolution of the mass, momentum and energy equations as a function of the time along the three space coordinates. These equations represent a non-linear system of partial differential equations that are solved in the control volume, properly schematized in a computational grid. Due to its complexity, the system is general solved through Computational Fluid Dynamics (CFD) software, through three possible approaches:

1. *Direct Numerical Simulation (DNS*): is based on the direct discretization of the Navier-Stokes equations. Nevertheless, the computational cost is extremely expensive in terms of both time and memory. Indeed, in order to have a correct solution, the computational grid must be so fine that it is able to capture all the temporal and spatial turbulent scales, up to the smallest one (Kolmogorov scale).

2. *Reynolds Averaged Navier-Stokes (RANS) equations:* the turbulent field is decomposed into its time-averaged and fluctuating quantities. The RANS equations are derived from the time-averaging operation of the original flow equations. Therefore, RANS express the time-averaged behaviour, or in case of quasi-periodic flows such as those in internal combustion engines, phase-averaged flow realizations. The time-averaging introduces new terms, the so-called “Reynolds stresses”, whose solution require the development of proper turbulence submodels to close the problem.

3. *Large Eddy Simulation (LES):* the larger eddies, which are strongly influenced by the geometry of the domain, are directly solved. To reduce the computation efforts, only the smaller scales are properly modelled.

It is worth to underline that the high level of accuracy obtainable from 0D-1D models, such as the one employed in this PhD Thesis, is due to the integration of all the previously described approaches. Nowadays, in the automotive industry, to support the engine development phase, it is a common practice the employment of both 0D-1D and 3D simulations. This practice, indeed, allows to overcome the limits and merge the benefits of each methodology. On the one hand, 3D models allow to obtain realistic analyses of the engine fluid-dynamic behaviour, but the high computational costs limit the study to few cases. Generally, the aim of 3D study is to obtain information which cannot be easily acquired with the experimental campaign, allowing to better understand the physical phenomena. On the other hand, 0D/1D models are able to explore with a reduced time and high accuracy the whole engine system. However, if the formulation of the in-cylinder process is inadequate, the results cannot be considered as realistic enough.

As an example, in the following, it is briefly reported how 0D/1D/3D approaches were integrated during this research activity. In particular, four main steps were followed to characterize the engine with the conventional spark plug system:

- *Step 1*: Starting from the geometric characteristic of the engine, a 0D/1D model was developed. Preliminary 1D simulations under motored operations were performed for different engine speed.
- *Step 2:* The 1D computed time-varying pressure and temperature were imposed as the boundary condition for the 3D in-cylinder motored analyses, focused on the characterization of the in-cylinder flow motion. In particular, the mean and turbulent flow fields were extracted over the entire engine cycle.
- *Step 3:* The results obtained from step 2 were utilized to calibrate the 0D turbulence model, necessary for the combustion model closure, which will be discussed in detail in the following paragraph.
- *Step 4:* Once the turbulence model was tuned, the 1D engine model was performed under fired conditions. The tuning of the combustion model was mainly carried out against the experimental data with the aim to fit in-cylinder pressure cycles.

It must be emphasized that when a new engine, far away from the state of art, is under study, it may be required to develop new in-cylinder models or, if possible, reinforce the ones previously available. This was the case of the pre-chamber SI engine analysed in this PhD Thesis. In that case, the 3D simulations also contributed to clarify the physical phenomena occurring in this novel architecture.

3.4. Turbulent combustion modelling for conventional SI Engine

The original version of the fractal combustion model has been proposed some decades ago [15] This approach is directly founded on the combustion regime occurring in a conventional SI engine, falling in the wrinkled-corrugated flamelet zone, as previously shown in *Figure 2-6*. Here, as already pointed out, the flame front exhibits an increased surface, A_T, due to the interaction with the turbulence, leading in an enhancement of the combustion rate. This geometrical increment is described by the model through the concepts of the fractal geometry. Indeed, several experimental observations proved that a wrinkled flame front presents a fractal behavior, resulting in the auto-similarity of its basic structure [12], [16], [17], [18]. This gives the possibility to relate the turbulent flame front extent to the laminar one, according to turbulence characteristic speed, time and length scales [15], [19].

Under this hypothesis, the burn rate can be written as a function of the wrinkling factor, defined as the ratio between the turbulent and the laminar flame area A_T/A_L

$$\left(\frac{dm_b}{dt}\right)_{fractal} = \rho_u A_T S_L = \rho_u A_L S_L \left(\frac{A_T}{A_L}\right) = \rho_u A_L S_L \left(\frac{L_{max}}{L_{min}}\right)^{D_3-2} \tag{3.11}$$

This wrinkling ratio is evaluated, according to the classical expression reported in [8], based on the fractal dimension, D_3, and the maximum and minimum wrinkling scales L_{max}, and L_{min}. D_3 is assumed to depend on turbulence intensity, u' ,and laminar flame speed S_L, as reported in [18], according to the eq. (3.12).

$$D_3 = \frac{2.35u' + 2.00S_L}{u' + S_L} \tag{3.12}$$

Whereas the wrinkling scales can be interpreted as the scales of macro and micro vortices of the turbulent flow field. L_{max} is related to a macroscopic characteristic dimension of the flame front, here assumed proportional to the flame radius r_f, by the tuning constant c_{wrk} (wrinkling multiplier).

$$L_{max} = c_{wrk} r_f \tag{3.13}$$

L_{min} is commonly taken equal to the size of the smallest turbulent eddy [15], expressed by the Kolmogorov length scale, L_k.

$$L_{mim} = L_k \tag{3.14}$$

The above described model, schematized in *Figure 3-2*, actually applies for a fully developed and freely expanding turbulent flame. Concerning the early flame development and the combustion completion, proper modifications of the model are required.

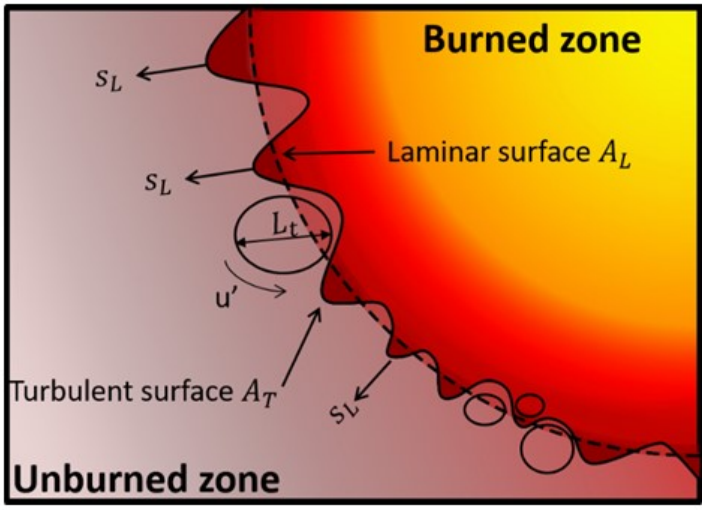

Figure 3-2 Schematic of the fractal combustion model [14].

As already pointed out, the combustion beginning is characterized by a laminar propagation rather than a turbulent one for which the flame front in not effectively corrugated. The transition from laminar to turbulent combustion is then described by a progressive increase of the fractal dimension D_3, according to eqs. (3.15) and (3.16).

$$D_3 = \frac{D_{3,max}u' + D_{3,min}S_L}{u' + S_L} \tag{3.15}$$

$$D_{3,min} = 2.00\ ;\ D_{3,min} = 2.00(1 - \ w_{trans}) + 2.35w_{trans} \tag{3.16}$$

The wrinkling evolution is handled by the variable w_{trans}, reported in the eq.(3.17), as a function of a characteristic time scale, t_{trans}, and a tuning constant of the model c_{trans} (transition multiplier). Whereas the characteristic time scale is computed through the turbulence kinetic energy, k, and its the dissipation rate, ε.

$$w_{trans} = \int \frac{dt}{c_{trans}t_{trans}};\ t_{trans} = \frac{k}{\varepsilon} \tag{3.17}$$

On the opposite, when the flame front interacts with the combustion chamber walls, another modification of the burning rate is introduced. Although a detailed description of flame-wall interaction is far beyond the possibility offered by a quasi-dimensional model, it can be argued that flame front wrinkling no more occurs near the walls, and the burning rate slows down.

The overall burning rate is, hence, expressed as a weighted average between a purely fractal burning rate and a laminar wall combustion, according to eqs. (3.18) and (3.19).

$$\left(\frac{dm_b}{dt}\right) = (1 - w_{wall})\left(\frac{dm_b}{dt}\right)_{fractal} + w_{wall}\left(\frac{dm_b}{dt}\right)_{wall} \tag{3.18}$$

$$\left(\frac{dm_b}{dt}\right)_{wall} = \rho_u A_L S_L \tag{3.19}$$

Also here, a variable, w_{wall} defines the transition from turbulent to wall combustion through the ratio between the area wetted by the flame front on piston, head and cylinder, A_w, and the total flame front area, A_{tot} This ratio is multiplied by the mass fraction of burned gas, x_b, raised by an exponent which is amplified by the tuning constant x_{wc} (wall combustion multiplier).

$$w_{wall} = \frac{A_w}{A_{tot}} x_b^{10x_{wc}} \tag{3.20}$$

For the A_L estimation a tabulated approach is followed to improve the computational time, under the classical assumption of a smooth spherically shaped surface, centered on the sparkplug. The off-line automatic procedure computes the intersections between an “ideal” spherically smoothed flame front and the piston/head/cylinder surfaces. At each time step, the look-up table is read and based on the current piston position and the burned gas volume carried out the related laminar flame area.

The laminar flame speed can be estimated by a numerical correlation. An analysis of the literature works puts into evidence that various laminar flame speed formulations for gasoline have been suggested in the past by different authors. These can be divided in two main categories; experimental-based, such as [20] and [21], and reaction kinetic calculations based likely [22],[23]. On the one hand, the major disadvantage of the former approach is connected to the limited measurement range of relative air/fuel ration and low pressure, due to technical issues [22],[24]. As a consequence, these correlations may lead to inaccurate predictions when applied outside the measurement range, such as in the case of the high pressures and temperatures typical of SI engine operations. On the other hand, the kinetic-based approach allows to explore a wider range of boundary conditions through kinetic calculations, but the accuracy of these models strongly depends on the adopted kinetic scheme, and surrogate fuel formulation. A comparative study between these methods has been carried out during this research activity [25].

In particular, three correlations, based on a laminar flame speed power law formula of eq.(3.21), were analyzed. Two of them are experimentally derived, the remining is chemical kinetics based.

$$S_L = S_{L,0}\left(\frac{T_u}{T_0}\right)^a \left(\frac{p}{p_0}\right)^b EGR_{factor} \tag{3.21}$$

The first correlation, labelled as "Cor A", is based on the well-known Metghalchi et al. approach [26], properly modified to reproduce the results shown in [21]:

$$S_{L0} = B_m + B_\Phi(\Phi - \Phi_m)^2 \tag{3.22}$$

$$\alpha = \alpha_0 + \alpha_1\Phi^{\alpha_2};\quad \beta = \beta_0 + \beta_1\Phi^{\beta_2};\quad EGR_{factor,1} = (1 - e_1 X_{EGR}^{e_2}) \tag{3.23}$$

In eq.(3.22) Φ is the equivalence ratio and in eq.(3.23) X_{EGR} represents the molar fraction of the residual gas, the other variables are constant parameters listed in *Table 3.2.*

The second correlation, labelled as "Cor B", is taken from to [27]. In particular, S_{L0} is modelled according to the Gülder formulation[24], as reported in eq. (3.24), while exponents α and β are considered to be second-order polynomial functions of Φ, as proposed by Liao et al. [28].

$$S_{L0} = W\Phi^\eta e^{-\xi(\Phi-\sigma)^2} \tag{3.24}$$

$$\alpha = \alpha_0 + \alpha_1\Phi + \alpha_2\Phi^2;\quad \beta = \beta_0 + \beta_1\Phi + \beta_2\Phi^2;\quad EGR_{factor,2} = e^{(e_1 X_{EGR})} \tag{3.25}$$

The values of each parameter, whose estimation process is reported in [27], are listed in *Table 3.2.* The correlations do not consider the effect of the EGR on the laminar flame speed correlation. As a consequence an new $EGR_{factor,2}$ has been introduced to avoid the negative value of flame speed given by $EGR_{factor,1}$ higher than X_{EGR}*= 0.3912*, as shown in [4]. The last correlation (Cor C) [29] results from the fitting of 1D laminar flame speeds computed by a chemical kinetic solver (CHEMKIN) and based on the Liu et al. reaction mechanism [30] for a Toluene Reference Fuel (TRF).

$$S_{L0} = A + B\Phi + C\Phi^2 + D\Phi^3 + E\Phi^4 \tag{3.26}$$

$$A = a_1 + a_2 S;\ B = b_1 + b_2 S;\ C = c_1 + c_2 S;\ D = d_1 + d_2 S;\ E = e_1 + e_2 S \tag{3.27}$$

$$\alpha = \alpha_1 + \alpha_2\Phi;\ \beta = \beta_1 + \beta_2\Phi;\ \gamma = \gamma_1 + \gamma_2\Phi;\ EGR_{factor,2} = (1 - \kappa x_{EGR,m})^\gamma \tag{3.28}$$

Where RON and MON are the fuel Research and Motor Octane Numbers, respectively, S=RON-MON is the fuel sensitivity, $X_{EGR,m}$ is the mass fraction of the residual exhaust gas, and all constants are reported in *Table 3.2.*

Table 3.2 Coefficients of the considered laminar flame speed correlations.

Cor A [26] *Experimentally-derived* T_0=298 K, P_0=1.01325 bar T_{range}= [350-550 K]; P_{range}= [0.4-12 atm]; ϕ_{range}= [0.7-1.6]				**Cor B [27]** *Experimentally-derived* T_0=298 K, P_0=1.01325 bar T_{range}= [298-500 K]; P_{range}= [1-25 atm]; ϕ_{range}= [0.6-2.0]				**Cor C [29]** *Numerically-derived* T_0=423 K, P_0=1.00000 bar T_{range}= [323-473 K]; P_{range}= [1-10 bar]; ϕ_{range}= [0.7-1.6]					
B_m	*0.35*	β_2	*2.77*	W	36.82	a_0	5.93	a_1	101.7068	d_1	-1360.444	β_1	-0.3952267
B_ϕ	*-0.549*	β_1	*0.14*	η	0.22	b_2	-0.9250	a_2	-16.80694	d_2	84.03323	β_2	0.1766350
ϕ_m	*1.1*	β_0	*-0.357*	ξ	4.86	b_1	2.0120	b_1	-777.2416	e_1	340.6086	γ_1	1.311202
α_2	*3.51*	e_1	*2.06*	σ	1.11	b_0	-1.3650	b_2	76.07949	e_2	-19.61888	γ_2	0.6858792
α_1	*-0.27*	e_2	0.77	a_2	3.28	e_1	-3.69	c_1	1763.747	α_1	1.388656	κ	1.538489
α_0	*2.4*			a_1	-7.52			c_2	-125.1039	α_2	0.3742516		

3.4.1. Turbulence model

For combustion model closure, the fractal approach requires several parameters connected to the turbulent field established in the combustion chamber, namely u', L_k, L_t, and ε. To this aim a phenomenological procedure, derived from the 3D RNG $k-\varepsilon$ turbulence formulation presented in [31] has been synthesize in a 0D framework, leading to the following system:

$$\begin{cases} \dfrac{dmk}{dt} = \left(\dot{mk}\right)_{inc} - \left(\dot{mk}\right)_{out} + \dfrac{2}{3}\dfrac{\dot{\rho}}{\rho}\left(-mv_t\dfrac{\dot{\rho}}{\rho} + mk\right) + p - m\varepsilon \qquad (I) \\ \dfrac{dmK}{dt} = \left(\dot{mK}\right)_{inc} - \left(\dot{mK}\right)_{out} - f_d\dfrac{mK}{\tau_T} + mK\dfrac{\dot{\rho}}{\rho} - P \qquad (II) \\ \dfrac{dmT}{dt} = \left(\dot{mT}\right)_{inc} - \left(\dot{mT}\right)_{out} - f_d\dfrac{mT}{\tau_T} \qquad (III) \end{cases} \tag{3.29}$$

Th system of equation defined in (3.29) includes the balance equations of turbulent kinetic energy, k, mean flow kinetic energy, K, and tumble angular momentum, T, defined as follows:

$$k = \frac{3}{2}u';\ K = \frac{1}{2}U_{fK}^2;\ T = U_r r_T \tag{3.30}$$

where *u'* is the turbulence intensity, U_{fK} is the mean flow velocity, U_T is the tumble velocity, r_T is the radius of the tumble vortex and v_t is the turbulent viscosity:

$$v_t = c_\mu \frac{k^2}{\varepsilon} \tag{3.31}$$

The first and the second terms in all the three equations describe the incoming and outcoming convective flows through the valves. The third term in equations (II) and (III) expresses the decay due to the shear stresses with the combustion chamber walls. To model this effect, a decay function, f_d, and a characteristic time scale, t_T, are introduced:

$$f_d = c_{fd0} + c_{fdm}\left[max\left(\frac{B}{H}, 1\right), -1\right] \tag{3.32}$$

$$t_T = \frac{r_T}{u'} \tag{3.33}$$

The decay function only depends on the instantaneous geometrical dimensions of the combustion chamber eq.(3.32). It is built to be particularly high near the TDC, where the tumble vortex collapse is expected to occur. The tuning constant c_{fd0} acts as an offset for the tumble and kinetic energy dissipations due to internal viscous forces. The above offset allows to improve the tumble prediction around the BDC. Whereas the c_{fdm} is a multiplier utilized to adjust the intensity of the tumble collapse.

Coherently with the k formulation, the K equation includes an additive compressibility term, $mK\,\dot{\rho}/\rho$, and a subtractive turbulent production term, P, expressing the energy cascade mechanism. The latter quantity is related to the difference between the overall mean flow kinetic energy, K, and the one associated to the tumble motion, $K_T = U_T^2/2$, according to:

$$P = c_{pKk} m \frac{K - K_T}{t_T} \tag{3.34}$$

c_{PKk} is a model constant, modulating the energy transfer from the mean flow to the turbulent one. Concerning the convective terms in system (3.29) the following relations eqs.(3.35), (3.36), (3.37) are utilized, based on cylinder incoming and outcoming contributions, for both forward and reverse flow (*f* and *b* subscripts, respectively). In the eqs .(3.36), (3.37), the mean flow and tumble velocities (v_K and v_T) include flow losses though the valves. In particular, they comprise tumble and discharge coefficient, respectively. Those coefficients are specified as a function of the valve lift.

The tumble coefficient is also affected by the angle between intake runner and cylinder axis. The global multipliers c_{Tin0} and c_{Kin0} allows to tune the above parameters. The turbulence integral length scale is not directly modeled, but its evolution during the engine cycle is described by a sequence of S-shaped functions. It is assumed to not change with the engine operating conditions.

$$\left(\dot{m}k\right)_{inc} = 0; \quad \left(\dot{m}k\right)_{out} = k(\dot{m}_{inb} + \dot{m}_{exf}); \tag{3.35}$$

$$\begin{gathered}\left(\dot{m}K\right)_{inc} = \frac{1}{2}\left[\dot{m}_{inf}\left(c_{Kin0}v_{Kinf}\right)^2 + \dot{m}_{exf}v_{Kexf}^2 + \dot{m}_{exb}v_{Kexb}^2\right]; \\ \left(\dot{m}K\right)_{out} = K(\dot{m}_{inf} + \dot{m}_{exf});\end{gathered} \tag{3.36}$$

$$\begin{gathered}\left(\dot{m}T\right)_{inc} = r_t(\dot{m}_{inf}c_{Tin0}v_{Tinf} - \dot{m}_{exf}v_{Texf} - \dot{m}_{exb}v_{Texb}); \\ \left(\dot{m}T\right)_{out} = 2T(\dot{m}_{inf} + \dot{m}_{exf});\end{gathered} \tag{3.37}$$

The dissipation rate, ε, needed to integrate the k equation, is calculated by:

$$\varepsilon = c_\mu^{3/4}\frac{k^{3/2}}{L_t} \tag{3.38}$$

The tumble radius is assumed as a pure geometrical parameter, not depending on the operating conditions. It is specified by a simple formulation in (3.39) where c_{rT0} and c_{rTm} are two adjustable constants.

$$r_t = c_{rT0+}c_{rTm}\frac{1}{4}\sqrt{B^2 + H^2} \tag{3.39}$$

3.4.2. Sensitivity analysis of the tuning constants

The above described combustion model, coupled with the turbulence one, has in total 8 tuning constants, three of them (c_{trans} , c_{wrk}, x_{wc}) acting on the combustion process and the remaining (c_{Kin0} , c_{Tin0}, c_{fd0}, c_{fdn} , c_{PKk}) on the turbulence field prediction. In order to assess the impact of these parameters on the combustion and turbulence submodels, a sensitivity analysis is here reported. The latter is carried out on a reference engine architecture at WOT for different engine speed. Starting from a reference setting, labelled in the next figures as "Ref", each constant is modified by ± 30% one by one.

For the fractal tuning constant, the effects of the above changes are depicted as a function of a non-dimensional engine speed in terms of characteristic combustion durations, namely $MFB_{0\text{-}10}$, $MFB_{10\text{-}50}$, and $MFB_{50\text{-}90}$ (angular periods between typical combustion events: spark, MFB_{10}, MFB_{50}, and MFB_{90}).

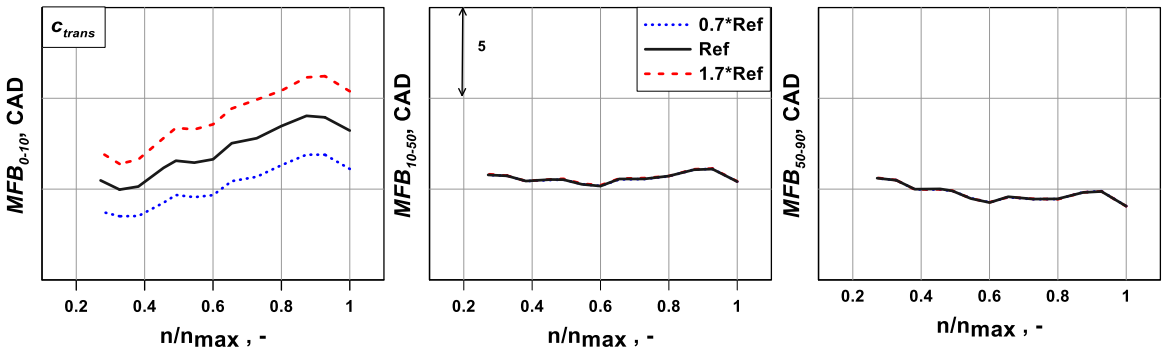

Figure 3-3 Sensitivity analysis in terms of characteristic combustion durations on c_{trans}[14].

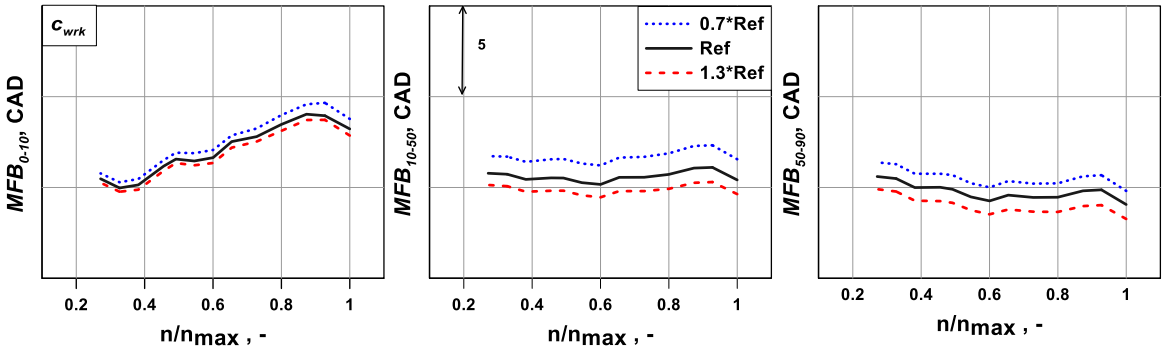

Figure 3-4 Sensitivity analysis in terms of characteristic combustion durations on c_{wrk}[14].

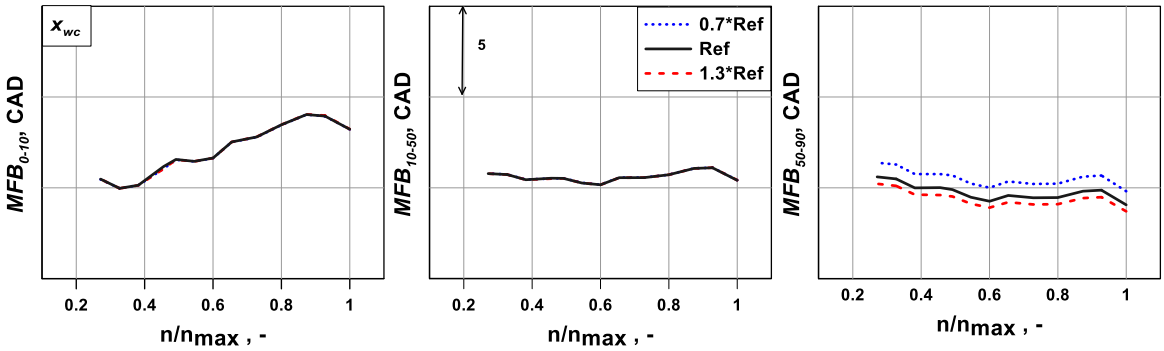

Figure 3-5 Sensitivity analysis in terms of characteristic combustion durations on x_{wc}[14].

Figure 3-3 refers to the constant c_{trans} that mainly affect the early stage of the combustion with a negligible effect on the other combustion phases. The c_{wrk} assessment is reported in *Figure 3-4,* this variable exerts a localized effect on angular periods $MFB_{10\text{-}50}$ and $MFB_{50\text{-}90}$, for which a higher value determines an enhancement of the combustion. In last comparison, depicted in *Figure 3-5* it visible that the cconstant x_{wc} only affects the tail of the combustion.

For the turbulence model constants, the effects of the above changes are depicted as a function of the engine speed in terms mean flow velocity, turbulence intensity and tumble velocity.

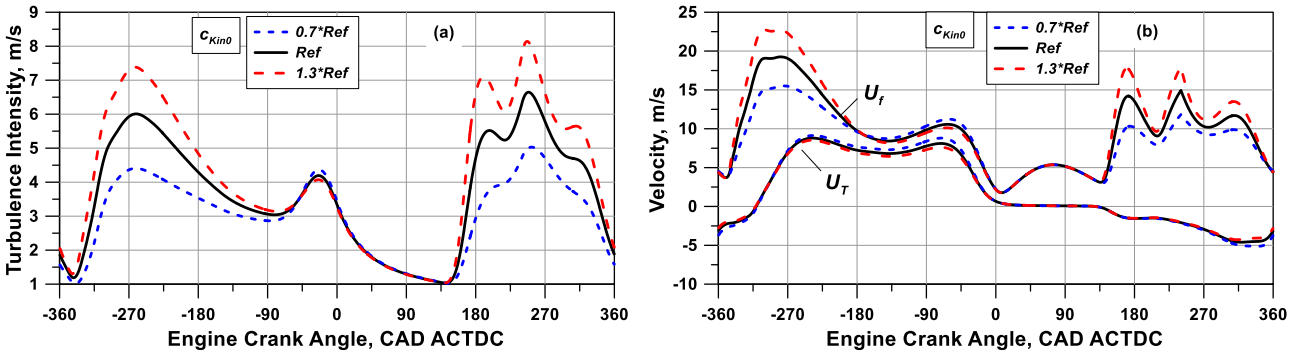

Figure 3-6 Sensitivity analysis in terms of mean flow, tumble and turbulence intensity on c_{kin0} from [31].

The c_{Kin0} constant significantly modifies the mean flow and turbulence peaks in the middle of the intake stroke, as reported in *Figure 3-6*. However, it turns in a reduced modification of the turbulence enhancement close to TDC. On the contrary, c_{Tin0} impacts on each monitored parameter, such as U_f, U_T and u' as shown in *Figure 3-7*. Actually, a higher tumble level at the compression stroke end determines a greater mean flow velocity. Moreover, the collapse of the more intense tumble motion turns in an increased turbulence speed-up.

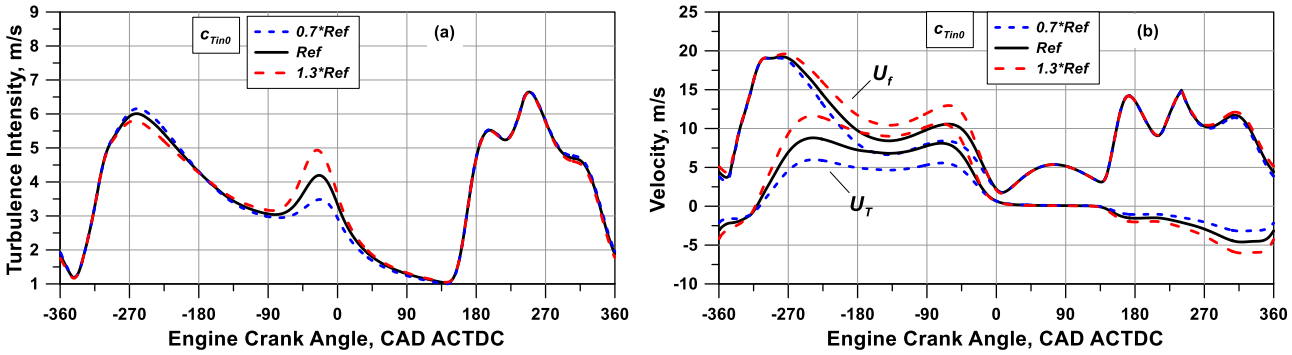

Figure 3-7 Sensitivity analysis in terms of mean flow, tumble and turbulence intensity on c_{Tin0} from [31].

The parameter c_{fd0}, reported in *Figure 3-8*, acts on the decay of both mean flow and tumble velocities, turning in more (less) intense turbulence production close to TDC. The variable c_{fdm} controls the crank angle for tumble collapse, with minor impact on turbulence peaks, as reported in *Figure 3-9*. The final comparison refers on the effect of c_{PKk}, *Figure 3-10*. This constant does not affect the tumble levels, while it modifies turbulence trend during compression stroke. However, even if the different turbulence change during compression, due to lower U_f, similar u' peaks are reached.

Globally looking to the above trends, proper strategies for model tuning can be drawn. As previously mentioned, firstly the turbulence is tuned through the comparison of 3D calculation carried out in motored condition. Secondly, the combustion is calibrated with the aim to minimize the global speed-averaged error between the computed and experimental characteristics combustion angles.

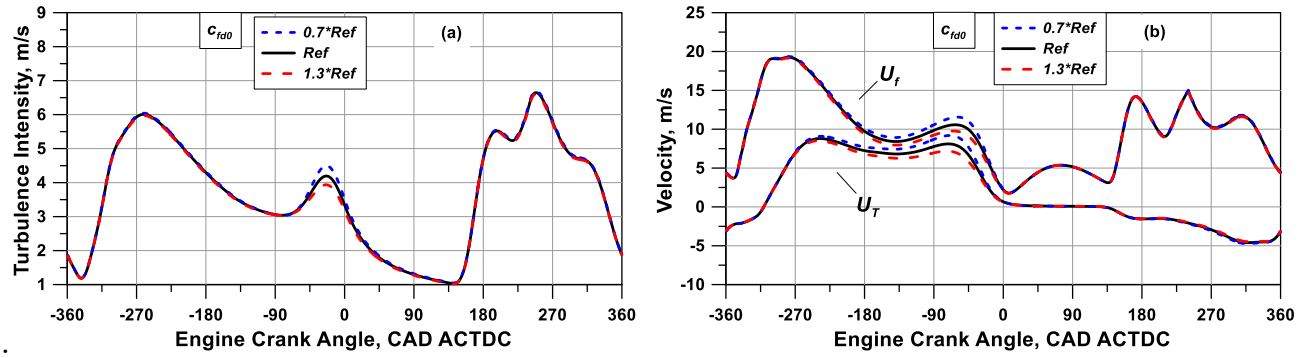

Figure 3-8 Sensitivity analysis in terms of mean flow, tumble and turbulence intensity on c_{fd0} from [31].

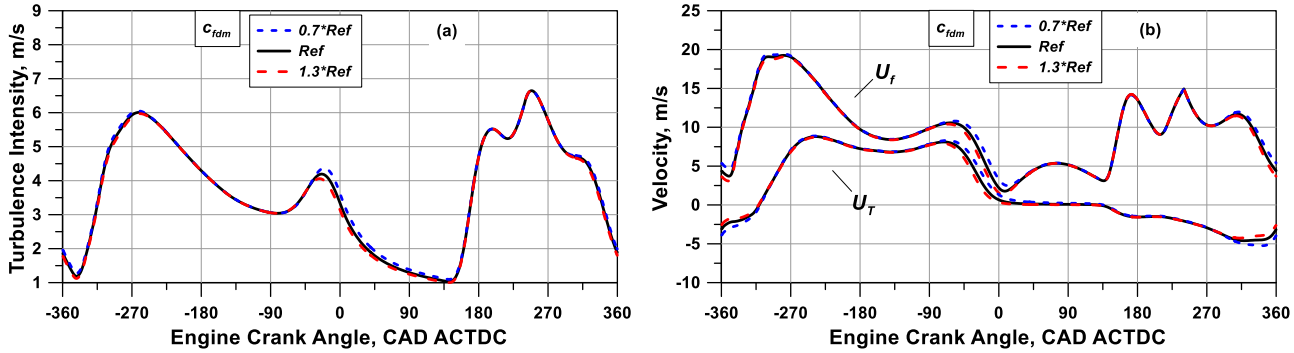

Figure 3-9 Sensitivity analysis in terms of mean flow, tumble and turbulence intensity on c_{fdm} from [31].

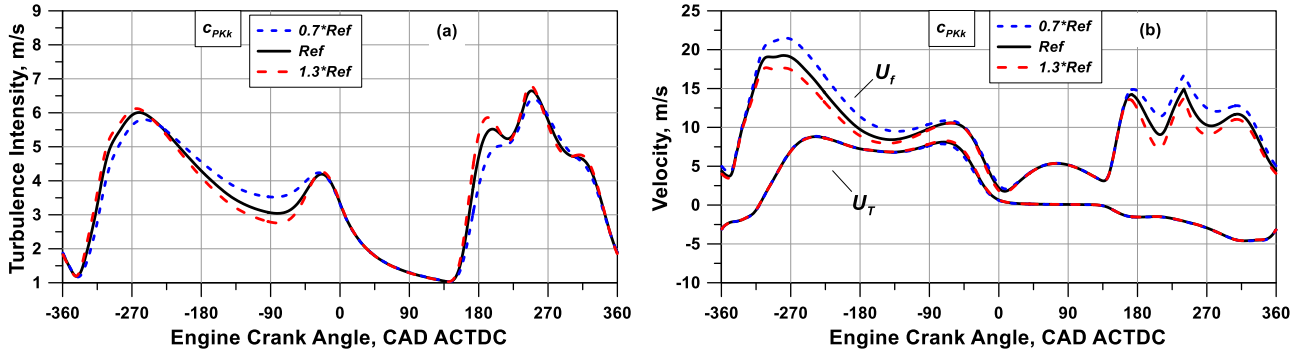

Figure 3-10 Sensitivity analysis in terms of mean flow, tumble and turbulence intensity on c_{pKk} from [31].

Concerning the turbulence, most important tuning constant appears to be c_{Tin0}: Its value is adjusted to gain a good matching with 3D-derived tumble level and turbulence speed-up during the compression stroke. Secondly, c_{Kin0} is identified to reproduce the 3D mean flow velocity peak.

Tumble collapse and close-to-TDC turbulence peak can be further handled by c_{fd0} and c_{fdm} constants. Finally, the c_{PKk} multiplier is, if needed, fine-tuned to adjust the mean flow and turbulence trends, without any significant impact on tumble levels and turbulence speed-up.

Regarding the combustion, this procedure applies generally when full load experimental data are available at various speeds, that is the more common case in the practical experiences. The calibration is composed of three steps, listed below:

1. $MFB_{10\text{-}50}$ error is minimized through c_{wrk} adjustments.
2. $MFB_{0\text{-}10}$ error is controlled by c_{trans} tuning.
3. $MFB_{50\text{-}90}$ error is minimized by a proper x_{wc} selection.

3.5. Turbulent combustion modelling for Pre-chamber SI Engine

Despite the numerous experimental study available in the literature on a pre-chamber SI engine [32],[33],[34],[35],[36],[37],[38] the employment of numerical analyses is of fundamental importance to improve and understand the basic physics beyond this novel architecture. Indeed, experimental campaign for this kind of engine are strongly limited by technological and economic issues. Hence, experimental studies on mixture preparation and combustion development within such a small pre-chamber volume can be challenging even with optical engines. Additionally, the analysis of the impact of different design features, such as the injector location, the spark plug position, the hole's number, length and diameter, requires considerable time and cost. Under this point of view, a 3D-CFD model can provide detailed insights into the pre-chamber mixing and combustion processes, helping to properly understand and optimize a jet ignition process. To this aim, several studies were carried out, some of them more focused on design optimization, other more related to the analysis of different operating conditions. Shah [39] investigated the impact of the pre-chamber volume and the hole diameter on the jet propagation in the main chamber, leading to the conclusion that the optimal design has to be selected balancing two contrasting effects. Indeed, in a smallest pre-chamber the pressure built up across the chambers causes a short burst of pre-chamber ejection instead of a long-lasting jet which promotes turbulent mixing in the main chamber. Whereas the largest pre-chamber causes sufficient pressure buildup but may not exhaust completely before main chamber ignites, hence contributing to loss in overall combustion efficiency [39]. Additionally, for a given pre-chamber volume, a smaller nozzle diameter will cause a higher flow restriction across the chamber, which results in high combustion enhancement, but quenching phenomena may occur. Whereas, a larger nozzle diameter causes a short-lived bursts of pre-chamber ejection, not ensuring a sufficient turbulence level to sustain the lean combustion. In [40] the effects of the hole orientations and the pre-chamber volume on the turbulence field were analyzed.

The results show a higher TKE-level at the spark plug for the biggest pre-chamber, due to the establishment of tumble motion, not visible in the smallest one. However, the high turbulence level required near the spark plug can be achieved only with a hole orientation that establishes a swirl motion, too. A more detailed study has been carried out by [41] in which 3D-CFD simulation and experimental activity were performed to analyze the influence of both relevant design and engine parameters on the fluid mechanics and thermodynamic proprieties of active and passive pre-chambers.

The discussed results and many other available in the literature put into evidence that the optimum layout depends on the behavior of many different pre-chamber parameters in the right combination. Hence, a highly specific knowledge of the engine under study it is mandatory since it will not be possible to attain all the indicated advantages simply by putting an available pre-chamber in combustion system.

Due to the complexity of all the phenomena explained, 3D analysis is certainly the most suitable approach to well-describe the interaction between combustion, chemical kinetics, and turbulence occurring in a pre-chamber engine. However, the high computational time doesn't allow to explore the entire engine operating plane. On the contrary, this can be done either through time consuming experimental activity, or through a numerical engine calibration based on 0D/1D approaches, accepting of course to lose of some degree of accuracy. In particular, in this research activity, a 0D/1D calibration was mandatory, since the experimental campaign on the multi-cylinder pre-chamber engine was not available, while it is only currently ongoing. The obtained results are presently employed to reduce the number of tests, which are only focusing on values of control parameters close to the ones set on the numerical engine calibration.

To reach the above target, the development of the 0D/1D model must be able to properly sense the main physical phenomena controlling the combustion process in a pre-chamber engine, which was, of course, a great challenge. The activity related to the model development started obviously from the analysis of the current literature.

For this reason, several models, proposed in the literature, were firstly individually analyzed mainly evaluating their ability to physically describe the different phenomena occurring in a pre-chamber. A turbulence (K-k-ε) and heat transfer models have been proposed for a passive pre-chamber in [42]. The model is able to accurately reproduce 3D reference results in terms of pressure traces and turbulence variables. However, this study was limited to the analysis of the compression stroke, due to the absence of a coupling with a combustion model. In [43], the heat transfer was evaluated by a PC-engine-adapted correlation. A Wiebe function was imposed to describe the combustion processes in both the chambers at the expense of the model predictiveness.

Other approaches describe in a more phenomenological way the combustion process in an active PC [44]. A common hypothesis is that a conical hot jet from the PC controls the initial phase of the MC combustion. As an example, a model dependency was introduced in [45] based on the second Karlovitz number, estimated at the PC hole outlet. Until the Karlovitz number is higher than one, the combustion is assumed to be controlled by the hot jet turbulent flow generated by the PC. Subsequently, the flame propagation is considered self-sustained thanks to the in-MC turbulence enhancement, similarly to a conventional engine. In [46], the combustion development was computed by an additional entrainment effect, for which the fresh charge is entrained in the burning jet. In [47], an increment of the flame front area was also hypothesized, due to jet penetration. A transition from a drop-shaped flame to a hemisphere was assumed, as a function of a characteristic jet length.

Although, all these approaches include a reasonably detailed description of the phenomena occurring in a pre-chamber engine, the range of validation is often limited to few operating conditions, especially in terms of air/fuel quality. As a consequence, these approaches don't have enough reliability for performing simulations able to investigate the whole engine in different load, speed or mixture quality.

3.5.1. Model Development

Main focus of this PhD thesis is the development of a quasi-dimensional model for a pre-chamber SI engine able to physically sense different engine control variables and aiming to explore the entire engine operating domain. The model is based on an enhanced version of the fractal approach, developed at University of Naples Federico II and described in the previous section. Here, the procedure followed to model the basic phenomena occurring in an engine with PC, such as mixture preparation, turbulence evolution, flame area enhancement, burn rate development, etc., will be briefly described.

In *Figure 3-11*, the 0D schematization of the Pre-Chamber Spark Plug engine (PCSP) is reported: the main chamber (MC) of the engine is considered as a variable 0D volume, connected to the constant volume pre-chamber (PC) through an orifice. Mass and energy balance equations are solved in both volumes and a filling/emptying method is used to estimate the mass exchange between them, based on pressure difference, overall cross-sectional area and discharge coefficient of the orifice.

During the valve opening and the compression stroke, the two volumes are characterized by a time-varying homogenous composition, due to the mass exchange between the two chambers. During the compression stroke, a very rich air-fuel mixture establishing inside the PC after the direct fuel injection inside it, is progressively leaned by high-lambda air-fuel mixture coming from the MC.

During this phase, some air-fuel stratification may probably occur inside the PC, however, to preserve model simplicity, a homogeneous fully-mixed composition was considered in the present model version. As soon as the combustion starts, the burn rate is evaluated in the PC through a two-zone approach. Only fresh charge initially flows out from the PC, and as soon as the flame approaches the orifices, the burned gasses are pushed out, too. At this moment, the combustion, evaluated with a two-zone approach, starts in the MC, too. At the end of the combustion, a single zone approach is restored.

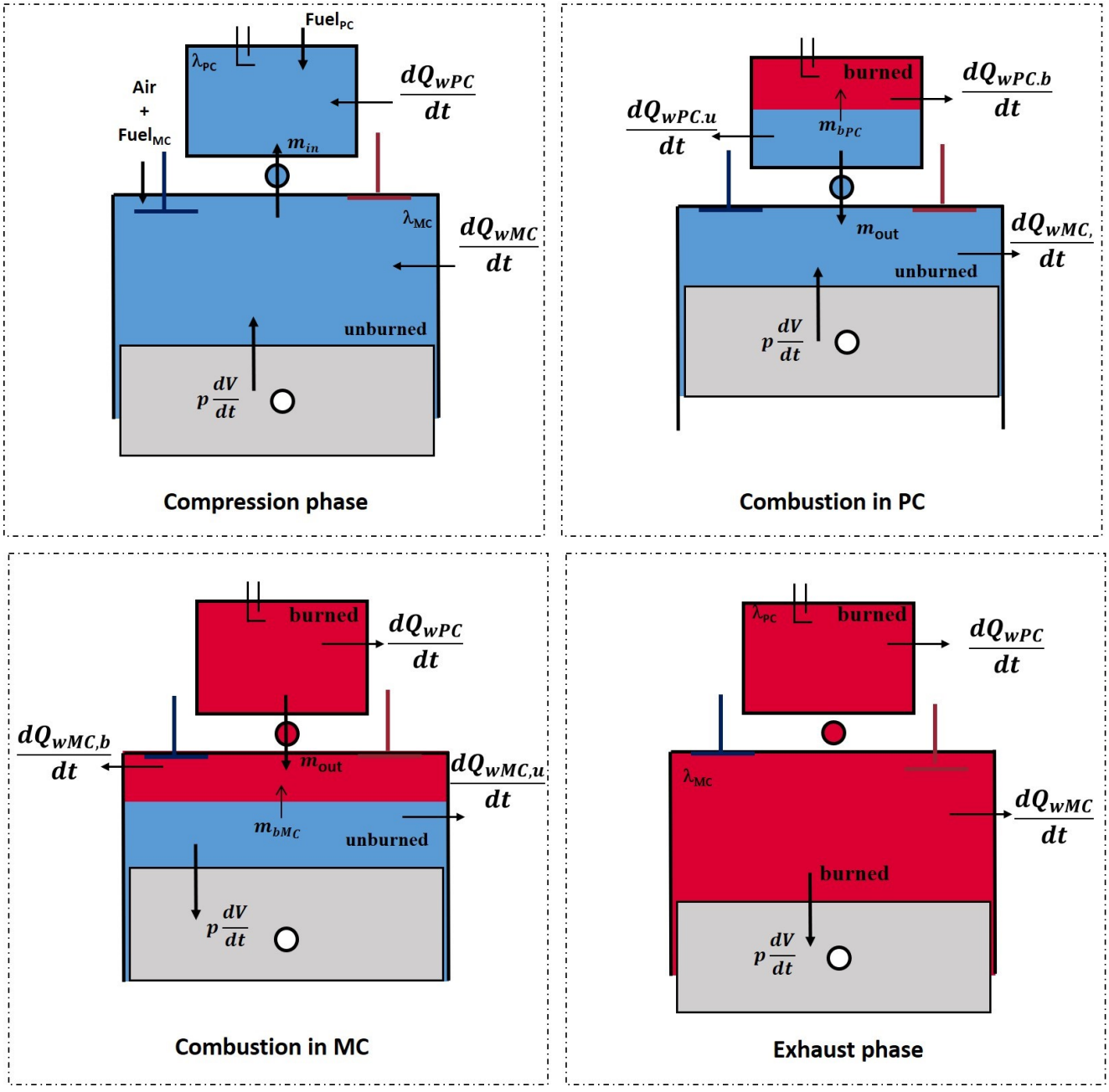

Figure 3-11 0D schematization of the pre-chamber spark plug engine model.

In *Figure 3-12a* is reported the mass evolution in both PC and MC, together with their unburned and burned shares, along with the combustion progress, using the described approach.

The total mass in the PC increases during the compression stroke, while it slightly decreases in the MC. The overall in-cylinder content is pictured by the thick black line, to verify its conservation during the closed valve period (no crevices and blow-by flows).

Concerning the outcoming pre-chamber flux, and consistently with a two-zone combustion description, unburned fresh mixture initially is expelled from the PC (blue line in *Figure 3-12b*) together with some limited residual gases (red dashed line). As soon as the flame approaches the orifices, fully burned gases (if any) are pushed out into the MC.

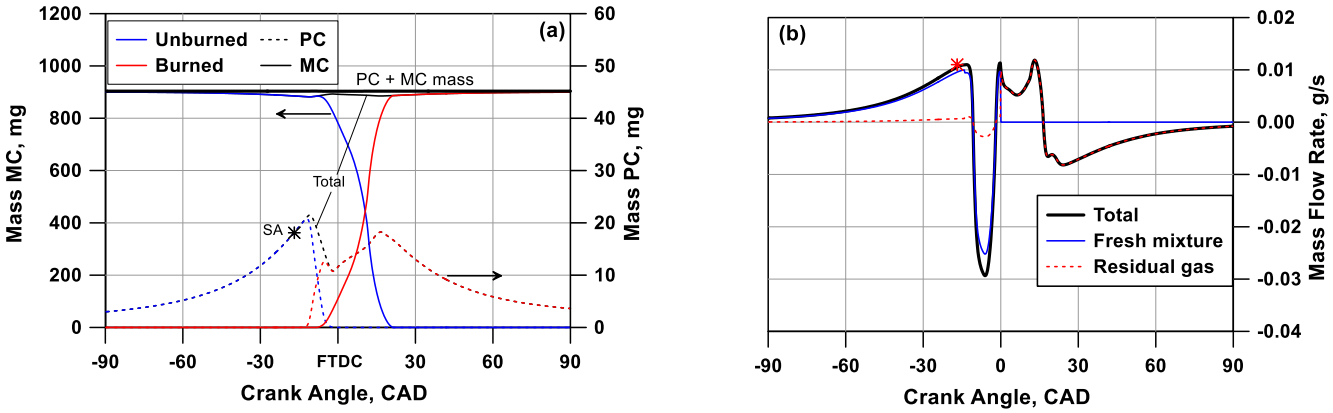

Figure 3-12 (a) Mass evolution of the unburned and burned gases in the PC and MC, (b) instantaneous mass flow rate through the PC orifices [48].

The estimation of the burning rate in both PC and MC is certainly the most difficult challenge due to the high complexity of the phenomena occurring in this novel architecture. Intense turbulence levels and organized flow motions are developed inside the PC due to the incoming flux during the compression stroke. Experimental and 3D results [41], [32] clearly show a flame propagation within it, expected to still occur in the corrugated flame regime. Under this hypothesis, the burn rate inside it can be still modeled using the fractal approach, and considering a smooth spherically shaped surface, centered on the sparkplug. Some minor corrections are only required to properly handle the turbulence formation and evolution inside the PC. Similar modifications has to be done to describe the turbulence production inside the MC, induced by the hot jet gases coming from the PC.

To better understand and physically model the burn rate in the MC, in *Figure 3-13*, different phases of the typical combustion development, deduced from preliminary 3D calculations, carried out at IFPEN, are reported. Additionally, in *Figure 3-14b*, typical crank-angle evolution of the burn rate in the MC and PC are shown, evaluated by a two-zone/two-volume inverse analysis of the experimental pressure cycles, *Figure 3-14a.*

Concerning the PC, the typical bell-shaped burn rate profile of a conventional SI engine is visible, further strengthening the assumption of a quasi-spherical propagation in a corrugated flame regime. On the contrary in MC a more complex evolution of the burn rate is noticeable.

Firstly, an initial knee of the burning rate can be observed, related to the turbulence enhancement generated by the jet issuing from the PC. In particular, during this phase it can be argued that the jets entrain directly the fresh charge (air and fuel) and the entrained mass very rapidly burns and releases heat in turn. The combustion is here mainly controlled by jets velocity and mixture entrainment. Once the turbulent jets have almost dissipated their initial kinetic energy, a quasi-spherical propagation starts from multiple ignition sites. Here, the enhancement of the combustion is mainly connected to the increment of the overall burned surface, but with a lower extent respect to the first phase. As soon as the different flame spheres interacts each other and with the cylinder walls, the flame propagation direction changes into a quasi-conical propagation. Finally, an abrupt flame area collapse occurs and the combustion rapidly ends.

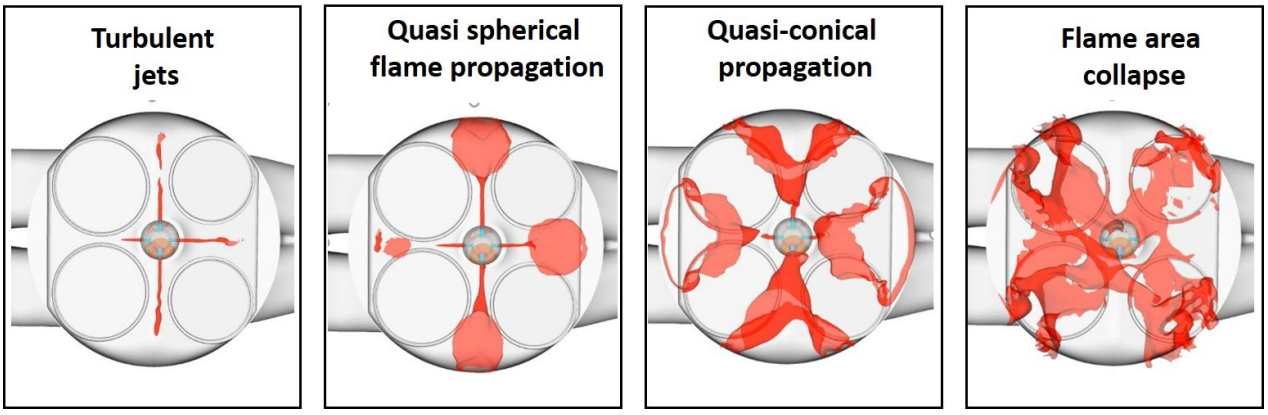

Figure 3-13 3D flame propagation within the MC for at 3000@13 bar IMEP, λ=1.8.

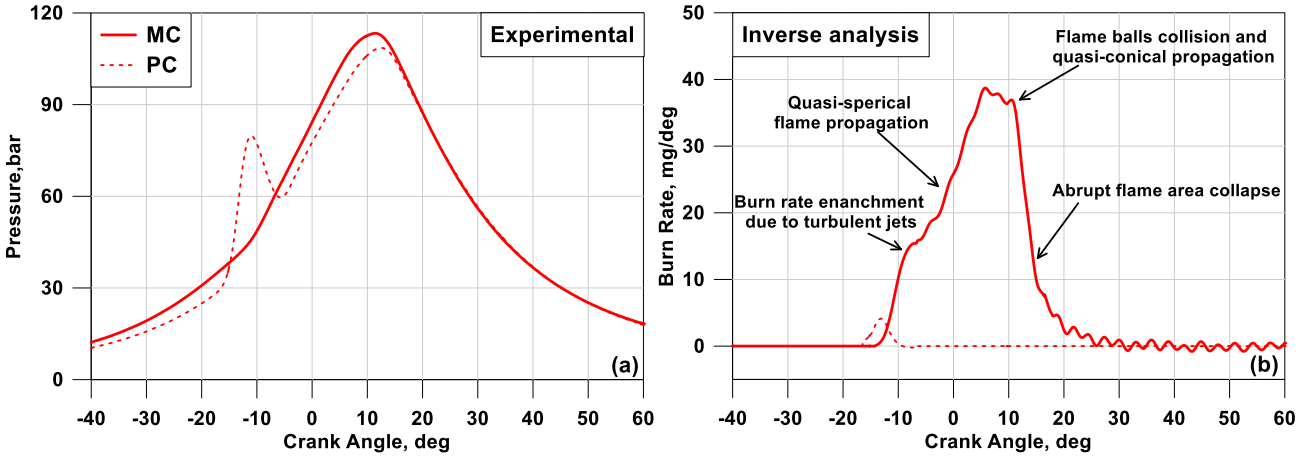

Figure 3-14 (a) Experimental pressure in PC and MC, (b) burn rate in the PC and MC, carried out through an inverse analysis.

On the light of the above considerations, the burn rate in the MC can be mainly described as the superimposition of two phenomena: the flame propagation from multiple ignition sites, initially enhanced by the turbulent jets.

Therefore, the overall burn rate can be expressed as the sum of "*classical flame propagation"* characterized by multiple corrugated flame fronts, and a "*turbulent jet combustion*", leading to the expression eq. (3.40).

$$\left(\frac{dm_b}{dt}\right)_{overall} = \left(\frac{dm_b}{dt}\right)_{fractal} + \left(\frac{dm_b}{dt}\right)_{jet} \tag{3.40}$$

The first term, applied in both PC and MC, describes the burning rate through the fractal approach, as a function of the laminar flame speed, S_L, and of the turbulent surface of the unique (PC) or multiple (MC) flame fronts A_T. The second term is only active in the MC. It considers the burning rate contribution due to the turbulent jets under the hypothesis that the jets entrain fresh charge (air and fuel) and the entrained mass rapidly burns and releases heat. This release rate is assumed to be proportional to the difference between the current entrained mass (m_{entr}) and its burned portion ($m_{b,entr}$), eq.(3.41). This expression mimics the well-known eddy burn-up approach [49], for which τ is a characteristic time scale. This last is calculated as the ratio between the Taylor length scale, Λ_T, and the laminar flame speed, S_L. The current total entrained mass, m_{entr}, is computed by the integration of its time derivative, eq. (3.42), which, in turn, is estimated by the semiempirical correlation proposed in [45]. The aforesaid term depends on the mass flow rate coming out of the PC, $\dot{m}_{jet}$, on a tuning constant, c_{jet} and on the density ratio between PC and MC. Similarly, the burned entrained mass, $m_{b,entr}$, is computed by the integration of eq.(3.41).

$$\left(\frac{dm_b}{dt}\right)_{jet} = \frac{dm_{b,entr}}{dt} = \frac{m_{entr} - m_{b,entr}}{\tau};\ \tau = \frac{\Lambda_T}{S_L} \tag{3.41}$$

$$\frac{dm_{entr}}{dt} = c_{jet}\dot{m}_{jet}\sqrt{\frac{\rho_{PC}}{\rho_{MC}}} \tag{3.42}$$

The combustion start in the PC is univocally defined by the spark timing, given as a simulation input. On the contrary, the combustion onset in the MC is predicted according to the current flame radius in the PC. As soon as it exceeds a critical value, named r_{crit}, the MC combustion is activated.

This parameter, directly correlated to the PC height, can be considered as an additional tuning constant, adjusting the combustion start in the MC. No direct estimation of the flame quenching through the PC holes is included in the model formulation. This phenomenology is roughly considered by a proper selection of the tuning constants.

The laminar flame area A_L in eq. (3.40), is schematized following the representative flame fronts reported in *Figure 3-15*. It is evaluated at each simulation time step as a function of the burned gas volume and, in the MC case, also of the piston position. For the pre-chamber, as already mentioned, a smooth spherically shaped propagation is considered with a center moving at a speed proportional to the jet velocity. For the main-chamber, it is assumed that the flame mainly develops when the turbulent jets have almost dissipated their initial kinetic energy [50]. Presumed ignition sites are located along each turbulent jet, from which the flame propagates spherically. The position of sphere centers, differently from the PC, is assumed fixed during the combustion development, assigned as an additional input parameter. During the model development, it was verified that a moving center in the MC does not significantly improve the simulation accuracy, but on the other hand increases considerably the computational time.

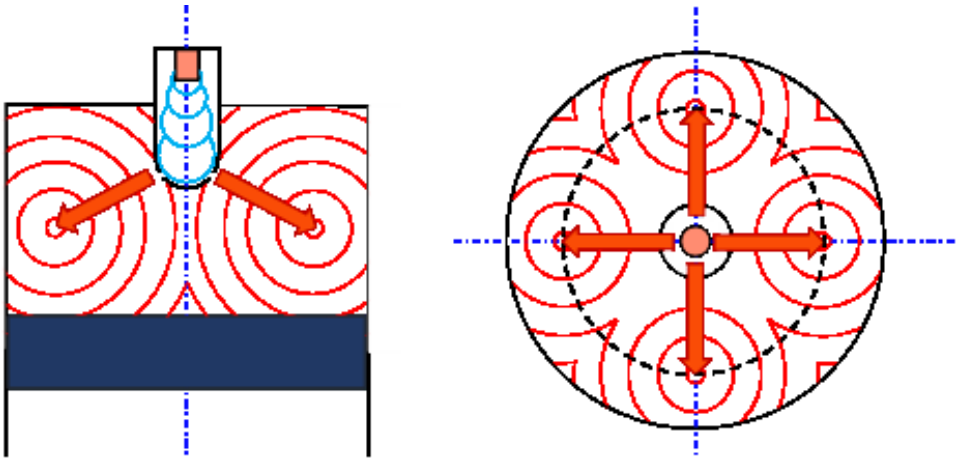

Figure 3-15 Flame front schematizations for PCSP engine [48].

3.5.1. Turbulence model

As already pointed out, for the combustion model closure, a turbulence sub-model is also required. In particular, the one previously described has been further extended to include the turbulence production induced by the incoming/outcoming flow through the orifices. Looking at the 3D outcomes (black lines) in *Figure 3-16,* in which the turbulent intensity and the integral length scale are reported for both PC and MC, additional turbulence peaks occur, respect to the profile of a conventional engine.

A first peak is visible in the pre-chamber at beginning of the intake phase, due to the injection in the pre-chamber.Differently from the MC, in which this contribution can be neglected, in the PC it has to be considered, although the *u'* soon collapses after the end of injection. At the end of the compression stroke, the turbulent intensity in the pre-chamber increases again, due to the incoming flux from the main chamber through the orifice. As soon as the combustion starts in the PC, *u'* decreases and a slightly increment in the main-chamber is visible due to the hot jets gases penetration in MC. Referring to the PC profile, another peak arises, which results from the reversed pressure differences between PC and MC. This is due to the pressure increase in the MC, caused by the progressing combustion.

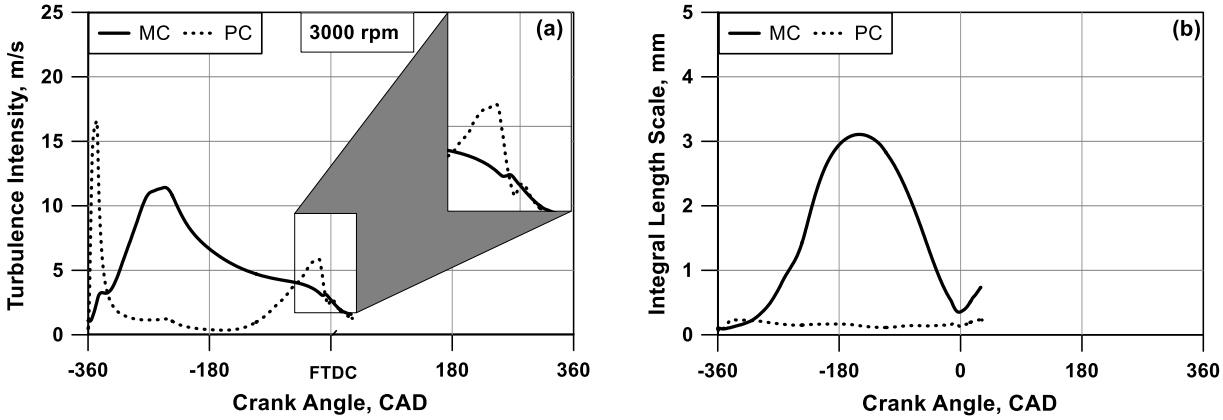

Figure 3-16 3D results of turbulence intensity(a) and integral length scale (b) in PC and MC under fired condition.

In order to model the described phenomena, the turbulence model assumes the following forms:

$$\begin{cases} \dfrac{dmk}{dt} = (mk)_{inc} - (mk)_{out} + \dfrac{2}{3}\dfrac{\dot{\rho}}{\rho}\left(-mv_t\dfrac{\dot{\rho}}{\rho} + mk\right) + p - m\varepsilon \quad (I) \\ \dfrac{dmK}{dt} = (mK)_{inc} - (mK)_{out} - f_d\dfrac{mK}{\tau_T} + mK\dfrac{\dot{\rho}}{\rho} - P + \dot{K}_{inj} + \dot{K}_p \ (II) \\ \dfrac{dmT}{dt} = (mT)_{inc} - (mT)_{out} - f_d\dfrac{mT}{\tau_T} \quad (III) \end{cases} \tag{3.43}$$

The *K* production due to the fuel injection (active pre-chamber) is introduced with the term $\dot{K}_{inj}$, included in the *K* equation, following the eq. (3.44).

$$\dot{K}_{inj} = \frac{1}{2}\dot{m}_{inj}\left(c_{inj}v_{inj}\right)^2 \tag{3.44}$$

The mass exchange between main- and pre-chamber, $\dot{K}_p$ (only taken into account in the mass-receiving volume) is estimated as:

$$\dot{K}_p = \frac{1}{2}\dot{m}_p\left(c_p v_p\right)^2 \tag{3.45}$$

where v_p is an equivalent velocity, c_p is a tuning constant, and $\dot{m}_p$ is the mass flow rate passing through the PC holes.

v_p is calculated by the following equation:

$$v_p = \frac{\dot{m}_p}{A_p \rho_p} \tag{3.46}$$

where A_p is the overall geometrical flow area of the pre-chamber holes ($Ap = n_{holes}\, \pi\, D_{hole}^2/4$) and ρ_p is the density in the volume from which the flow comes out (either MC or PC during the engine cycle). As previously pointed out, the integral length scale, L_t, has to be estimated based on the 3D calculation, as shown in *Figure 3-16*. Concerning the MC, L_t, can be specified by a sequence of S-shaped curves, while, for the PC, the assumption of a constant value seems reasonable. The tuning of the turbulence can follow the same main step reported in the chapter of the conventional engine.

As far as the combustion model tuning is concerned, it must be stressed that it now presents 8 constants: the set (c_{wrk}, c_{trans}, and x_{wc}) must be in fact specified for both PC and MC volumes, and two additional constants were introduced, namely r_{crit} and c_{jet}. As often happens in the first engine development phase, experimental data on CSP version of the same PCSP engine are available, too. In this case, a sequential methodology can be followed for the model tuning:

1. Tuning of the CSP engine (no pre-chamber), following the procedure described in in the previous chapter. Thereby a first set of the 3 tuning parameters (c_{wrk}, c_{trans}, and x_{wc}) is identified.
2. Tuning of the pre-chamber engine. In this stage, the constants c_{wrk} and x_{wc} are borrowed from step 1 and applied to handle the MC combustion. c_{trans} for the MC is indeed imposed equal to 0, under the hypothesis that the combustion begins in a fully turbulent stage. The constants (c_{wrk}, c_{trans}, and x_{wc}) needed to handle the burn rate prediction inside the PC are identified according to the procedure used for conventional SI engine. In this case, of course, the knowledge of the experimental pressure trace or the burn rate in the PC is required. The values of r_{crit} and c_{jet} are finally selected with the aim of reproducing the combustion onset and burning speed in the MC at the beginning of the process.

3.6. Knock and Heat Transfer modelling

During the calibration phase in the test bed, in order to avoid the occurrence of abnormal combustions, the Knock Limited Spark Advance (KLSA) has to be identified. If a numerical calibration has to be carried out, a knock model must be also coupled to the combustion model.

The more suitable way to describe the complex Auto-Ignition (AI) processes is to handle the solution of detailed chemical kinetic schemes, implying hundreds of species and thousands of reactions [51]. The major drawback of this approach it is the expensive CPU time. On the contrary, simpler modelling based on empirical formulations of auto-ignition delay [52] can be used. The main weakness of such formulation is the limited possibility to utilize the correlation out from air/inert/fuel proportions considered for the correlation development. An additional drawback is the poor predictivity of the chemical effects induced by advanced knock suppression strategies, such as EGR or water injection. In [53] a tabulated approach, relying on the off-line solution of chemical reactions in a Constant-Pressure (CP) or Constant Volume (CV) reactor, for the estimation of the AI demonstrates to be a good compromise between accuracy and complexity. For this reason, this last approach has been considered for this PhD Thesis. In particular, the table collects the AI time, τ_{AI}, as a function of pressure, temperature, equivalence ratio, and residual content. In the engine model, the knock event actually occurs when the AI integral, expressed by eq. (3.47) exceeds unity.

$$\int \frac{dt}{\tau_{AI}} \tag{3.47}$$

Actually, in order to introduce a small safety margin, tunable less than unit threshold level is specified. As already mentioned, the AI table is obtained by the off-line solution of a kinetic scheme performed at various pressure, temperature and air/fuel ratio of the unburned reactants in a constant pressure rector. For this PhD thesis two kinetic schemes were used since different fuels where considered. For the conventional engine, the kinetic scheme adopted is the one developed by Andrae at al.[54] and includes 5 elements,138 species and 633 reactions. Whereas, for the pre-chamber the AI table was given by the IFPEN Partner of the EAGLE project. The table developed in [55] is employed, including 5 elements, 201 species and 1548 reactions. The scheme is modified with the addition of a skeletal sub-mechanism for toluene oxidation to handle a TRF.

The heat transfer in the pre- and main-chamber is described by a Hohenberg-like correlation [4]. As known, this correlation estimates the gas-cylinder wall heat transfer as a function of the instantaneous in-cylinder volume, pressure, and temperature.

A dependence on the engine speed is also considered by the mean piston speed. In the case of the PC, the heat transfer extent is assumed to be controlled only by the in-PC pressure and temperature, while the dependence on the engine rotational speed is neglected. No particular treatment is applied to estimate the heat losses in the PC holes.

References

[1] De Nola, F., Giardiello, G., Gimelli, A., Molteni, A. Muccillo, M., "Definition of a Methodology Promoting the Use of 1D Thermo-Fluid Dynamic Analysis for the Reduction of the Experimental Effort in Engine Base Calibration," SAE Technical Paper, 2019-24-0013, 2019, doi:10.4271/2019-24-0013.

[2] Boretti, A. Scalzo, J., "Exploring the Advantages of Variable Compression Ratio in Internal Combustion Engines by Using Engine Performance Simulations," SAE Technical Paper 2011-01-0364, 2011, doi:10.4271/2011-01-0364.

[3] Woschni, G. "A universally applicable equation for the instantaneous heat transfer coefficient in the internal combustion engine," SAE Technical paper, 670931, 1967, doi:10.4271/670931.

[4] Hohenberg, G., "Advanced Approaches for Heat Transfer Calculations," SAE Technical Paper 790825, 1979, doi:10.4271/790825.

[5] Thermodynamics and Fluid Mechanics Group, Annand, W., "Heat transfer in the cylinders of reciprocating internal combustion engines," Proceedings of the Institution of Mechanical Engineers, 177(1), 973-996,1963, doi:10.1243/PIME_PROC_1963_177_069_02.

[6] Demesoukas, S., Caillol, C., Higelin, P., Boiarciuc, "Zero-Dimensional Spark Ignition Combustion Modeling-A Comparison of Different Approaches", SAE Technical Paper, 2013-24-0022, 2013, doi:10.4271/2013-24-0022.

[7] Richard, S., Bougrine, S., Font, G., Lafossas, F.A., Le Berr, F., "On the Reduction of a 3D CFD Combustion Model to Build a Physical 0D Model for Simulating Heat Release, Knock and Pollutants in SI Engines", *Oil & Gas Science and Technology* 64(3):223-242, 2009, doi:10.2516/ogst/2008055.

[8] Matthews, R., D., Chin, Y., W., "A Fractal-Based SI Engine Model: Comparisons of Predictions with Experimental Data", *SAE transactions* 910075, 1991, doi:10.4271/910079.

[9] Perlman, C., Frojd, K., Seidel, L., Tuner, M. et al., "A Fast Tool for Predictive IC Engine In-Cylinder Modelling with Detailed Chemistry," SAE Technical Paper 2012-01-1074, 2012, doi:10.4271/2012-01-1074.

[10] Rakopoulos, C., Michos, C., Giakoumis, E., "Thermodynamic analysis of SI engine operation on variable composition biogas-hydrogen blends using a quasi-dimensional, multi-zone combustion model," *SAE International Journal Engines* 2(1):880-910, 2009, doi:10.4271/2009-01-0931.

[11] Verhelst, S., Sheppard, C., G., W., "Multi-zone thermodynamic modelling of spark-ignition engine combustion–an overview,*" Energy Conversion and management* 50(5): 1326-1335, 2009, doi:10.1016/j.enconman.2009.01.002.

[12] Franke, C., Wirth, A., Peters, N., "New Aspects of the Fractal Behaviour of Turbulent Flames," 23 Symp. (Int.) on Combustion, Orleans, 1990.

[13] De Bellis, V., Severi, E., Fontanesi, S., Bozza, F., "Hierarchical 1D/3D approach for the development of a turbulent combustion model applied to a VVA turbocharged engine. Part II: Combustion model," Energy Procedia 45, 1027-1036, 2014, doi:10.1016/j.egypro.2014.01.108.

[14] De Bellis, V., Bozza, F. and Tufano, D., "A Comparison Between Two Phenomenological Combustion Models Applied to Different SI Engines," SAE Technical Paper, 2017-01-2184, 2017, doi:10.4271/2017-01-2184.

[15] Gouldin, F., "An application of Fractals to Modeling Premixed Turbulent Flames", *Combustion and Flame* 68(3):249-266, 1987, doi:10.1016/0010-2180(87)90003-4.

[16] Gatowsky, J., A., Heywood, J., B., "Flame Photographs in a Spark-Ignition Engine", *Combustion and Flame* 56:71-81, 1984.

[17] Bates, C., S., "Flame Imaging Studies of Combustion Completion in a SI Four-Stroke Engine", TvU Thoughtventions Unlimited LLC, http://www.tvu.com/.

[18] North, G., L., Santavicca, D., A., "The fractal nature of premixed turbulent flames," *Combustion Science and Technology* 72(4-6): 215-232, 1990, doi:10.1080/00102209008951648.

[19] Peters, N., "Laminar flamelet concepts in turbulent combustion," Symposium (International) on Combustion 21(1): 1231-1250, 1988, doi:10.1016/S0082-0784(88)80355-2.

[20] Rhodes, D. B., Keck, J. C. "Laminar burning speed measurements of indolene-air-diluent mixtures at high pressures and temperatures," SAE Technical Paper, 850047, 1985.

[21] Hara, T., Tanoue, K. "Laminar flame speed of ethanol, n-heptane, iso-octane air mixtures," *JSAE paper*, 20068518, 2006.

[22] Bougrine, S., Richard, S., Nicolle, A., Veynante, D. "Numerical study of laminar flame properties of diluted methane-hydrogen-air flames at high pressure and temperature using detailed chemistry," *International journal of hydrogen energy* 36(18), 12035-12047, 2011, doi:10.1016/j.ijhydene.2011.06.053.

[23] Hann, S., Grill, M., & Bargende, M. "Reaction Kinetics Calculations and Modeling of the Laminar Flame Speeds of Gasoline Fuels," SAE Technical Paper, 2018-01-0857, 2018, doi:10.4271/2018-01-0857.

[24] Gülder, Ö. L. "Correlations of laminar combustion data for alternative SI engine fuels," SAE Technical Paper, 841000, 1984, doi: 10.4271/841000.

[25] Teodosio, L., Bozza, F., Tufano, D., Giannattasio, P., Distaso, E. Amirante, R., "Impact of the laminar flame speed correlation on the results of a quasi-dimensional combustion model for Spark-Ignition engine,". *Energy Procedia*, 148, pp.631-638, 2018, doi: org/10.1016/j.egypro.2018.08.151.

[26] Metghalchi, M., and Keck, J., "Laminar burning velocity of propane-air mixtures at high temperature and pressure," *Combustion and flame*, 38, pp.143-154, 1980, doi:10.1016/0010-2180(80)90046-2.

[27] Amirante, R., Distaso, E., Tamburrano, P., Reitz, R. D., "Laminar flame speed correlations for methane, ethane, propane and their mixtures, and natural gas and gasoline for spark-ignition engine simulations," *International Journal of Engine Research*, 18(9), 951-970, 2017, doi:10.1177/1468087417720018.

[28] Liao, S. Y., Jiang, D. M., Cheng, Q, "Determination of laminar burning velocities for natural gas," *Fuel*, 83(9), 1247-1250, doi:10.1016/j.fuel.2003.12.001.

[29] Bozza, F., De Bellis, V., Giannattasio, P., Teodosio, L., Marchitto, L. "Extension and Validation of a 1D Model Applied to the Analysis of a Water Injected Turbocharged Spark Ignited Engine at High Loads and over a WLTP Driving Cycle*," SAE International Journal of Engines*, 10(2017-24-0014), 2141-2153, 2017, doi: www.jstor.org/stable/26422601.

[30] Liu, Y. D., Jia, M., Xie, M. Z., Pang, B. "Development of a new skeletal chemical kinetic model of toluene reference fuel with application to gasoline surrogate fuels for computational fluid dynamics engine simulation" *Energy & Fuels*, 27(8), 4899-4909, 2013, doi:10.1021/ef4009955.

[31] Bozza, F., De Bellis, V., Berni, F., D'Adamo, A. Maresca, L., "Refinement of a 0D turbulence model to predict tumble and turbulent intensity in SI engines. Part I: 3D analyses," SAE Technical Paper, 2018-01-0850, 2018 doi: org/10.4271/2018-01-0850.

[32] Mueller, C., Morcinkowski, B., Habermann, K., Uhlmann, T., Schernus, C. "Development of a pre-chamber for spark ignition engines in vehicle applications," 4th International Conference on Ignition Systems for Gasoline Engines, Dec. 2018.

[33] Pape, J., Getzlaff, J., Gruenig, C., Kuhnert, D. and Latsch, R., "Investigations on Pre-Chamber Spark Plug with Pilot Injection," SAE Technical Paper 2007-01-0479, 2007, doi:10.4271/2007-01-0479.

[34] Attard, W.P., Fraser, N., Parsons, P. and Toulson, E., "A Turbulent Jet Ignition Pre-Chamber Combustion System for High Fuel Economy Improvements in a Modern Vehicle Powertrain," SAE Technical Paper 2010-01-1457, 2010, doi:10.4271/2010-01-1457.

[35] Roethlisberger, R., Favrat, D., "Comparison between direct and indirect (prechamber) spark ignition in the case of a cogeneration natural gas engine, part I: engine geometrical parameters," Applied Thermal Engineering, 22(11), 1217-1229, 2002, doi: 10.1016/S1359-4311(02)00040-6.

[36] Xu, G., Wright, Y., Schiliro, M., Boulouchos, K., "Characterization of combustion in a gas engine ignited using a small un-scavenged pre-chamber," International Journal of Engine Research, 2018, doi: 10.1177/1468087418798918.

[37] Jamrozik, A., "Lean combustion by a pre-chamber charge stratification in a stationary spark ignited engine," *Journal of Mechanical Science and Technology*, 29(5):2269-2278, 2015, doi:10.1007/s12206-015-0145-7.

[38] Toulson, E., Schock, H., Attard, W., "A Review of Pre-Chamber Initiated Jet Ignition Combustion Systems," SAE Technical Paper 2010-01-2263, 2010, doi:10.4271/2010-01-2263.

[39] Shah, A., Tunestål, P., Johansson, B., "CFD Simulations of Pre-Chamber Jets' Mixing Characteristics in a Heavy Duty Natural Gas Engine," SAE Technical Paper 2015-01-1890, 2015, doi:10.4271/2015-01-1890.

[40] Serrano, D., Zaccardi, J.M., Müller, C., Libert, C. Habermann, K., "Ultra-Lean Pre-Chamber Gasoline Engine for Future Hybrid Powertrains," SAE Technical Paper, 2019-24-0104, 2019, doi:10.4271/2019-24-0104.

[41] Sens, M., Binder, E., Benz, A., Kramer, L., at all. "Pre-chamber ignition as a Key Technology for Highly Efficient SI Engines-New Approaches and Operating Strategies," 39th International Vienna Motor Symposium, Apr. 2018

[42] Bardis, K., Xu, G., Kyrtatos, P., Wright, Y. et al., "A Zero Dimensional Turbulence and Heat Transfer Phenomenological Model for Pre-Chamber Gas Engines," SAE Technical Paper 2018-01-1453, 2018, doi:10.4271/2018-01-1453.

[43] Cruz, I., Alvarez, C., Teixeira, A., Valle, R., "Zero-dimensional mathematical model of the torch ignited engine," *Applied Thermal Engineering*, 103, 1237-1250, 2016, doi:10.1016/j.applthermaleng.2016.05.017.

[44] Kouremenos, D.,A, Rakopoulos C.,D., Hountalas, D., D. "Thermodynamic Analysis of Indirect Injection Diesel Engines by Two-Zone Modeling of Combustion", *ASME. J. Eng. Gas Turbines Power,* 112(1):138-149, 1990. doi:10.1115/1.2906468.

[45] Hiraoka, K., Nomura, K., Yuuki, A., Oda, Y. et al., "Phenomenological 0-Dimensional Combustion Model for Spark-Ignition Natural Gas Engine Equipped with Pre-Chamber," SAE Technical Paper 2016-01-0556, 2016, doi:10.4271/2016-01-0556.

[46] Shojaeefard, M. H., Keshavarz, M. "Flame propagation model for a rotary Atkinson cycle SI engine," *International Journal of Automotive Technology,* 19(1), 9-25, 2018, doi:10.1007/s12239-018-0002-7.

[47] Auer, M., Wachtmeister, G. "Phenomenological models for pre-calculation of the combustion in gas engines," MTZ worldwide,70(6), 52-59, 2019, doi:10.1007/BF03226962.

[48] Bozza, F., De Bellis, V., Tufano, D., Malfi, E. et al., "A Quasi-Dimensional Model of Pre-Chamber Spark-Ignition Engines," SAE Technical Paper 2019-01-0470, 2019, doi:10.4271/2019-01-0470.

[49] Blizard, N., Keck, J., "Experimental and Theoretical Investigation of Turbulent Burning Model for Internal Combustion Engines," SAE Technical Paper 740191, 1974, doi:10.4271/740191.

[50] Mastorakos, E., Allison, P., Giusti, A., De Oliveira, P., Benekos, S., Wright, Y., Boulouchos, K., "Fundamental Aspects of Jet Ignition for Natural Gas Engines," *SAE International Journal of Engines*, doi:10.4271/2017-24-0097.

[51] Lu, T., Law C., "Toward accommodating realistic fuel chemistry in large scale computations," *Progress in Energy and Combustion Science* 35(2):195-215, 2009, doi:10.1016/j.pecs.2008.10.002.

[52] Livengood, J., C., Wu, P., C., "Correlation of Autoignition Phenomena in Internal Combustion Engines and Rapid Compression Machines," *Symposium (International) on Combustion* 5(1):347-356, 1955, doi:10.1016/S0082-0784(55)80047-1.

[53] Bozza, F., De Bellis, V. Teodosio, L., "A Tabulated-Chemistry Approach Applied to a Quasi-Dimensional Combustion Model for a Fast and Accurate Knock Prediction in Spark-Ignition Engines" SAE Technical Paper, 2019-01-0471, 2019, doi: 10.4271/2019-01-0471.

[54] Andrae, J., "Comprehensive chemical kinetic modeling of toluene reference fuels oxidation", Fuel 2013; 107:740-748, doi:10.1016/j.fuel.2013.01.070.

[55] Bounaceur, R., Herbinet, O., Fournet, R., Glaude, P. et al., "Modeling the Laminar Flame Speed of Natural Gas and Gasoline Surrogates," SAE Technical Paper 2010-01-0546, 2010, doi: 10.4271/2010-01-0546.

4. Methodologies for Vehicle Simulation

In the recent years, the numerical analysis has become essential also in the field of vehicle behaviour description. Indeed, the introduction of additional components in the car, such as the electric units, combined to necessity of developing proper energy management strategies, has exponentially increased the complexity of the development process. To support the design phase numerical analyses can be used to determine the optimal sizing of all the different components of the vehicle or such as in hybrid vehicles, these approaches can be adopted for the development of the Energy Management Strategy (EMS). This last can be eventually embedded in the control unit of the vehicle if the computational time is reasonably low, otherwise these EMS are generally used for the definition of the benchmark. In this PhD Thesis, instead, vehicle simulations were performed to assess the CO_2 emission along the WLTC in order to quantify the potentiality of the investigated engines.

To this aim, three different architectures were tested: a conventional vehicle, a HEV and PHEV. The vehicle powertrains were modelled according to the state of art [1],[2],[3] while three Energy Management Strategy (EMS) for hybrid architectures were considered. The first one, it is based on the well-assessed off-line Pontryagin's Minimum Principle (PMP) [4]. The second one, it is related to the Dynamic Programming (DP) approach [5]. The latter, it is a novel approach developed in the framework of this research activity, labelled as Efficient Thermal Electric Skipping Strategy (ETESS), suitable for the control of a parallel/series hybrid vehicles. In particular ETESS and PMP were adopted in the filed of HEV equipped with the pre-chamber engine, whereas the DP was employed among the activity carried out at the Ohio State University.

In this chapter, the vehicle architectures will be firstly discussed. Then, the methodology used for modelling the vehicle components will be briefly reported. Finally, the three EMS will be described in detail.

4.1. Vehicle classification

A typical classification of the modern vehicles, reported in *Figure 4-1*, is based on the sizes of thermal engine and electric machine, resulting in six different architectures:

1. *Conventional ICE vehicles:* The only source of power is the ICE, this means that all the torque propelling the vehicle is produced by the ICE.

2. *Micro hybrids (start/stop):* The system allows the ICE shut down and restart to reduce the fuel consumption at idle condition. This solution is very advantageous for urban vehicles, due to the large amount of time usually spent waiting the green traffic light. This application can be available for a conventional vehicle (micro-hybrid), while it is always present in a hybrid vehicle.
3. *Mild hybrids (start/stop + kinetic energy recovery + engine assist*): in this configuration the ICE is coupled to an electric machine, allowing to turn off the thermal unit whenever the car is coasting, braking or stopping. This vehicle can also have regenerative braking and some level of power assist, but the electric unit is not able to move alone the vehicle.
4. *Full hybrids (mild hybrid capabilities + electric launch):* The vehicle can be moved alternatively by the thermal engine, the electric machine or combination of both. To this aim, a high-capacity battery pack is required for ensuring the electric launch. Differently from the mild hybrid, a vehicle energy management strategy is mandatory to fully exploit the benefit of the hybridization.
5. *Plug-in hybrids (full hybrid capabilities + electric range):* The battery can be recharged through the connection to an external electric power source, such as the grid. As a consequence, the electric autonomy is higher than a full hybrid vehicle.
6. *Electric Vehicles (battery or fuel cell):* in this configuration, the vehicle propulsion is realized by only the electric units, which are powered by a battery or a hydrogen fuel cell.

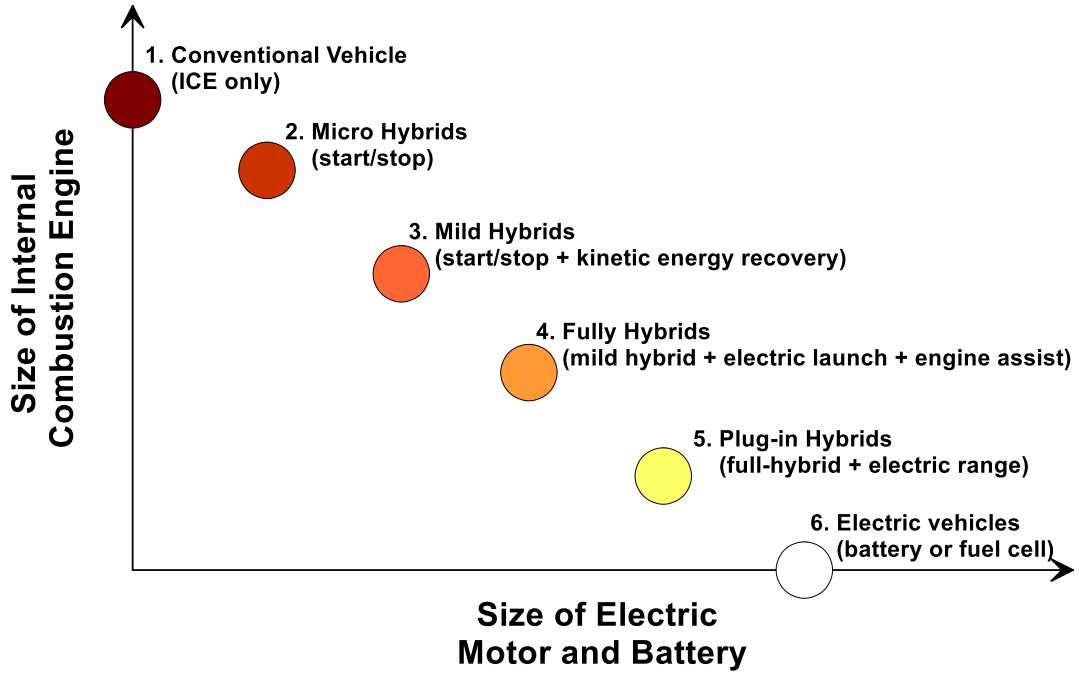

Figure 4-1 Vehicle classification as a function of the ICE and electric motor/battery size [6].

A further classification can be done for the HEV architecture, depicted in *Figure 4-2.*

1. *Series:* The electric motor alone drives the vehicle. The electricity required by the electric unit can be supplied by either a battery or an engine-driven generator.
2. *Parallel:* The required power for driving the vehicle is the sum of two sources: the engine and the electric machines. The driving units are connected by a gear set, a chain or a belt, summing their torque to be transmitted to the wheels.
3. *Power split:* In this configuration, one ICE and two electric units are connected to a power split (generally a planetary gear set). Hence, the power from the engine and the electric machines can be merged through both mechanical and electrical paths, combining series and parallel modalities.
4. *Series/parallel:* The vehicle presents clutches which allow to modify the powertrain configuration from series to series/parallel or only parallel. The flexibility of this architecture allows the selection of the most suitable configuration for the current operating condition.

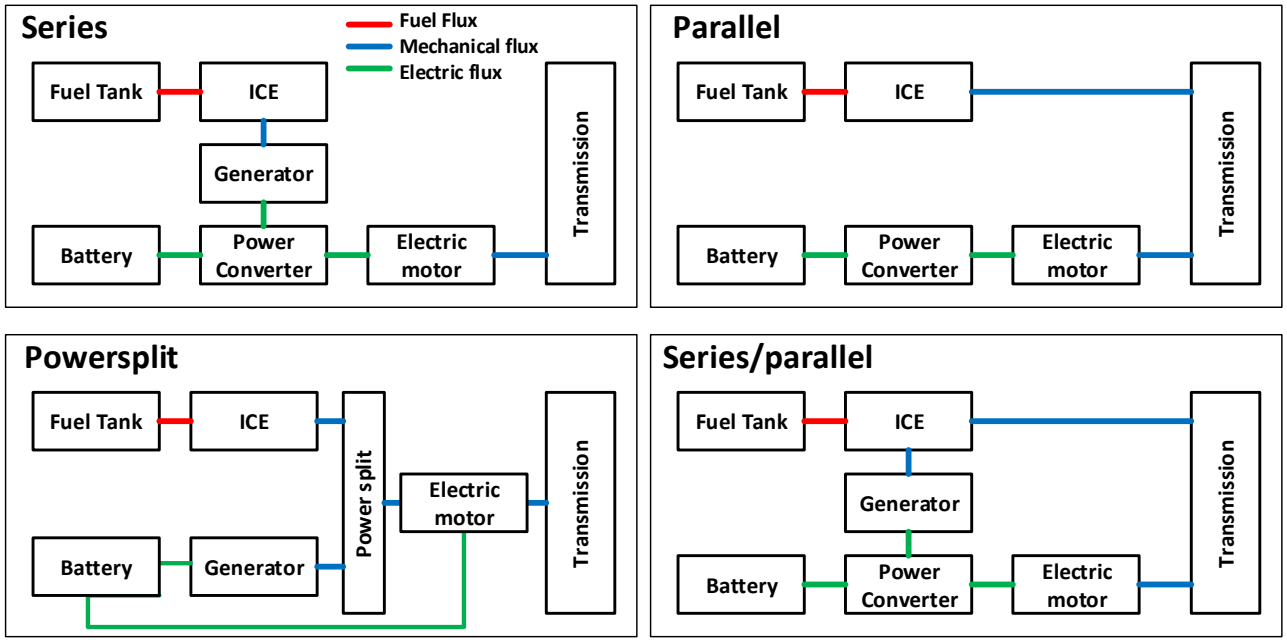

Figure 4-2 Classification of the HEV architectures

Whatever configuration is considered, the aim of a vehicle simulation is to reproduce the energy flows within the powertrain and the vehicle, obtaining an accurate estimation of all the relevant vehicle parameters, such as fuel consumption, pollutant emissions or battery state of charge. A vehicle-level energy analysis is the approach widely used for the estimation of the above parameters, and it is the one considered for this PhD Thesis.

In particular, the vehicle is considered as a point mass and its interaction with the external environment is studied. This approach allows to properly analyse the vehicle longitudinal dynamic and the energy flows inside the powertrain.

4.2. Equations of motion

Under the simplification that the vehicle is considered as a point mass, the forces acting on the vehicle along the longitudinal axis are the ones shown in the *Figure 4-3*.

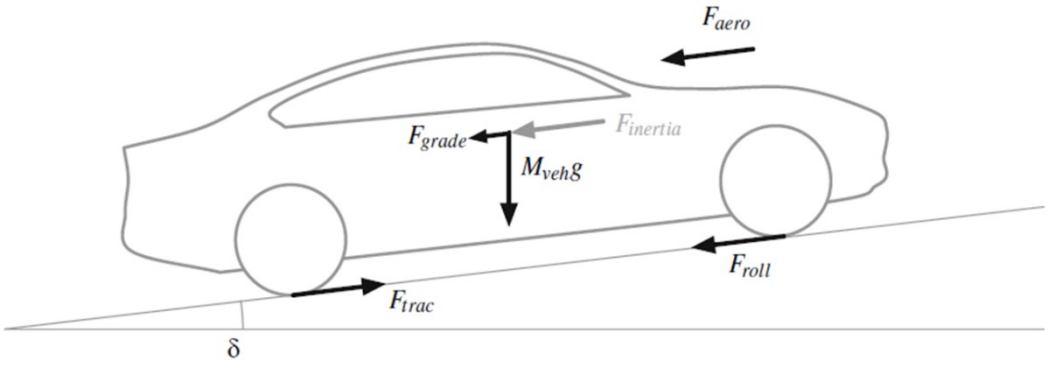

Figure 4-3 Forcing acting on a vehicle [6].

The vehicle dynamic equation can be written from the equilibrium of forces, as follows:

$$M_{veh}\frac{dv_{veh}}{dt} = F_{inertia} = F_{trac} - F_{roll} - F_{aero} - F_{grade} \tag{4.1}$$

In eq. (4.1), M_{veh} and v_{veh} are the effective vehicle mass and longitudinal vehicle velocity. $F_{inertia}$ represents the inertial force, positive when the vehicle is accelerating and negative when it is decelerating. The first terms of eq. (4.1) of the right hand, F_{trac}, is the tractive force generated by the powertrain F_{pwt} (or by the brakes at the wheels F_{brake} during the braking phases). F_{roll} is the rolling resistance factor and it takes into account the friction due to the tire deformation and losses. It is usually modeled as reported in eq. (4.2) as a function of a rolling resistance coefficient, c_{roll}, the gravity acceleration, g, the vehicle mass and the road slope δ:

$$F_{roll} = c_{roll}(v_{veh}, p_{tire}, \dots.)M_{veh}gcos\delta \tag{4.2}$$

In eq. (4.2), the product ($M_{veh}\ gcos\delta$) represents the vertical component of the vehicle weight. Whereas c_{roll} can be assumed constant or as a function of vehicle speed, tire pressure p_{tire}, and temperature, etc….

The order of magnitude of c_{roll} is 0.01-0.03, which means that the rolling resistance can be considered as 1-3% of the vehicle weight. This force is always positive and dissipative since it opposes the motion of the vehicle.

F_{aero} is the aerodynamic resistance, function of the density of the air ρ, A_f the vehicle frontal area, C_d the aerodynamic drag coefficient. This force, as well as F_{roll}, is always positive and dissipative.

$$F_{areo} = \frac{1}{2}\rho C_d A_f V_{veh}^2 \tag{4.3}$$

F_{grade} considers the force due to road slop. It is positive when the vehicle is driven uphill and negative when it is going downhill:

$$F_{grade} = M_{veh} g sin\delta \tag{4.4}$$

These basic equations represent the starting point for vehicle modelling and can be sufficiently accurate if the parameters are correctly identified. Typical values of the described parameters are reported in *Table 4.1.*

Table 4.1 Typical values of vehicle-dependent parameters for longitudinal vehicle dynamics models [6].

Parameter	**Compact Car**	**Full-size**	**SUV**
M_{veh}	*1200-1500 kg*	*1700-2000 kg*	*1900–2200 kg*
C_d	*0.3-0.35*	*0.28-0.33*	*0.32-0.38*
A_f	*1.3–1.7 m²*	*1.8–2.2 m²*	*2–2.5 m²*
C_{roll}	*0.01–0.03*	*0.01–0.03*	*0.01–0.03*

The eq. (4.1) can be rewritten with the aim to explicit the tractive force required to the powertrain:

$$F_{trac} = F_{pwt} - F_{brake} = F_{inertia} + F_{grade} + F_{roll} + F_{aero} \tag{4.5}$$

The different forms of the equilibrium of forces in eq. (4.1) and (4.5) basically correspond to the forward and backward modelling approaches. In the former mode, the vehicle acceleration (dv_{veh}/dt) is computed as a balance between the tractive force generated by the powertrain and the passive resistance acting on it. Hence the vehicle speed is obtained by the integration of the acceleration.

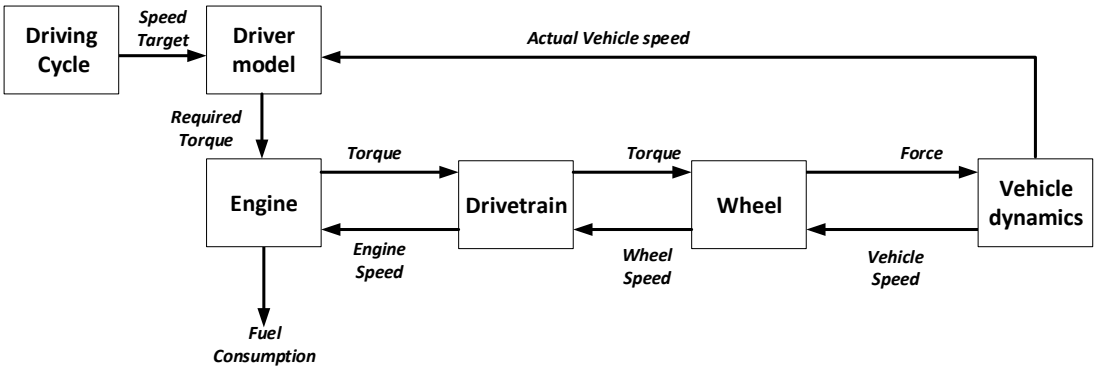

Figure 4-4. Information flow of a forward approach [1].

This approach reproduces the physical causality of the system; therefore, it is the option typically chosen in most simulation. It is characterized by the information flow as shown in *Figure 4-4*, for which the required speed profile is the input and it is compared with the actual vehicle speed, returning the required torque at the engine. To this aim a driver model, usually schematized by a PID controller, is employed able to generate the braking or throttle command in order to follow the prescribed vehicle velocity. The driver command is sent to the supervisory block that is responsible for issuing the actuators setpoints (engine, electric machines, and braking torques) to the rest of the powertrain components, which ultimately produce a tractive force. Finally, the force is applied to the vehicle dynamics model, where the acceleration is determined with eq. (4.1) taking into account the road load information.

In the backward approach, the velocity is imposed and the tractive force is calculated starting from the inertia force. It is assumed that the vehicle will always follows the prescribed vehicle velocity and acceleration. F_{trac} represents the force that the powertrain must supply. As a consequence, no driver model is necessary since the desired speed is a direct input of the simulator, whereas the engine torque and the fuel consumption are outputs. In *Figure 4-5*, the information flow for a backward approach is depicted. The simulator directly determines the net tractive force to be applied as a function of the velocity, considering all the vehicle characteristic. Starting from this information, the torque required to move or rest the vehicle is calculated, with the related fuel consumption.

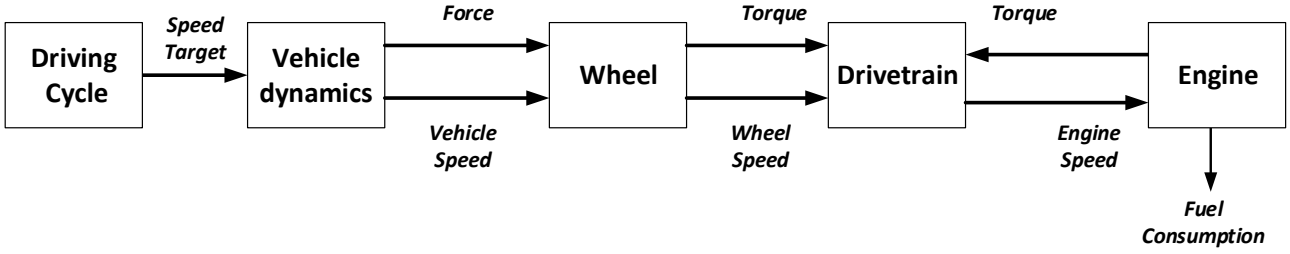

Figure 4-5 Information flow of a backward approach [1].

When the simulation of the fuel consumption of a vehicle along a prescribed driving cycle is required, a backward simulator guarantees that the vehicle will follow exactly the profile, ensuring consistency of the simulation results. On the contrary, for a forward simulator, a proper tuning of the driver block has to be performed in order to reduce the error between the actual and the desired velocity. However, a backward approach assumes that the vehicle powertrain will be always able to follow the speed trace, without consider the constraints of the powertrain components. Whereas, a forward simulation does not have this issue, since the speed is computed from the torque/force provided by the powertrain. For this reason, forward simulations are commonly used for acceleration tests, or analysis of the system behavior. Additionally, when it is required the assessment of an online control strategies, the forward method is the most appropriate.

In addition to the force balance equilibrium, power and energy balances can be computed in a vehicle simulation. Multiplying all terms of eq. (4.5) by the vehicle speed (v_{veh}), the balance of power is obtained:

$$P_{trac} = P_{inertia} + P_{grade} + P_{roll} + P_{aero} \tag{4.6}$$

When eq.(4.6) is greater than zero, the powertrain generates power to propel the vehicle, while when it is negative the brakes are activated. For conventional vehicles, this negative power is lost, mainly through friction losses, and pumping losses of the engine. For a hybrid vehicle, the electric machine, working in a reverse way, can absorb this negative contribute.

Through the integration of eq.(4.6) over the duration of a prescribed trip, the energy balance can be obtained, too:

$$E_{trac} = \int_{t_o}^{t_f} P_{trac}(t)dt = E_{kin} + E_{pot} + E_{roll} + E_{aero} \tag{4.7}$$

Where the integral of the inertial power is the variation of the kinetic energy (E_{kin}), and the integral of the grade power is the variation of the potential energy (E_{pot}).

Solving the equations described , namely (4.1)- (4.6)- (4.7), it is possible to univocally identify the energy requirement of the vehicle necessary for pursuit a prescribed profile speed. In particular, for a conventional vehicle, the E_{trac}^{+} is entirely supplied by the ICE and E_{trac}^{-} is convert in the friction losses at the brakes or at the ICE. On the contrary, for a hybrid architecture, E_{trac}^{+} can be provided by both ICE and/or electric machines as a function of the architecture and the energy strategy chosen. Whereas, E_{trac}^{-} is recovered by the electric units, within the allowed limit. The ICE and electric powers are then calculated starting from the tractive power, taking into account all the losses from the thermal and electric units, through the driveline, up to the wheels.

To this aim, a proper description of all the powertrain components has to be considered. In the following section, the models used for describing the internal combustion engine, the electric unit and the battery will be briefly recalled.

4.3. Internal Combustion Engine, Electric unit and battery modelling

For the vehicle simulation, two different approaches are widely used for modelling the ICE: a static map or a static map combined with lumped-parameter dynamic mode. The former considers the engine like a perfect actuator, which responds immediately to the commands. All the variable in the maps, such as the fuel consumption, are computed from the map (table) as a function of the engine speed and torque, both of which are assumed to be known. The static map approach can be modified including dynamic limitation in the torque output, leading to a lumped-parameter dynamic model. In this approach, a delay between the commanded torque and the actual torque generated is considered. To this aim, a transfer function has to be coupled to the map, representing the air/fuel dynamics during transients and, possibly, the crankshaft inertia. Concerning the electric machine, a map-based approach is widely used to model the motor efficiency. Also in this case, the map can be expressed as a function of the speed and torque or speed and electric power. This last is generally computed on the base of the following expression:

$$P_{mec} = \omega_{EM} * T_{EM} = \begin{cases} \eta_{EM}(\omega_{EM}, P_{El}) * P_{el} & if\ P_{el} \geq 0\ (\ motoring\ mode) \\ \dfrac{1}{\eta_{EM}(\omega_{EM}, P_{El})} * P_{el} & if\ P_{el} < 0\ (\ generating\ mode) \end{cases} \tag{4.8}$$

Where η_{EM} is the efficiency of the electric unit.In the current literature, several models have been proposed for the battery system [7] characterized by a different degree of accuracy. A reliable prediction of the battery dynamic in a hybrid electric vehicle is a challenge due to the mutual correlation between all the main variables that characterize the battery behaviour such as State of Charge (SOC), voltage and temperature. Since in a vehicle simulator the main objective is mainly the prediction of the SOC, a simple dynamic model is considered reliable enough. In particular, the SOC is defined as the amount of electrical charge stored in the battery ($Q(t)$) normalized by the total capacity (Q_{nom}).

$$SOC(t) = \frac{Q(t)}{Q_{nom}} = \begin{cases} -\dfrac{1}{\eta_{coul}} \dfrac{I(t)}{Q_{nom}} & if\ I(t) > 0 \\ -\eta_{coul} \dfrac{I(t)}{Q_{nom}} & if\ I(t) < 0 \end{cases} \tag{4.9}$$

In eq.(4.9), $I(t)$ is the battery current, positive/negative during discharge/charge, η_{coul} is the Coulombic efficiency, function of the current intensity and temperature. Even if the battery capacity and the Coulombic efficiency depend on several parameters, the calculation of the SOC from eq.(4.9) is usually done assuming those quantities as constants. The battery current and voltage are then related to the power exchanged with the rest of the powertrain using a simplified circuit model, leading to the following expression:

$$IV_{oc} - I^2 R_{int} - \eta_{coul} P_{batt} = 0 \tag{4.10}$$

Solving the eq.(4.10), an explicit expression of the current can be defined, in which V_{oc} is open circuit voltage and R_{int} is internal resistance of the battery. To determine these two values, proper maps can be adopted as a function of temperature and SOC.

$$I = \frac{-V_{oc} + \sqrt{V_{oc}^2 - 4R_{int}P_{batt}\eta_{coul}}}{2R_{int}} \tag{4.11}$$

During battery charging, eq (4.11) yields always real roots, since the P_{batt} is negative. Whereas in battery discharge condition, it is possible to obtain imaginary roots from the quadratic equation above. This means that the power requested by the motor exceeds the power available from the battery.

As a consequence, a different equation should be included in the model, with the aim to determine the maximum current that the battery can supply.

$$I_{max} = \frac{V_{oc}}{2R_{int}}; V = V_{oc} - \mathrm{I_{max}}\, R_{int}; \quad P_{batt} = \mathrm{I_{max}}\ V \tag{4.12}$$

It has to be remarked that the integration of the current to calculate the state of charge is a widely adopted model but has some limitations. Firstly, in a real application, this approach is not enough stable and accurate and for this reason different algorithms are used, which estimate the SOC from available measurement of terminal voltage and current.

Additionally, this method does not take into account the aging of the battery. This phenomenon, indeed, contributes to lose the capacity and increases the internal resistance, leading to the reduction of vehicle performance. However, the dependence on aging does not affect the battery performance in the short term, for this reason it is not take into account in this study.

4.4. Mechanical component and auxiliary loads

In addition to the components which "provide" the energy requested by the system, also the ones which transmit or convert it have to be modelled, such as the gearbox or the wheels.

The gearing has the aim to change the speed and the torque between two shafts without altering the power flow. However, due to the friction losses, the output power is always reduced with the respect to the input one. To take into account these power losses, a lossy gear model is introduced, for which the speed ratio is fixed for the selected gear (g_{GB}) and the output power is function of the transmission efficiency (η_{GB}).

$$T_{out} = \begin{cases} \frac{\eta_{GB}}{g_{GB}} T_{in} & if\ P_{in} = T_{in}\omega_{in} \geq 0 \\ \frac{1}{\eta_{GB} g_{GB}} T_{in} & if\ P_{in} = T_{in}\omega_{in} < 0 \end{cases} \tag{4.13}$$

The efficiency η_{GB} in eq.(4.13) can be assumed constant or variable with the gear ratio, speed and input torque with a map or an analytic expression. Generally, more complex models, in which all the degrees of freedom are included, are used for drivability studies. Concerning the wheels and brakes, a quasi-static model is usually enough for longitudinal vehicle simulation for which:

$$F_{trac} = \frac{1}{R_W}\left(T_{pwt} - T_{brake}\right);\ \ \omega_{wh} = \frac{v_{veh}}{R_{wh}} \tag{4.14}$$

Where T_{pwt} is the toque generated by the powertrain at wheel shaft and T_{brake} is the braking torque and $R_{wh}$is the wheel radius. The wheel angular speed ω_{wh} can be computed from the longitudinal vehicle speed.

Finally, the engine passive power related to the auxiliaries is often modelled in a very simplified way, due to the lack of detailed data which can be collected during a driving cycle. In particular, this energy is considered as an additional engine load depending on its current operating point.

4.5. The Energy Management Problem in HEVs

The control of a hybrid vehicle from both a numerical and real viewpoint, requires an energy management strategy able to decide the amount of power delivered at each instant by the energy sources available in the powertrain, while meeting several constrains. The majority of the EMSs of HEV are addressed to the minimization of a cost function, especially accounting for the fuel consumption, while controlling the SOC of the battery. Two main categories can be identified in the energy management problem, namely rule-based and model-based optimization problem [2], [8],[9].

The former approaches can be implemented in a realtime application, since they do not involve explicit minimization or optimization. Generally, rule-based strategies rely on a set of rules to decide the value of the control to be applied at each time. In the latter approaches, the power split is optimized, minimizing a cost function over a fixed and known driving cycle, leading to a global optimal solution. Although these optimizations cannot be implemented on a real vehicle due to the missing knowledge of future information and their huge computational time, they constitute a valuable design tool. In fact, they can be used to design the rules of an on-line application or represent a benchmark solution for comparing different control strategies. Additionally, these model-based optimization problems can be solved numerically or analytically. In the former, the entire driving cycle is taken into consideration and the global optimum is found numerically. Among the different approach, the Dynamic Programming (DP) method [5] is widely used in the vehicle application. On the other hand, the analytical optimization methods solve an analytical problem formulation to find the solution in closed/ analytical form or, at least, provide an analytical formulation which makes the numerical solution faster than the purely numerical methods. Among these methods, Pontryagin's minimum principle [4] is the most commonly employed.

4.6. The Optimal Control Problem in Hybrid Electric Vehicles

Regardless of the powertrain topology, the aim of a control strategy for the vehicle powertrain is the minimization of predefined quantities, for instance, the consumed fuel or the pollutant emissions along a driving mission, complying with some constraints, such as the maximum or minimum engine torque or rotational speed. This means that the control objectives are mostly of integral nature, while the control action are local in time. The general mathematical formulation of the optimization problem can be written as follows:

$$\arg\min_{u(t)} J[x(t),t]; \; u(t) \epsilon U; \; x(t) \epsilon X \tag{4.15}$$

where J is the so-called performance index to minimize, x is the generic state variable, u is the generic control variable, and X and U are the related range of variation. The performance index depends on the integral of a cost function L from time range $[t_0\text{-}\ t]$ and state of charge balance, through the penalization factor β.

$$J[x(t),t] = \int_{t_o}^{t} L[x(t),u(t),t]dt + \beta(x(t_0) - x(t)) \tag{4.16}$$

Under the common hypothesis for hybrid vehicle that the total mass of fuel, m_f must be minimized during a driving mission, the only state variable is the battery SOC and the control variable is the power-split between the motor units ($u = P_{el}/P_{trac}$).

$$J[x(t),t] = \int_{t_o}^{t} \dot{m}_f[u(t),t]dt + \beta(SOC(t_0) - SOC(t)) \tag{4.17}$$

Generally, the optimization problem is subject to several constraints. Some of them are integral in nature, such as the second term of the right hand of eq.(4.17) required by ensure the energy-storage balance. Others are local in nature, such as instantaneous power limits or state of charge boundaries. The local constraints of SOC is necessary to make the battery work at high efficiency and preserve its cycle life. Whereas the local constraints on the control variable are imposed to guarantee the physical operation limits. Overall local constrains can be written as follows:

$$\begin{cases} SOC_{min} \leq SOC(t) \leq SOC_{max} \\ P_{batt,min} \leq P_{batt}(t) \leq P_{batt,max} \\ T_{x,min} \leq T_x(t) \leq T_{x,max} \\ \omega_{x,min} \leq \omega_x(t) \leq \omega_{x,max} \end{cases} x = eng, mot, gen \tag{4.18}$$

where the last two inequality of eq. (4.18) are the limitations on the instantaneous motors torque and speed, respectively; $(\cdot)_{min}$, $(\cdot)_{max}$ are the minimum and maximum value of SOC/power/torque/speed at each instant. Additionally, constraints can be included in the model such as the limit of the frequency of switching between operating modes to ensure an acceptable vehicle drivability. It worth to underline that the supervisory controller has also to ensure that the total power demand at the wheels is satisfied.

4.7. Pontryagin Minimum Principle

The Pontryagin Minimum Principle is based on the Hamiltonian function, defined in (4.19) for HEV application:

$$H[u(t), SOC(t), t, \lambda(t)] = \dot{m}_f[u(t),t] + \lambda(t)\dot{SOC}[u(t), SOC(t), t] \tag{4.19}$$

The first term of the Hamiltonian function in eq. (4.19) is the instantaneous cost, while $\lambda(t)$ is a vector of the optimization variable, also known as *adjoint states* or *co-states* of the system.

The PMP states that the optimal solution (u^*) can be found at each time by minimizing the Hamiltonian, considering the following necessary condition:

$$\begin{cases} u^* = \underset{u(t)\epsilon U}{argmin}\, H(u(t), SOC(t), \lambda(t)) \\ \dot{\lambda}(t) = -\lambda(t)\dfrac{\partial \dot{SOC}[u(t), SOC(t), t]}{\partial SOC} \\ SOC^* = f(SOC^*(t), u^*(t)) \\ SCO^*(t_0) = SOC_0 \\ SOC^*(t_f) = SOC^*(t_0) \end{cases} \tag{4.20}$$

The second equation of (4.20) describes the dynamic of the co-state and, with the third equation, constitutes a system of two first-order differential equations in the variables SOC and λ. The last two equality ensure the battery energy balance between the initial time, t_0, and the final one, t_f. However, this problem is generally simplified using the common assumption of not-dependence of the SOC time derivative on its current level [10], the costate is constant over time, and the optimal costate, λ^*, has only to satisfy the energy balance for the battery between the beginning and the end of the driving cycle.

One possible way to identify the solution of the PMP is through the shooting method. Starting from an initial guess of the co-state λ_0, the minimum principle condition is solved throughout the entire time horizon [t_0,t_f], typically the whole duration of the driving cycle. At the end, the final SOC is compared to the initial SOC. Depending of the difference, the value of λ_0 adjusted and the simulation is repeated as soon as the difference reaches the zero with a pre-defined tolerance.

4.8. Dynamic Programming

The Dynamic programming (DP) is a numerical method for solving multistage decision and, like the PMP, it requires the knowledge of the entire optimization horizon. In this technique, the control problem is expressed as a deterministic discrete-state and finite-state system. In this context, the discrete state is defined as:

$$x_{k+1} = f(x_k, u_k),;\ u_k \in U_k;\ \ x_k \in X_k \tag{4.21}$$

where k is an integer value, x_k represents the state variable (generally SOC for HEV) and u_k is the control variable (power-split for HEV). Both state and control variables are discrete and bounded, namely they can assume a value only in their respective domain (U_k, X_k).

At each control policy (u_k), the system moving from the state (x_k) to the subsequent state (x_{k+1}), generates a cost called *arc cost* in the context of dynamic programming. The aim of the DP principle is to find the sequence of optimal control policy that allows to find minimum cost, expressed as the sum of the arc-cost, for a prescribed horizon. To this aim, the Bellman's theory of optimality is considered [5]. Starting from the final stage of the problem, the algorithm proceeds backward using the sequence of controls that generate the optimal cost-to-go, storing in a matrix μ* the optimal choice at each time instant k and the related state value x_k.

The cost -to-go is defined as follows:

$$u_k = \mu^*(x_k, k) = \underset{u \in U_k}{argmin}(L_k(x_K, u) + Y_{k+1}(f_k(x_k, u_k)) \tag{4.22}$$

where k=N-1, N-2, ….1. $Y(x_1, 1)$ is generated in the last iteration and is equal to the optimal cost. $Y(x_N, N) = L_N(x_N)$ is the terminal cost which depends on the final state x_N. It has to remark that most of physical systems are defined by a continuous state rather than a discretized one. As a consequence, the application of a given control action might result in state not discretized, but intermediate between two of them. In this case, the computation of the cost at the grid is based on interpolation.

A graphical example of the DP approach is reported in *Figure 4-6,* in which the problem is discretized in 4 stages [1,2,3,4], the state variable SOC in 3 [0.3, 0.5, 0.7], the control variables are the arrows and the initial/final states are fixed. Starting from the $k-1$ stage (a), for each arrow, the arc-cost incurred (during a single time step) in choosing the different available control action is evaluated. This step is done for each control variables, moving backward as soon as the initial state is reached (b). The cost-to-go is then evaluated, basically summing the arc-cost of each possible policy action. The DP optimal solution is the one that ensures the minimum cost-to-go (c).

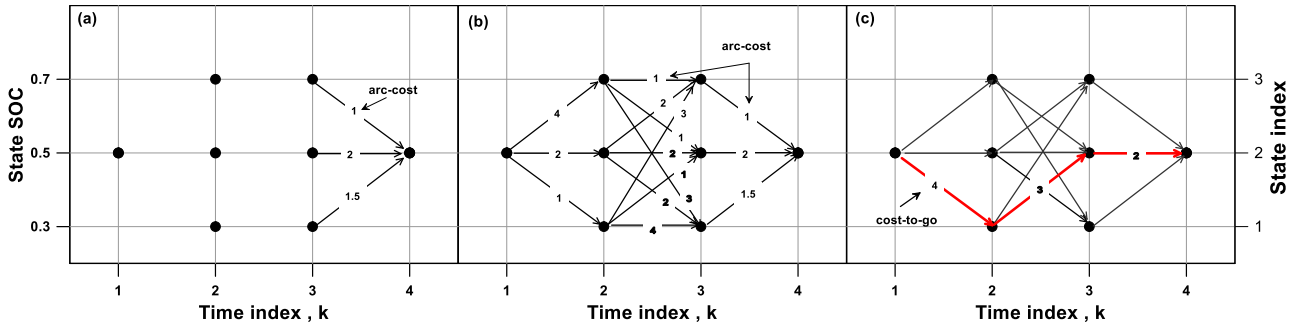

Figure 4-6 Graphical example of DP in which the arrows are the control variable, the SOC is the state variable. In (a), (b) the numbers represent the arc-cost whereas in (c) the numbers are the minimum cost-to-go of the problem.

Although, the discussed DP provides a numerical optimal solution, its accuracy is limited by the discretization of the solutions.

Additionally, DP cannot be used in real time, because of the necessity to know "a-priori" the driving cycle and the high computational effort required to solve the problem. Consequently, DP is often used as a design tool or a benchmark for implementable control strategies [11].

4.9. Efficient Thermal Electric Skipping Strategy

In this chapter the EMS, developed in this research activity, for a parallel/series hybrid vehicle is described in detail. This strategy, named as Efficient Thermal Electric Skipping Strategy (ETESS), solves a local optimal problem at each time, selecting the control variable with the aim of minimizing the cost function, but not the "global" one, along the driving cycle. In particular, the developed logic chooses the vehicle mode that allows to obtain the lowest instantaneous fuel rate, as well the CO_2 emissions. Differently from the PMP and DP, this strategy is specifically conceived for series/parallel hybrid powertrains. The choice to move away from the current literature is mainly due to the possibility to use an EMS for both off-line and on-line application with minor modifications. Indeed, the major limitation of the model-based optimization problem in real application is the huge computational time rather than the knowledge of the driving cycle. Differently, the proposed methodology despite its vehicle-dependent logic, allows to drastically reduce the computational time, showing the potential for the implementation in a modern ECU.

In order to better explain the ETESS strategy, in *Figure 4-7* the vehicle schematic is reported. The main features will be described in the chapter of the vehicle simulation results, while here they are only briefly introduced. The powertrain is composed of an ICE, two Electric Motor/Generator units, (EG and EM), a battery (Ba), three clutches (Cl_{1-3}) and two Gear-Boxes (GB_{1-2}).

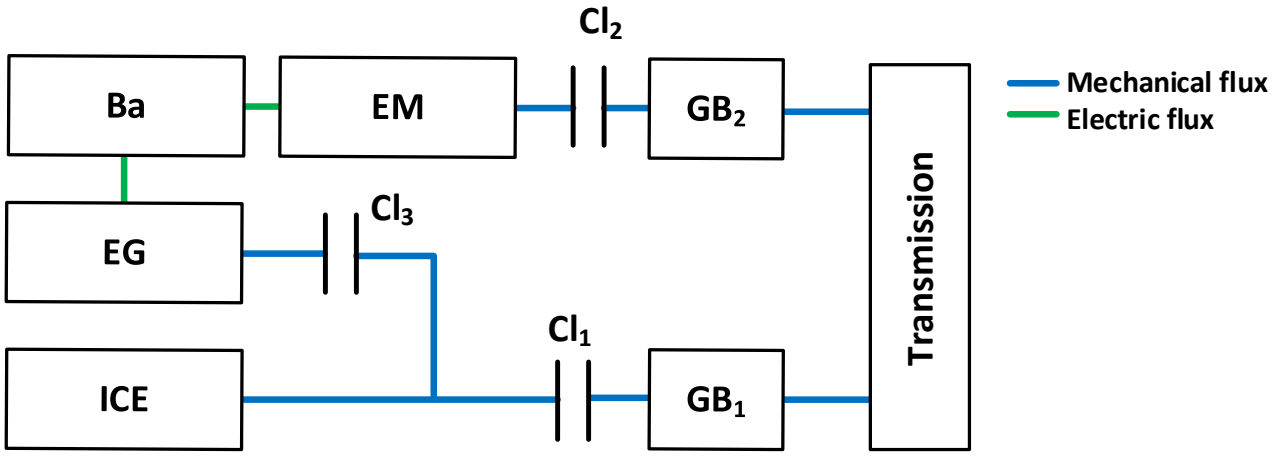

Figure 4-7 Powertrain schematic of the tested HEV

This architecture favors a flexible control of its components, thanks to the presence of the three clutches. Moreover, they contribute to minimize the mechanical losses when one of the motors is not used, avoiding load-less operations. In particular, the vehicle considered for this research activity can work in two main modalities, *series* and *parallel*. In the former, the vehicle is moved only by the electric units, whereas in the latter, the vehicle is driven by the ICE. The choice between the two modes depends, at each time, on the comparison between the actual fuel consumption of the thermal engine, operating to fully satisfy the power demand, $\dot{m}_{f,th}$ and an equivalent fuel consumption, $\dot{m}_{f,el}$ associated to a pure electric driving of the vehicle. Based on the above assumption, the local optimization problem can be written as follows:

$$\forall t \in [t_0, t_f] \begin{cases} \dot{m}_{f,el} < \dot{m}_{f,th} \rightarrow Series\ mode \\ \dot{m}_{f,el} > \dot{m}_{f,th} \rightarrow Parallel\ mode \end{cases} \tag{4.23}$$

$\dot{m}_{f,th}$can be easily defined based on the power demand, P_{trac}, and on the losses in the GB_1 and in the differential, leading to the following definition:

$$\dot{m}_{f,th} = \frac{P_{trac} BSFC}{\eta_{GB_1} \eta_{diff}} \tag{4.24}$$

where η_{GB_1} is the efficiency of GB_1 and BSFC is the actual Brake Specific Fuel Consumption (BSFC) of the engine operating with the load and speed imposed by the vehicle velocity and by P_{trac}. Before the comparison with $\dot{m}_{f,el}$, the control logic has to identify the optimal gearbox setting. To this purpose, once fixed the current vehicle speed, the engine rotational speed is derived for each gear.

Due to noise, vibration and harshness issues, the only gear ratios considered are the ones ensuring an ICE speed above a certain threshold level. Then, the gear ratio which leads to the lowest fuel rate is selected.

The most crucial point of the proposed strategy is the estimation of the fuel rate in series, since no fuel is consumed by the ICE in this modality. For this reason, the control strategy can only estimate an "equivalent" fuel rate. The basic concept for the identification of $\dot{m}_{f,el}$ is that, in a series mode, the power delivered by the electric motor to fulfill a certain power demand at the wheels, P_{trac}, is produced by the thermal engine in an undefined time, working in its optimal operating point, characterized by a $BSFC_{min}$. As consequence, the $\dot{m}_{f,el}$ is considered starting from a "*virtual*" power flux from ICE to the wheels, passing through the electric units, taking into account all the related losses.

The adjective “virtual” indicates that there is a temporal misalignment between the time when the driving power is transferred to the wheels and the time when this power was produced by the ICE. Under this hypothesis , the fuel consumption is expressed as a function of the tractive demanded P_{trac} and an “equivalent” $BSFC_{min}$, which is corrected by the efficiencies of the components posed along the power flux from the ICE to the wheel in a series mode:

$$\dot{m}_{f,el} = c_o \frac{P_{trac} BSFC_{min}}{\eta_{GB_2} \eta_{EG} \eta_{EM} \eta_{diff}} \tag{4.25}$$

The denominator of eq (4.25) contains the losses of the “virtual” power flux through the GB_2,(η_{GB_2}) EG (η_{EG}), EM, (η_{EM}) and differential (η_{diff}). Whereas c_o is a tuning variable introduced to realize the SOC balance at the end of the driving cycle. This parameter can be considered as equivalence factor that promote or discourage the battery usage. In the off-line application c_0 is a constant evaluated with the knowledge of the driving cycle, ensuring the SOC balance. While in the on-line application, due to the absence of the future events, this c_0 becomes a variable function of the SOC.

References

[1] Miller, J., "Propulsion systems for hybrid vehicles," Vol. 45. Iet, 2004.

[2] Guzzella, L., Sciarretta, A., "Vehicle Propulsion Systems, Introduction to Modeling and Optimization," 2005, ISBN: 978-3-642-35913-2.

[3] Guzzella, L. Sciarretta, A., "Electric and hybrid-electric propulsion systems. In Vehicle Propulsion Systems," Springer, Berlin, Heidelberg, (pp. 67-162), 2013, doi:10.1007/978-3-642-35913-2_4.

[4] Kim, N., Cha, S. Peng, H., "Optimal control of hybrid electric vehicles based on Pontryagin's minimum principle," *IEEE Transactions on control systems technology*, 19(5), pp.1279-1287,2010, doi:10.1109/TCST.2010.2061232.

[5] Bellman, R., "Dynamic Programming," Princeton University Press, Princeton, 1957.

[6] Onori, S., Serrao, L. Rizzoni, G., "Hybrid electric vehicles: energy management strategies," Berlin Heidelberg, Springer, doi:10.1007/978-1-4471-6781-5.

[7] Drouilhet, S., Johnson, B., Drouilhet, S. Johnson, B., "A battery life prediction method for hybrid power applications," in 35th Aerospace Sciences Meeting and Exhibit (p. 948), 1997, doi:org/10.2514/6.1997-948.

[8] Salmasi F. R. "Control Strategies for Hybrid Electric Vehicles: Evolution, Classification, Comparison, and Future Trends," *IEEE Transactions on Vehicular Technology*, 56(5), 2393–240, 207, doi:10.1109/TVT.2007.899933.

[9] Salman M., Chang, M., Chen. J., "Predictive energy management strategies for hybrid vehicle," Proceedings of the 2005 IEEE Vehicle Power and Propulsion Conference,2005.

[10] Sciarretta, A., Guzzella, L., "Control of hybrid electric vehicles," IEEE Control Systems Magazine 27(2):60-70, 2007, doi: 10.1109/MCS.2007.338280.

[11] Sundström, O., Ambühl, D. Guzzella, L., "On implementation of dynamic programming for optimal control problems with final state constraints," *Oil & Gas Science and Technology*– Revue de l'Institut Français du Pétrole, 65(1), pp.91-102, doi:org/10.2516/ogst/2009020.

5. Short term solution: High efficiency conventional spark plug engine

The first study carried out during this PhD Thesis is focused of the estimation of the CO_2 along the WLTC for a conventional vehicle, with the aim to define a state of art of ICE-based propulsion system. The engine under study is a downsized turbocharged VVA 2-cylinder engine, with the main features listed in *Table 5.1*, in which the effect of different advanced technologies (VCR, EGR and WI), either singularly, combining two of them or all together, on the fuel consumption was assessed.

Table 5.1. Conventional SI engine main features

SI engine data	
Compression ratio	10:1
Displaced volume, cm^3	875.4
Bore, mm	80.5
Stroke, mm	86
Connecting rod length, mm	136.85
Maximum brake power, kW	63.7@5500 rpm
Maximum brake torque, Nm	146.7@2000 rpm
Valve number	4 valve/cylinder
IVO – IVC at 2mm lift, CAD AFTDC	342/356 – 400/624
EVO – EVC at 2mm lift, CAD AFTDC	134 – 382

The main characteristics of the tested vehicle, belonging to the A segment, are reported *Table* 5.2 This chapter will follow the steps described in *Figure 1-4,* analyzing firstly the tested engine in its base architecture. Under this configuration, the 1D model validation is presented against measured data collected at full and part load operation. Subsequently, the virtual calibration of the base engine architecture is described.

Table 5.2 Conventional vehicle main features

Vehicle data	
Vehicle mass, kg	1074
Cross section area, m^2	1.7
Aerodynamic drag coefficient, -	0.32
Tire rolling radius, mm	292
Tire rolling resistance factor, -	0.01
Gear ratio I, -	3.909
Gear ratio II, -	2.174
Gear ratio III, -	1.345
Gear ratio IV, -	0.974
Gear ratio V, -	0.766
Axle ratio, -	3.44

In particular, a Rule-Based (RB) strategy, based on PID, is settled to identify the calibration which minimizes the BSFC in a predefined grid of points of the engine operating domain. Subsequentially, the base engine is virtually modified to adopt various techniques, including two-stage variable CR, external cooled EGR and ported WI. For all the investigated technologies, an "ad-hoc" virtual calibration is performed. The effectiveness of each technique is hence discussed, highlighting their relative strengths and weaknesses. Finally, vehicle simulations are performed to quantify the potential benefits of the above systems in terms of CO_2 emission reduction over the WLTC.

5.1. Engine description

As stated above, the engine under study is a small-size VVA twin-cylinder turbocharged SI engine. It features a pent-roof combustion chamber and a fixed Compression Ratio (CR) of 10. The engine boosting is realized by a waste-gate turbocharger. Each cylinder is equipped with a centred spark-plug, and two intake/exhaust valves. The control of the intake valves is based on the multi-air system which allows to modify the valve lift and the opening/closure timing. Whereas, the exhaust side presents a fixed timing. Representative valve lift profiles are plotted in *Figure 5-1* against the engine crank angle, referred to the firing TDC. Opening and closure angles of the valves are reported in *Table 5.1*, together with the range of variation of IVO and IVC.

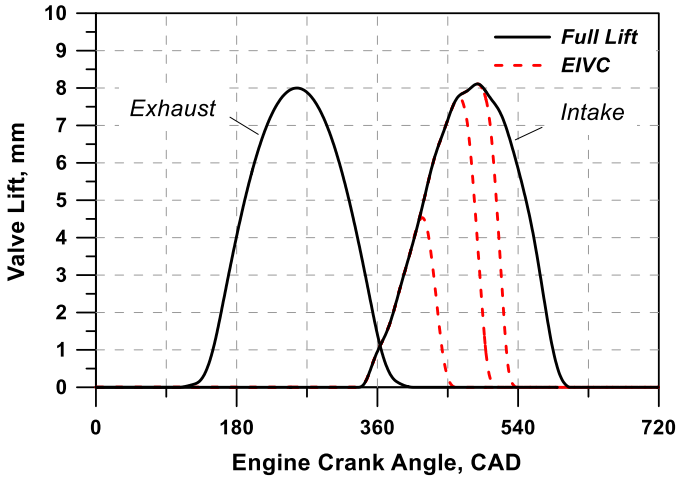

Figure 5-1. Representative valve lifts profiles for the conventional SI engine

As previously pointed out, an EVIC strategy allows to reduce the pumping losses, with a consequent decrement of the turbulence motion at the spark event. With the aim to guarantee a satisfactory turbulence level to support the combustion process at low load, a lower limit of 420 CAD AFTDC for IVC is imposed.

An extended experimental data set, collected before of this PhD Thesis, is available for this engine [1]. In particular, full and part load operations were investigated at various speeds and intake valve strategies (EIVC and Full-Lift), including also the water injection impact [2],[3]. More than 280 operating points were recorded in terms of overall performance data, main combustion events and setting of control parameter, namely IVC, Air-to-Fuel (A/F) ratio, boost level, and Spark Advance (SA).

5.2. 1D Model tuning and validation

A 1D model of the above described engine is developed within a 0D/1D modelling environment, where the system is schematized through a network of 1D pipes and 0D volumes. The cylinder description is based on a 0D approach, coupled with quasi-dimensional phenomenological models to predict the in-cylinder process. The combustion and the turbulence are simulated according to the models of chapter 3 of this thesis, namely the fractal approach and *K-k-T* turbulence model, suitable for a conventional SI engine. A modified Hohenberg correlation is adopted for heat transfer modelling. As discussed in chapter 3, the auto-ignition table for the knock modelling is based on the kinetic scheme developed by Andrae [4]. The knock model validation was performed at full load, where the selected engine always operates at the knock borderline. In these analyses, the Spark Advance (SA) was iteratively modified in order to realize a numerical knock index below a predefined threshold level [5],[6],[7]. This methodology allowed to correctly agree with the experimental knock limited spark advance, with a maximum error of 1-2 CADs.

5.2.1. Laminar flame speed correlation

The laminar flame speed correlation reported in the chapter 3, namely ‘Cor A’[8], ‘Cor B [9] and ‘Cor C’[3] , were analyzed to choice the most suitable for the tested engine. To this aim, the 0D/1D model for the conventional SI engine under study was adopted in which each flame speed correlation was implemented in the fractal combustion sub-model. Then, the model was tuned for each of the formulation with the aim to ensure the best agreement with the experimental data at full load. *Figure 5-2*, briefly summarize the results of the comparative study. In *Figure 5-2a*, BSFC and the related error to the respect of the experimental data at full load is reported. Whereas, in *Figure 5-2b-c* the results at partial load are depicted for all the operating points analyzed, including internal and external EGR.

Looking at the comparison, the results are of comparable accuracy for the combustion evolution and engine performance at full load, mainly due to the dedicate tuning procedure of each correlation.

However, when the EGR amount is introduced in the engine, the Cor B and Cor C, result in a more accurate predictions of combustion duration and fuel consumption at high-EGR part-load operating points.

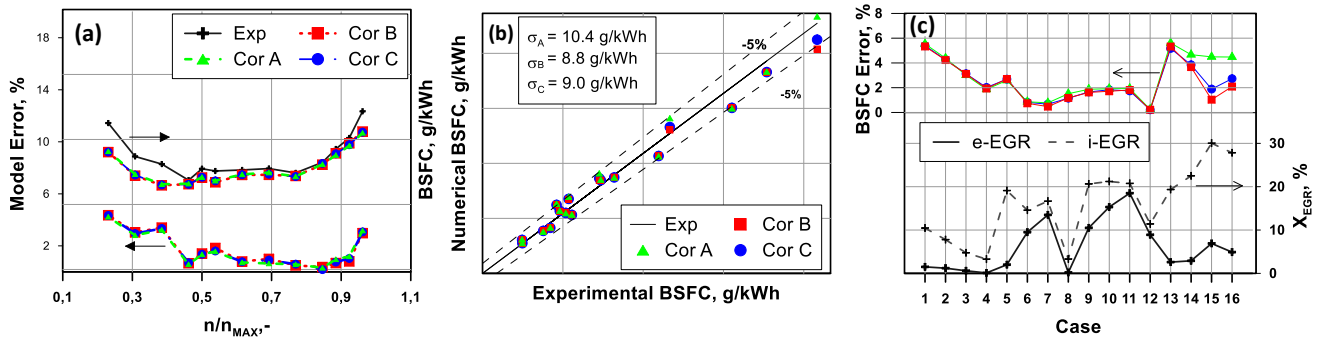

Figure 5-2 Numerical/experimental comparison of BSFC at full load (a) and partial load (b), 1D computed EGR fraction and percent BSFC error (c) at part loads, for Cor A, B and C [10].

The choice of the laminar flame speed fell in Cor C since the conventional engine under study would have been tested considering high EGR extent and WI injection. Indeed the Cor C, differently from the others two correlations, if properly modified is able to sense also of the effect of the water, through a WI_{factor}:

$$S_L = S_{L0}\left(\frac{T}{T_{ref}}\right)^{\alpha}\left(\frac{p}{p_{ref}}\right)^{\beta} * EGR_{factor,3} * \ WI_{factor} \tag{5.1}$$

$$WI_{factor} = (1 - \chi x_w)^{\delta}; \delta = \delta_1 + \delta_2 \Phi; \tag{5.2}$$

Where:

$$\delta = \delta_1 + \delta_2 \Phi; \delta_1 = 1.264575 \ \ \delta_2 = 1.169524; \ \chi = 1.961413; \tag{5.3}$$

More details of the above analysis can be found in [10]

5.2.2. Model validation

In a first stage, not detailed in this manuscript, the turbulence and the models were tuned. Following a well-assessed hierarchical 1D/3D approach [11], the turbulence sub-model constants were identified on the basis of 3D CFD results for various valve strategies and engine speeds.No case-dependent tuning was required to fit the 3D results.

The identification of the combustion model was carried out through the comparison with the measured in-cylinder pressure cycles, the global performance parameters and combustion events at full load [12],[13].

The second step was the model validation of the engine through the comparison of 284 operating points, including part and high load operations. At this step, the manufacturer calibration for each control parameter, namely the combustion phasing (MFB_{50}), and the A/F ratio, is imposed in the calculations. Depending on the load level, a PID controller selects the waste-gate (WG) and throttle (THR) valves openings to match the experimental BMEP level. The VVA setting (either *EIVC* or *Full-Lift*) is imposed in the simulations according to experimental setting depending on the operating point.

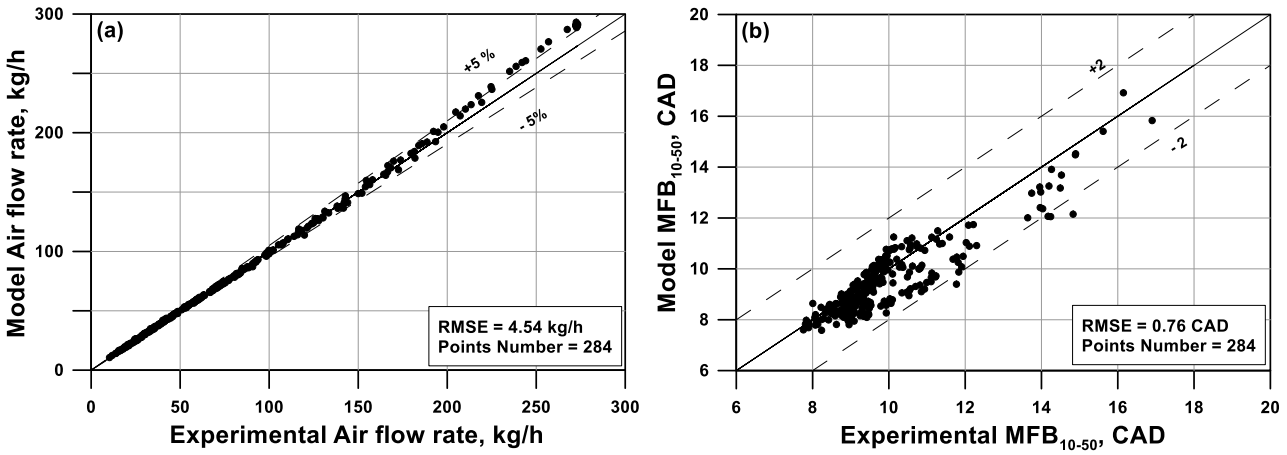

Figure 5-3 Experimental vs. numerical air flow (a) and $MFB_{10\text{-}50}$ (b) comparison.

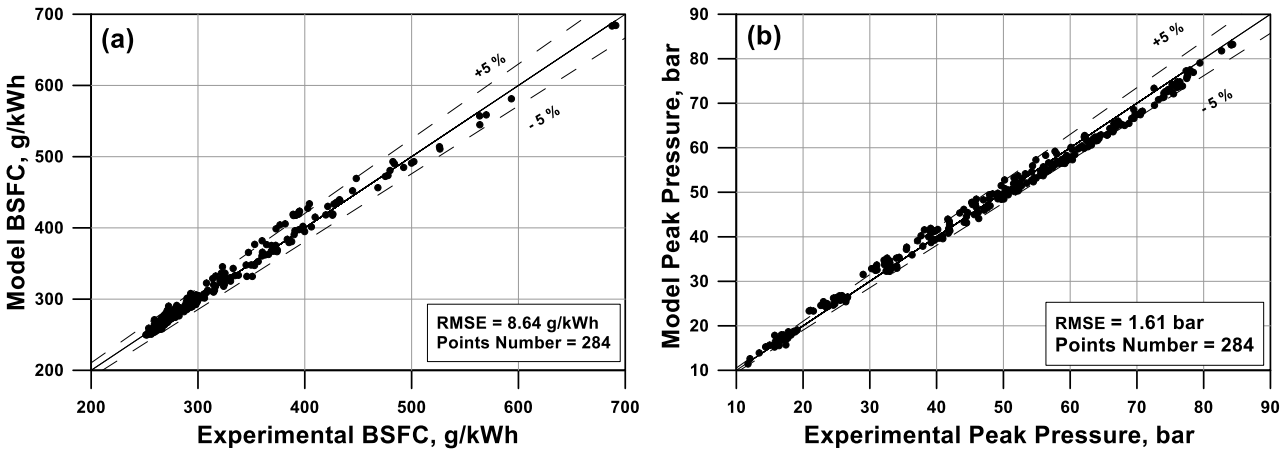

Figure 5-4 Experimental vs. numerical BSFC (a) and in-cylinder Peak Pressure (b) comparison.

In *Figure 5-3,* the numerical/experimental comparisons in terms of air flow rate, burn duration ($MFB_{10\text{-}50}$) are reported, with the related Root Mean Squared Error (RMSE), σ.

The air flow rate is satisfactory predicted with most of the examined points within the error band ±5%, hence highlighting the good accuracy in the engine geometry schematization. Referring to the combustion process description, the model shows a good reliability, with a MSE of only 0.76 CAD.

The accuracy of flow, combustion and heat transfer models is reflected in the BSFC prediction, reported in *Figure 5-4a*. This last puts into evidence an average error lower than ±5% in most cases. A good correlation with experimental data is similarly found for the in-cylinder peak pressure, as shown in *Figure 5-4b*, with a MSE of 1.61 bar.

On the light of the above results, the employed model is considered validated, since it is able to predict with an allowable error band ±5% the above-mentioned performance parameters. It is worth to underline that the results were obtained using a unique set of tuning constants in whole operation plane, demonstrating that the physics behind the model is accurate enough to utilize it in a predictive way.

5.3. Analysed Configurations and Virtual Engine Calibration

In this work, as already stated, a numerical calibration procedure is setup to derive the engine performance map (specifically the BSFC map) by an optimized calibration strategy for the base and the modified engine architectures. Indeed, for the vehicle simulation, the engine maps of all the investigated variants must be integrated in the code, as stated in chapter 4, for the proper estimation of the CO_2 emission along the WLTC.

It has to emphasized that, engine calibration in the test bed is usually realized through the adoption of Design of Experiment (DoE) methodologies [14], which it is generally an expensive and time-consuming process. Indeed, each control parameter is varied around a presumed set point for a predefined operating condition, until the desired performance target is obtained, comply with a number of constraints to limit thermal and mechanical stresses of the engine and its subcomponents. Consequently, an engine pre-calibration through numerical models would be very helpful also for the manufacturers during the engine development, in order to reduce the time to market.

Concerning the engine under study, the proposed numerical virtual calibration strategy is able to select the engine control parameters, such as the SA, the Waste-Gate (WG) opening or the A/F ratio, with the aim to minimize the fuel consumption over the whole operating plane. Additionally, the calibration strategy includes the constrained parameters in order to preserve the engine and its mechanical components.

The maximum allowable levels imposed for each variable are shown below.

- Maximum Temperature Inlet Turbine (TIT): 930 °C
- Maximum in-cylinder pressure: 85 bar
- Maximum boost pressure: 2.5 bar
- Maximum turbocharger speed: 255'000 rpm
- Optimal combustion phasing: 9.0 CAD AFTDC
- A/F ratio range: 10.6-14.55
- IVC range: 420 to 624 CAD

The optimal combustion phasing is imposed equal to 9 CAD AFTDC, even if the MFB_{50} realizing the Maximum Brake Torque (MBT) can slightly change with the operating conditions. This optimal value can be reach only under knock free operation, otherwise, the combustion phasing has to be delayed in order to guarantee a knock index below the specified threshold, defined in [5]. The minimum A/F ratio is imposed by the maximum fuel injection rate and duration, while the maximum is the stochiometric level. As already pointed out, the engine under study is equipped with a VVA system. The same range of valve maximum lift and duration as the real engine is imposed in the model. In particular, the minimum setting of 420 CAD AFTDC corresponds to the most advanced IVC, while the maximum setting of 624 CAD identifies the most delayed one (*Full-Lift* profile).

Although the minimum VVA setting allows the engine to work with a fully opened throttle at low load, a certain reduced throttling is applied in the calibration at the test-bench to limit the undesirable gas-dynamic noise radiated by the intake mouth. However, in this study, a fully unthrottled engine is considered to get the lowest possible BSFC.

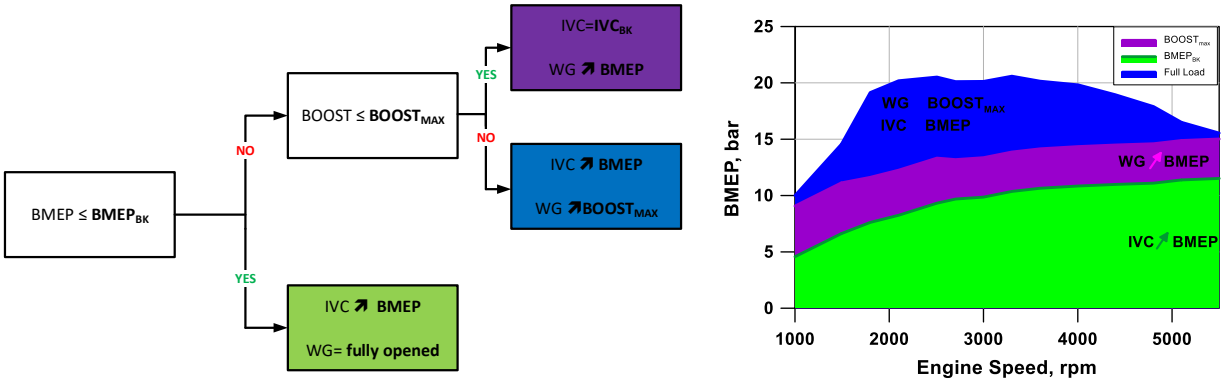

Figure 5-5 Flowchart summarizing the logics of PID controllers for engine calibration.

Based on the above constrains, a Rule Based (RB) calibration strategy is conceived, as schematized in *Figure 5-5*. The control parameters available for the engine calibration are spark advance, or equivalently the combustion phasing (MFB_{50}), IVC, WG opening and A/F ratio. Through 4 PIDs, the mentioned parameters are selected following a Rule-Based (RB) strategy.

To this aim, preliminary calculations are performed by imposing the optimal combustion phasing, a fully opened WG and a stoichiometric A/F.

Then, the load level of incipient knock (Base knock- BK) is evaluated, changing the VVA setting and obtaining the setting of IVC (IVC_{BK}) and maximum load ($BMEP_{BK}$) at knock borderline. Below the knock limit zone ($BMEP \leq BMEP_{BK}$), stochiometric A/F ratio and optimal MFB_{50} can be safely specified, where the PID of the IVC follows the prescribed BMEP, assigning a fully opened WG.

Whereas, above the knock limit zone ($BMEP > BMEP_{BK}$), a setting of IVC lower than IVC_{BK} able to limit the knock index is automatically imposed by another PID controller (knock mitigation by the reduction of the effective CR). Here, a PID controller for the WG setting is utilized to follow the assigned load level. Advancing the IVC may lead to an increment of the boost pressure to meet the prescribed load. If the boosting level exceeds the limit of 2.5 bar, the WG control switches to constraint the boost pressure, while the PID of the IVC is activated again to follow the assigned BMEP. Moreover, both the A/F ratio and the MFB_{50} are changed by additional PIDs to avoid knock onset, and simultaneously satisfying the constraints on the TIT and on the in-cylinder pressure peak.

The following PID calibration is utilized to estimate the performance map of the 'Base' engine. In the left of *Figure 5-6* the BSFC contour plot is depicted, while on the right the A/F ratio and MFB_{50} isoline are reported. As typically of turbocharged downsized SI engine, the minimum BSFC is attained at medium load/speed (about 12 bar BMEP /3000 rpm). However, the EIVC strategy allows to reduce the fuel consumption penalization at low load. On the other hand, at high load, the BSFC degradation is due to the knock-related MFB_{50} delay. Additionally, at high-speed/load, the mixture enrichment, needed to limit the TIT, contributes to further increase the BSFC.

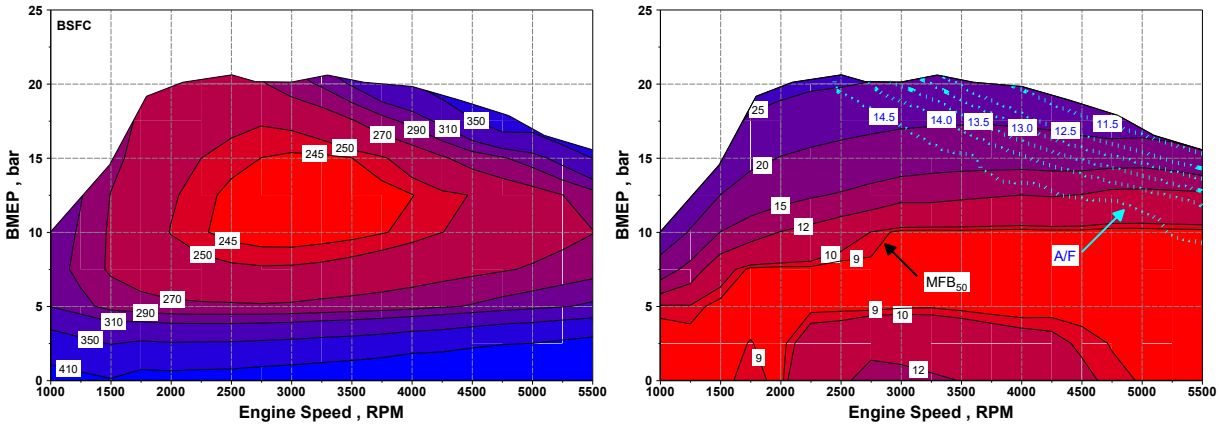

Figure 5-6 BSFC (left), MFB_{50} (continuous line) and A/F (dashed line) maps for the 'Base' architecture (right).

Subsequently, the base engine architecture is virtually modified to adopt various techniques, listed in *Table 5.3*. To this aim, the above PID based procedure is properly modified to take into account new degrees of freedom introduced by the mentioned technology.

Table 5.3. Analyzed architectures for the conventional SI engine

Case #	Label	CR	EGR	WI
1	**Base**	10	No	No
2	**HCR**	14	No	No
3	**TSCR**	10-14	No	No
4	**EGR**	10	Yes	No
5	**TSCR-EGR**	10-14	Yes	No
6	**WI**	14	No	Yes
7	**WI-EGR**	14	Yes	Yes

Seven different architectures are investigated, as listed in the following:

1. *'Base'*: is the base engine architecture with CR equal to 10, previously described.
2. *'HCR'*: In this configuration, the CR is increased from 10 to 14. The same control strategy of the *'Base'* case is employed.
3. *'TSCR*': Performance maps estimated for the base and the high-CR engine are combined, mimic an engine equipped with a two-stage CR (10-14) mechanism [15]. The reason is mainly to the fact, with a CR of 14 for the tested engine is not possible to achieve the same brake torque of the 'Base' case due to knock limitation.
4. *'EGR'*: This architecture considers an EGR circuit, consisting of an EGR valve and a cooling heat exchanger. The latter achieves a recycled gas temperature of 433 K, similar to the level proposed in [16]. This assumption mimics an "ideal" cooling system, which is able to maintain the EGR temperature at the prefixed value whatever is the condition at the heat exchanger inlet. The EGR percentage becomes a new control parameter, properly selected by a new PID control with the constrain of maximum trapped residual mass faction of 20%. This choice is done with the aim to avoid excessive cycle-by cycle variations in real application of this solution. With the EGR increment, a delayed IVC and/or an enhanced boost level is mandatory. At increased load, however, both these strategies become ineffective since their own operating limits are reached. For these reasons, the amount of recycled gases has to be decreased, and a linear load-diminishing trend is assumed. The EGR valve is, hence, fully closed at full load.
5. '*TSCR-EGR'*: combination of *'TSCR'* and *'EGR'* cases.
6. '*WI'*: This architecture is combined with the *'HCR'* engine, introducing water fed upstream the fuel injectors. Hence, a further PID is introduced to define the amount of injected water, complying with a maximum Water/Fuel (W/F) ratio of 0.5. This limit is introduced to elude the water condensation and oil emulsion in real application. The PID selects the minimum water amount for knock suppression and TIT limitation. In this way, the MFB_{50} moves towards its optimal value and overfueling is minimized.
7. '*WI-EGR'*: combination of *'WI'* and *'EGR'* cases.

The reliability of the Rule Based (RB) virtual engine calibration procedure is verified through the assessment with a more complex calibration methodology, widely detailed in [17]. Differently from the RB strategy, the engine controls are freely modified by the optimizer to identify the calibrations of minimum BSFC, which comply with the constraints listed above. The weakness of this approach is the high computational time and for this reason it was applied only for 5 representative operating points.

Those points are the ones more frequently experienced by the considered engine, if coupled to a segment A vehicle along the WLTC. They are chosen on the basis of vehicle simulations, detailed in the following. *Figure 5-7* summarizes the results of the comparison, in which the most relevant control parameters for each considered architecture are depicted for both the RB and Optimizer approaches at different speed-load condition. Even if not shown her for sake of brevity, the PID calibration procedure is able obtain results similar to the optimizer ones for all considered engine variants and speed/load points. The developed RB strategy can be considered hence reliable enough to perform a virtual engine calibration over the entire operating domain.

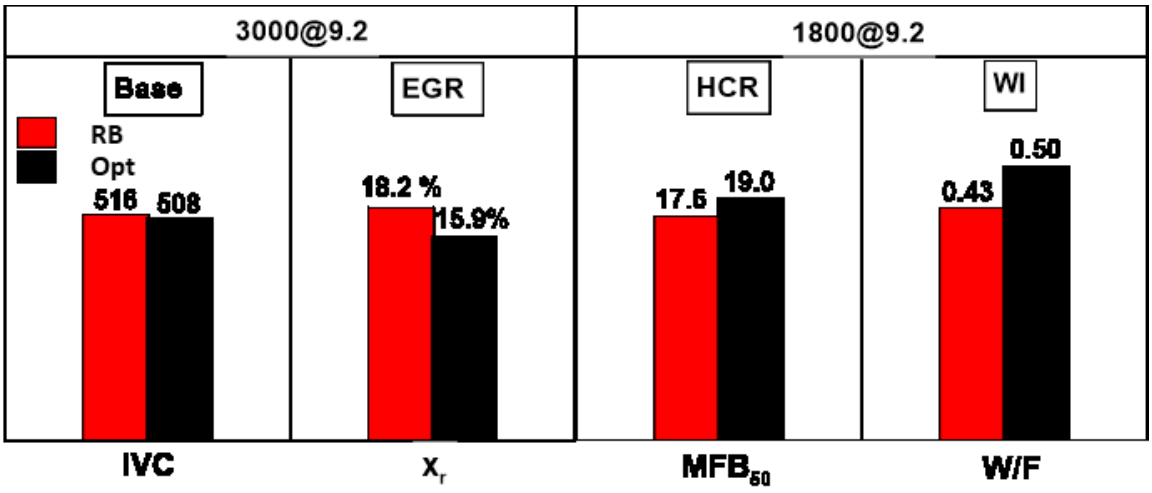

Figure 5-7 RB and Optimizer outcomes comparisons on selected architectures and speed-load conditions [17].

5.4. Computation of the performance maps

Based on the RB strategy previously described, the engine performance maps of all the investigated architecture were estimated.

In total 6 additional BSFC maps were evaluated and reported in the form of percent BSFC difference compared to the *'Base'* architecture (it will be labelled as ΔBSFC - a positive value indicates a lower BSFC). In *Figure 5-8*, the BSFC percent advantage maps for *'HCR'* and *'TSCR'* architecture is reported. As expected, the increment of the compression ratio allows to improve the BSFC in the low-medium load region, especially at high speeds.

On the other hand, the high CR increases the knock propensity at high load, which causes a later and later MFB_{50} timing. Simultaneously, an A/F enrichment is also required to control the TIT. As a consequence, starting from a certain load, ΔBSFC attains negative values, and the full-load curve of '*Base*' engine cannot be achieved, due to excessive MFB_{50} delay. Because of this drawback, this engine variant will be not considered in the vehicle analyses presented in the following.

The *'TSCR'* allows to overcome the above issues by the combination of the *'Base'* and *'HCR'* configuration. This means that below (above) the a 0-ΔBSFC curve, the *'Base'* (*'HCR'*) architecture is adopted, as shown in *Figure* 5-8.

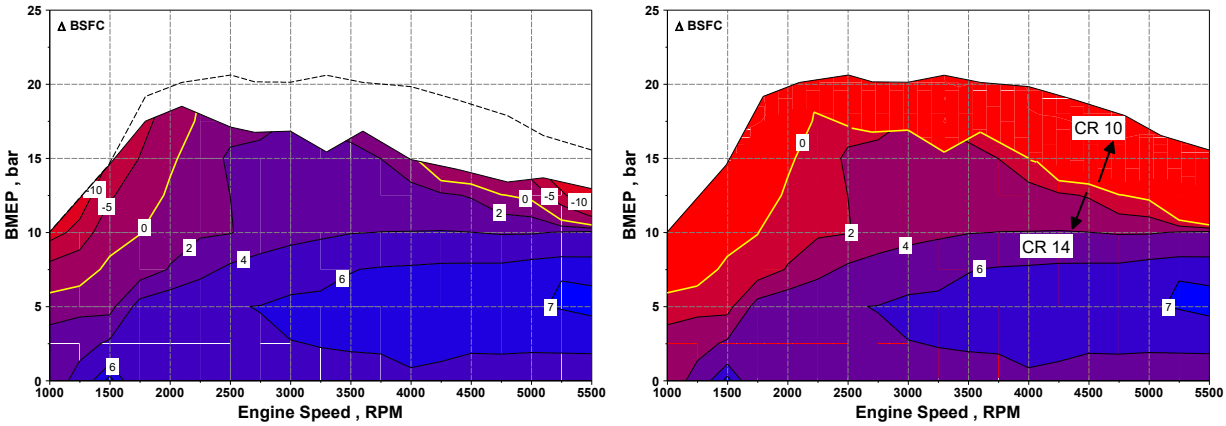

Figure 5-8 BSFC percent advantage map for the *'HCR'* (left) and *'TSCR'* (right) architectures [17].

The ΔBSFC maps related to the *'EGR'* and *'TSCR-EGR'* architectures are represented in *Figure* 5-9. A negligible EGR-related knock suppression is observed, bringing to very reduced and local BSFC benefits. The latter also partly arise from lower heat losses. The maximum BSFC gain in the *'EGR'* case, around the 2% in a limited portion of the operating domain, namely, low speed / mid-low loads, is mainly due to the following physical effect. Under these conditions, compared to the '*Base*' architecture, a longer intake phase is needed to meet the prescribed load, which determines a higher effective CR and an improved thermodynamic efficiency.

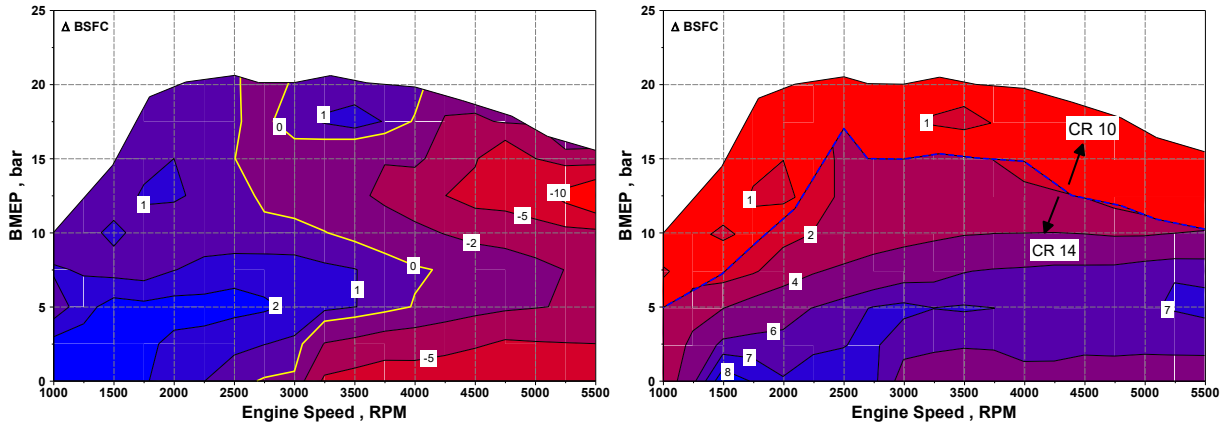

Figure 5-9 BSFC percent advantage map for the *'EGR'* (left) and *'TSCR-EGR'* (right) architectures. [17].

At increasing engine speeds, the EGR technique requires a higher boosting to match the load, resulting in a backpressure rise, with relevant BSFC penalizations. The advantages of a greater effective compression ratio at low/medium loads are furtherly exploited in the '*TSCR-EGR*' architecture. Such engine variant collects pros and cons of the EGR and TSCR technologies, resulting in maximum fuel consumption improvements in the region of low-load and low-speed.

In *Figure 5-10*, the maps concerning the last two architectures, namely *'WI'* and *'WI-EGR'*, are depicted. The highest benefit of the WI injection is visible at high load, up to a peak of 30%. Indeed, the water injection highly contributes to mitigate the knock, improving the combustion phasing and hence the BSFC. At higher speeds, it also helps to reduce the TIT, allowing a mixture overfueling reduction and, once again, an improved fuel consumption. As expected, the most complex engine architecture 'WI-EGR' allows to merge all the mentioned benefits, using simultaneously EGR and WI only when their combination involves additional BSFC gains compared to adoption of the single technique. While at high-speed / high-load, the map resembles the one of the 'WI' variant, some further benefits emerge by the EGR presence at low load.

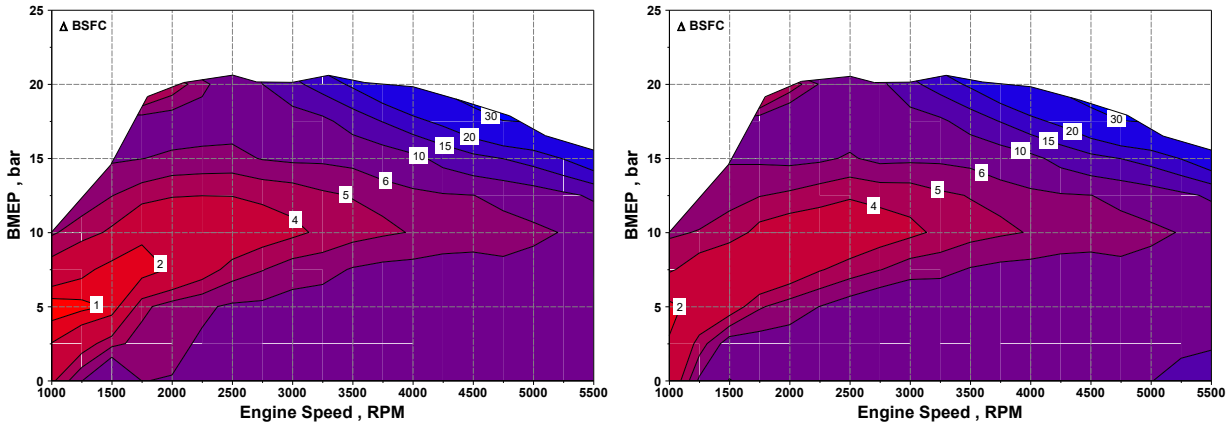

Figure 5-10 BSFC percent advantage map for the *'WI'* (left) and *'WI-EGR'* (right) architectures [17].

5.5. Vehicle simulation outcomes

The last step of this analysis is the estimation of the impact of the considered engine variants on the CO_2 emissions of a segment A vehicle *Table 5.2*, over the WLTC.

To this aim, a forward analysis is executed based on the model approach previously described in the chapter 4. In particular, a "virtual driver", based on PID logics, defines the torque demand as function of the vehicle speed and selected gear ratio, imposed by the technical regulation No. 15 on WLTC [18]. The thermal unit is described by the fuel consumption maps presented in the previous section. Whereas, the efficiency of the components (gearbox and differential) along the driveline is assumed constant. Due to the lack of experimental data, a preliminary simulation is performed for the '*Base*' architecture over the NEDC for the vehicle model validation.

Despite of the model simplicity, the model estimated CO_2 emission is very close to the manufacturer declared value of 98 g/km. The CO_2 emission is derived by the vehicle fuel consumption expressed in g_{fuel}/km, by a constant conversion factor of 3.09 g_{CO2}/km. This last refers to a reference commercial gasoline (E10), distributed in the EU market. The application of a constant conversion factor is suitable considering that, whatever is the considered architecture, the engine mainly operates under stoichiometric conditions. Otherwise, a A/F dependent factor would have been used. This is confirmed by the bubble chart in *Figure 5-11*, which depicts, over a speed-load grid, some circles, whose dimension is proportional to the fuel consumed. The figure underlines that the engine mainly works with speeds and BEMP lower to 3000 rpm and to 15 bar, respectively, along the WLTC, where the A/F ratio is stoichiometric, *Figure 5-6*. This result is even more true for the NEDC case, considering that this is less severe than the WLTC. Hence, also for the NEDC case, the hypothesis of a constant conversion factor can be properly applied for the CO_2 estimation. In *Figure 5-12,* the CO_2 emissions of the different engine variants along the WLTC and their percent reduction with respect to the *'Base'* configuration are reported. The *'Base'* engine provides CO_2 emission of about 100 g/km, slightly higher, as expected, than the one along a NEDC.

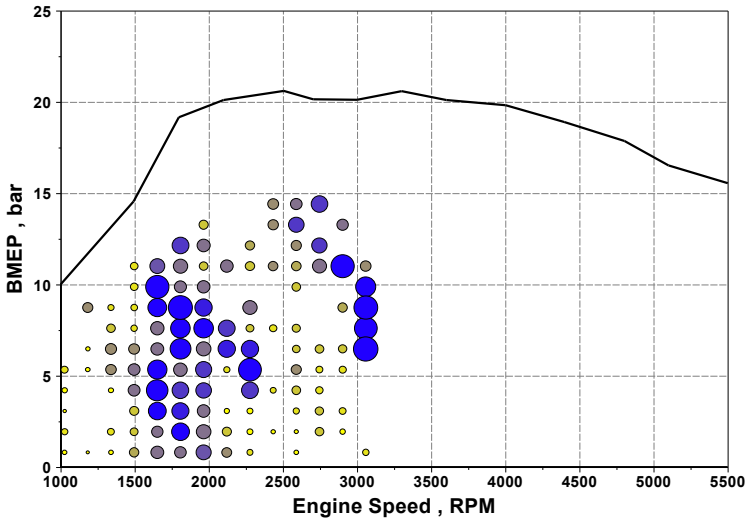

Figure 5-11. Bubble chart of the fuel consumed along the WLTC [17].

Concerning the architecture comparison, the EGR addition on the *'Base'* engine allows CO_2 emission reduction lower than 1%, while more relevant benefits arise with the *'TSCR'* architecture (3.8%). Their combination (*'TSCR-EGR'*) leads to a slight improvement (4.0 %). The most effective variant is based on the application of the water injection with an increased CR, allowing for a CO_2 reduction of about 4.4%. The combination of all the above technologies (*'WI-EGR'*) leads to an additional limited gain (5.0 %). Despite of the higher benefit of the *'WI-EGR'* variant, the application of WI and increased CR concepts seems the most interesting.

Indeed, this solution is characterized by a higher simplicity and requires minor modifications of the engine architecture (reduction of the piston TDC clearance and installation of a conventional low-pressure injector for the water introduction). The main drawbacks of this solutions are an adequate water vaporization before the combustion and the oil dilution in the crankcase; in addition, a tank of proper sizing or an on-board recovery system have to be foreseen to face the water [19].

On the other end, the *'EGR'* engine variant, which shows the lowest CO_2 advantage, would require firstly the redesign of the engine layout and packaging. Secondly, the engine control has to be properly modify to manage transient maneuvers and ensuring combustion stability in case of very high in-cylinder inert content (above 25% [20]). As a consequence, this technique does not appear a promising approach for carbon dioxide reduction. Concerning the *'TSCR'* solution, it is still not cost-competitive with the *'WI'* case, since the higher cost connected to the replacement of a conventional connecting rod with one having a variable length [21].

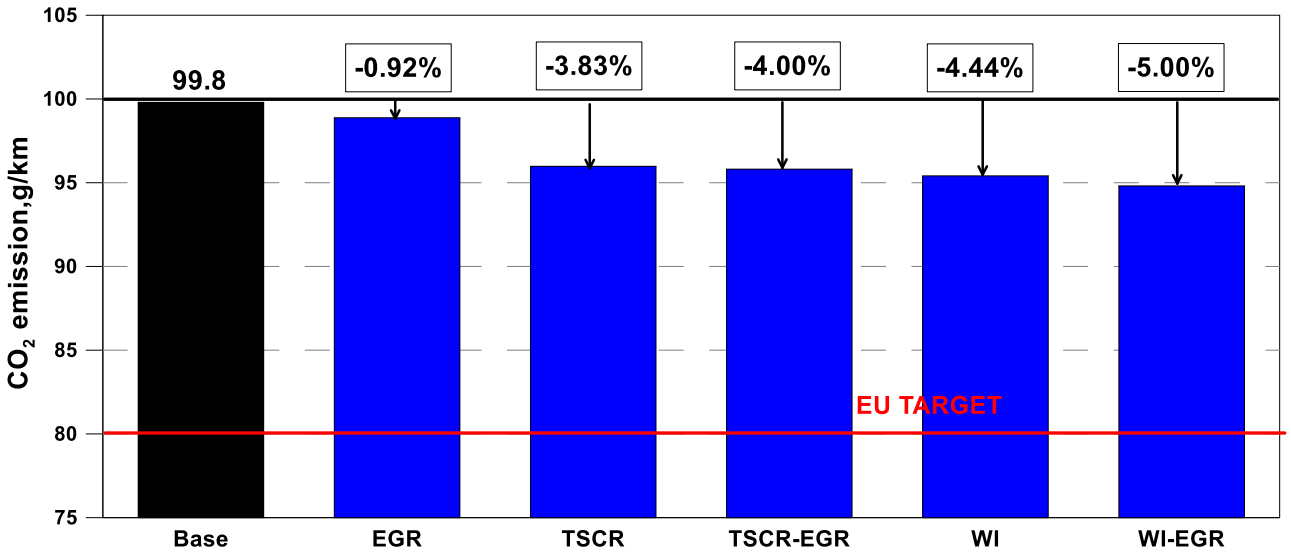

Figure 5-12 Comparison of CO_2 emissions of a segment A vehicle along a WLTC for the considered engine variants.

Although the maximum potential BSFC benefits of these techniques can reach locally value of 20%, the benefit along the driving cycle are quite limited.

The reason is mainly due to the fact very low load/speed are most frequently covered by the engine during WLTC driving cycle, in which those technologies are not enough effective. Additionally, looking at *Figure 5-12*, the maximum benefit that can be obtained by the most complex architecture is 94.8 g/km CO_2. However, this value is still far away from the EU target of 2026 equal to 80 g/km CO_2, although the engine is coupled to a very lightweight vehicle (segment A). This leads to the conclusion that the modern SI engines will not meet the CO_2 target unless their efficiency is strongly improved, especially at low load conditions.

Alternatively, the integration of the engine in a hybrid powertrain has to be considered, so that the ICE more frequently will work in the med/high load region and the above concerns at reduced loads will be less felt. Of course, the combination of the above solutions could enhance the advantages of both, leading to the possibility to fulfill CO_2 emission target.

References

[1] Teodosio, L., De Bellis, V., Bozza, F. Tufano, D., "Numerical Study of the Potential of a Variable Compression Ratio Concept Applied to a Downsized Turbocharged VVA Spark Ignition Engine," SAE Technical Paper, 2017-24-0015, 2017

[2] Bozza, F., De Bellis, V., Teodosio, L., "Potentials of cooled EGR and water injection for knock resistance and fuel consumption improvements of gasoline engines," *Applied Energy*, 169, 112-125, 2017, doi:j.apenergy.2016.01.129.

[3] Bozza, F., De Bellis, V., Giannattasio, P., Teodosio, L., Marchitto, L., "Extension and Validation of a 1D Model Applied to the Analysis of a Water Injected Turbocharged Spark Ignited Engine at High Loads and over a WLTP Driving Cycle*," SAE International Journal of Engines*, 2141-2153, 2017, doi:jstor.org/stable/26422601.

[4] Andrae, J., "Comprehensive chemical kinetic modeling of toluene reference fuels oxidation", *Fuel* 2013; 107:740-748, doi:10.1016/j.fuel.2013.01.070.

[5] Bozza, F., De Bellis, V., Minarelli, F. Cacciatore, D., "Knock and Cycle by Cycle Analysis of a High Performance V12 Spark Ignition Engine. Part 2: 1D Combustion and Knock Modeling," *SAE International Journal of Engines*, 8(5), pp.2002-2011, 2015 doi: www.jstor.org/stable/26278098.

[6] De Bellis, V., Teodosio, L., Siano, D., Minarelli, F. et al., "Knock and Cycle by Cycle Analysis of a High Performance V12 Spark Ignition Engine. Part 1: Experimental Data and Correlations Assessment" *SAE International Journal of Engines* 8(5):1993-2001, 2015, doi:10.4271/2015-24-2392.

[7] Corti, E., Moro, D., "Knock Indexes Thresholds Setting Methodology", SAE Technical Paper 2007-01-1508, 2007, doi:10.4271/2007-01-1508.

[8] Metghalchi, M., and Keck, J., "Laminar burning velocity of propane-air mixtures at high temperature and pressure," *Combustion and flame*, 38, pp.143-154, 1980, doi:10.1016/0010-2180(80)90046-2.

[9] Amirante, R., Distaso, E., Tamburrano, P., Reitz, R. D., "Laminar flame speed correlations for methane, ethane, propane and their mixtures, and natural gas and gasoline for spark-ignition engine simulations," *International Journal of Engine Research*, 18(9), 951-970, 2017, doi:10.1177/1468087417720018.

[10] Teodosio, L., Bozza, F., Tufano, D., Giannattasio, P., Distaso, E. Amirante, R., "Impact of the laminar flame speed correlation on the results of a quasi-dimensional combustion model for Spark-Ignition engine," *Energy Procedia*, 148, pp.631-638, 2018, doi: 10.1016/j.egypro.2018.08.151.

[11] De Bellis, V., Bozza, F., Fontanesi, S., Severi, E. et al., "Development of a Phenomenological Turbulence Model through a Hierarchical 1D/3D Approach Applied to a VVA Turbocharged Engine", *SAE International Journal of Engines* 9(1): 506-519, 2016, doi:10.4271/2016-01-0545.

[12] Bozza, F., De Bellis, V., Teodosio, L., "A numerical procedure for the calibration of a turbocharged spark-ignition variable valve actuation engine at part load," *International Journal of Engine Research*, 2016. doi: 10.1177/1468087416674653.

[13] Teodosio L., Tufano D., Bozza F., "Development of a virtual calibration methodology for a downsized SI engine by using advanced valve strategy," *Energy Procedia* 126: 923-930, 2017, doi: 10.1016/j.egypro.2017.08.164.

[14] Castagné, M., Bentolila, Y., Chaudoye, F., Hallé, A., Nicolas, F. Sinoquet, D., "Comparison of engine calibration methods based on design of experiments (doe)," *Oil & Gas Science and Technology-Revue de l'IFP*, 63(4), pp.563-582, 2008, doi:org/10.2516/ogst:2008029.

[15] Tomazic D., Kleeberg, H., Bowyer, S., Dohmen, J., Wittek, K, Haake, B., "Two-Stage Variable Compression Ratio (VCR) System to Increase Efficiency in Gasoline Powertrains," DEER Conference 2012, Dearborn, October 16th, 2012.

[16] Grandin, B., Angström, H., "Replacing Fuel Enrichment in a Turbo Charged SI Engine: Lean Burn or Cooled EGR," SAE Technical Paper 1999-01-3505, 1999, doi: 10.4271/1999-01-3505.

[17] Bozza, F., De Bellis, V., Teodosio, L., Tufano, D. Malfi, E., "Techniques for CO_2 emission reduction over a WLTC. A numerical comparison of increased compression ratio, cooled EGR and water injection," SAE Technical Paper, 2018-37-0008, 2018, doi:10.4271/2018-37-0008.

[18] https://www.vehicle-certification-agency.gov.uk/fcb/wltp.asp

[19] Thewes, M., Baumgarten, H., Dohmen, J., Uhlmann, T. et al., "Gasoline Combustion Systems Beyond 2020", Proceeding of the 23rd Aachen Colloquium Automobile and Engine Technology 2014, pag. 267-292, Aachen, 2014.

[20] Francqueville, L., Michel, J., "On the Effects of EGR on Spark-Ignited Gasoline Combustion at High Load", *SAE Intenational Jorunal of Engines* 7(4):2014, doi:10.4271/2014-01-2628.

[21] Wittek, K., Tiemann, C., Pischinger, S., "Two-Stage Variable Compression Ratio with Eccentric Piston Pin and Exploitation of Crank Train Forces," *SAE Intenational Jorunal of Engines* 2(1):1304-1313, 2009, doi:10.4271/2009-01-1457.

6. Midterm solution - Innovative ultra-lean pre-chamber SI engine

The midterms solution investigated in this PhD thesis is an innovative ultra-lean pre-chamber SI engine, suitable for hybrid powertrain. As well as for the conventional SI engine, the aim of this analysis is the estimation of the CO_2 along the WLTC, coming from the combination of a high-efficient engine with a hybrid architecture.

The engine under study is a prototype four-cylinder SI engine, equipped with an active pre-chamber ignition system. Its main features, listed in Table 6.1, were defined by the two EAGLE partners, IFPEN and Renault SA (RSA). The pre-chamber has four orifices connecting it to the main chamber. Each cylinder presents two exhaust and intake valves. A VVT system allows to modify the intake camshaft, on the base of the Miller concept [1]. The engine is fed with liquid gasoline through four port fuel injectors just upstream the intake valves, and four direct injectors located into each PC.

Table 6.1 Multi-cylinder equipped with PCSP main features.

Multi-cylinder pre-chamber engine	
Bore, mm	76
Stroke, mm	90
Displacement, cm^3	1633
Peak pressure limit, bar	180
Geometrical compression ratio	15.8 (including PC volume)
Fuel in main-chamber	PFI injector, gasoline RON 95
Fuel in pre-chamber	DI injector, gasoline RON 95
Pre-chamber volume mm^3	~ 1000
$V_{pre\text{-}chamber}$ / V_{TDC}	~ 3 %
Pre-chamber holes	4 - two pairs of different hole size
$A_{jet\ holes}$ / $V_{pre\text{-}chamber}$, cm^{-1}	~ 0.03
Intake Valve Opening Range (IVO)	3/48 CAD BTDC (@0.2 mm lift)
Exhaust Valve Closure (EVC)	19 CAD ATDC (@0.2 mm lift)
Start of Port Fuel Injection	140 CAD BTDC
Start of Direct Injection inside PC	300 CAD BTDC

A two-stage boosting system is required to achieve the prescribed load under ultra-lean conditions. In particular, a Low-Pressure Compressor (LPC) is connected to a variable geometry Low-Pressure Turbine (LPT) and a High-Pressure (HP) compressor (E-Comp) is driven by an Electric Motor (EM).

The above engine will drive a HEV, belonging to the C segment, whose main characteristics are listed in *Table 6.2,* according to RSA indication. It presents a combined parallel/series powertrain composed of an ICE, two Electric Motor/Generator units, (EM and EG), a battery (Ba), three clutches (Cl_{1-3}) and two Gear-Boxes (GB_{1-2}). This architecture favours a very flexible control of its components, thanks to the presence the clutches. Moreover, they contribute to minimize the mechanical losses when one of the motors is not used, avoiding load-less operations. A PHEV version has been analysed too, having the same features of the HEV, but with a higher battery capacity of 5 kWh.

Table 6.2. Hybrid vehicle main features

HEV		
Vehicle	Mass, kg	1730
	Car aero drag, m^2	0.775
	Tire rolling resistance, kg/t	8
	Wheel diameter, m	0.723
	Axle ratio, -	4.4
	Axle inertia, kg*m^2	1.5
Internal Combustion Engine	Displacement, cm^3	1633
	Max Power, kW	125
	Inertia, kg*m^2	0.35
Electric Motor	Max Power, kW	55
	Max Torque, Nm	165
	Inertia, kg*m^2	0.10
Electric Generator	Max Power, kW	50
	Max Torque, Nm	240
	Inertia, kg*m^2	0.10
Battery	Internal Resistance, Ohm	0.375
	Voltage, Volt	400.0
	Energy density, Wh/kg	170.00
	Usable battery sizing, kWh	0.50/5
	SOC limits, -	0.2-0.9
Gear Box_1	Gear 1 Ratio, -	2.72
	Gear 2 Ratio, -	1.64
	Gear 3 Ratio, -	0.99
	Gear 4 Ratio, -	0.6.
Gear Box_2	Gear 1 Ratio, -	2.76
	Gear 2 Ratio, -	1.03

Also in this case, the research activity followed the main steps reported in *Figure 1-4,* as summarized in this chapter. Firstly, a 1D model development and validation is described in detail, with reference to a preliminary single-cylinder thermal unit (SCE).

The model reliability is tested against the experimental data collected on the SCE in different engine architectures and operating conditions. The SCE, in fact, is equipped with either an active or passive pre-chamber.

A Conventional Spark Plug (CSP) ignition system is also considered as a reference. 39 experimental points are investigated, with the aim to evaluate the model sensitivity to the PC configuration, fuel type, engine speed and relative air/fuel ratio (λ) variations.

Secondly, the Multi-Cylinder Engine (MCE) model and the numerical RB calibration procedure is detailed. Due to the lack of measurements, the MCE model accuracy is simply claimed, based on the SCE results. Concerning the RB calibration procedure, its reliability, like the conventional SI engine in the previous section, is verified against a multi-purpose optimizer. Subsequentially, the performance maps are shown, highlighting the advantages of the lean-combustion concept.

Finally, the hybrid vehicle (HEV/PHEV) simulations are performed using both PMP and ETESS strategy to properly define the CO_2 emission along the WLTC.

6.1. Single cylinder engine description and experimental setup [2]

In this chapter the experimental campaign performed by two partners of the EAGLE project, FEV/VKA will be briefly described. In particular it was done at the Institute for Combustion Engines (VKA) of the RWTH Aachen University, more details of the layout process can be found in [2]. Differently from the MCE, the SCE is equipped with a direct fuel injection inside the main-chamber. The *Table 6.3* lists the major SCE specifications. The long stroke of 90.5 mm, combined with the arrangement of the valves with the intake port and the combustion chamber shape, allows the SCE to obtain a charge motion level comparable to state-of-the-art series production turbocharged engines. In *Figure 6-1*, the SCE design it reported, for which the pre-chamber is equipped with 4 CFD optimized holes, and a 350 bar DI fuel injection system. An ignition module is integrated in the cylinder head and the combustion chamber is designed based on the size of a generally used M12 spark plug. Thus, the 12 mm outer diameter of the pre-chamber shaft perfectly fits into the defined combustion chamber geometry.

As already stated, the prototype SCE has three different configurations: Conventional Spark Plug (CSP), active or passive pre-chamber. The CSP operation is achieved equipping the engine head with an adapter, instead of the pre-chamber, realizing the conventional engine design with undivided combustion chamber. This design reproduces a conventional SI engine architecture with spark plug and allows an easy replacement with different pre-chambers geometries. For both pre-chamber and conventional SI operation, a single electrode M10 spark plug with a heat value of 8 has been used.

Table 6.3 Single cylinder PCSP engine features from [2],[3],[4].

Single-cylinder pre-chamber engine	
Bore, mm	75
Stroke, mm	90.5
Stroke / Bore Ratio	1.207
Displacement, cm^3	399
Peak pressure capability, bar	170
Geometrical compression ratio	13
Injection system	Lateral solenoid, 350 bar
Fuel in main-chamber	DI injector, gasoline RON 98
Fuel in pre-chamber	DI injector (CNG or H_2)
Pre-chamber volume mm^3	1080
$V_{pre\text{-}chamber}$ / V_{TDC}	3.6 %
Pre-chamber holes	4 - two pairs of different hole size
$A_{jet\ holes}$ / $V_{pre\text{-}chamber}$, cm^{-1}	0.033
Intake valve opening	3 CAD BTDC (@1mm lift)
Exhaust valve closure	3 CAD ATDC (@1mm lift)
Start of injection MC	295 CAD BTDC
Start of injection PC	180-215 CAD BTDC

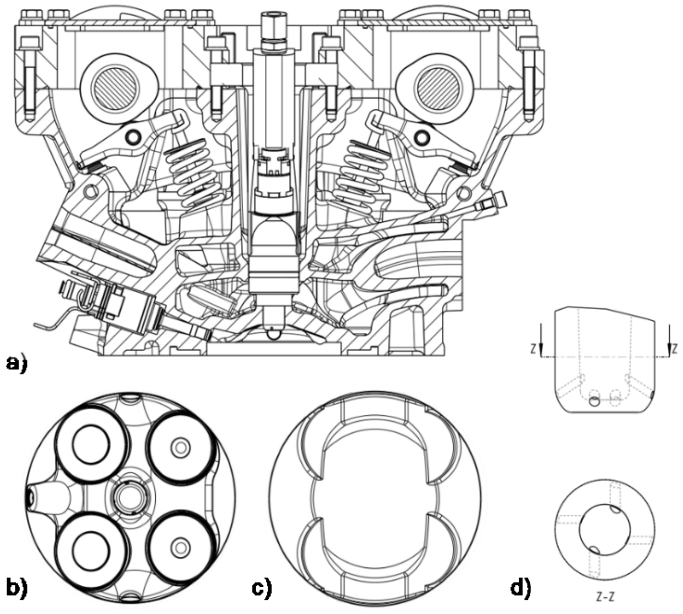

Figure 6-1 PCSP engine layout: a) sectional view of cylinder head b) combustion chamber dome c) piston crown for CR=13, d) pre-chamber from [2],[3],[4].

The pre-chamber can be fed by CNG or hydrogen from pressure bottles. In the case of the CNG, the injection pressure is between 4.5-8 bar, depending on the desired mass flow rate. Whereas, for the hydrogen, a higher pressure is set (about 20 bar). In passive conditions, the pre-chamber injection is simply switched off. Hence, the same pre-chamber geometry is used in either active or passive mode.

Considering the environmental condition, the intake air is conditioned to 30 °C in the intake runner. The pressure in the intake is always fixed equal to the one in the exhaust manifold. Both of course increase at higher relative air-fuel ratio, obtained by the formula of Spindt [5]. The share of the employed fuels (CNG, H_2 and gasoline) is taken into account to establish the correct air/fuel ratio.

Concerning the experimental set-up, the Spark Advance (SA) is chosen to realize an optimal combustion phasing, namely an angular position of the 50% of the Mass Fraction Burned (MFB_{50}) at 7-8 CAD AFTDC. If knocking combustions are detected, the SA is properly retarded. Pressure measurements are carried out with the equipment listed below:

1. two Kistler A6045 B pressure transducers are flush-mounted in the combustion chamber side roof;
2. one Kistler 6054 BR pressure transducer is flush mounted in the pre-chamber;
3. signal sampling is performed via Kistler charge amplifiers and a FEV combustion analysis system at a resolution of 0.1 CAD;
4. for the dynamic intake and exhaust gas pressures, Kistler 4045 A5 pressure transducers are chosen and data are sampled with a resolution of 1 CAD.

For the measurement of the static pressures and temperatures, conventional pressure transducers and thermocouples are adopted (measurement averaging interval: 30 s). Oil and water conditioning systems enable steady-state operations.

With the aim of developing and validating the model, 39 different operating points, listed in *Table 6.4*, are investigated. Different λ sweeps at constant load have been performed at various engine speeds. In particular, for each operating point, 500 consecutive cycles are recorded, and an ensemble average of these cycles is examined for the model comparison. All the operating points have shown a satisfactory stability with a CoV of the IMEP lower than 1-2% even with very lean combustion. The available experimental database gave the possibility to validate the model predictive potential at changing mixture composition (from stoichiometric to very lean) and turbulence levels.

Table 6.4 List of investigated points of the PCSP engine [2]

Case	**Operating condition rpm @ IMEP**	**Engine**	**λ**	**SA** CAD AFTDC	**MFB_{50}** CAD AFTDC
1	2000 rpm @ 15 bar	CSP	1.0	2.1	23.3
2		CSP	1.2	0.8	25.5
3		CSP	1.4	-4.5	22.1
4		CSP	1.6	-8.8	21.2
5	2000 rpm @ 15 bar	PASSIVE	1.0	11.7	29.1
6		PASSIVE	1.4	2.7	24.1
7	4000 rpm @ 15 bar	PASSIVE	1.0	3.6	20.1
8		PASSIVE	1.4	-3.4	17.6
9	2000 rpm @ 3 bar	CNG	1.6	-15.8	8.6
10	2000 rpm @ 4 bar	CNG	1.0	-11.3	8.1
11		CNG	1.4	-10.8	7.5
12		CNG	1.8	-17.6	7.9
13	2000 rpm @ 10 bar	CNG	1.0	2.3	17.1
14		CNG	1.5	-7.6	7.7
15		CNG	2.0	-16.4	7.1
16	2000 rpm @ 15 bar	CNG	1.0	14.9	33.2
17		CNG	1.4	6.8	25.6
18		CNG	1.8	-3.4	16.7
19		CNG	2.0	-7.5	14.2
20		CNG	2.4	-17.2	9.8
21	2500 rpm@ 12 bar	CNG	1.0	4.0	21.7
22		CNG	1.4	-2.6	15.8
23		CNG	1.8	-13.2	7.78
24		CNG	2.0	-16.4	7.7
25		CNG	2.2	-23.0	7.9
26	2500 rpm @ 6 bar	CNG	2.0	-21.3	7.50
27	3000 rpm @ 13 bar	CNG	1.0	5.8	23.6
28		CNG	1.4	0.3	20.3
29		CNG	1.8	-12.2	9.1
30		CNG	2.0	-16.9	7.8
31		CNG	2.2	-21.0	7.8
32	3000 rpm @ 7 bar	CNG	2.0	-22.7	7.4
33	4000 rpm @ 16 bar	CNG	1.0	11.4	33.7
34		CNG	1.4	5.7	32.2
35		CNG	1.6	2.3	35.2
36	2000 rpm @ 15 bar	H_2	1.4	11.9	29.7
37		H_2	1.8	1.9	20.2
38		H_2	2.0	-4.1	13.8
39		H_2	2.4	-15.7	7.9

6.2. Engine model validation

Consistently with the experimental setup, a detailed 0D/1D scheme is developed for all the investigated engine architectures (conventional and PC engine, both active and passive) in a commercial modelling framework. The description of the flow inside the intake and the exhaust pipes is based on a 1D simulation approach, whereas the previously described phenomenological 0D sub-models are used to reproduce in-cylinder phenomena inside the pre-chamber engine.

Hence, the combustion evolution is handled by the re-assessed quasi-dimensional fractal model to take into account the turbulent jets propagation. Since the engine can be fed with three fuels, different laminar flame speed correlations S_L are embedded in the code. In the MC, a simulation-derived correlation for a TRF gasoline blend is utilized in all the tested operating points [6]. The same formulation is also applied for the passive PC. For the active pre-chamber, the correlations proposed in [7] and [8] are employed for the combustion of CNG and H_2, respectively. However, it must be considered that, due to the mass exchanges, some fuel blending may occur in an active pre-chamber. For this reason, the employment of pure-fuel correlations does not perfectly hold for the actual operation of this engine. However, fuel blending effect on S_L is not taken into account in the model.

For the model closure, the phenomenological K-k-T turbulence model described in the chapter 3 is applied to both chambers, including the turbulence production due to incoming flow through the orifices. A Hohenberg-like correlation is employed for the heat transfer in the pre- and main-chamber [9], neglecting the heat losses in the PC holes. Some preliminary comparisons are performed with 3D CFD results provided by IFP Energies Nouvelles (IFPEN), for a similar pre-chamber engine. A single operating point was available at 3000rpm@13bar IMEP, with an average relative air/fuel ratio of 1.8. The pre-chamber is directly fed with a commercial gasoline, whereas a homogenous premixed charge is supplied through the inlet port in the MC. More details on the 3D analysis can be found in [10].

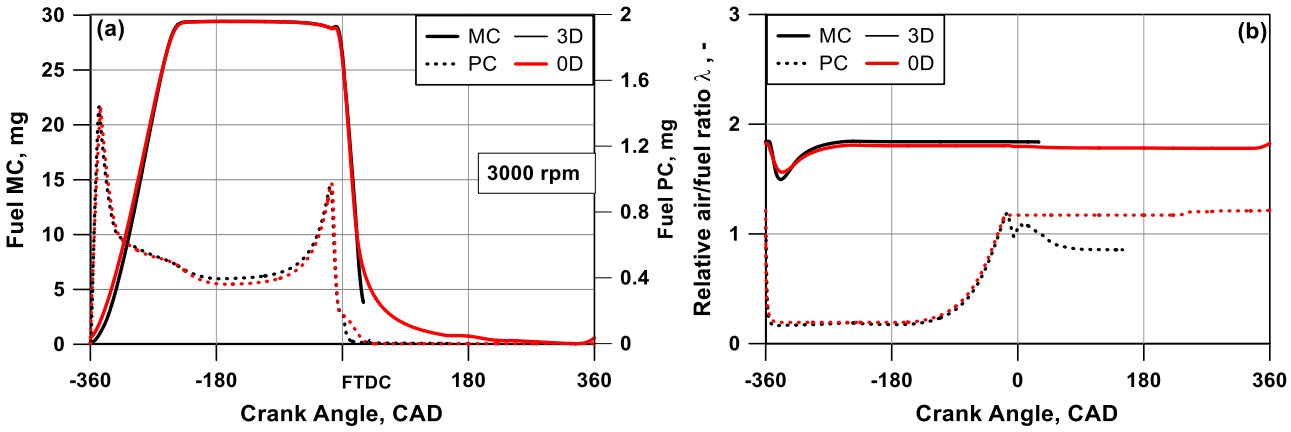

Figure 6-2 0D/3D comparison of fuel mass (a) and λ (b) in PC and MC at 3000rpm@13bar, λ=1.8.

Firstly, the ability of the 1D in reproducing the mass exchange is analyzed. In *Figure 6-2*, the fuel in both the chambers and the related air/fuel ratio are reported as a function of the crank angle. The agreement is quite satisfactory, denoting the ability of the model to properly sense the mass flux through the orifice, and the related variations in composition. In particular, looking at *Figure 6-2a*, the sudden increment of the fuel mass due to the in-PC injection during the intake phase is well captured by the model, and the subsequent decrement due to outflow in the MC, as well. Near the TDC, the fuel mass increases again in the PC, since the pressure gradient between the two chambers pushes the fresh charge within the PC. As expected the MC is less sensitive mass exchange, even if a λ decrement is visible around -340 CAD due to the injection in the PC, *Figure 6-2b.* The good agreement in terms of both fuel mass and relative air/fuel ratio implies that also the trapped air in the cylinder is correctly estimated. This activity allowed to mainly tune the k-K-T model, according to the 3D results, as shown in *Figure 6-3*. The model tuning gave the possibility to follow the 3D profiles of the turbulence intensity and integral length scale along the entire engine cycle with satisfactory accuracy, in both the chambers.

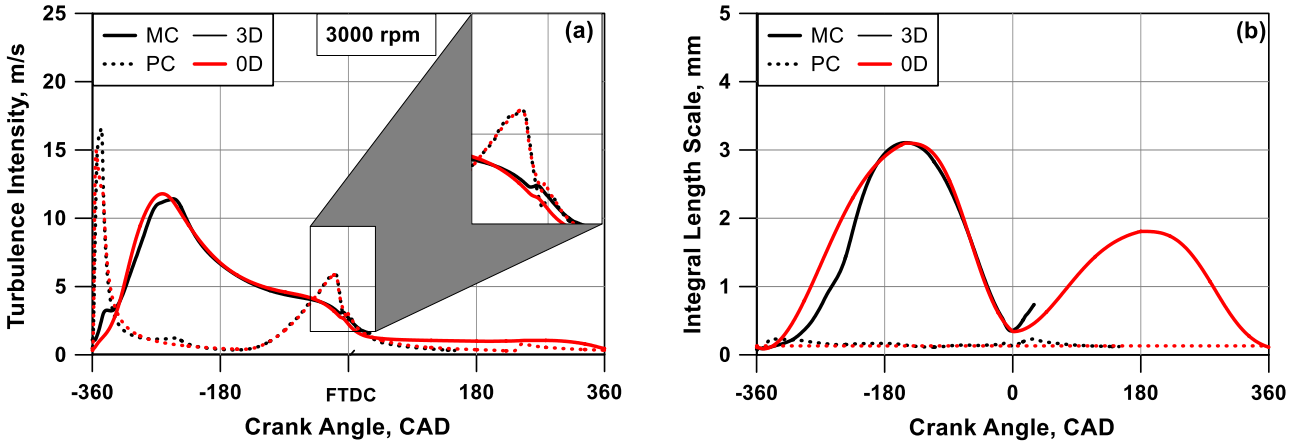

Figure 6-3 0D/3D comparison of turbulence intensity (a) and integral length scale(b) in PC and MC at 3000rpm@13bar, λ=1.8.

The identified turbulence tuning constants are then borrowed in the 1D model of the tested engine, for the subsequent combustion model tuning and validation. In particular, this is done by comparing the simulation predictions with the experimental findings for all the operating points listed in *Table 6.4*. To get the maximum experimental/numerical congruence, the same boundary conditions as in the experiments have been assigned in the simulations, namely the spark timing, intake and exhaust pressures and temperatures, and the injected fuel masses.

Using a trial-and-error procedure, a single set of tuning constants has been identified, determining the lowest average experiment/simulation error for all the investigated configurations, especially with regard to the pressure cycles in both PC and MC.

In the following the results of the model validation is deeply discussed. In a first stage, the global performance through a numerical/experimental [2] comparison, including the Root Mean Squared Error (RMSE) as a global indicator of the model accuracy are analyzed.

The first comparison concerns the air flow rate, depicted in *Figure 6-4*, denoting a satisfactorily prediction, since all the investigated points are within an error band ± 5%. The related RMSE of 1.92 kg/h proves that an accurate schematization of the intake and exhaust pipe geometry and a proper specification of the valve flow coefficients has been done. The IMEP values, illustrated in *Figure 6-4*, remains in most cases in the allowable error band of ± 5%, indicating again a good agreement with the experimental data.

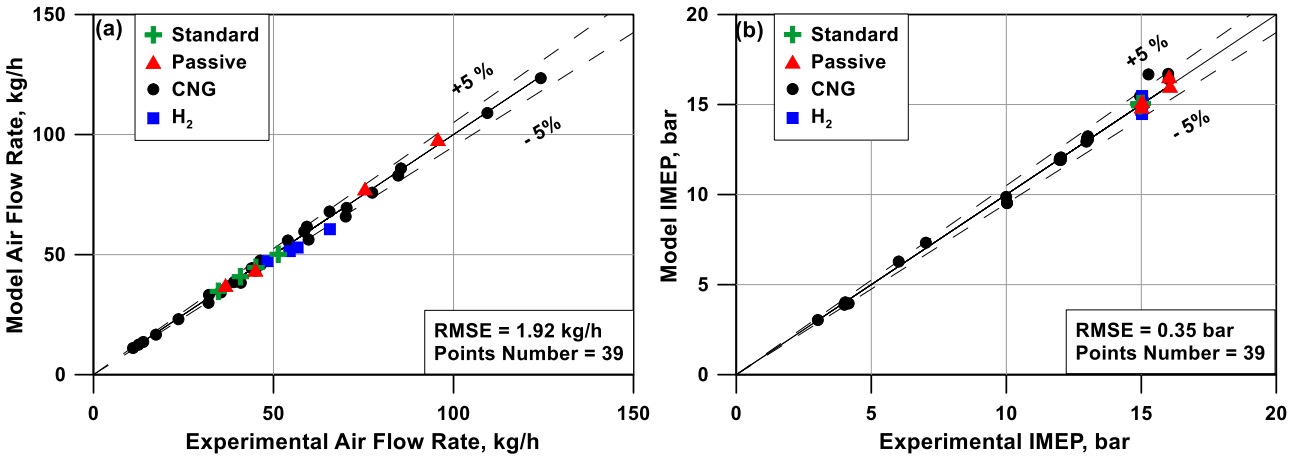

Figure 6-4. Experimental vs. numerical air flow rate (a), IMEP (b) comparisons [4].

On the contrary, the exhaust temperature reported in Figure *6-5*, is affected by a certain systematic overestimation, with a RMSE of around 56.4 K. The underestimation of the heat exchange in the cylinders or in the exhaust pipes could be a possible reason.

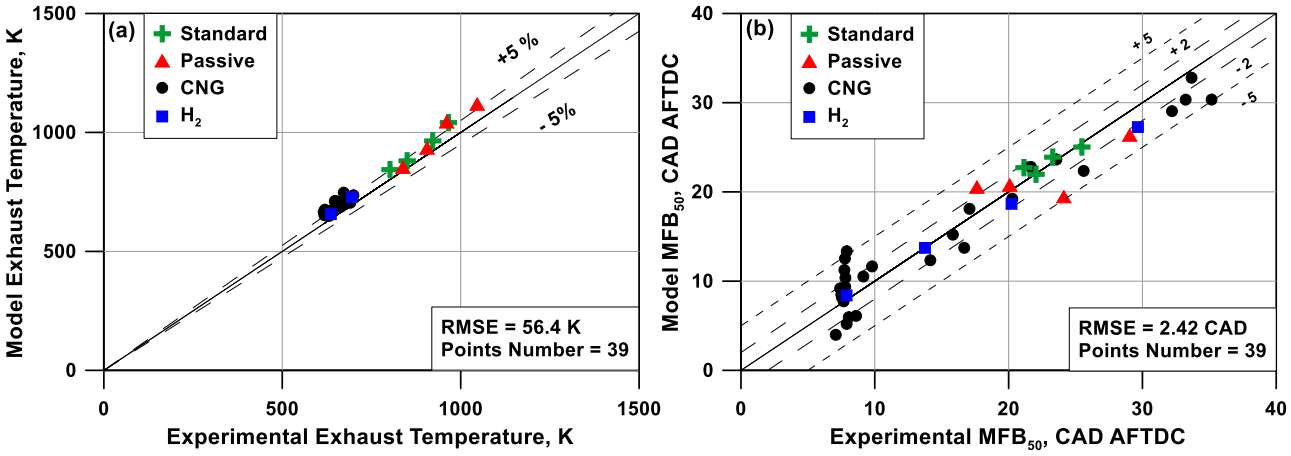

Figure 6-5. Experimental vs numerical exhaust temperature (a), MFB_{50} (b) comparison [4].

Concerning the combustion phasing, the MFB_{50} is analyzed as a measure of the overall combustion model reliability, since the spark timing is imposed in the simulation. A satisfactory model accuracy is visible in Figure *6-5* showing an error within a ± 5 CAD band in most cases, and an average of 2.42 CAD. A further analysis in terms of combustion phasing and duration in both PC and MC is reported in *Figure 6-6*, confirming the high reliability of the model. The peak location estimation appears better in the PC (RMSE equal to 2.09 CAD) than the MC case (RMSE equal to 2.83 CAD). Indeed, in the latter case, the combustion prediction is more complex, due to its dependence on the on the superimposition of various effects (combustion processes in both PC and MC).

On the other side, in the PC, the results are more directly related to the spark timing, which is an imposed datum. Moreover, the air/fuel ratio in the PC is almost stoichiometric for all of the considered operating conditions, while it widely changes in the MC among the different tested cases.

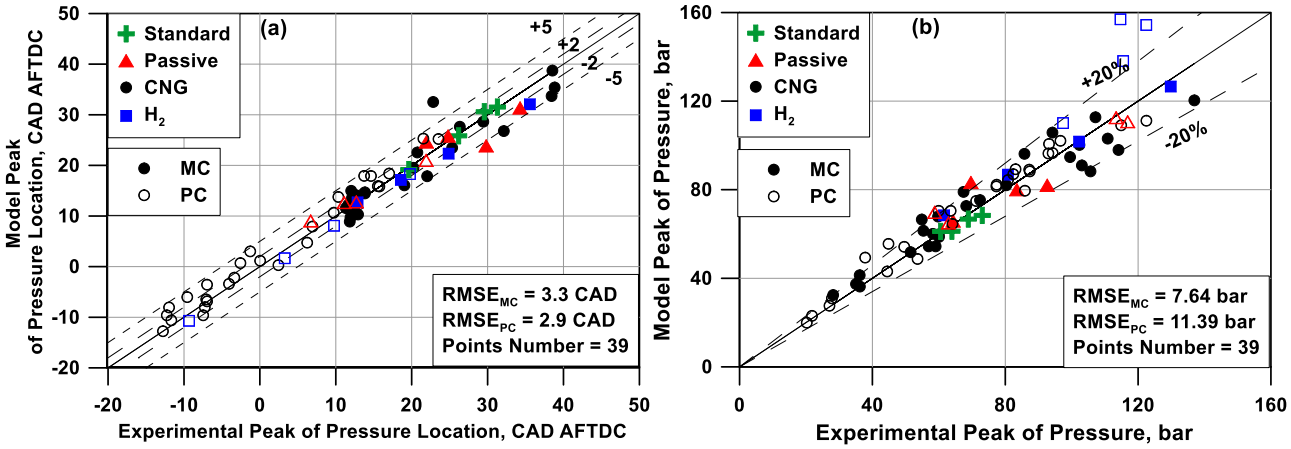

Figure 6-6. Experimental vs numerical angle of pressure peak(a) pressure peak (b) for both MC and PC (a) [4].

A further global verification of the combustion model is reported in *Figure* 6-7, showing the angular positions of representative combustion stages (spark event and 10%, 50% as well as 90% of MFB) for different air/fuel ratio. These trends concern all the investigated engine architectures for a representative low speed / high load operating point (2000 rpm @ 15 bar IMEP). An overall good model accuracy is visible for the considered architecture in all the combustion phasing. However, for the pre-chamber device (both active and passive modes), a certain underestimation of the combustion duration for the cases at reduced λ is present. As expected, increasing λ, a combustion slow-down is evident (more prominent for the CSP configuration). This behavior is compensated for the pre-chamber architecture by the effect of the turbulent jets emerging from the PC, above all for the active version. Both these trends are well captured by the model and an overestimation of the combustion duration only occurs at the leanest air/fuel mixtures for the CNG case.

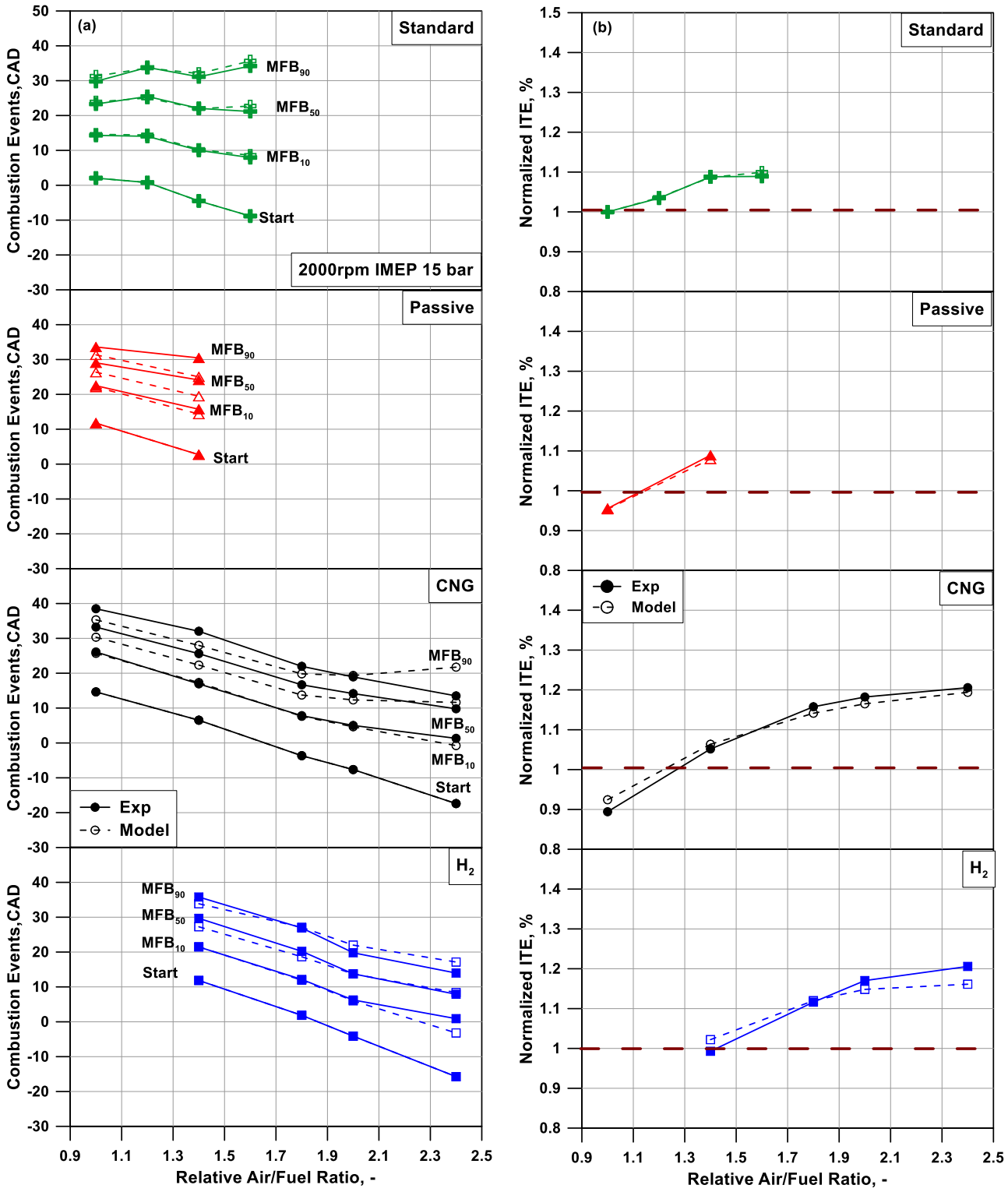

Figure 6-7 Experimental vs numerical angles of significant combustion stages (Spark, MFB_{10}, MFB_{50}, MFB_{90}) (a) and of the normalized ITE (b) as a function of the relative air/fuel ratio for different engine architectures at 2000 rpm @ 15 bar IMEP [4].

The final check of the simulation reliability is reported in *Figure 6-7 right*, through an experimental/numerical comparisons of the Indicated Thermal Efficiency (ITE) for all the tested variants at 2000 rpm@15 bar IMEP. All the data are normalized by the efficiency of the conventional engine under stoichiometric operation, due to confidentiality reason.

Also, here the model well captures the efficiency improvement which is achievable with leaner air/fuel rates, for all the considered ignition devices. However, the mentioned advantages are rather limited in CSP and passive variants, due to the excessively high IMEP CoV and misfires, that limits the lean operation at λ equal to 1.5-1.6. This limit is indeed extended up to 2.4 by the active pre-chamber, fueled with either CNG or H_2, reaching a maximum improvement of 20% to the respect of CSP in stoichiometric conditions. Another interesting outcome is that a conventional ignition device is preferable in terms of efficiency if the engine works with a stoichiometric or slightly lean air/fuel mixture. With λ values greater than 1.1, a pre-chamber system becomes indeed better from the ITE viewpoint, and the advantages constantly rise with increasing air/fuel ratio. The model, as stated above, demonstrates to capture this behavior with adequate accuracy.The combustion model reliability is further tested through the experimental / numerical comparisons of the pressure traces and of the related burn rates, shown in *Figure 6-8, Figure 6-9*, and *Figure* 6-10, for 15 representative cases. In the reported figures, the experimental (numerical) data are represented with black (red) curves, continuous or dashed for the MC or PC, respectively.

Concerning the conventional engine configuration a λ sweep at 2000rpm@15 bar IMEP is reported in *Figure* 6-8, denoting a quite satisfactory agreement for both pressure traces and burning rate. The experimental / numerical accuracy slightly worsens at increasing λ, probably because of a reduced sensitivity of the adopted laminar flame speed correlation to the air/fuel ratio.

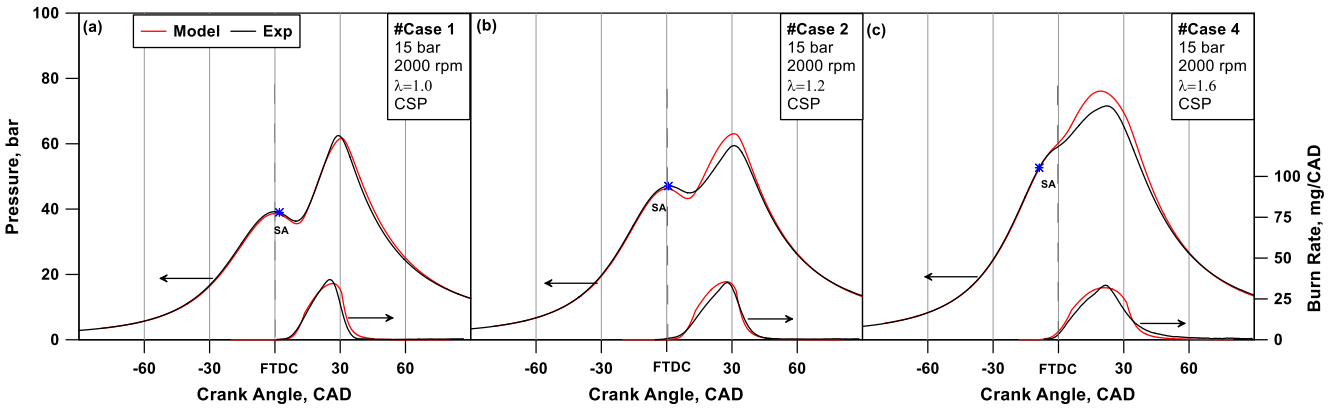

Figure 6-8 Experimental vs. numerical comparison of cylinder pressure traces and burn rates at 2000 rpm@15 bar IMEP for a CSP engine configuration, (a) λ=1.0, (b) λ=1.2, (c) λ=1.6 [4].

In *Figure 6-9,* three different operating variants with the PC configuration (CNG and H_2 injection as well as no injection) are compared at 2000rpm@15 bar IMEP in each case for the minimum/maximum leaning of the air/fuel ratio. Comparing the right and left of *Figure 6-9*, it is visible an increment of the boost pressure since it is the only possible way to gain the prescribed load with lean mixtures.

During the compression phases, the model well reproduces the gap between PC and MC pressure traces, thanks to a proper selection of the PC hole discharge coefficient. Concerning the combustion development, the model is able to properly sense the different fuels injected in the PC, detecting the maximum (minimum) burning speeds in the PC for H_2 (passive) mode. An intermediate behavior emerges for CNG PC fueling. The pressure peaks in both main- and pre-chamber are rather well predicted in most cases. In H_2 operation, the model generally overestimates the PC burning speed due to probably the absence of fuel blending coming from the main chamber. In some cases (#20 and #39), the numerical burning rate in the MC has lower peaks than the experimental datum, compensated by a faster burning rate at the combustion beginning.

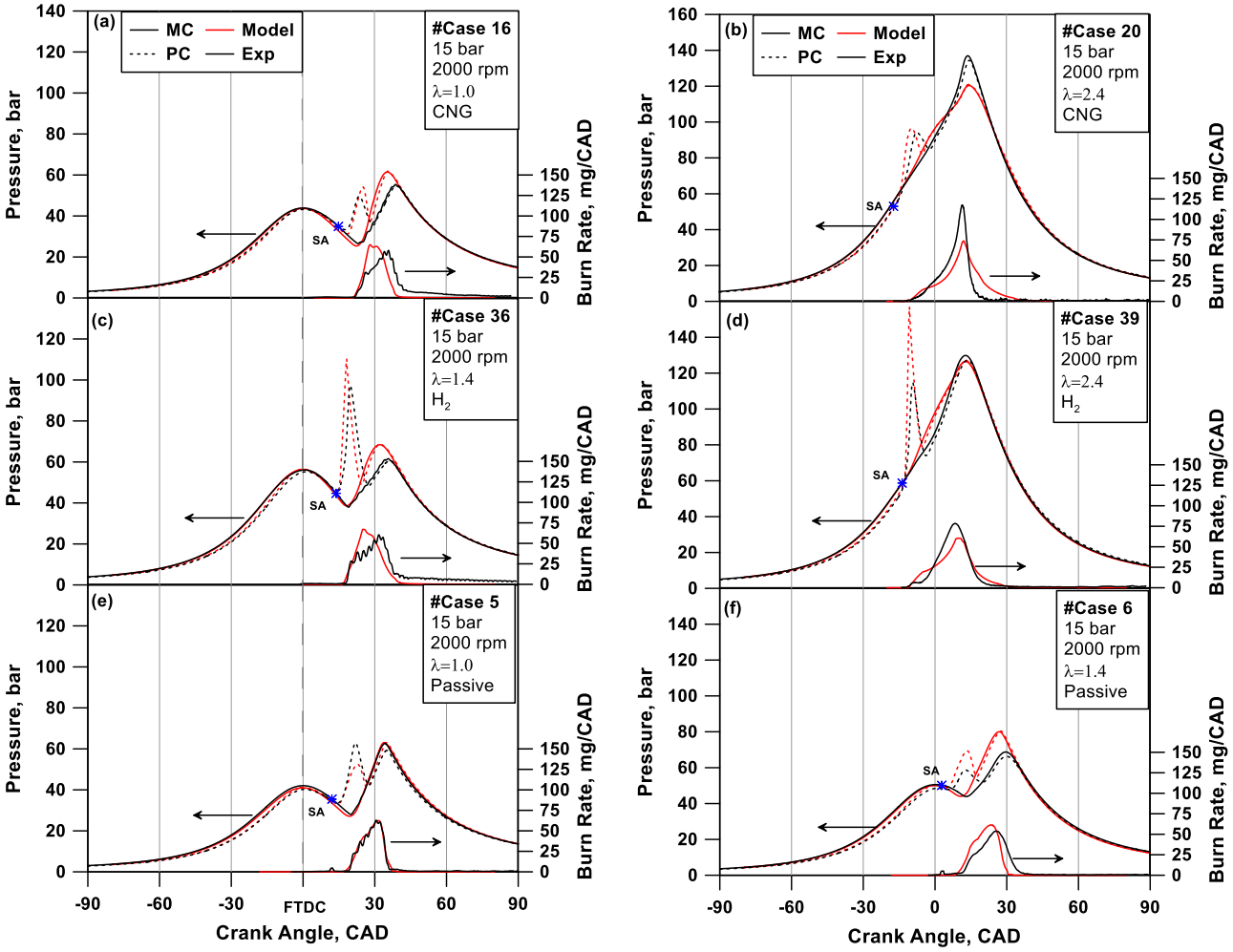

Figure 6-9 Experimental vs. numerical comparison of cylinder pressure traces and burn rates at 2000 rpm@15 bar IMEP, (a) λ=1.0 CNG (b) λ=2.4 CNG, (c) λ=1.4 H_2 (d) λ=2.4 H_2, (e) λ=1 passive (f) λ=1.4 passive [4].

Two additional experimental / numerical comparisons are reported to deeper investigate the model sensitivity regarding air/fuel proportion variations and the its capability at low load operating condition. The assessment, reported in *Figure 6-10*, shows a pressure trends predicted quite well in terms of global shape, phasing and location of the peaks in both MC and PC.

In some cases, at medium loads (operating points # 26 and # 32), the PC pressure peak is overestimated, probably due to an incorrect simulation of the pre-chamber scavenging under these operating conditions. All the results reported in this section in terms of global performance parameters and combustion events demonstrate the consistency and reliability of the proposed numerical approach, considering the relevant range of operating conditions (speed, load and air/fuel ratio).

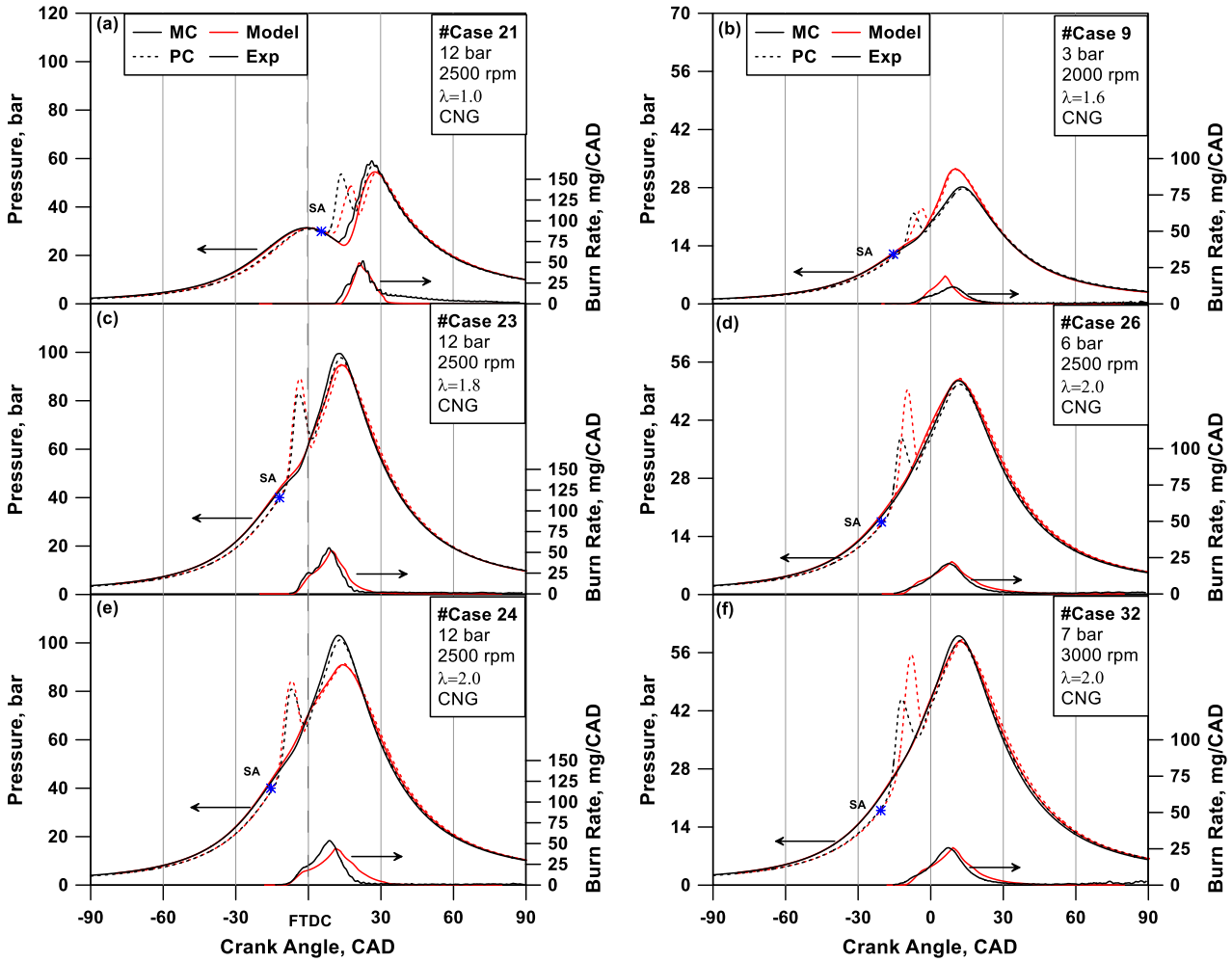

Figure 6-10 Experimental/numerical comparison of cylinder pressure traces and burn rates for CNG configuration with (a) λ=1.0, (b) λ=1.4, (c) λ=2.0 at 2500 rpm@12 bar IMEP and at low load with (d) λ=1.6 2000 rpm @3bar, (e) λ=2.0 2500rpm@6bar, (f) λ=2.0 3000rpm@7bar IMEP [4].

Subsequently to this engine model validation phase, the pre-chamber engine features, listed in *Table 6.3*, were slightly modified according to the prototype four-cylinder engine, reported in *Table 6.1*.

Table 6.5 List of the investigated points of SCE PCSP at IFPEN.

SCE PCSP 3000 rpm 13 bar IMEP

	#1	#2	#3	#4	#5	#6	#7	#8	#9	#10	#11	#12
λ	1.01	1.12	1.26	1.44	1.55	1.61	1.66	1.75	1.81	2.00	2.09	2.14

In this new configuration, PC and MC are both fed by RON 95, a higher bore and CR are considered, and a port fuel injector rather than a DI one for the MC is employed. Consequently, the 1D model has been properly re-assessed to take into account the above geometrical modifications. For this SCE an additional experimental campaign was performed at IFPEN, for a fixed load (13 bar IMEP) and speed (3000rpm) with a sweep of air/fuel quality, as reported in *Table 6.5*. Also, in this case, to get the maximum experimental/numerical congruence, the same boundary conditions as in the experiments have been assigned in the simulations, and trial-and-error procedure have been used for setting the tuning constants.

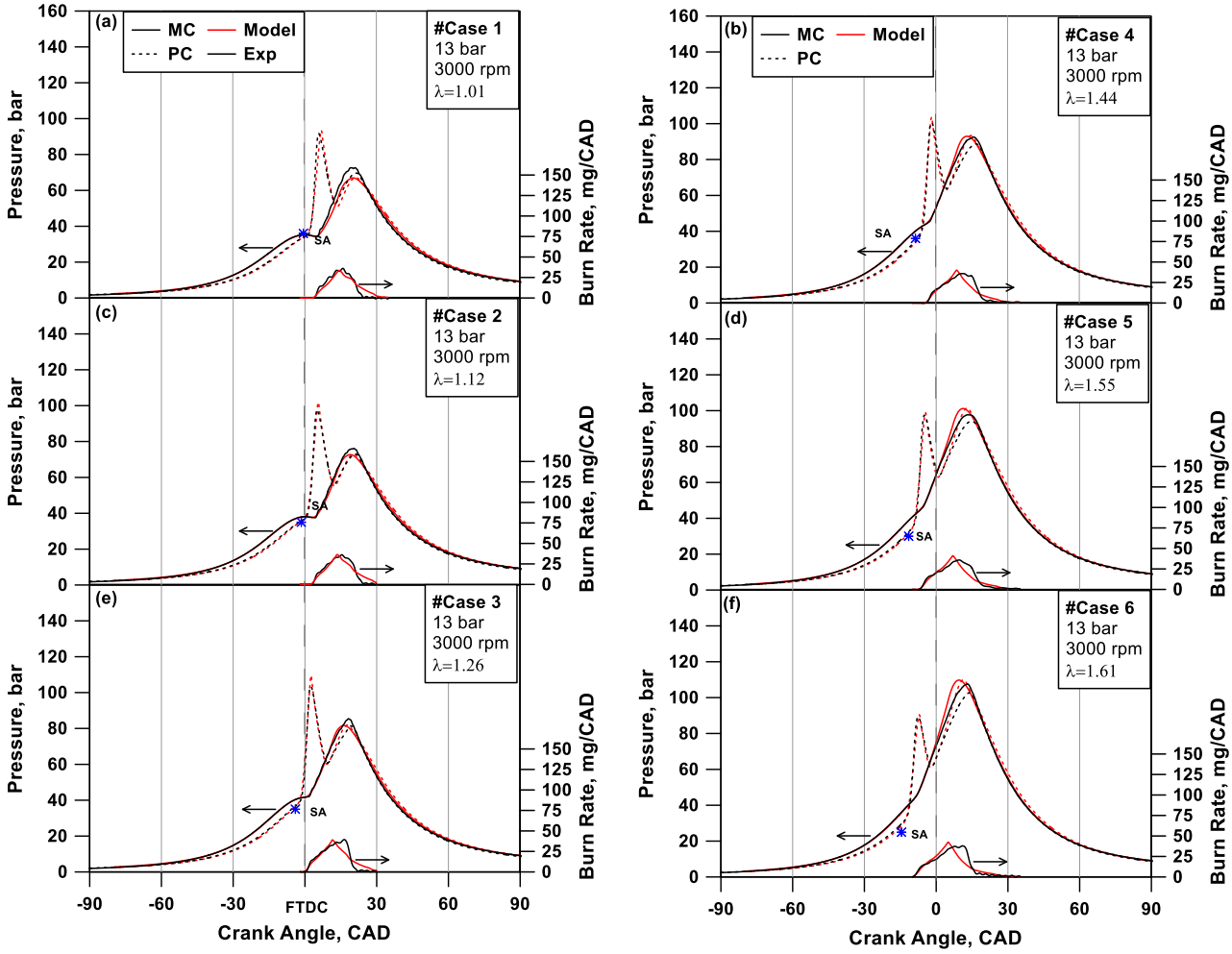

Figure 6-11 Experimental vs. numerical comparison of cylinder pressure traces and burn rates for EAGLE SCE at 3000 rpm@13 bar IMEP (a) λ=1.01, (b) λ=1.44, (c) λ=1.12, (d) λ=1.55, (e) λ=1.26, (f) λ=1.561.

In *Figure 6-11*, *Figure 6-12* the pressure traces for all the investigated points in both MC a PC are reported, denoting a still better matching than the previous SCE. The peak of pressure, its location and the shape in both PC and MC are always very-well captured. It can be noted that increasing the λ leads to more and more advanced SAs, due to the superimposition of a longer combustion duration and a reduced knock tendency.

Consequently, a less intense pressure peak in the PC is reached, since the combustion starts at a lower pressure level. The reason for the better agreement is probably due to the absence of fuel blending, and to the simpler model tuning, since a single speed and load operation is considered.

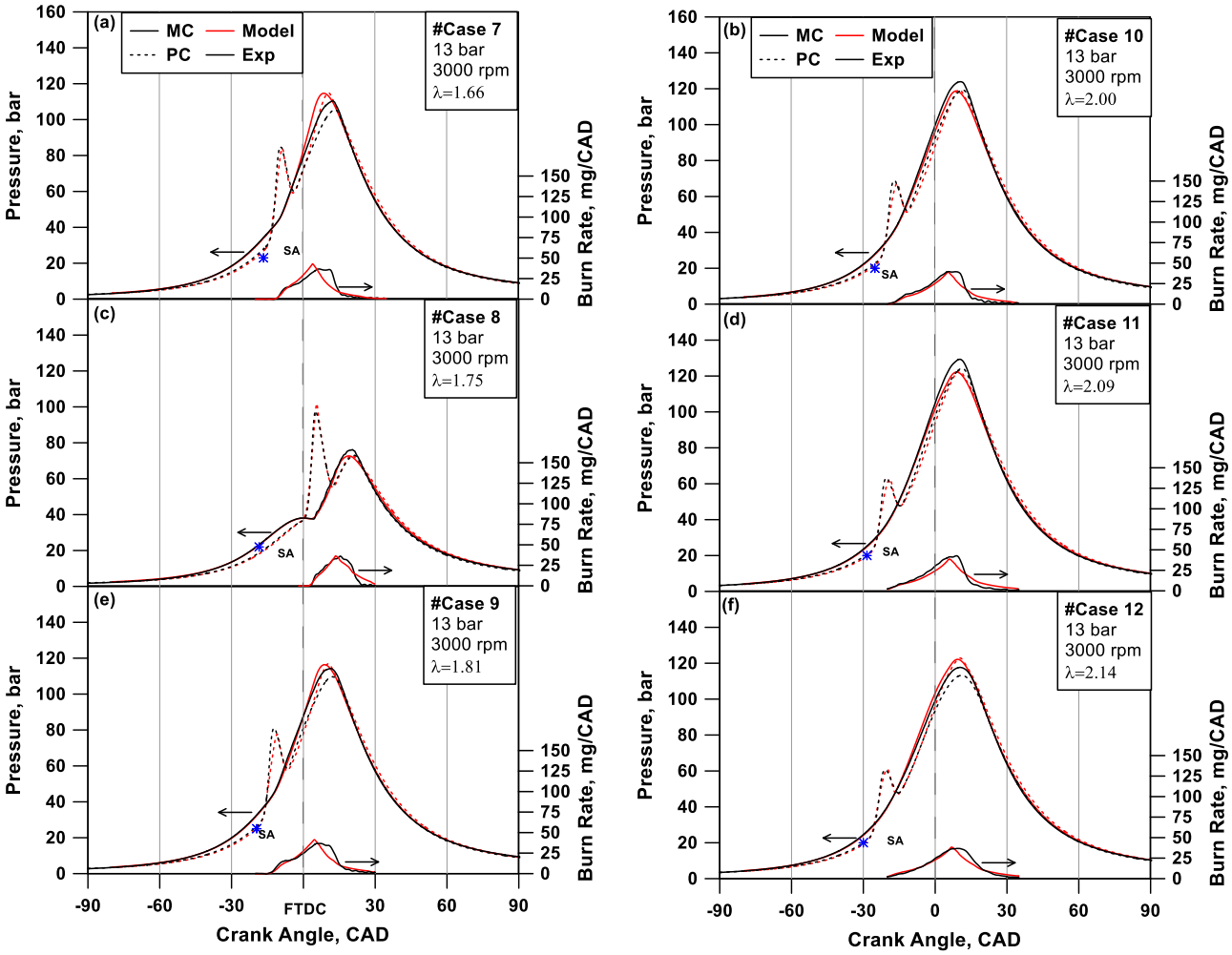

Figure 6-12 Experimental/numerical comparison of cylinder pressure traces and burn rates for EAGLE SCE at 3000 rpm @13 bar IMEP (a) λ=1.66, (b) λ=2.00, (c) λ=1.75, (d) λ=2.09, (e) λ=1.81, (f) λ=2.14.

6.3. Multi-cylinder engine model and calibration

The validated SCE model, with few enhancements, is applied to foresee the complete multi-cylinder engine performance maps. To this aim, a 1D model of the engine with the geometrical characteristic reported in *Table 6.1*, is developed.

The pipe network is modelled through a 1D approach, whereas the in-cylinder phenomena are modelled like the SCE model, using the same set of tuning constants. The boosting system is reproduced by a standard map-based approach.

During PFI and DI injections, 30% of the injected fuel is assumed to instantaneously evaporate, while no advanced treatment of spray evolution and liquid wall film formation are considered.

The mechanical friction losses are estimated by an empirical correlation, as a function of engine speed, combustion phasing and in-cylinder pressure peak.

To better clarify the engine architecture, its layout is schematized in *Figure 6-13*.

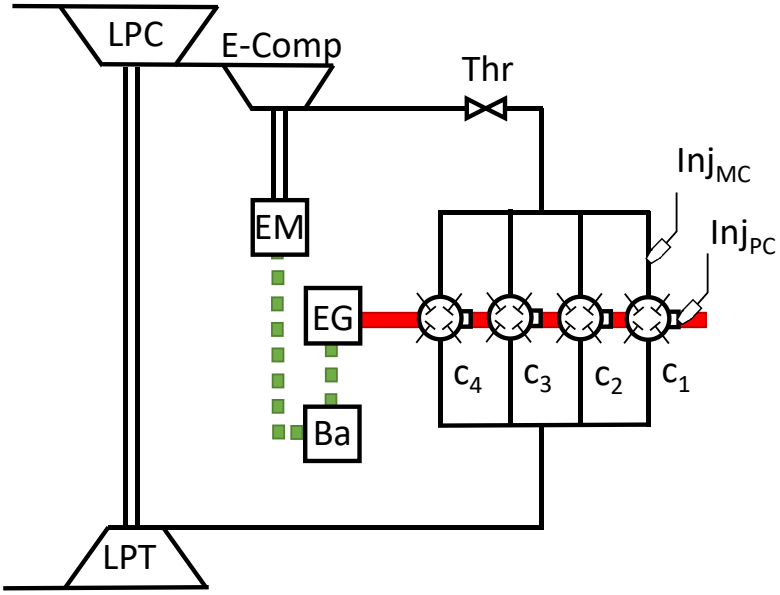

Figure 6-13 Schematic engine layout [12].

The development of a numerical calibration for such a complex engine is very challenge due to high number of degrees of freedom of the system. In particular, the engine has seven control parameters, namely the air/fuel mixture quality (λ) in both the chamber (labelled as λ_{PC}, and λ_{MC}, respectively), the rack position of the LPT, the electrical power absorbed by the E-Comp (or equivalently its rotational speed), the intake valve timing, the spark advance and the throttle valve position. As previously demonstrated, the introduction of a pre-chamber allows to strongly extend the lean burn limit respect to a conventional SI engine, *Figure 6-7*. Consequently, with the aim to improving the engine efficiency and reduction the NO_X emission, this engine is designed to operate at very lean air/fuel mixtures in the as wide as possible zone of the operating plane.

The RB calibration strategy proposed for the multi-cylinder engine is based on the maximization of the engine efficiency in each operating point, while complying with the classical constraints of a SI engine, such as knock intensity, and the additional ones related to the introduction of a pre-chamber, such as the maximum in-PC pressure.

The maximum allowable levels imposed for the constrained parameters with additional limitations are reported in the following:

- Maximum in-PC and in-MC pressures: 180 bar
- Optimal combustion phasing (MFB_{50}): 4.5 CAD AFTDC
- Maximum AI time integral = 0.8
- Injection duration in PC: 300-900 μs
- IVC range: 505 to 540 CAD AFTDC
- Maximum spark advance: -80 CAD AFTDC
- Maximum speed LP group: 205.000
- Maximum speed E-Comp: 140.000

Differently from the conventional engine in which the optimal MFB_{50} was imposed at 9 CAD AFTDC, a slightly advanced value is now selected, as suggested in [10]. The prefixed MFB_{50} target of 4.5 CAD is effectively selected only under knock free operation. Otherwise, the combustion phasing is delayed until the specified threshold level for the knock index is reached. The fuel injected in the pre-chamber is metered to get a stoichiometric level, as long as the in-PC pressure peak is lower than 180 bar, otherwise a richer mixture is selected. The limit of the injection duration of 300 μs is due to the dynamic response of the injector, which does not guarantee a repeatable and reliable operation below such interval. The fuel injection in the main chamber is controlled to realize λ_{MC} = 2 over the widest possible operating domain. This setting is modified only at high speed / high load as discussed below.

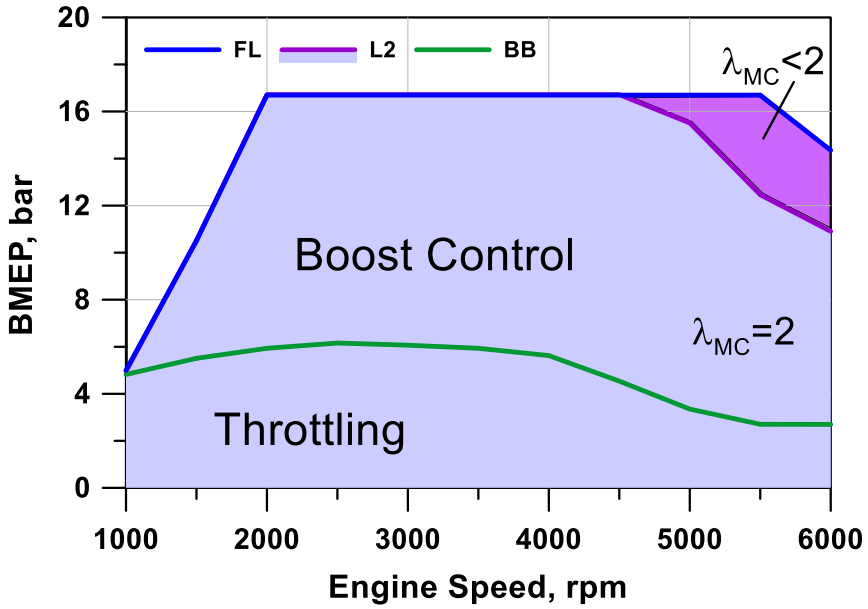

Figure 6-14 BMEP – rpm plane including the BMEP target (FL), and the L2 and BB lines [12].

The strategy to control the load level is differentiated according to the engine load/speed point, namely the engine map is divided in three main regions in which different logics apply.

These three regions are delimited by FL, L2 and BB lines, defined in the following. The Full Load (FL) represents the maximum BMEP target reported in *Figure 6-14*, blue line. To reach this target, the fuel metering in the MC is firstly controlled to get λ_{MC}= 2 over the whole engine speed range. An arbitrary running line is specified for the LP compressor, reported over a normalized LPC map in *Figure 6-15-left*. The selection of the LPC running line is based on the compromise between an adequate surge margin, and a sufficiently high-pressure ratio, to limit the power absorbed by the E-Comp. Subsequently, with the aim to match the prescribed maximum BMEP target, the E-Comp running line *(Figure 6-15-right*) is identified. However, the FL target is not fulfilled above 4500 rpm, since the E-Comp reaches its maximum rotational speed and the overall pressure ratio is limited. This constrained condition defines the L2 line of *Figure 6-14*, for which maximum BMEP level with λ_{MC} = 2 is detected. Below L2, the considered engine and boost system can always work with λ_{MC}= 2 (highlighted in powder blue in *Figure 6-14*).

The only way to fulfill the FL target is to increase the mass of fuel injected in the MC, leading to a λ_{MC}< 2 (pink region in *Figure 6-14*). Alternatively, if a λ_{MC} equal to 2 has to be selected in the whole operating plane, a limited reduction of the full power performance will occur.

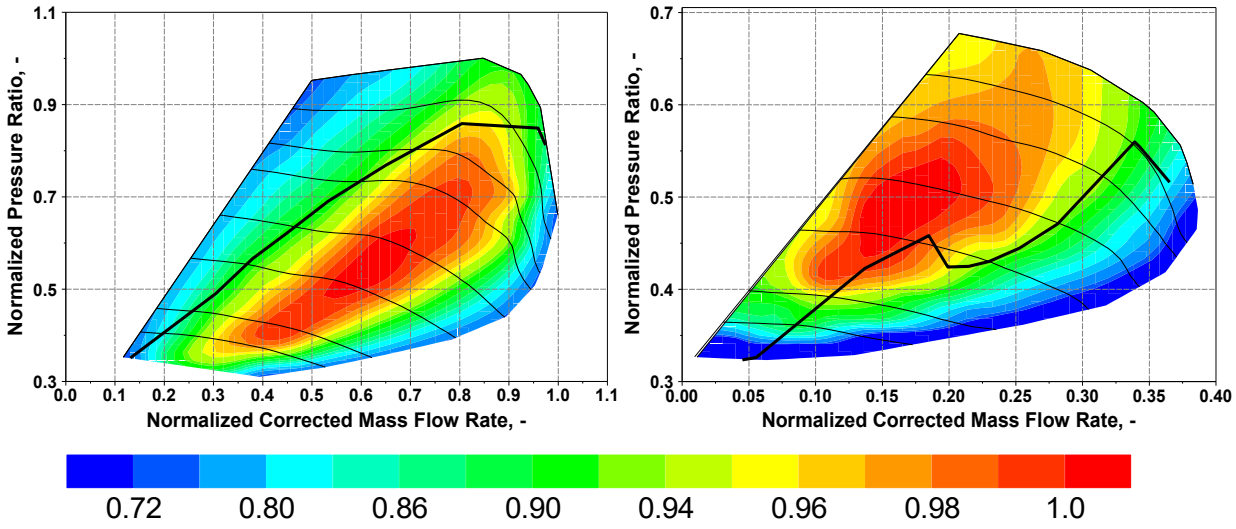

Figure 6-15 LP (left) and HP (right) compressor maps, including the running lines at full load. Due to confidentiality reasons, the pressure ratio, the mass flow rate and the iso-efficiency lines are reported in a normalized form (min-max range converted to 0-1) [12].

Between the purple and the green lines of *Figure 6-14*, the load control is realized by progressively opening the LPT and reducing the E-Comp speed, starting from the settings identified by the above described steps. The green line, labelled as BB (namely Base Boost), represents the load level when the LPT is fully opened, and the E-Comp pressure ratio is equal to 1. Consequently, below this line the LP and HP compressor settings remain fixed and the load is controlled by progressively closing the throttle valve.

Concerning the intake valve management, the IVC is set at the maximum value of 540 CADs AFTDC with the aim of maximizing the cylinder filling and the effective compression ratio, under absence of knock. Otherwise, in knock limited operation (BMEP levels slightly above the BB line) the IVC is advanced as long as the computed knock intensity exceeds the prescribed threshold level, following the Miller concept. This allows to reduce the effective compression ratio, mitigating the knock. If required, the MFB_{50} is progressively delayed, too. On the contrary, in the region of the map below the BB line, the IVC is advanced to minimize the pumping losses, complying also the concurrent throttle valve closure, acting only at very reduce BMEP levels.

The objective of the above described rule-based calibration is the maximization of the Overall Brake Thermal Efficiency (OBTE), which is defined as:

$$OBTE = \frac{P_{ICE} - P_{HPC}/\eta_{HPC}}{\dot{m}_f LHV} \tag{6.1}$$

In the eq.(6.1) P_{ICE} is the brake power at the engine shaft, and P_{HPC} represents the mechanical power at the E-Comp shaft. η_{HPC} is the electro-mechanical efficiency of the E-Comp. It takes into account the overall losses in the electric units (EM and EG) and in the battery, while the adiabatic efficiency of the HP compressor is taken into account in the P_{HPC} term. A constant η_{HPC} equal to 0.81 is imposed whatever is the operating condition. While $\dot{m}_f$ and LHV are the total fuel flow rate and lower heating value, respectively. The OBTE definition in eq. (6.1) is consistent with a "self-sustaining" engine operation mode, namely, at each time, the engine delivers the power required to sustain the battery for driving the E-Comp. Such a choice can be judged conservative, not taking into account the possibility that the battery charging could be realized under a different operating condition, more convenient from the powertrain management viewpoint along a vehicle driving mission.

6.4. Numerical calibration strategy validation

The reliability of the RB engine calibration is verified through the assessment with the same complex methodology used for the conventional SI engine. Differently from the RB a multi-objective optimization problem is here set, corresponding to the simultaneous maximization of the overall brake thermal efficiency and the minimization of the Brake Specific Nitric Oxides ($BSNO_x$, gNO_x/kWh). To include NO_X formation, the well-known extended Zeldovich mechanism is applied in each cylinder [11]. Since noxious emissions for an ultra-lean engine are mainly composed of NO_2, the NO production derived by the Zeldovich mechanism is assumed to completely convert to NO_2 along the exhaust pipes up to the after-treatment system.

Due to the high computational time, the direct optimization is performed only along a load sweep at a constant engine speed of 3000 rpm, namely the rotational speed where the maximum OBTE is expected to occur for the examined engine.

The optimization tool employs a genetic algorithm (MOGA-II), which is the best suited one for a multi-variable multi-objective problem. As said, two objective functions are considered, namely OBTE and $BSNO_x$, while the PIDs control of the RB strategy are converted into free variables, complying with the same constraints as the ones specified for the rule-based calibration. The inputs of optimization are the following:

- Thr: 0-90 degrees
- MFB_{50}: 2-9 CAD AFTDC
- IVC: 505-540 CAD AFTDC
- Normalized LPT rack opening: 0-1
- ω_{HPC}: 0-1
- λ_{MC}: 1.5-2.4
- λ_{PC}: 0.8-1.3

For model simplicity the normalized rack position of the LPT and the non-dimensional velocity of E-Comp (ω_{HPC}) are considered. In the case of the LPT, the highest value refers to the maximum opening of the turbine rack, which corresponds to the lowest possible turbine expansion ratio. The second parameter is the E-Comp compressor rotational speed, normalized according to the following expression:

$$\omega_{HPC} = \frac{\eta_{HPC} - \eta_{HPC,min}}{\eta_{HPC,min} - \eta_{HPC,max}} \tag{6.2}$$

where n_{HPC} is the actual rotational speed of the E-Comp, with the related maximum and minimum levels.

In *Figure 6-16* the logical scheme of the considered optimization process is reported. The optimizer, at each step of the process, iteratively selects the above control variables, which are passed to the 1D model to perform the numerical analysis. At the end of the simulation, the computed values of the objective functions are passed back to the optimizer for the next iteration, until the optimal levels, belonging to the Pareto Frontier, are obtained. Each optimizer evaluation is post-processed to verify that some monitored variables do not exceed the corresponding threshold levels. To verify the RB calibration methodology, the outcomes of the two described methodologies are here compared. The optimization results (labelled as Opt), shown in the next figures, refer to the solutions which belong to the Pareto Frontier.

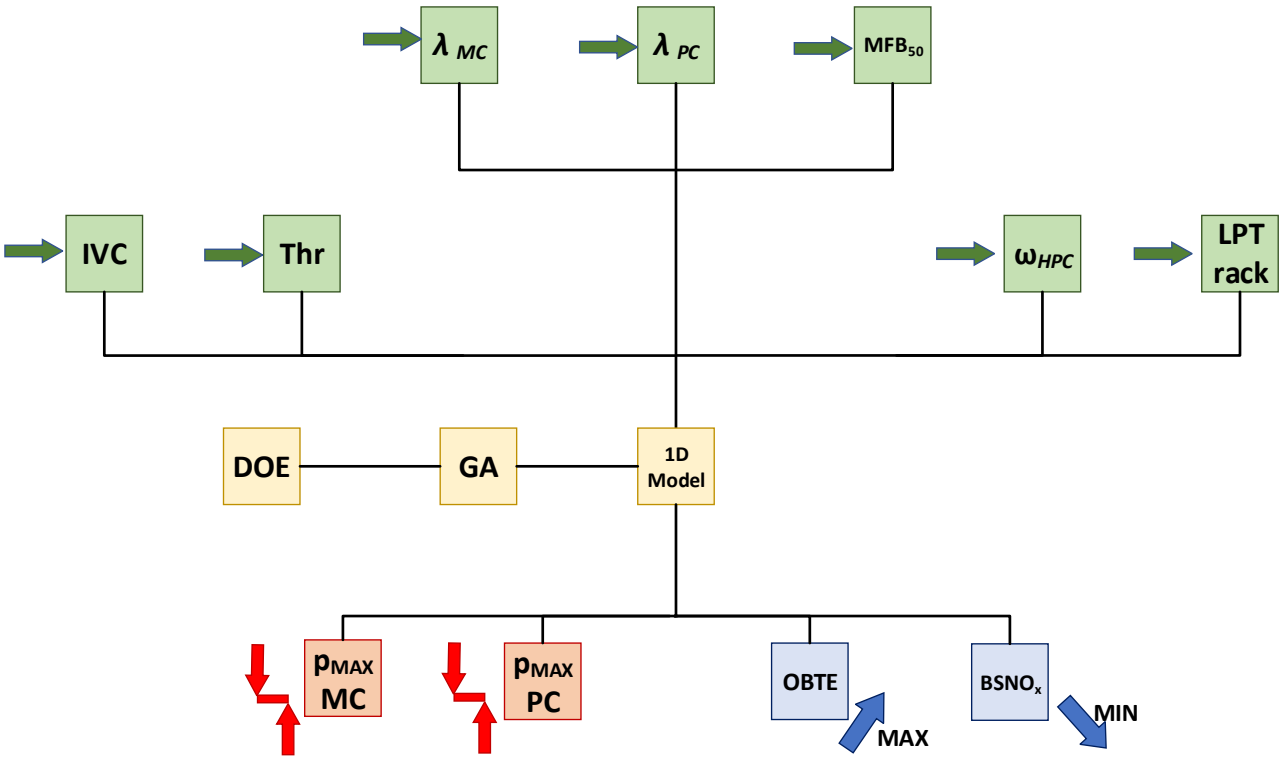

Figure 6-16 Workflow of the optimization process [12].

In *Figure 6-17*, the OBTE comparison of puts into evidence a quite good agreement all along the BMEP sweep between the considered numerical procedures.

In the following all the RB calibration variables are compared against the optimal ones, showing an averaged good agreement. Starting the discussion from the mixture qualities in MC and PC reported in *Figure 6-18*. To reach the maximum OBTE, the optimization problem founds a λ_{MC} values close to 2 and λ_{PC} trend against the BMEP, the RB well captures this behavior, confirming the assumption done.

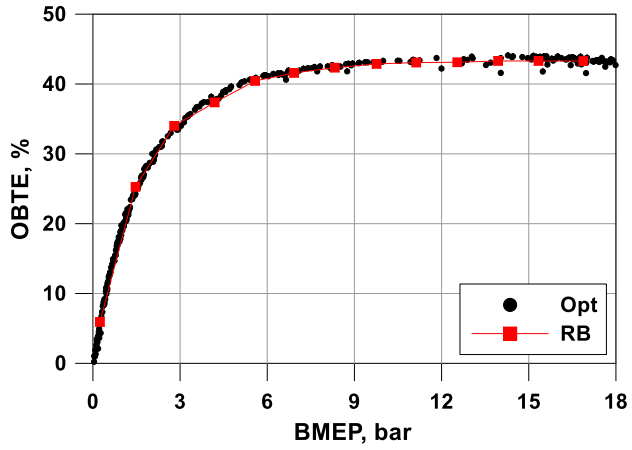

Figure 6-17 OBTE comparison in a BMEP sweep at 3000 rpm for the RB and optimizer calibrations [12].

Concerning the λ_{MC}, a certain scatter around this optimal value emerges, with a band of ± 0.2. This depends on the complexity of optimization task here considered, consisting in a variable-load, constrained, 7-variable, 2-objective problem. Although more than 5000 iterations have been carried out, the identification of the Pareto Frontier, counting about 650 points, is achieved with a certain scatter band. Regarding the λ_{PC} trend, in a medium load range (4-13 bar BMEP), a close-to-stoichiometric mixture is preferred, once again with some scatter. For the lower BMEP, the limitation of the minimum PC injection lead to the selection of a rich λ_{PC}. On the contrary, at the higher loads, a certain mixture leaning is adopted to limit the PC pressure and temperature peaks, so to reduce the NO_x production. For some solutions, the maximum allowed injection duration is attained, leading once again to λ_{PC} >1.

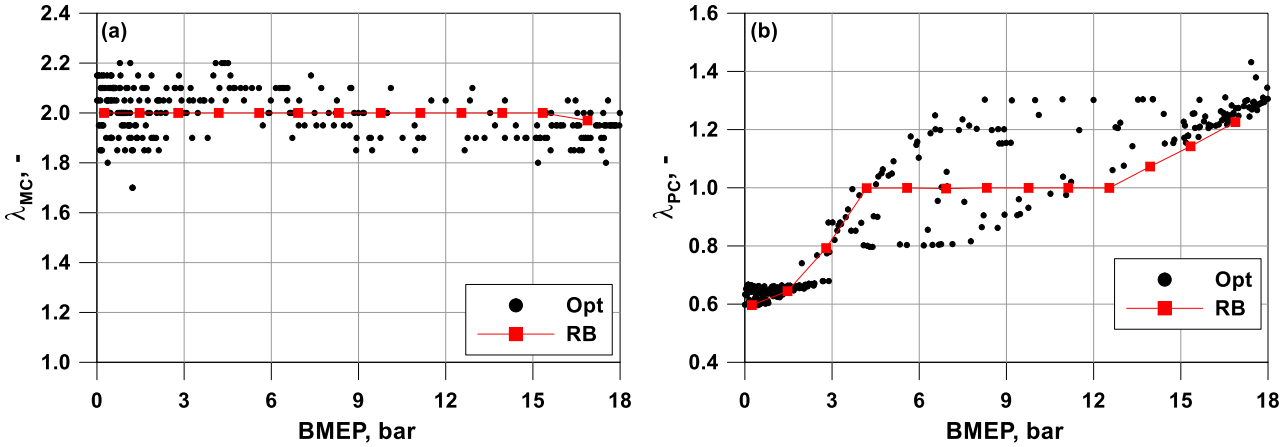

Figure 6-18 λ_{MC}(a) and λ_{PC} (b) comparison in a BMEP sweep at 3000 rpm for the RB and optimizer calibrations [12].

The MFB_{50} and the throttle valve position comparisons are depicted in *Figure 6-19*. The optimizer outputs present an almost flat trend in the medium load range, with most of points with an MFB_{50} about 8-9 CAD AFTDC. At high load, the optimal value is delayed limiting the knock, while at low load, the upper shift it is a consequence of the combustion lengthening and of the constraint on SA.

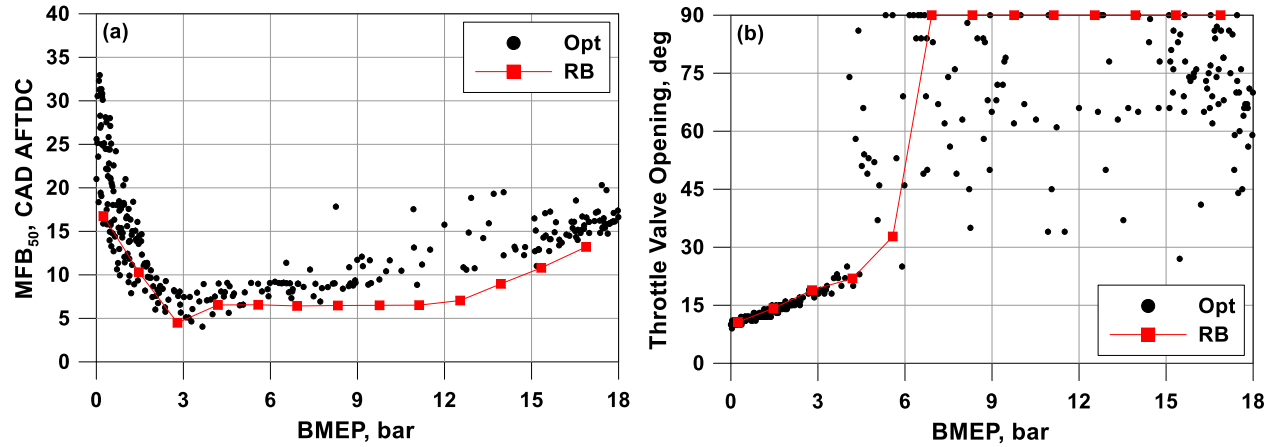

Figure 6-19 MFB_{50} (a) Throttle valve opening (b) comparison in a BMEP sweep at 3000 rpm for the RB and optimizer calibrations [12].

The MFB_{50} derived by the RB calibration presents a similar trend, even if with a slightly earlier MFB_{50} on average. Concerning the throttle valve position both RB and Opt strategies are very comparable at BMEP lower than about 5 bar, in which the valve closure control the load. A larger scattering of the Opt points for BMEP levels above 5 bar is a consequence of the low load sensitivity to throttle valve openings, when this last is greater than 40-50 degrees.

As soon as the throttle valve is fully opened, the overall boost is progressively modulated by a partial closure of the LPT rack and by a simultaneous increase of the E-Comp rotational speed *Figure* 6-20. The overall boosting is shared between the two compressors, according to the pressure ratios plotted in *Figure 6-21*.

These figures underlines that, for the optimal calibration, the load is mainly controlled by the LPC, while the E-Comp operates with the minimum possible pressure ratio. This results in a quite relevant exhaust backpressure for the cylinders, but in the minimum possible power request by the E-Comp. In the overall efficiency balance, this calibration strategy proves to be the most effective compared to a calibration which privileges a higher E-Comp boosting.

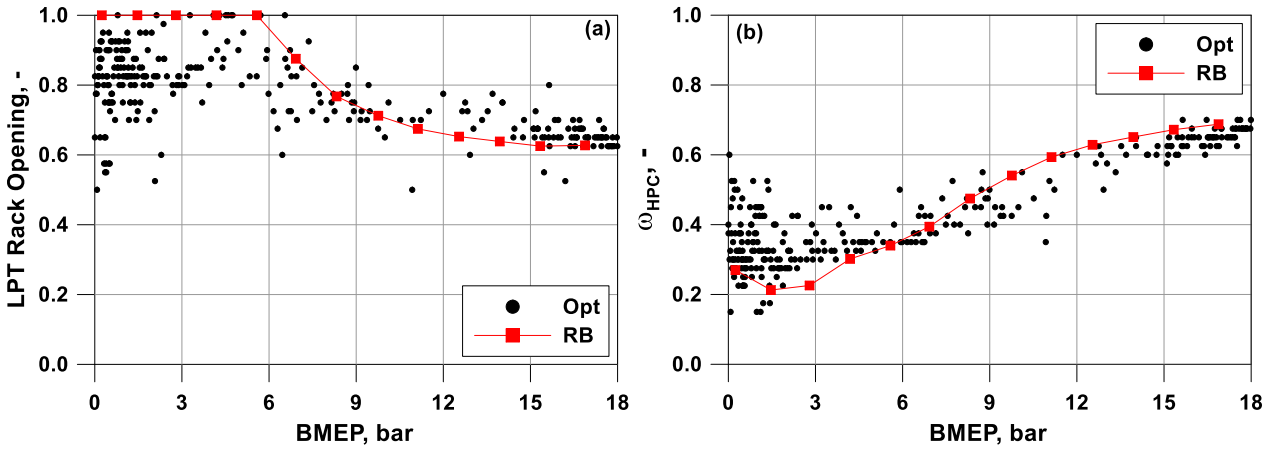

Figure 6-20 Rack position of LPT (a) and normalized rotational speed of E-Comp (b) comparison in a BMEP sweep at 3000 rpm for the RB and optimizer calibrations [12].

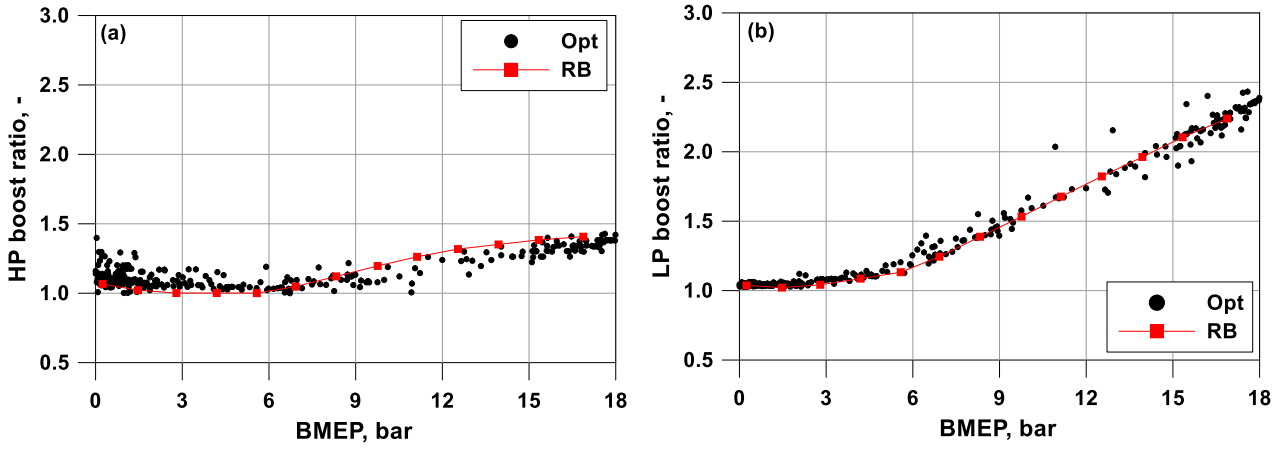

Figure 6-21 HP (a) and LP (b) boost ratio comparison in a BMEP sweep at 3000 rpm for the RB and optimizer calibrations [12].

The last assessment regards the intake valve timing, which is depicted in *Figure 6-22*. Generally, a setting close to the most advanced timing is preferred. This choice arises from the opportunity to minimize the pumping losses at low load and control the knock at high load. In the medium BMEP range, the IVC is slightly delayed enhancing the effective volumetric compression ratio and hence the engine thermal efficiency.

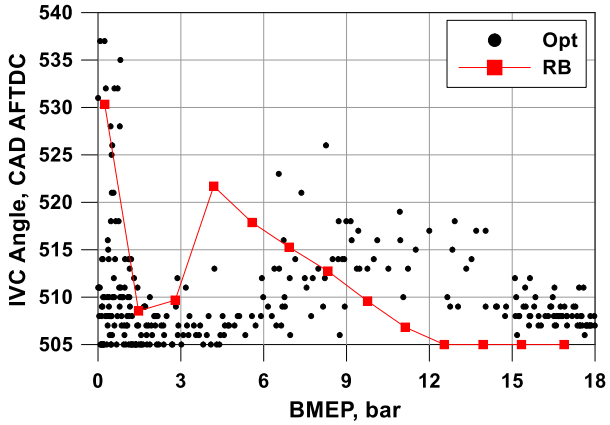

Figure 6-22 IVC comparison in a BMEP sweep at 3000 rpm for the RB and optimizer calibrations [12].

The presented results, show a satisfactory agreement in terms of optimal setting control between the two methodologies, denoting the high reliability of RB calibration procedure to reach OBTEs very close to the ones derived by the optimizer-based approach.

In the light of this observation, the RB strategy extended to the full engine speed range, to explore the close-to-optimal engine performance in the entire operating plane, as discussed in the following section.

6.5. Engine Performance Maps Discussion

The engine performance maps are computed following the RB control strategy previously described for the whole engine operating plane, composed of 143 operating points - 11 rpm x 13 BMEP. The maps of the most important performance parameters, namely the standard Brake Thermal Efficiency (BTE) and of the OBTE are reported in *Figure 6-23*. A maximum level occurs in both the cases, at medium speed (2500-3500 rpm) and high load (above 12-13 bar BMEP). The peak of BTE (OBTE) of about 46% (42%) confirms the potential of such engine architecture for a very high efficiency. Nevertheless, the *EAGLE* target of 50% is not still reached and, consequently, further improvements are ongoing to attain even higher BTE / OBTE values. Among these, the employment of an extreme Miller concept and a further VVT device on the exhaust camshaft are under testing. It is worth to remark that BTE and OBTE can be considered as best and worst case, respectively, depending on the availability of stored energy in the batteries to drive the E-Comp.

This, in turn, affects the instantaneous powertrain efficiency along a driving cycle, relaying upon the management of the energy accumulation device (battery).

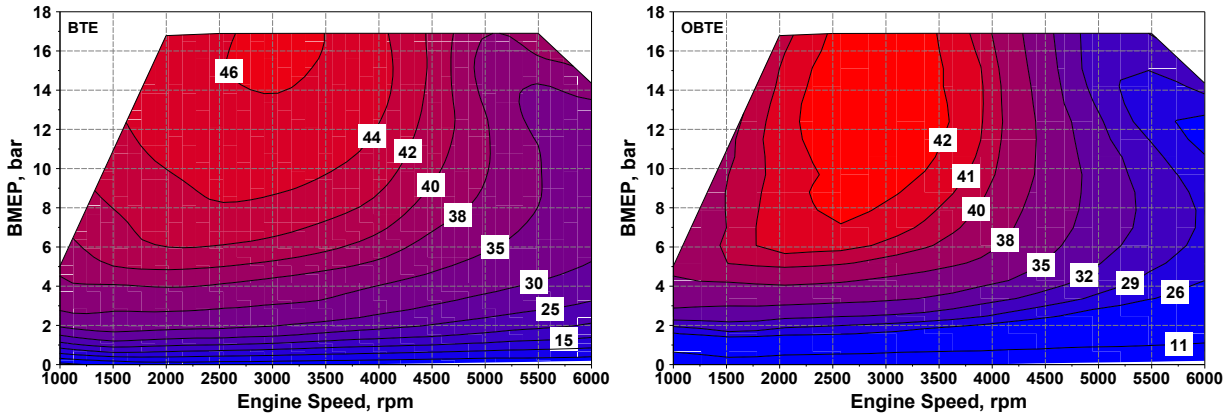

Figure 6-23 Map of BTE [%], Map of OBTE [%] [12].

The difference between BTE and OBTE is of about 4 percent in the maximum efficiency zone, and progressively increases at higher speeds, especially in the high load zone. This is mainly due to the power absorbed by the E-Comp, as shown in *Figure 6-24*. It can be observed that the compressor requires up to 17 kW, which represents about the 13.4 % of the power rated by the engine. However, the E-Comp power request substantially reduces moving to the map region which is expected to be most frequently experienced by the engine along a WLTP driving cycle, namely close to the maximum efficiency zone. There, the E-Comp power is of about 3 kW.

As for conventional SI engine, the BTE reduction at increasing speed is mainly due to the pumping losses rising, as shown in the right of *Figure 6-24.* Whereas, moving down from the full load zone, the efficiency reduction is mainly due to the percent increase of heat losses (*Figure 6-25,left*), which primarily impact at low speeds.

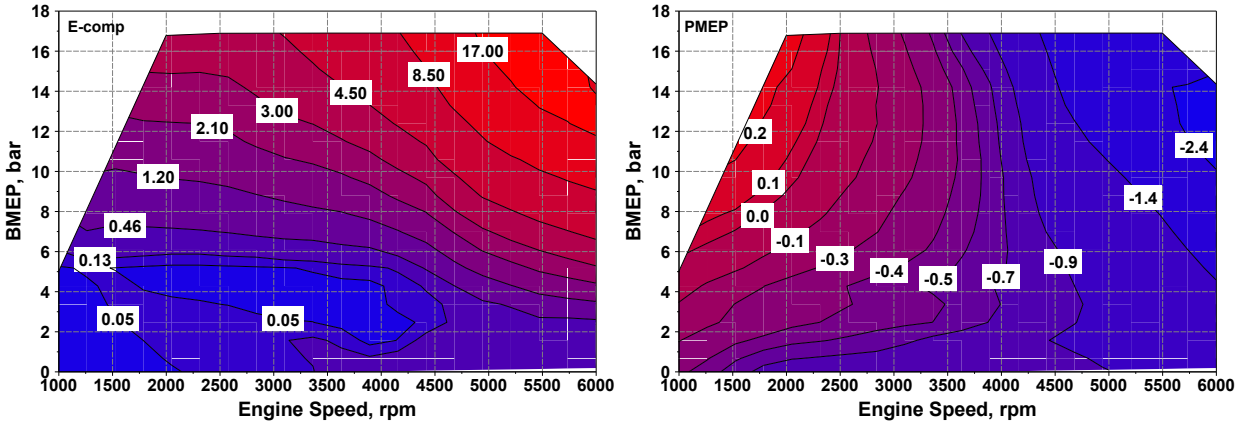

Figure 6-24 Map of E-Comp power consumption [kW] and PMEP [bar] [12].

Concerning the combustion phasing, MFB_{50}, reported in *Figure 6-25 right*, near to the full load operation, a certain delay is required to limit the knock.

At medium speeds and loads, a level closer to the MFB_{50} target is reached. The reduced delay of the MFB_{50} is also related to the valve closure advancement that allows to limit the knock at high BMEP, especially at low speeds (*Figure 6-26,rigth*). At low load, the same strategy is applied to reduce the intake throttling. In this way, the intake plenum pressure maintains above 1.0 bar in most of the map (*Figure 6-26,left*), and above 0.5 bar even in the region at very low BMEP. It worth to underline, that the only way to reach the prescribed load target with an ultra-lean air/fuel mixture and a Miller strategy, a very high plenum pressure is required, with peaks of 3.8 bar at the highest speeds and loads.

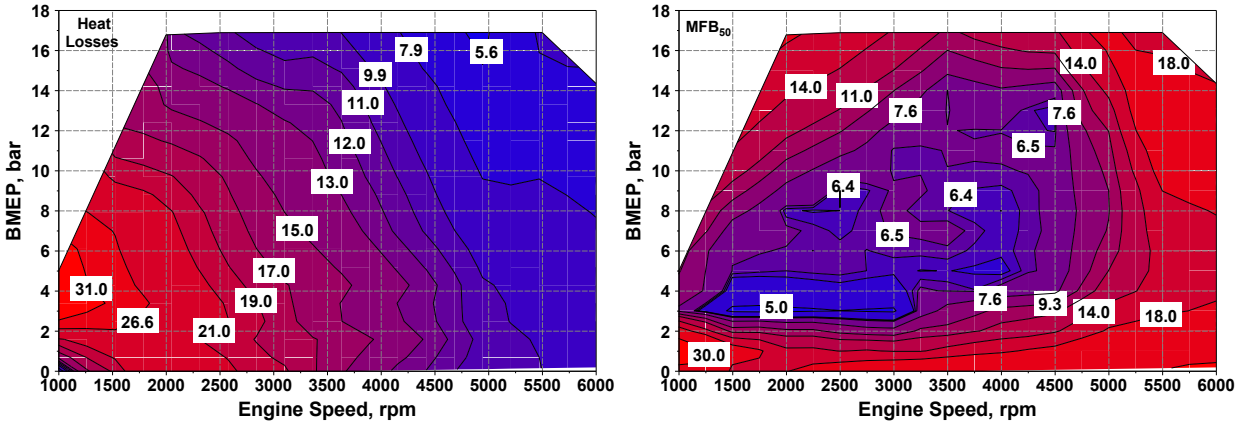

Figure 6-25 Map of heat losses fraction of total fuel energy [%] and MFB_{50} for the main chamber [CAD AFTDC] [12].

Despite the considered ultra-lean operation an adequate combustion speed occurs, namely MFB_{10-90}, over the whole plane. Indeed, as shown in *Figure 6-27*, the combustion duration maintains below 43 CADs at the higher speeds, while at the lower speeds and mid/high loads, it reduces even down to 10 CADs. Only at very low loads, a combustion lengthening can be observed, which reflects on the MFB_{50} delay (*Figure 6-25*).

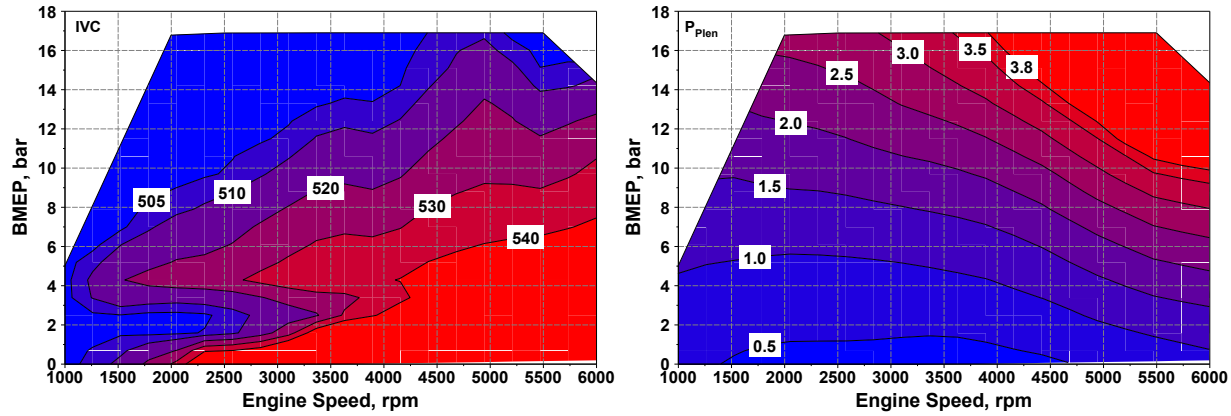

Figure 6-26 Map of the IVC [CAD AFTDC] and Map of intake plenum pressure [bar] [12].

The combustion slowdown is related to the limitation of the minimum duration of the PC injection, leading to a rich λ_{pc} below the minimum acceptable level of 0.8.

Consecutively, the combustion speed in the pre-chamber becomes very slow, losing the effectiveness of the hot jet entering in the MC for the combustion enhancement. As reported in *Figure 6-27*, rich mixture occurs about at BMEP lower than 2 bar at low speeds up to full load for speeds above 4000 rpm.

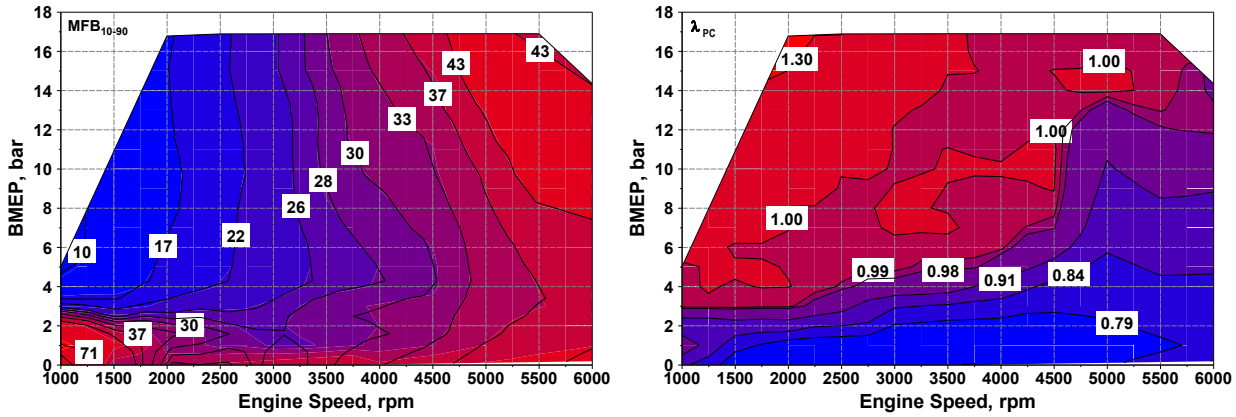

Figure 6-27 Map of $MFB_{10\text{-}90}$ [CAD] and λ_{PC} [-] [12].

It is worth to underline that the criticisms emerged at very low speeds and loads (combustion lengthening and mixture richness in the PC) should not affect the actual application of the considered engine architecture, since, as stated above, it will be integrated in a hybrid powertrain and hence it will unlikely operate under low load conditions. An additional point to be highlighted is that very low load conditions were not considered for the model validation.

For this reason, although the numerical results appear reasonable from a physical viewpoint under these conditions, an experimental verification seems appropriate in the next step of this activity.

6.6. Vehicle simulation outcomes

The last analysis of this chapter regards the vehicle simulation of the hybrid vehicle in both configuration variants, HEV and PHEV listed in *Table 6.2*. The vehicle model is based on a forward kinematic approach, as reported in the chapter 4 of this thesis. The thermal unit is characterized by a quasi-steady map-based approach, using some of the maps reported in the previous section. In particular, the BSFC map, *Figure 6-28,* is implemented as a function of the engine BMEP and speed. For both electric units, the maximum and minimum shaft torque curve are assigned. Even if their efficiencies could be described by a map-based approach, in this study they are assumed constant. The battery is treated by a simple SOC model, as described in the previous section. Whereas, the mechanical losses in the gearboxes are evaluated assuming a constant efficiency.

The effects of the ICE thermal transient are not considered in the simulations, resulting a null fuel consumption penalization at cold start. This is a simplified physical vehicle and powertrain modelling, but for the analysis at this stage of the research activity can be considered accurate enough.

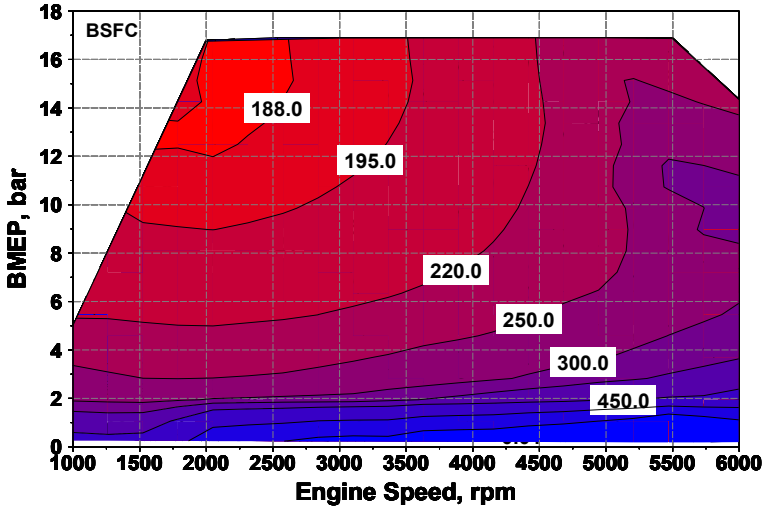

Figure 6-28 Map of BSFC [g/kWh] [12].

Concerning the energy management strategy (EMS) for the control of the hybrid powertrain, the ETESS and the PMP are both used in an off-line simulation, to benchmark the CO_2 emission along the WLTC for this hybrid vehicle. To this aim, the co-state variable of PMP, λ^*(see eq. (4.19)), and the tuning parameter of ETESS, c_0, (see eq. (4.25)) are properly selected to ensure the battery energy balance between the cycle start and end. In *Figure 6-29 and Figure 6-30,* the results of the simulations are reported in vehicle speed profile, motor powers, SOC, gear number for GB_2, fuel rate and vehicle mode (series/parallel) along the driving cycle. In particular, the PMP and the ETESS results are reported with dashed black lines and red lines, respectively.

The vehicle speed profile is represented in *Figure 6-30 a*. The management of the EM and ICE is quite similar along the driving cycle, which reflect on the trends of fuel rate, SOC, and hybrid modality (parallel (0) or series (1)). Concerning the EG, the ETESS does not involve the possibility to use this unit to charge the battery by the thermal engine, while for the PMP a reduced and sporadic battery charging emerges. Although the overall good agreement of the management of the different units (both thermal engine and electric machines), some discrepancies occur in the overall performance. Indeed, the PMP provides 82 g/km CO_2 against 87 g/km CO_2 of the ETESS. This is probably due to higher frequency of the gear shift as highlighted in *Figure 6-30 g*. Although the ETESS did not find the optimal solution of the problem as the PMP, the lower number of possible configurations to be analyzed, namely pure thermal and pure electric driving instead of different power-split options, allows to reduce drastically the computational time.

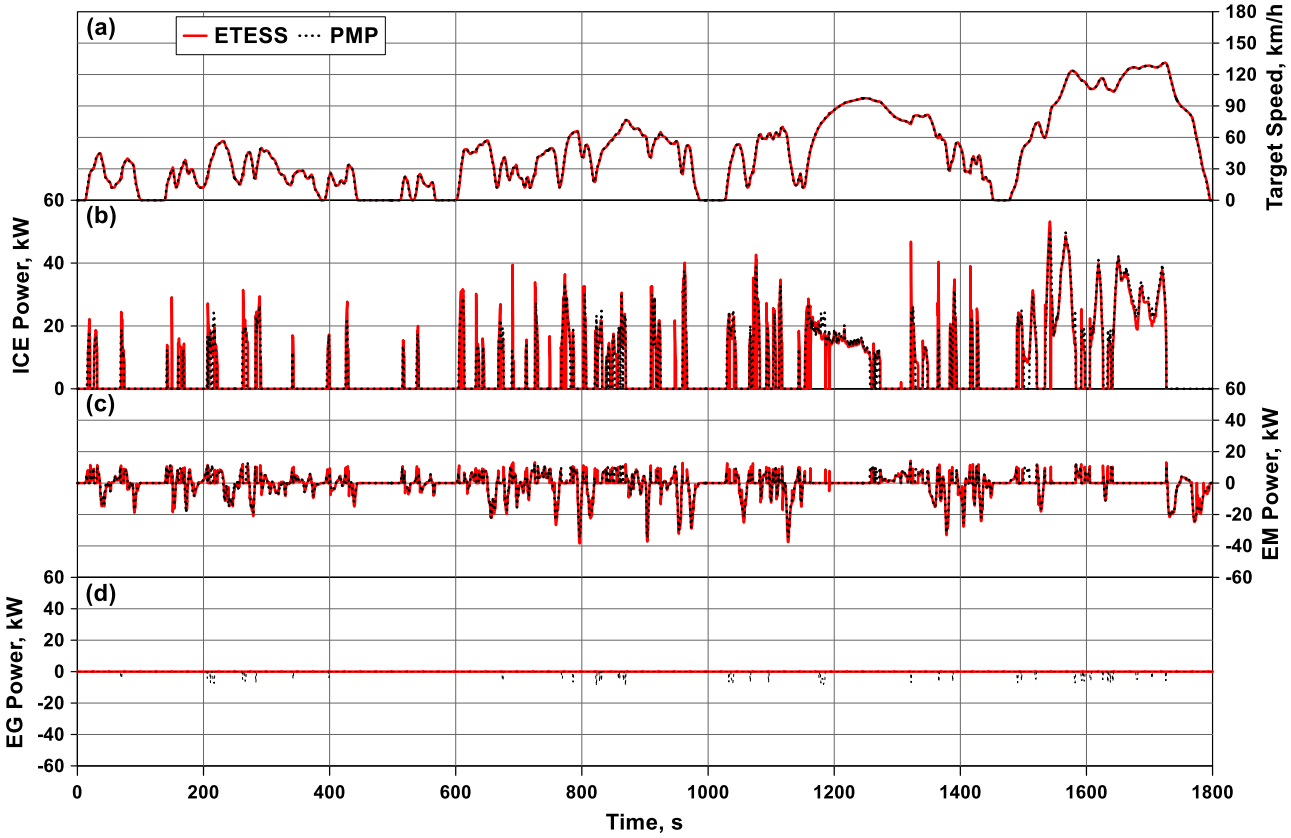

Figure 6-29 PMP/ETESS comparison of vehicle speed (a), ICE power (b), EM Power (c), EG Power (d).

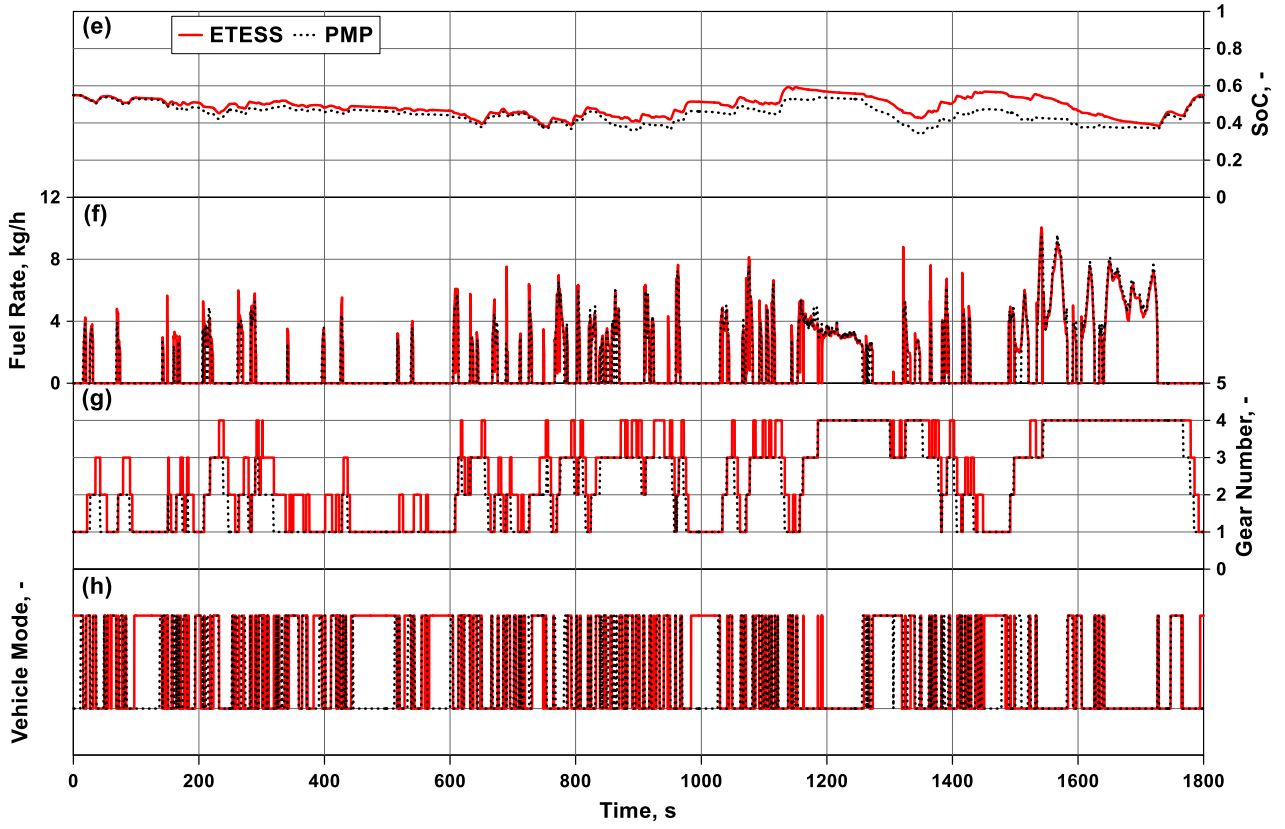

Figure 6-30 PMP/ETESS comparison of vehicle SOC (e), fuel rate (f), Ger Number (g), Vehicle mode (h) along the WLTC.

As a future development, the proposed control strategy will be assessed by on-line simulations, to verify the possibility to be used in a real-time vehicle application. Moreover, ETESS will be tested in more complex simulation frameworks (variable electric unit efficiency and components dynamics) and with more stringent limitations on ICE switch on/off frequency.

Once observed the global reliability of the ETESS, it is used to carry out a further analysis aiming to assess the improvements connected to the hybridization of a conventional engine, and the one related to the hybridization of the pre-chamber high-efficiency engine here studied. Specifically, four different architectures, listed in *Table 6.6,* are tested. The former, labeled as '*Base*', is the conventional segment C vehicle, from which the investigated HEV derives. It has the same architecture as the one detailed in *Table 6.2*, except for a different gearbox (5 gears instead of 4), and a different engine, not fitted with a PC but with a conventional spark plug (CSP). Its performance map was provided by one of the partners of the EAGLE project and cannot be reported for confidentiality reason. This engine is a 1.2-liter 4-cylinder turbocharged unit, having a minimum BSFC of 253 g/kWh. The second architecture '*HEV+CSP*' involves the hybridization of the CSP engine, according to the combined series/parallel configuration reported in *Figure 4-7*. In the third case, '*HEV+PCSP*', the difference with previous case is the adoption of the pre-chamber engine (PCSP) instead of the conventional CSP engine. In this case, the engine maps developed in this thesis are embedded in the simulator. The last configuration, *'PHEV'*, is the same as *'HEV+PCSP'*, with a battery ten times bigger than other analyzed hybrid architectures, so to define a plug-in hybrid powertrain.

Table 6.6 Investigated architectures

Case #	Label	ENGINE	BATTERY kWh
1	**Base**	CSP	N/A
2	**HEV+CSP**	CSP	0.5
3	**HEV+PCSP**	PCSP	0.5
4	**PHEV**	PCSP	5

Concerning the PHEV, the estimation of the CO_2 is done according to the WLTP [13]. In this procedure, one or more WLTC are performed starting with a full-charged battery and realizing (if possible) a pure-electric driving, until the state of charge reaches a prescribed lowest threshold (Charge Depleting mode). After this phase, the control strategy switches towards a Charge Sustain (CS) modality, where the battery energy balance between the start and the end of the driving cycle has to be satisfied.

The CO_2 emissions is evaluated as a weighted average between the emissions in CD mode (usually null) and the ones in CS mode, according to the rules prescribed in [12]. In the specific case, the battery and the electric motor are sized to cover a single WLTC in CD mode. In *Figure 6-31*, the results of the simulations are depicted in terms of CO_2 emission along the WTLC. Comparing cases 'Base' and 'HEV+CSP', it emerges that the hybridization of a conventional engine allows to reduce the emission of 8.80%. The adoption of a high-efficiency engine permits an CO_2 emission drop of 37.2 %. The highest benefit is achieved with the PHEV configuration, with a 69.1% of CO_2 decrement. This advantage mainly arises from the possibility to realize an entire WLTC in CD mode, reducing drastically the overall CO_2 emission, also including the contribution of the second WLTC in CS mode. Nerveless, the 37.2 % reduction from *'Base'* architecture to *'HEV+PCSP'* confirms that the right path to be followed by the automaker is to combine and improve those technologies, namely internal combustion engine and hybrid powertrain.

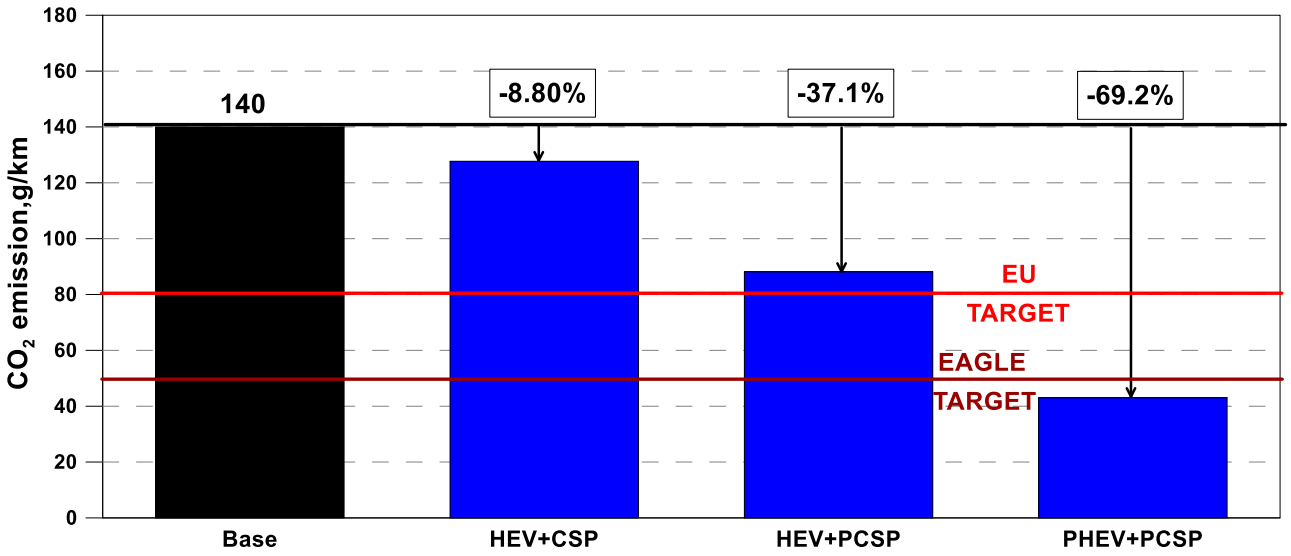

Figure 6-31 Comparison of CO_2 emissions of a segment C vehicle along a WLTC for the considered vehicle variants.

References

[1] Gottschalk, W., Lezius, U., Mathusall, L., "Investigations on the Potential of a Variable Miller Cycle for SI Knock Control," SAE Technical Paper 2013-01-1122, 2013, doi: 10.4271/2013-01-1122.

[2] Mueller, C., Morcinkowski, B., Schernus, C., Habermann, K., Uhlmann, T., "Development of a pre-chamber for spark ignition engines in vehicle applications," 4th International Conference on Ignition Systems for Gasoline Engines, Dec. 2018, doi: 10.5445/IR/1000088588.

[3] Bozza, F., De Bellis, V., Tufano, D., Malfi, E. et al., "A Quasi-Dimensional Model of Pre-Chamber Spark-Ignition Engines," SAE Technical Paper 2019-01-0470, 2019, doi:*10.4271/2019-01-0470*.

[4] Bozza, F., De Bellis, V., Tufano, D., Malfi, E. et al., "1D Numerical and Experimental Investigations of an Ultra lean Pre-Chamber Engine," *SAE International Journal of Engines*, 03-13-02-0012.

[5] Spindt, R., "Air-Fuel Ratios from Exhaust Gas Analysis," SAE Technical Paper 650507, 1965, doi: 10.4271/650507.

[6] Bounaceur, R., Herbinet, O., Fournet, R., Glaude, P. et al., "Modeling the Laminar Flame Speed of Natural Gas and Gasoline Surrogates," SAE Technical Paper 2010-01-0546, 2010, doi:10.4271/2010-01-0546.

[7] Amirante, R., Distaso, E., Tamburrano, P., Reitz, R. D., "Laminar flame speed correlations for methane, ethane, propane and their mixtures, and natural gas and gasoline for spark-ignition engine simulations," *International Journal of Engine Research*, 18(9), 951-970, 2017, doi:10.1177/1468087417720018.

[8] Verhelst, S., Sierens, R., "A quasi-dimensional model for the power cycle of a hydrogen-fuelled ICE," *International Journal of Hydrogen Energy*, 32(15), 3545-3554, 2007, doi: 10.1016/j.ijhydene.2007.02.011.

[9] Hohenberg, G., "Advanced Approaches for Heat Transfer Calculations," SAE Technical Paper 790825, 1979, doi: 10.4271/790825.

[10] Serrano, D., Zaccardi, J.M., Müller, C., Libert, C. Habermann, K., "Ultra-Lean Pre-Chamber Gasoline Engine for Future Hybrid Powertrains," SAE Technical Paper, 2019-24-0104, 2019, doi:10.4271/2019-24-0104.

[11] Lavoie, G., Heywood, J., Keck, J., "Experimental and theoretical study of nitric oxide formation in internal combustion engines" *Combustion science and technology*, 1(4): 313–326, 1970, doi:10.1080/00102206908952211.

[12] Bozza, F., Tufano, D., Malfi, E., Teodosio, L., Libert, C. De Bellis, V., “Performance and Emissions of an Advanced Multi-Cylinder SI Engine Operating in Ultra-Lean Conditions”, SAE Technical Paper, No. 2019-24-0075, doi: 10.4271/2019-24-0075.

[13] https://www.vehicle-certification-agency.gov.uk/fcb/wltp.asp

7. A look-ahead in the future

Whatever will be the choice that the car automaker will make to reach the ambitious target of CO_2 emissions reduction, an increasingly availability of Advanced Driver Assistance Systems (ADAS) or Connected and Automated Vehicle (CAV) will be expected in the years to come. Here, the powertrain controls have a very important rule, since it has to properly manage the vehicle system using look-ahead information from the route or the vehicle cloud. This means that the control problem is shifted from an instantaneous optimization of fuel consumption into a global optimization over the prescribed route.

However, the current regulatory tests forbid the use of advanced information of the route, leading these last inadequate to assess fuel economy for CAVs. A possible way to overcome this issue is to assess the vehicle performance on real-world driving scenarios. However, the huge variability of external conditions that can affect the fuel economy poses significant challenges when attempting to compare the performance and fuel economy of different powertrain technologies, vehicle dynamics and powertrain control methods. This is the main reason why a proper procedure to benchmark the fuel economy over real-world routes is not yet defined.

It has to remark that a methodology for the estimation of the fuel economy on RDE cycles regards the entire automotive sector. Indeed, RDE cycles have been recently introduced for the homologation of the vehicles, since current regulatory driving cycle are not representative enough of the operating and environmental conditions of the vehicle in the “real-world”. Several studies have demonstrated a discrepancy in the fuel economy estimated between regulatory driving cycle and actual driving, with a maximum difference of 15%[1].

The objective of this work, carried out at the Ohio State University Center for Automotive Research (CAR) as part of the ongoing ARPA-E NEXTCAR project [2], is to describe a numerical methodology to benchmark and evaluate the fuel economy benefits of a CAV over real-world driving scenarios. A Monte Carlo simulation [3] has been designed to determine the statistical distribution of the fuel consumption induced by driving styles and Signal Phase and Timing (SPaT) conditions, for a conventional (driver-operated) vehicle and for Level 1 CAV. In this last, the vehicle dynamics and powertrain control are optimized using look-ahead route information.

In this work, two vehicle configurations are analyzed. The former, representing the baseline, is a 48V mild-hybrid vehicle, for which a model of the powertrain and longitudinal vehicle dynamics was previously developed and validated in [4] by the NEXTCAR team.

An Enhanced Driver Model (EDM) [5] is also embedded in the code with the aim to reproduce a conventional driver. In particular, the EDM is able to predict various driving behaviors, taking into account traffic information such as the presence of a leader vehicle and actual Signal Phase and Timing (SPaT).The latter vehicle is a Level 1 CAV with the same 48V mild-hybrid powertrain, including advanced cylinder deactivation via Dynamic Skip Fire (DSF) [6] and an Adaptive Cruise Control (ACC) system. The VD&PT control is optimized to minimize the fuel consumption, using the look-ahead information over a prescribed route, namely speed limits and elevation data. These last are used to determine the optimal vehicle speed profile and energy management strategy. The VD&PT optimization is based on Dynamic Programming (DP) to ensure global optimality of the solution obtained.Using both the EDM and VD&PT models, a Monte Carlo simulation study is conducted over a specific route. For the baseline, the study is performed by introducing two random variables, namely driver aggressiveness and SPaT information. For the VD&PT optimizer, the only random variable considered is the SPaT information. The results of this study are used to determine statistical distributions of the fuel consumption and travel time.

This chapter will be divided as follows. Both the vehicle models used in this activity will be described only briefly, since developed at the OSU before this research activity. Subsequently, the EDM calibration will be explain in detail. This calibration process makes the EDM able to more realistically capture different driving behaviors. Finally, the Monte Carlo simulations outcomes will be discussed.

7.1. Vehicle Dynamic and Powertrain model

The powertrain considered for the vehicle simulator is schematized in *Figure 7-1*. It is a 48V mild-hybrid with a P0 Belt-starter Generator (BSG). The simulator contains a low frequency, quasi-static model of the engine (fuel map), BSG (torque and efficiency maps), transmission (efficiency calculation), and 48V battery pack (for SOC calculation). The vehicle longitudinal dynamics are described using a low-frequency model based on the road load equation, discussed in the previous chapter. The model is a forward-looking vehicle simulator focused on energy and fuel consumption prediction, and control strategy implementation and verification. In particular, a simplified Electronic Control Module (ECM) model provided by Delphi Technologies (DT) manages the motor units of the vehicle. This VD&PT model was calibrated and extensively validated in [4], using the experimental data collected over the FTP drive cycle. The comparison performed by assessing vehicle velocity, gear number, desired engine speed, desired engine torque, fuel consumed, desired BSG torque and battery SOC, shows an overall good agreement. In particular, for the FTP cycle, the model predicts the fuel consumption within 1% of the data.

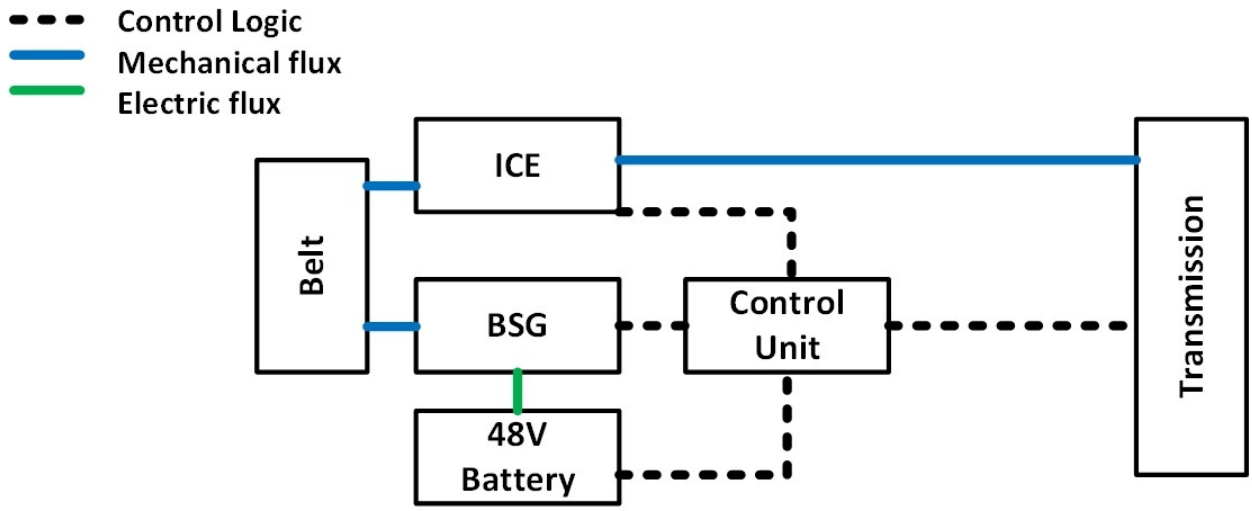

Figure 7-1 Scheme of the 48V P0 Mild-Hybrid powertrain architecture.

7.2. Baseline Vehicle with Human Driver Model

In real-world cycles, differently from the regulatory ones, a driver is required for accomplish the test. As a consequence, the fuel estimation is significantly affected by driving behavior. For example, a relaxed driver tends to consume less fuel than a relatively aggressive driver, but takes longer to complete the same route [8]. Hence, a human driver model, able to mimic different driving behavior, was included in the described VD&PT simulator to take in to account those variabilities.

In particular, the EDM developed at OSU [5] was used. It is a deterministic reference velocity predictor that can generate velocity profiles that represent different levels of driver aggressiveness. Basically, the velocity profiles generated by the EDM becomes the trajectory followed by the VD&PT simulator.

The EDM consists of three operating modes, as depicted *Figure 7-2*:

1. *Freeway Driving*: is activated when traffic is absent. If the ego velocity (v) is less than the speed limit (v_0), the rate of change in vehicle velocity is bounded by the maximum acceleration, a. The repulsive braking strategy in the freeway mode ensures that the vehicle never violates the speed limits and, if required, decelerates with maximum deceleration b. The acceleration exponent δ defines how aggressively the driver accelerates or decelerates. The speed limit (v_0) is offset by an additional calibration parameter (θ_{offset}) used to vary the degree of aggressiveness. In other words, according to this model, a relatively relaxed driver would drive the vehicle slightly below the speed limit and therefore would take longer to reach the destination.

2. *Car Following*: occurs in the presence of a lead vehicle. In this mode, as soon as a vehicle is detected, a braking strategy to ensure a safe gap from the vehicle ahead is determined by the parameter x_{safe}. Also, in this mode, the acceleration exponent δ defines the driver aggressiveness.
3. *Stop Mode:* is actuated when the distance to the stop sign becomes less than the critical braking distance (s_{brake}), the vehicle decelerates to a standstill a few meters before the stop sign. This critical distance is reported in eq.(7.3) is function of a calibration term $\left(\frac{c_1}{\delta}\right)$, used to capture the dependence of braking distance on aggressiveness.

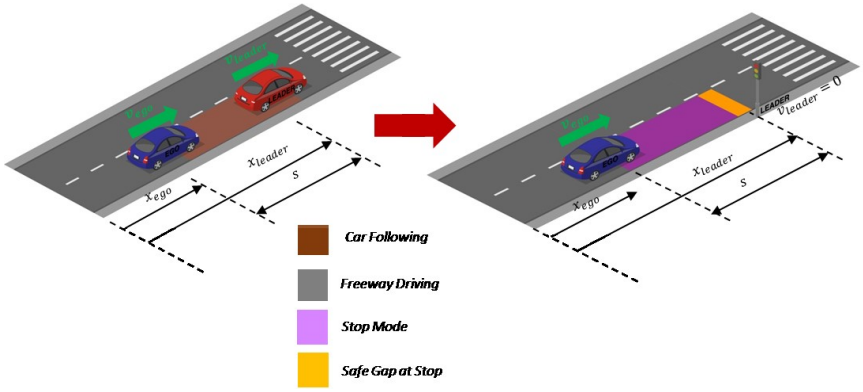

Figure 7-2 Overview of the EDM model with the Freeway and Car-Following mode [5].

The equations that define the EDM model are:

$$\frac{dv}{dt} = \begin{cases} a\left[1 - \left(\dfrac{v}{v_0 - \theta_{offset}}\right)^{\delta}\right] & if\ v < v_0\ \ [Freeway\ Driving] \\ -b\left[1 - \left(\dfrac{v_0 - \theta_{offset}}{v}\right)^{\delta}\right] & if\ v > v_0\ \ [Freeway\ Driving] \\ a\left[1 - \left(\dfrac{v}{v_{leader}}\right)^{\delta}\right] & if\ v < v_{leader}\ \ [Car\ Following] \\ -b\left[1 - \left(\dfrac{v_{leader}}{v}\right)^{\delta}\right] & if\ v > v_{leader}\ \ [Car\ Following] \\ -\dfrac{1}{b}\left(\dfrac{v^2}{2s}\right) & [Stop] \end{cases} \tag{7.1}$$

$$s = x_{leader} - x_{ego} - x_{safe} \tag{7.2}$$

$$s_{brake} = \left(1 + \frac{c_1}{\delta}\right)\frac{v^2}{2b} \tag{7.3}$$

Considering the SPaT information, a dynamic binary state (0: green, 1: red) is assigned to the traffic lights. The EDM keeps track of the upcoming traffic light state and stop sign location. Depending on the current state, the decision to pass-at-green or decelerate to a stop is taken.

7.2.1. Calibration of EDM

The described EDM was validated in real-world driving routes in [5], showing its capability in reproducing with accuracy the behavior of a driver. In this activity, the calibration of the EDM is carried out, identifying the value of tuning parameters $[a, b, \delta, c_1, \theta_{offset}]$ which allows to reproduce multiple and different drivers.

To this aim, 45 driver were collected on a test vehicle over an urban route chosen in Columbus, OH, reported in *Figure 7-3*. In particular, GPS and the measured vehicle velocity were collected through the OBDI II port of the vehicle using an ELM 327 Bluetooth interface and transmitted wirelessly over an Android device.

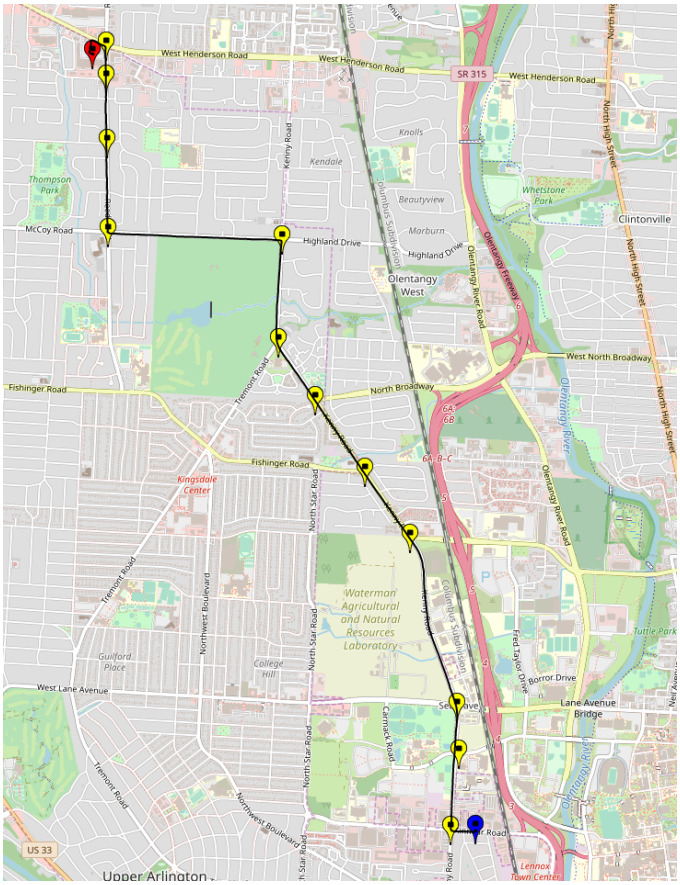

Figure 7-3 Route on Open Street Maps used for data collection and EDM calibration (blue marker: start, red marker: end, yellow: traffic lights) [9].

The identification of the parameters $[a, b, \delta, c_1]$ of the EDM was done considering only the acceleration and deceleration portions of the driving data. The parameter θ_{offset} is tuned separately considering only the cruising portions.

The EDM parameters are obtained by solving a least squares optimization problem aiming to minimize the Route Mean Square (RMS) error on the measured velocity profile:

$$RMS = \sqrt{\sum_{j=1}^{N}(V_{EDM_j}^2 - V_{data_j}^2)} \tag{7.4}$$

To solve the above optimization, a genetic algorithm was employed, where the minimum and maximum limits on the model parameters were adjusted to avoid that the optimal solution is located on a constraint. In *Figure 7-4,* a representative result of the EDM calibration is shown. The numerical velocity follows the experimental data quite well, with $R^2 > 0.9$, and the optimized parameters were found to be well within the typical limits found in literature [10],[11]. Some discrepancies occur in regions of the launch events. This is mainly because the real drivers tend to overshoot the vehicle speed above the limits, and then decelerate to be within the speed limits. In contrast, the EDM produces a velocity profile that always respects the speed limits, leading to the inaccuracy observed.

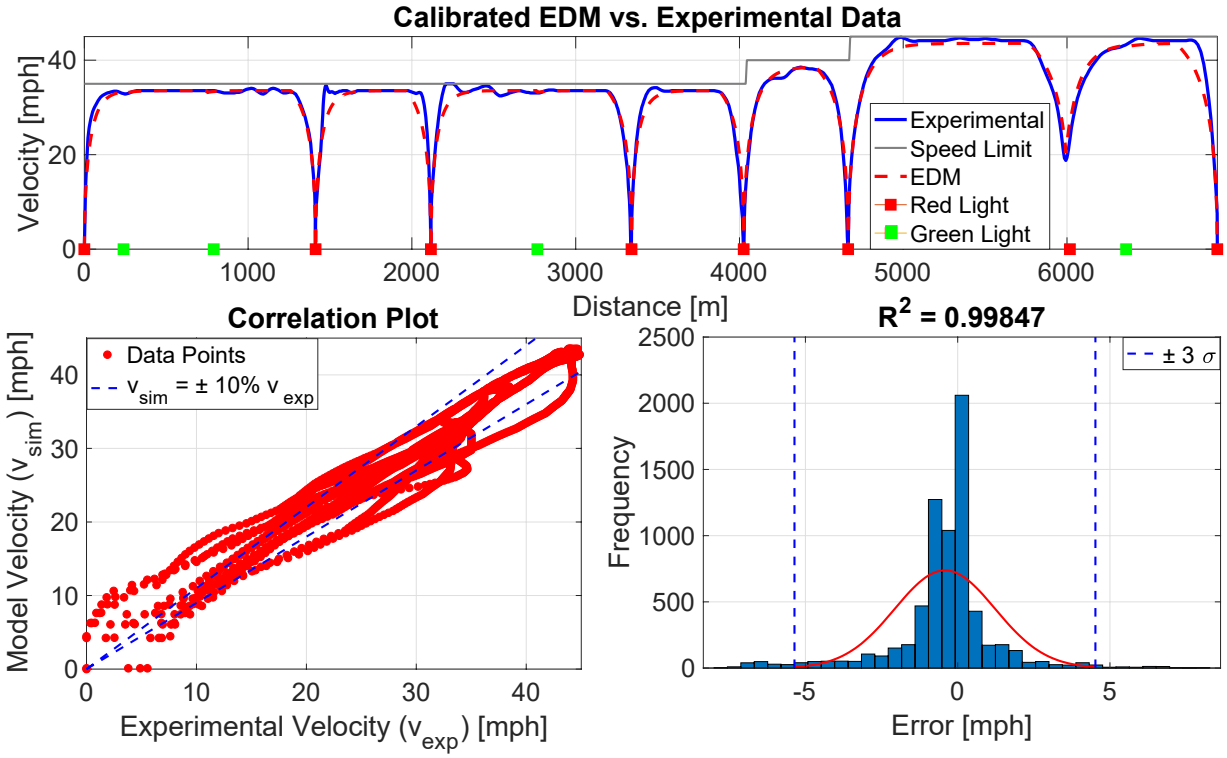

Figure 7-4 Representative, EDM calibration results for one of the drivers [9].

7.2.2. Correlation between EDM Parameters

Several studies have shown that the overall driving behavior may follow specific patterns [12],[13]. This means that each driver style, as well the five parameters of the EDM, can occur with unequal probability. Consequently, the distributions of the calibrated EDM parameters obtained from the data collection were studied, indicating that a, b, c_1, θ_{offset} and δ can be generally grouped into multiple distinct clusters. A representative result of this distribution is reported *Figure* 7-5, related to δ. Under this hypothesis, different literatures, such as in [14], approximate the 4 parameters as a function δ, leading to a unified metric of the driver aggressiveness.

Figure 7-5 shows three dominant peaks in the frequency of δ, typical of a multi-modal distribution. These modes can be considered as different levels of aggressiveness for the driver data for calibration: relaxed ($\delta = 2$), normal ($\delta = 3.5$) and aggressive ($\delta = 4.5$). The dashed line in *Figure* 7-5 represents a non-parametric probability density function known as the Kernel Density Estimator (KDE) [15], sed to fit the histogram plot. The KDE algorithm is generally used when a parametric distribution cannot accurately describe the data and is often applied to bivariate distributions.

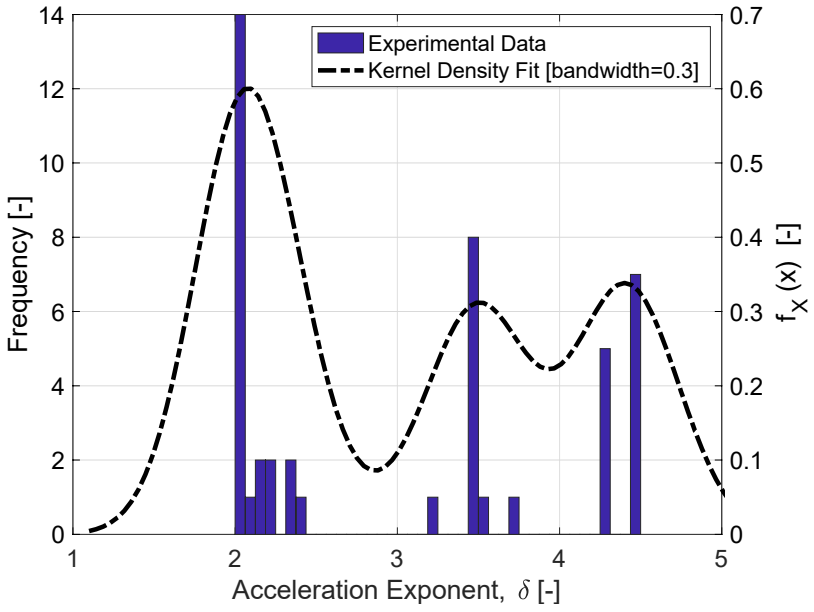

Figure 7-5 Distribution of acceleration exponent δ and probability distribution function fit for the calibrated δ [9].

In *Table 7.1*, the numerical correlations between EDM parameters and the related coefficients of determination are reported. Whereas the coefficient of determination obtained for some of the regressions is relatively low, it is important to note that using a unique driver parameter the computational effort to generate the driver population can be drastically reduced.

Additionally, the process followed is generally applicable, and that results could significantly improve if more driver data were collected.

Table 7.1 Correlation of EDM parameters as a function of acceleration exponent (δ) and coefficient of determination (R^2) [9]

Parameters	**Equations**	R^2
$a(\delta)$	$-0.055 + 0.924\delta - 0.0862\delta^2$	0.827
$b(\delta)$	$-0.453 + 0.570\delta - 0.041\delta^2$	0.734
$c_1(\delta)$	$5.30e^{-0.422\delta+0.186}$	0.730
$\theta_{offset}(\delta)$	$2.04e^{-0.753\delta+0.225}$	0.792

7.3. VD&PT Optimization for CAVs

In CAVs, the control unit, thanks to the knowledge of look-ahead information, has to ensure the minimization the fuel consumption over the entire trip. In particular, for the hybrid vehicle, this can be reached by jointly optimizing the vehicle velocity profile and the power-split of the motor units. To this aim, in the VDP&PT model, a DP algorithm has been developed at OSU [4]. In particular, the DP model equations are discretized and expressed in distance-based coordinates to properly handle the route-dependent constraints, such as stop signs, or traffic lights. The cost function of the DP is reported below:

$$L\big(u(s_{1:N})\big) = \sum_{i=1}^{N} \left\{ \gamma \cdot \frac{\dot{m}_{f,i}(x_i(s_i), u_i(s_i), s_i)}{\dot{m}_f^{norm}} + (1-\gamma) \right\} \cdot \frac{\Delta s}{\bar{V}_{veh,i}(s_i)} \tag{7.5}$$

where γ is a weighting factor to penalize the travel time versus fuel consumption, ensuring a non-trivial solution of this problem $\dot{m}_f^{norm}$s a normalized factor, necessary to obtain comparable orders of magnitude between each terms of the cost function. Additionally, x and u are the state and the control variable, respectively.Δs is the distance traveled and $\bar{V}_{veh}(s_i)$ is the average velocity over one step. Finally, γ can be also considered as a penalty factor, which can assume values between zero and the unit. This parameter is used to trade-off the fuel consumed and the time traveled, namely a driver-desired aggressiveness parameter. The following constraints are imposed on the optimization problem:

$$\begin{gathered} V_{veh,min}(s_i) \le V_{veh}(s_i) \le V_{veh,max}\ (s_i) \\ SOC_{min} \le SOC(s_i) \le SOC_{max} \\ SOC(s_N) = SOC(s_0) \\ T_{eng,min} \le T_{eng}(s_i) \le T_{eng,max} \\ T_{bsg,min} \le T_{bsg}(s_i) \le T_{bsg,max} \\ x(s_{i+1}) = f_{PT}(x(s_i), u(s_i), \Delta s, s_i) \end{gathered} \tag{7.6}$$

7.4. Monte Carlo Simulation

Generally the Monte Carlo simulation is used to understand the impact of uncertainty and risk, and to model the probability of different outcomes that cannot be easily predicted because of random variables [16],[17]. Hence, a large-scale Monte Carlo simulation is selected for this research activity to analyze the impact on the fuel consumption and travel time due to two randomly generated inputs, driver aggressiveness and the SPaT.

For the baseline case, a set of 2500 simulations were executed, varying the two random variables. In particular, 50 drivers were generated according to the probability distribution of δ provided by KDE.

As shown in the previous section, parameter selection of δ results into a unique combination of parameters that defines a specific driver behavior. Whereas, the SPaT information are defined with a the discrete probability (probability mass function, $(f(k;p))$ of a traffic light in which value 1 with probability, p (red) and value 0 with probability $q = 1 - p$ (green):

$$\mathrm{P(TL = 1) = p = 1 - P(TL = 0) = 1 - q} \tag{7.7}$$

$$\mathrm{f(k;p) = p^k(1-p)^{1-k}} \;\; \forall \; \mathrm{k}\epsilon\{0,1\} \tag{7.8}$$

In particular, 50 random signal phase profiles were generated without bias between green or red phase ($p = 50$). A pre-imposition of the signal phasing means that each generation of random numbers creates a unique variation of the route. For the VD&PT optimizer case, 700 simulations were performed considering as the only random variable the signal phase information from the traffic light (100 different combination). To obtain a similar range of travel time values as the baseline, 7 values of γ are identified.

7.5. Results and conclusion

The Monte Carlo simulation outcomes are reported in *Figure 7-6* for both baseline and optimizer model with respect to fuel consumption and travel time. Considering the baseline, a huge variability in both the fuel consumption and travel time is visible, confirming the impact of (randomly) varying the driving styles and signal phase information. The green stars (Real-World Driver) in *Figure* 7-6 are the results of vehicle simulation using a forward approach with EDM parameters carried out from the experimental data over the same route. The majority of the green points are inside the cloud of the results of the Monte Carlo simulation, demonstrating the consistency of the analysis.

Concerning the optimizer, a lower spread of travel time and fuel is visible, mainly due to the absence of huge variability induced by different driver behavior.

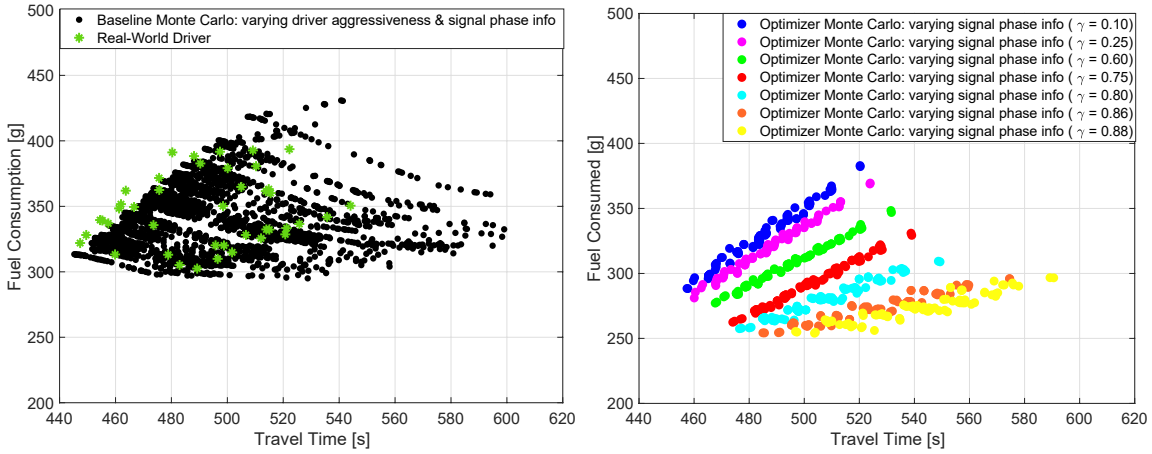

Figure 7-6 Monte Carlo Simulation for real-world drivers and VD&PT Optimizer (DP) [9].

To assess a consistent comparison between optimizer and baseline, the spread of points for γ equal to 0.75 is chosen for the optimizer model and subsequently for the baseline the points with the same spread of travel time is only considered. The distribution of travel time and the fuel consumption of selected points is reported in *Figure 7-7*, whit the related normal distribution that, in most cases, closely fits the histogram. The mean and standard deviation obtained from this normal distribution are then considered at the yardstick of the comparison between the baseline and the optimizer.

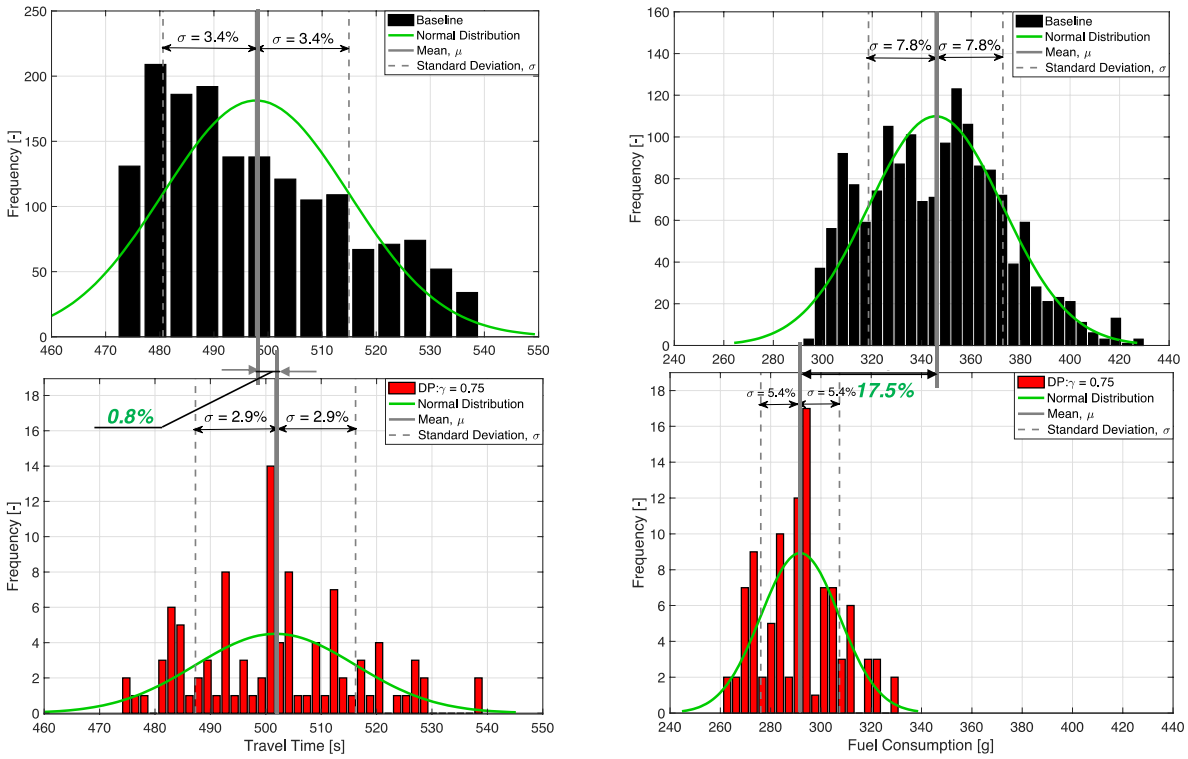

Figure 7-7 Comparison of travel time and fuel consumption obtained from the Monte Carlo simulation for baseline and DP (γ=0.75) [9].

Although, the baseline tends to be faster than the optimizer by 0.3%-1.3% with maximum likelihood of 0.8%, the fuel consumption benefit from the optimizer is consistently higher with a range of 15.1%-19.9% over the baseline and with maximum likelihood indicating 17.5%.

The proposed methodology confirms the huge variability induced on the fuel consumption from different driving behavior and SPaT, but nevertheless it is able to estimate a range of fuel saving potential of CAVs, which is found to be around 15%-20% over the considered baseline.

This analysis can be further extended adding the effect of traffic density information from a simulator such as SUMO or adding more driving data over multiple route to reduce the route dependency on the analysis.

Despite this work was focused mainly on a methodology for benchmarking the fuel consumption, it is possible to roughly estimate the CO_2 along this cycle. Indeed, using the same CO_2 factor emission considered in the previous section and the mean value of the fuel consumed, the maximum likelihood of CO_2 for the optimizer architecture is equal to 128 g/km. This value is still quite far away from the EU target of 80 g/km, but it has to remark that this limit is set for a specific drive cycle. On the contrary, the energy optimization with look-ahead capabilities is conceived to obtain fuel benefit on real-word driving cycles. Consequentially, the results that should be emphasizing is that leveraging connectivity, and specifically knowledge of the future route and speed limits, in the context of energy and speed optimization for a Level 2 ADAS system allows for optimizing fuel economy by 15%-20% compared to vehicle conventional vehicle with no road preview.

The entire research work is part of the ARPA-E NEXTCAR (Next-Generation Energy Technologies for Connected and Automated On-Road Vehicles) program. The aim of the project is to demonstrate that it is possible to achieve at least a 20% reduction in the fuel consumption of future CAVs compared to a baseline vehicle, without these VD&PT control technologies. The partners of the project include (OSU), which is the project lead, Delphi Technologies, Aptiv, Tula Technology, and the Transportation Research Center (TRC).

The author is grateful to Professor Giorgio Rizzoni and Marcello Canova for the opportunity of work at CAR and to the ARPA-E NEXTCAR team at OSU (Shreshta Rajakumar Deshpande, Shobhit Gupta, Dennis Kibalama, Zhaoxuan Zhu, David Cooke).

References

[1] Thomas, D., Li, H., Wang, X., Song, B., Ge, Y., Yu, W. Ropkins, K., "Comparison of Tailpipe Gaseous Emissions for RDE and WLTC Using SI Passenger Cars," SAE International, 2017, doi:10.4271/2017-01-2391.

[2] https://arpa-e.energy.gov/?q=arpa-e-programs/nextcar.

[3] Metropolis, N. Ulam, S., "The monte carlo method," Journal of the American statistical association, 44(247), 335-341, 1949.

[4] Olin, P., Aggoune, K., Tang, L., Confer, K., Kirwan, J., Deshpande, S.R., Gupta, S., Tulpule, P., Canova, M. Rizzoni, G., "Reducing Fuel Consumption by Using Information from Connected and Automated Vehicle Modules to Optimize Propulsion System Control," SAE Technical Paper 2019-01-1213, 2019, doi:10.4271/2019-01-1213.

[5] Gupta, S., Deshpande, S.R., Tulpule, P., Canova, M. Rizzoni, G., "An Enhanced Driver Model for Evaluating Fuel Economy on Real-World Routes," IFAC-PapersOnLine, 52(5), 574-579, 2019, doi:10.1016/j.ifacol.2019.09.091.

[6] Eisazadeh-Far, K., Younkins, M., "Fuel economy gains through dynamic-skip-fire in spark ignition engines, SAE Technical Paper 2016-01-0672, 2016, doi:10.4271/2016-01-0672.

[7] Sciarretta, A., Back, M., Guzzella, L., "Optimal Control of Parallel Hybrid Electric Vehicles," IEEE Transactions on Control Systems Technology 12(3):352-363, 2004, doi:10.1109/TCST.2004.824312.

[8] Liu, Z., Ivanco, A., & Filipi, Z. S. "Impacts of real-world driving and driver aggressiveness on fuel consumption of 48V mild hybrid vehicle," SAE International Journal of Alternative Powertrains 5(2), 249-258, 2016, doi:10.4271/2016-01-1166.

[9] Gupta, S., Deshpande, S.R., Tufano, D., Canova, M., Rizzoni G., at all "Estimation of Fuel Economy on Real-Word Routes for Next-Generation Connected and Automated Hybrid Powertrain," SAE Technical paper, 2020.

[10] Hiraoka, T., Kunimatsu, T., Nishihara, O. and Kumamoto, H., "Modeling of driver following behavior based on minimum-jerk theory" In Proc. 12th World Congress ITS, 2005.

[11] Itkonen, T.H., Pekkanen, J., Lappi, O., Kosonen, I., Luttinen, T. and Summala, H., "Trade-off between jerk and time headway as an indicator of driving style," PloS one, 12(10):e0185856, 2017,.doi:10.1371/journal.pone.0185856.

[12] Ping, P., Qin, W., Xu, Y., Miyajima, C., and Takeda, K., "Impact of Driver Behavior on Fuel Consumption: Classification, Evaluation and Prediction Using Machine Learning," IEEE Access,7, 78515-78532, 2019, doi:10.1109/ACCESS.2019.2920489.

[13] Higgs, B., Abbas, M., "Segmentation and clustering of car-following behavior: Recognition of driving patterns," IEEE Transactions on Intelligent Transportation Systems, 16(1), 81-90, 2014, doi:10.1109/TITS.2014.2326082.

[14] Treiber, M., Hennecke, A., Helbing, D., "Congested Traffic States in Empirical Observations and Microscopic Simulations," Physical Review E 62(2), 2000, doi:10.1103/PhysRevE.62.1805.

[15] Santhosh, D., & Srinivas, V. V. "Bivariate frequency analysis of floods using a diffusion based kernel density estimator," Water Resources Research,49 (12), 8328-8343,2013, doi:10.1002/2011WR010777.

[16] Bird, G.A., 1981. Monte-Carlo simulation in an engineering context. Progress in Astronautics and Aeronautics, 74, pp.239-255.

[17] Papadopoulos, C.E. and Yeung, H., "Uncertainty estimation and Monte Carlo simulation method," *Flow Measurement and Instrumentation* 12(4), pp.291-298, 2001.

8. Conclusions

In this research activity, two innovative SI engines, eventually suitable for hybrid powertrains with a strongly reduced CO_2 impact, are numerically investigated, through a hierarchical simulation-level approach. The establishment of the state of art of conventional ICE-based propulsion system was defined with a downsized turbocharged VVA 2-cylinder engine. In particular, the impact of increased CR, external low-pressure cooled EGR, and ported Water Injection (WI) on CO_2 emission reduction along a WLTC was evaluated. Whereas, an innovative 4-cylinder SI engine, equipped with an active pre-chamber ignition system, capable to work in ultra-lean conditions in its whole operating range, was proposed as an alternative solution. Here, to assess the CO_2 emissions along the WLTC, HEV and PHEV architecture were considered. Additionally, the potential fuel economy benefits from Connected and Automated Vehicles (CAV), was investigate through a numerical methodology able to benchmark these last on real world-scenario.

To this aim, a 1D model of the above described engines was developed according to their main features, within a 0D/1D modelling environment. In particular, for the conventional engine, a quite-standard version of the fractal combustion model was coupled as a user procedure to the 1D code. Whereas, for the pre-chamber engine architecture, the development of a dedicated model was firstly required, able to describe the basic physics behind such a system. In particular, the original model, still based on the fractal theory, was enhanced to handle all the basic phenomena occurring in an engine fitted with a PC, such as mixture preparation, turbulence evolution, flame area enhancement, burn rate development, etc.

Subsequently, once developed, both engine models were tuned and validated according to 3D calculations and experimental data, by identifying a single set of tuning constants. The conventional engine was validated against 284 operating points, predicting with an allowable error band ±5% the tested engine performance parameters, such as combustion phasing, air flow rate or BSFC. For the pre-chamber engine, the numerical results were verified against 39 experimental data, considering pressure traces in both PC and MC, and against the global engine performance parameters. In particular, the experimental campaign referred to a prototype single-cylinder engine, including either a conventional spark plug ignition device, or a pre-chamber. In the latter case, both a passive and active PC was considered, with different injected fuels, namely CNG and H_2. The results obtained demonstrated that with the enhanced fractal model it is possible to reliably predict both the engine architectures (CSP and PCSP), with a unique engine-dependent set of tuning constants.

These outcomes further strengths the robustness of the fractal approach, leading to the conclusion that that the physics behind this model is accurate enough to allow its use in a predictive way.

Once validated, a Rule-Based (RB) calibration strategy was also set up for both the engines. The RB aims to properly define the optimal control parameter setting for each operating condition, trying to mimic the standard experimental calibration procedure at the test bench. The RB, verified against the outcomes of an external optimizer, is designed to identify close-to-optimal control variables aiming to minimize the overall fuel consumption.

Subsequently, the RB approaches were used to compute some performance/calibration parameters over the whole engine operating plane. These last were embedded in a vehicle simulation with the aim to quantify the CO_2 emission over a WLTC. The downsized turbocharged 2-cylinder engine was tested in a conventional powertrain/vehicle, while a parallel/series HEV/PHEV architecture was considered for the pre-chamber one. In this last case, a dedicated EMS was also developed during this research activity. The latter is an off-line local optimization procedure, for a parallel/series hybrid vehicle, able to minimize the CO_2 emissions along the driving cycle. The developed strategy (ETESS) was compared against the PMP well-assessed global optimization strategy, demonstrating a similar management of the control units, but a slightly higher CO_2 emission along the WLTC. However, the lower number of possible configurations to be analysed with the ETESS, namely pure thermal and pure electric driving instead of different power-split options, allowed to drastically reduce the computational time respect to the PMP. Consequently, a possible future step could be the implementation of the ETESS for an on-line application.

The results carried out in this research activity show that the ICE-based system can reach 94.81g/km CO_2. However, this value is still far away from the EU target of 80 g/km CO_2, although the engine is coupled to a very lightweight vehicle (segment A). On the contrary, the investigated pre-chamber engine, with its maximum Indicted Thermal Efficiency (ITE) higher than 50%, allows to attain a CO_2 emission of 43 g/km along the WLTC when embedded in a PHEV architecture (segment C). However, it must empathize this benefit is reached mainly due to the WLTC procedure, for which the possibility to realize an entire cycle in pure electric mode, reduces drastically the overall CO_2 emission. A more representative value is, indeed, the one related to the HEV configuration with a CO_2 emission equal to 88 g/km. This is a very impressive value, considering a segment C vehicle, leading to the conclusion that the combination of those technologies, namely a highly efficient internal combustion engine and a hybrid powertrain, is the most affordable solution. All the mentioned benefit, as also shown in this PhD Thesis, can be further improved through a connected and autonomous vehicle.

As a last conclusion, it must be stressed that, especially referring to the pre-chamber engine, the methodology followed in this PhD Thesis, resorting to model development, validation, engine calibration and vehicle simulation, was able to concretely support the entire engine/vehicle development process, starting from scratch up to detailed engine design and components' sizing.